

**RECONSTRUCTION OF TECTONOTHERMAL HISTORY OF THE  
SOUTHWESTERN HIGHLAND COMPLEX, SRI LANKA: IMPLICATION OF  
INTERNAL TEXTURES AND GEOCHRONOLOGY OF ZIRCON AND MONAZITE**

*A research report submitted to*

*The Department of Geosciences, Faculty of Science and Engineering, Shimane University*

*In partial fulfillment for the Doctoral Science Degree*

*By*

Dadayakkarage Nuwan Sanjaya Wanniarachchi

Under supervision of

Professor Masahide Akasaka

Department of Geosciences,

Faculty of Science and Engineering,

Shimane University, Nishikawtsu-cho 1060,

Matsue 690-0824, Japan.

August 2016

**RECONSTRUCTION OF TECTONOTHERMAL HISTORY OF THE  
SOUTHWESTERN HIGHLAND COMPLEX, SRI LANKA: IMPLICATION OF  
INTERNAL TEXTURES AND GEOCHRONOLOGY OF ZIRCON AND MONAZITE**

Dadayakkarage Nuwan Sanjaya Wanniarachchi

Department of Geosciences,

Faculty of Science and Engineering,

Shimane University, Nishikawtsu-cho 1060,

Matsue 690-0824, Japan.

August 2016

<b>CONTENTS</b>	<b>Page</b>
ACKNOWLEDGEMENTS	1-2
ABSTRACT	3-5
<b>I. INTRODUCTION</b>	<b>6-13</b>
I-1. SIGNIFICANCE AND PURPOSE OF THE STUDY	13-15
<b>II. STUDY AREA AND GEOLOGY</b>	<b>16</b>
II-1. STUDY AREA	16
II-2. GEOLOGY OF SOUTHWESTERN HIGHLAND COMPLEX AND STUDY AREA	17-19
II-3. SAMPLE LOCALITY	19-24
<b>III. SAMPLES</b>	<b>25-28</b>
<b>IV. METHODS</b>	<b>29</b>
IV-1. PETROGRAPHY	29
IV-2. CHEMICAL ANALYSIS OF MINERALS AND OBSERVATIONS OF INTERNAL TEXTURES OF ZIRCON AND MONAZITE USING ELECTRON MICROPROBE ANALYZER	29-30
IV-3. LASER ABLATION INDUCTIVELY COUPLED PLASMA MASS SPECTROMETRY (LA-ICP-MS) ANALYSIS FOR ZIRCON	30
IV-4. U-Th-TOTAL Pb ISOCHRONAL ANALYSIS FOR MONAZITE	31-33
<b>V. RESULTS</b>	<b>34</b>
V-1. SAMPLE DESCRIPTION AND PETROGRAPHY	34-40
V-2. MINERAL CHEMISTRY OF REPRESENTATIVE MINERALS	41
V-2-1. CHEMICAL COMPOSITION OF GARNET	41-44
V-2-2. CHEMICAL COMPOSITION OF BIOTITE	45-49
V-2-3. CHEMICAL COMPOSITIONS OF PYROXENE AND AMPHIBOLE	50-51
V-3. CHEMICAL COMPOSITION, MORPHOLOGY, DETRITAL CORES AND OVERGROWTHS, INTERNAL TEXTURES AND CHRONOLOGY OF ZIRCON	52
V-3-1. CHEMICAL COMPOSITION OF ZIRCON	52-54
V-3-2. MORPHOLOGY OF ZIRCONS	55
V-3-3. ABUNDANCES OF DETRITAL CORE IN ZIRCON IN EACH ROCK TYPE	55-58
V-3-4. INTERNAL TEXTURES: DETRITAL CORES AND OVERGROWTHS	59
V-3-4-1. GARNET-BIOTITE GNEISS (17-24GB, 14-21GB, 07- 10GB, 11-17GB, AND 03-04GB).	59-61
V-3-4-2. GARNET-BIOTITE-CORDIERITE GNEISS (23- 32CO)	62
V-3-4-3. HORNBLende-BEARING CHARNOCKITIC GNEISS (10-16B) AND CHARNOCKITIC GNEISS (04-05C, 02-02C, AND 20-30C)	62-63

V-3-5. GEOCHRONOLOGY AND INTERNAL TEXTURES OF ZIRCON	64
V-3-5-1. ZIRCONS IN THE 07-10GB GARNET-BIOTITE GNEISS	64-65
V-3-5-2. ZIRCONS IN 17-24GB	65-71
V-4. CHEMICAL COMPOSITION, INTERNAL TEXTURES, AND CHRONOLOGY OF MONAZITE	72
V-4-1. INTERNAL TEXTURES AND CHEMICAL COMPOSITIONS OF MONAZITE	72-74
V-4-2. CORE-RIM ZONED MONAZITE	75-79
V-4-3. INHERITED CORE-BEARING MONAZITE	80-84
V-4-4. COMPLEXLY ZONED MONAZITE	85-86
V-4-5. OSCILLATORY ZONED MONAZITE	87-88
VI. DISCUSSION	89
VI-1. GEOTHERMAL CONDITIONS OF HOST ROCKS	89-97
VI-2. SOURCE OF DETRITAL CORES OF ZIRCON	98-102
VI-3. FORMATION OF OVERGROWTHS AND INTERNAL TEXTURES OF ZIRCON	102-103
VI-4. INTERNAL TEXTURES AND CHRONOLOGY OF MONAZITE	104-106
VI-5. AGES OF MULTITHERMAL EVENTS DETERMINED ZIRCON AND MONAZITE CHROLOGICAL DATA	107-109
VI-6. RECONSTRUCTION OF TECTONOTHERMAL HISTORY OF THE SWHC	110-114
VII. CONCLUSIONS	115-117
REFERENCES	i-x
APPENDICES	xi-xxxii

<b>FIGURES</b>	<b>Page</b>
<b>Figure 1.</b> Simplified geological map of Sri Lanka showing major lithotectonic units (modified after Cooray (1994)).	7
<b>Figure 2.</b> Detrital core (dc) and overgrowth patterns of metamorphic zircons which were proposed by Vavra et al., 1996 as: rd; radial sector zoning, ft; fir-tree sector zoning, bd; planer growth banding, rs; resorption, eu; euhedral surfaces, sd; discrete peripheral zones. Pidgeon et al., 1998 used a schematic diagram to explain the changes from igneous oscillatory zoning into transgressive lobes and patches in zircon (a-e).	12
<b>Figure 3.</b> Location map of the samples of study area showing the major roads, district boundaries and drainage patterns. (Sri Lankan coordinate system is used) (modified after geological maps of the Geological Survey and Mines Bureau of Sri Lanka)	16
<b>Figure. 4</b> Geology Map of the studied sample area (modified after geological maps of the Geological Survey and Mines Bureau of Sri Lanka; geology data from 1:100000, geology map sheets 16 and 19)	21
<b>Figure. 5</b> Geology Map of the studied sample area (modified after geological maps of the Geological Survey and Mines Bureau of Sri Lanka; geology data from 1:100000, geology map sheets 16 and 19)	22
<b>Figure 6.</b> Simplified Geology Map of the studied sample area (modified after geological maps of the Geological Survey and Mines Bureau of Sri Lanka; geology data from 1:100000, geology map sheets 16 and 19)	24
<b>Figure 7.</b> Peak overlap simulations applying the program VIRTUAL WDS by Reed and Buckley (1996) (modified after Scherrer et al., 2000). The figure visualizes the critical interferences relevant to Th-U-Pb dating of monazite with the EPMA. (A) Y and Th interference on PbM $\alpha$ . (B) U and Ce interference in PbM $\beta$ . (C) Th interference on UM $\alpha$ . (D) Th interference on UM $\beta$ .	32
<b>Figure 8.</b> Background interference corrections.	33
<b>Figure 9.</b> Representative petrographic images. (a), (c), and (e) are optical microscopic images in plane-polarized light, and (b), (d) and (f) are back-scattered electron (BSE) images. (a) inclusion-free garnet porphyroblast and matrix monazite (17-24GB). (b) inclusion-bearing porphyroblastic garnet (17-24GB). (c) garnet porphyroblasts with inclusion-rich cores and inclusion-poor rims (11-17GB). (d) garnet porphiroblast and monazite in matrix (23-32Co). (e) garnet with monazite inclusions (17-24GB). (f) garnet porphiroblast in matrix (03-04GB).	37
<b>Figure 9 (cont.).</b> Representative petrographic images. (g), (h), (i), and (k) are optical microscopic images in plane-polarized light, (l) is optical microscopic images in cross-polarized light, and (j) is a hand specimen image. (g) reaction texture of garnet breakdown (10-16B). (h) second generation garnet (11-17GB).	38

(i) zircon around biotite layer and zircon inclusions in biotite (07-10GB). (j) spinel-rich and spinel-poor layers in garnet-biotite-cordierite gneiss (23-32Co). (k) fine-grained zircon inclusions in cordierite (23-32Co). (l) corundum inclusions in magnetite (23-32Co).

**Figure 9 (cont.).** Representative petrographic images. (n), (o), and (p) are optical microscopic images in plane-polarized light, and (m) is optical microscopic images in cross-polarized light. (q) is back-scattered electron (BSE) images. (k) reaction texture of magnetite + spinel + quartz  $\leftrightarrow$  cordierite (23-32Co). (l) garnet + biotite + clinopyroxene assemblage (04-05C). (m) The typical mineral assemblage of biotite-bearing charnockitic gneiss (20-30C). (n) The typical mineral assemblage of charnockitic gneiss without biotite (02-02C). (o) zircon inclusions in plagioclase (17-24GB). 39

**Figure 10.** Analysis positions in garnet grains from 17-24GB and 23-32 Co samples. These two figures are representative examples of selecting three types of biotites: (1) Bt (i) – biotite as inclusions; (2) Bt (e) – biotite at edges of garnets; (3) Bt (m) – biotite in matrix. 42

**Figure 11.** Variations of garnets in garnet-biotite gneiss and garnet-bearing cordierite gneiss. A. The variation of the end member components of the garnet according to the Figure 10 17-24GB. B. Grossular:pyrope:almandine-ratios (mol. %) in garnet for different samples. 43

**Figure 12.** Occurrences of garnet and biotite in the studied samples (a) 17-24GB garnet-biotite gneiss, (b) 23-32Co garnet-bearing cordierite gneiss, (c) 14-21GB garnet-biotite gneiss, (d) 07-10GB garnet-biotite gneiss, (e) 04-05C garnet-bearing cordierite gneiss, (f) 11-17GB garnet-biotite gneiss, and (g) 03-04GB garnet-biotite gneiss. 47

**Figure 13.** Backscattering images of orthopyroxene, clinopyroxene and hornblende in the samples 02-02C (a), 20-30C (b), 04-05C (c), and 10-16B (d). 50

**Figure 14.** Chemistry of altered or metamictized area of zircon. (a) BSE image and elemental distribution maps for Y, Hf, Zr, Si, and Ca; (b) Al (wt.%)–Ca (wt.%) relation; (c) Ca (wt.%) and Al (wt.%) contents against SiO<sub>2</sub> (wt.%). 54

**Figure 15.** Length to width ratios of zircon grains from the Southwestern Highland Complex 58

**Figure 16.** Cathodoluminescence images (CL1, CL2, CL4, CL7-CL11, CL14, and CL15) and backscattered electron images (Nos. 3, 5, 6, 12, and 13) of representative zircon grains. Scale bars are 50  $\mu$ m. dc: detrital core, eu: euhedral surface, sd: peripheral zone, bd: planar banded pattern, ft: fir-tree texture, rd: radial zone. CL1: rounded with transgressive zoning and three overgrowths. CL2: rounded detrital core with oscillatory zoning and four overgrowths. No. 3: subhedral detrital core with transgressive zoning. CL4: subhedral detrital core with oscillatory zoning. No. 5: detrital core with two overgrowths; the second overgrowth cuts the planar banding of the first. No. 6: rounded detrital core with transgressive zoning and five overgrowths 61

demarcated by fracture-truncated boundaries. CL7: doubled core and overgrowths. CL8-CL11, Nos. 12 and 13, CL14 and CL15: zircon grains showing cores with different ages and overgrowths.

**Figure 17.** Cathodoluminescence image (CL8) and backscattered electron images (Nos. 1-8) of representative zircon grains. Scale bars are 20  $\mu\text{m}$ . bd: planar banded pattern, ft: fir-tree texture, rd: radial zone. Nos. 1, 2, and 3: euhedral grains with several zoning in garnet-biotite-cordierite gneiss. No. 4: a grain from charnockitic gneiss lacking a detrital core. No. 5: a grain from charnockitic gneiss with four growth zonings. No. 6: well-rounded and fine-grained zircon in the detrital core. No. 7: skeletal detrital core. No. 8 and CL8: a grain with three sub-stages defined by fir-tree texture, radial zone, and planar banding. 63

**Figure 18.** (a) Th/U variation with  $^{207}\text{Pb}/^{206}\text{Pb}$  ages (Ma) in 07-10GB. (b) Concordia diagram of zircons from 07-10GB. (c) Relative probability diagrams of zircon population (d) Th/U variation with  $^{207}\text{Pb}/^{206}\text{Pb}$  ages (Ma) in 17-24GB. (e) Concordia diagram of zircons at positions having Th/U ratio  $<0.1$  in 17-24GB. (f) Concordia diagram of zircons at positions having Th/U ratio of 0.1-0.3 (g) Concordia diagram of zircons at positions having Th/U ratio  $>0.3$  67

**Figure 19.** BSE images of monazites. (a), (b), and (c) core-rim zoned monazite. (d),(e), and (f) inherited core-bearing monazite. (g) complexly zoned monazite. (h) oscillatory zoned monazite. 73

**Figure 20.** X-ray map images showing the distribution of U, Th, Pb, and Y in the core-rim zoned monazites (a-1, a-2, a-3, a-4; b-1, b-2, b-3, b-4). 76

**Figure 21.**  $\text{ThO}_2^*$ -PbO diagrams showing U-Th-total Pb isochrons and determined isochron ages (Suzuki and Adachi method) 76

**Figure 22.**  $\text{ThO}_2^*$ -PbO diagrams showing U-Th-total Pb isochrons and determined isochron ages (Suzuki and Adachi method) 77

**Figure 23.**  $\text{ThO}_2^*$ -PbO diagrams showing U-Th-total Pb isochrons and determined isochron ages (Montel method) 77

**Figure 24.** X-ray map images showing the distribution of U, Th, Pb, and Y in the core-rim zoned monazites (c-1, c-2, c-3, c-4). 79

**Figure 25.**  $\text{ThO}_2^*$ -PbO diagrams showing U-Th-total Pb isochrons and determined isochron ages (Suzuki and Adachi method) 79

**Figure 26**  $\text{ThO}_2^*$ -PbO diagrams showing U-Th-total Pb isochrons and determined isochron ages (Montel method) 79

**Figure 27.** X-ray map images showing the distribution of U, Th, Pb, and Y in the inherited core-bearing type monazites (d-1, d-2, d-3, d-4; e-1, e-2, e-3, e-4; f-1, f-2, f-3, f-4). 82

<b>Figure 28.</b> ThO <sub>2</sub> *-PbO diagrams showing U-Th-total Pb isochrons and determined isochron ages (Suzuki and Adachi method)	83
<b>Figure 29.</b> ThO <sub>2</sub> *-PbO diagrams showing U-Th-total Pb isochrons and determined isochron ages (Suzuki and Adachi method)	83
<b>Figure 30.</b> ThO <sub>2</sub> *-PbO diagrams showing U-Th-total Pb isochrons and determined isochron ages (Suzuki and Adachi method)	84
<b>Figure 31.</b> ThO <sub>2</sub> *-PbO diagrams showing U-Th-total Pb isochrons and determined isochron ages (Montel method)	84
<b>Figure 32.</b> ThO <sub>2</sub> *-PbO diagrams showing U-Th-total Pb isochrons and determined isochron ages (Suzuki and Adachi method)	86
<b>Figure 33</b> ThO <sub>2</sub> *-PbO diagrams showing U-Th-total Pb isochrons and determined isochron ages (Montel method)	87
<b>Figure 34.</b> ThO <sub>2</sub> *-PbO diagrams showing U-Th-total Pb isochrons and determined isochron ages (Suzuki and Adachi method)	87
<b>Figure 35</b> ThO <sub>2</sub> *-PbO diagrams showing U-Th-total Pb isochrons and determined isochron ages (Montel method)	88
<b>Figure 36.</b> Distribution of metamorphic temperatures in the studied area which is the same as the study area by Sajeev and Osanai (2005). Red lines indicate the current study. Black colored contours indicate the contours proposed by Sajeev and Osanai (2005). Green contouring is according to the Faulharber and Raith (1991) study for pressure.	97
<b>Figure 37.</b> Schematic diagram for growth stages in zircon. The sketches of representative zircons in Figure 16 are shown as they varying from each age ranges. The darker gray shows the core and lighter gray shows overgrowths. Grain descriptions follows the Figures 16 and 17 captions.	101
<b>Figure 38.</b> The summarized data plotted on the map to show the relationship of the temperature, monazite ages, and zircon ages	110
<b>Figure 39.</b> The position of Sri Lanka in Gondwana (modified after Dissanayake and Chandrajith, 1999). CHC, Central Highland Complex; KKB, Kerala Khondalite Belt; SWHC, South Western Highland Complex; VC, Vijayan Complex; WC, Wannai Complex.	113
<b>Figure 40.</b> PbO-ThO <sub>2</sub> * relation of zircons from the metamorphic rocks from the Southwestern Highland Complex and Kerala Khondolite Belt (KKB) in South India.	114



<b>TABLES</b>	<b>Page</b>
<b>Table 1</b> Studied rock samples.	25-28
<b>Table 2</b> Mineral assemblages of selected samples	36
<b>Table 3</b> Representative garnet chemical compositions	44
<b>Table 4</b> Average biotite chemical compositions for each sample	48
<b>Table 5</b> Representative biotite chemical compositions	49
<b>Table 6</b> Representative chemical compositions of orthopyroxene in the samples 02-02C, 20-30C, 04-05C and 10-16B.	51
<b>Table 7</b> Representative chemical composition of clinopyroxene in the sample 20-30C.	51
<b>Table 8</b> Representative chemical composition of hornblende in the sample 10-16B.	51
<b>Table 9</b> Variation of chemical compositions and average composition of zircon from each rock sample (bdl; below detection limit)	53
<b>Table 10</b> Abundances of zircon with detrital core and internal textures	57
<b>Table 11</b> 17-24GB zircon data	68-69
<b>Table 12</b> 07-10GB zircon data	70-71
<b>Table 13</b> Summary of U-Th-total Pb isochron age data for monazite domains	74
<b>Table 14</b> Calculated equilibrium temperature (°C) by garnet and biotite in 17-24GB	91
<b>Table 15</b> Calculated equilibrium temperature (°C) by garnet and biotite in 23-32Co	92
<b>Table 16</b> Calculated equilibrium temperature (°C) by garnet and biotite in 14-21GB	92
<b>Table 17</b> Calculated equilibrium temperature (°C) by garnet and biotite in 07-10GB	93
<b>Table 18</b> Calculated equilibrium temperature (°C) by garnet and biotite in 04-05C	93
<b>Table 19</b> Calculated equilibrium temperature (°C) by garnet and biotite in 11-17GB	94
<b>Table 20</b> Calculated equilibrium temperature (°C) by garnet and biotite in 03-04GB	94
<b>Table 21</b> Average $K_D$ values and Estimated equilibrium temperature ( $T$ ) for the Fe-Mg exchange between garnet and biotite	95
<b>Table 22</b> Four age groups according to the monazite isochron ages	105

## **MINERAL ABBREVIATIONS**

Ap, Apatite; Bt, Biotite; Cpx, Clinopyroxene; Crd, Cordierite; Crn, Corundum;  
Grt, Garnet; Hbl, Hornblende; Kfs, K-Feldspar; Mag, Magnetite; Mnz,  
Monazite; Opx, Orthopyroxene; Pl, Plagioclase; Qtz, Quartz; Sil, Sillimanite;  
Spl, Spinel; Zrn, Zircon.

## ACKNOWLEDGEMENTS

I express my gratitude to my supervisor Professor Masahide Akasaka, Senior Professor, Department of Geosciences, Faculty of Science and Engineering, Shimane University, Japan for his constant guidance, valuable advice, and the enthusiastic support is given throughout this work without concerning his demanding time. It has been an honor and privilege working under his tutelage, and I look forward to continuing our work for the good society and the world. I gratefully acknowledge the help provided by Professor Atsushi Kamei (Shimane University) as the present supervisor and for his comments, guidance, and discussion.

I extend my heartfelt thanks to Mr. L.R.K. Perera, Senior Lecturer, Geology Department, Faculty of Science, University of Peradeniya, Sri Lanka, who recommended me to perform my research and advised me throughout this work. Without him, I would have never found my place here at Shimane University, Japan.

I wish to thank Professors K. Yokoyama, R. Miyawaki, and Mrs. Shigeoka of National Museum of Nature and Science, Japan, who gave me much valuable help for CHIME dating of monazite in the early stages of this work. I thank Professor Yasutaka Hayasaka for his collaboration on with LA-ICP-MS analyses of zircon at Hiroshima University.

I also appreciate Professors Akira Takasu and Yoshikazu Sampei of Shimane University for their valuable comments and advice. I thank Associate Professor B.P. Roser (Shimane University) for his critical comments on this study and the manuscripts. I gratefully acknowledge the help provided by Associate Professor Hiroto Ohira for zircon separation.

Thanks are also due to Professors Toshiaki Tsunogae (Tsukuba University, Japan) and M. Satish-Kumar (Niigata University, Japan) who gave me much valuable suggestions and discussions.

I appreciate the friendly collaboration of members of Professor Akasaka Laboratory during this study.

I gratefully acknowledge the Japanese Government for financial support (MEXT scholarship) without the scholarship this work would never have been possible.

I express my thanks to the members of the academic staff of Department of Geosciences, Shimane University, and technical staff members who helped me in many ways. Last but not least, I wish to extend my heartfelt appreciation to my family, especially Sri Lankan community and all colleagues of Shimane University for their friendship, support, and encouragement given to me all the time.

## ABSTRACT

Internal textures of zircons and monazites, U-Pb ages of zircons, and Chemical U-Th-total Pb isochron method (CHIME) dating of monazites in garnet-biotite gneiss, garnet-biotite-cordierite gneiss, hornblende-bearing charnockitic gneiss and charnockitic gneiss of the Southwestern Highland Complex (SWHC), Sri Lanka, were investigated to evaluate the evolution of the metamorphic rocks which have been subjected to multiple thermal events during the Gondwana amalgamation.

The mineral assemblages are garnet + biotite + plagioclase + K-feldspar ± cordierite ± sillimanite + quartz + magnetite ± rutile ± spinel ± ilmenite ± calcite in the garnet-biotite gneiss; cordierite + plagioclase + magnetite + spinel ± corundum (thin spinel-rich and extremely quartz-poor layers) and garnet + biotite + K-feldspar + plagioclase + quartz ± magnetite ± spinel (spinel-poor layers) in garnet-biotite-cordierite gneiss; garnet + orthopyroxene + clinopyroxene + hornblende + anorthite ± quartz in hornblende-bearing charnockitic gneiss; and clinopyroxene + orthopyroxene ± biotite ± garnet + K-feldspar + anorthite + quartz ± magnetite in charnockitic gneiss.

The zircons from garnet-biotite gneiss consist of the detrital zircon cores and overgrowths with two to five growth stages. The detrital zircon cores are rounded or euhedral to subhedral in shape, and show transgressive internal textures or oscillatory zoning. In the garnet-biotite-cordierite gneiss sample, the zircons consist of euhedral core part (not detrital core) and four to five growth zones lacking internal texture. In the hornblende-bearing charnockitic gneiss and charnockitic gneiss, most of the zircons are fine-grained and rounded in form, and consist of cores (not detrital core) and rims lacking internal textures. In minor cases, zircons consist of rounded or skeletal cores containing inclusions and/or voids and overgrowths showing two or three generations. The first, second and third generations of core-absent grains exhibit fir-tree texture (ft), radial growth (rd) and a planar banded zone

(bd), respectively. Ages of the detrital cores are in a range of 3.3–1.7 Ga, and can be categorized into five ranges of 3380–3220, 2730–2660, 2550–2490, 2220–2170, and 1900–1700 Ma, implying source ages during 3.3–1.7 Ma. Most of the overgrowths gave ages in ranges of 2730–2660, 1900–1700, and 630–500 Ma. These age-ranges correspond to the growth stages of zircons by the repeated thermal events. Especially, zircons with ages in the ranges of 1900–1700 and 630–500 Ma have Th/U-ratios less than 0.1, implying formation by metamorphic events. Zircons lacking detrital cores and having growth zones with characteristic metamorphic internal textures gave ages in a range of 630–500 Ma, implying the generation at the latest metamorphic event stage.

Monazites are abundant in garnet-biotite gneisses. The monazites have core-rim zoned, inherited core-bearing, complexly zoned, and oscillatory zoned type internal textures. The core domains of the core-rim zoned, inherited core-bearing, and complexly zoned type monazites show 523–485, 1802–517, and 1648–527 Ma, respectively, and the rim domains show younger ages of 485–434 Ma. Even though its repeated zonings, oscillatory zoned type monazites show the only young age of  $452 \pm 27$  Ma. The determined isochron ages are grouped into four clusters: group I of 1830–1648 Ma,  $1766 \pm 140$  Ma,  $1788 \pm 30$  Ma; group II of  $803 \pm 99$  Ma,  $679 \pm 99$  Ma; group III of ages with 550–485 Ma,  $533 \pm 22$  Ma, and  $481 \pm 42$  Ma; and group IV of ages with 470–430 Ma,  $470 \pm 45$  Ma, and  $433 \pm 14$  Ma. The ages of the group I may imply either magma emplacement ages or depositional ages of sediments. The ages of the group II correspond to the stage of the most prominent thermal event recorded in the region. The groups III and IV can be identified as post-peak thermal events. However, the groups II to IV can be considered as one group or event within the error ranges of the ages.

The age data given for the monazites in the SWHC are consistent with the published data for the Central Highland Complex, and indicate that the SWHC has been subjected to the same thermal events as the Central Highland Complex. However, the repeated thermal events

in the SWHC are evidenced by the internal textures and the age data of the zircons from the SWHC, which signifies the complex evolution process of the high-grade basement of the SWHC. Five growth stages of overgrowths observed in some zircons suggest much more complex thermal events than that having been considered in the published simplified models. The results of my study show complex evolution processes of the high-grade basement of the SWHC, and seem to be consistent with the previous crustal model than the recent crustal models for CHC.

## I. INTRODUCTION

Sri Lanka is a Precambrian terrain, and 90% of the basement consists of high-grade metamorphic rocks. In Gondwana reconstructions, closure of Mozambique Ocean and the birth of Mozambique Belt were active tectonic events, and Gondwana fragments have been undergone multiple thermal events (Kriegsman, 1993; Grunow et al., 1996; Dissanayake and Chandrajith, 1999; Hoffman, 1999). In the Gondwana supercontinent, Sri Lanka was placed along the Mozambique belt between East and West Gondwana, and was juxtaposed with East Africa (Tanzania, Madagascar) and South India in the west, and with East Antarctica (Lützow-Holm Bay area) in the east (Kriegsman, 1993; Grunow et al., 1996; Dissanayake and Chandrajith, 1999; Hoffman, 1999).

The Sri Lankan Precambrian basement consists of four major crustal units named the Highland, Vijayan, Wannai, and Kadugannawa Complexes (Cooray, 1994) (Figure 1).



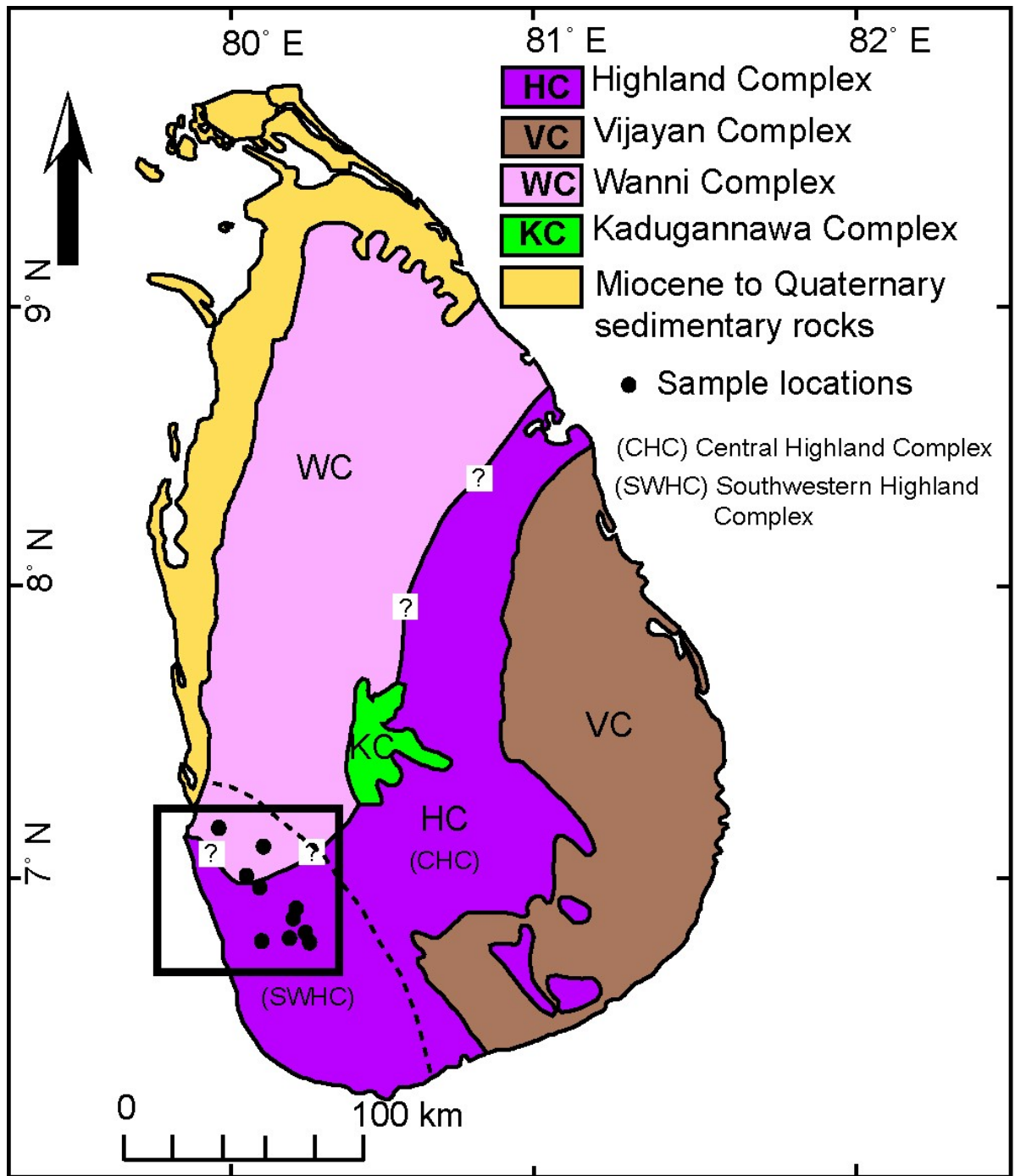


**Figure 1.** Simplified geological map of Sri Lanka showing major lithotectonic units (modified after Cooray (1994)).

The Highland Complex (previously known as the Highland Series and the Southwestern Group) is a central belt of granulite-facies rocks, which extends from the northeast to the southwest of the island. Inter-bedded pelitic gneisses, meta-quartzites, marbles, and charnockitic gneisses characterize the belt. The Vijayan Complex occupies eastern and southeastern Sri Lanka, and consists of amphibolite-facies migmatites, granitic gneisses, granitoids, and metasediments. The Wannu Complex lies to the west and northwest of the Highland Complex, and consists of migmatites, granitic gneisses, charnockitic gneisses, minor metasediments, and granitoids. The Kadugannawa Complex consisting of hornblende gneiss, biotite-hornblende gneiss, and migmatites occurs within elongate synformal basins around Kandy in central Sri Lanka (Cooray, 1994). Although a number of petrological studies have been carried out later on this terrain (e.g., Mathavan et al., 1999; Kehelpannala, 1997; Mathavan and Fernando, 2001; Kröner et al., 2003; Kröner et al., 2013; Dharmapriya et al., 2014; Santosh et al., 2014; He et al., 2016a, 2016b), lithological nomenclature and petrology of the terrain introduced by Cooray (1994) is widely recognized. One or two episodes of deformation (D1 and D2) prior to the formation of the major folds (D3) in these granulite-facies metamorphic rocks were suggested based on the geological structures, such as foliations, lineations, folds, boudinages, and pinch and swell structures (Berger and Jayasinghe, 1976). Additional information on the geological structures and events has been provided by later studies of the structural geology and tectonics of the Highland Complex (e.g., Kehelpannala, 1997, 2004).

Petrology of metamorphic rocks in the Central Highland Complex (CHC) and Southwestern Highland Complex (SWHC) has repeatedly been investigated in efforts to clarify the evolution of the major crustal units in Sri Lanka. Katz (1973) regarded the Highland Series (CHC) and Southwestern Group (SWHC) metamorphic rocks as Barrovian-type facies series and Abukuma-type facies series, respectively, based on their mineral

assemblages. Nevertheless, Perera (1984) suggested that the change in bulk chemical composition resulted in the differing mineral assemblages between the Highland Series and the SWG. Faulhaber and Raith (1991) estimated metamorphic pressures and temperature gradients in the southern part of Sri Lanka. By applying the garnet-biotite geothermometer and the estimated metamorphic pressures after Faulhaber and Raith (1991), Sajeev and Osanai (2005) proposed a thermal gradient with the highest temperature ( $>850\text{ }^{\circ}\text{C}$ ) in the CHC and gradually decreased temperature ( $<700\text{ }^{\circ}\text{C}$ ) towards the SWHC. Dharmapriya et al. (2014) described the spinel + quartz assemblages of spinel- and cordierite-bearing garnet-sillimanite-biotite-graphite gneiss in the SWHC are non-Ultra High Temperature (UHT) assemblage because of Zn and  $\text{Fe}^{+3}$  possibly incorporate into spinel under high oxidizing conditions. Therefore, the maximum temperature for the rock sample was  $870\text{--}900\text{ }^{\circ}\text{C}$  (Dharmapriya et al., 2014).

According to studies by U-Pb zircon dating (Kröner et al., 1987; Santosh et al., 2014; He et al., 2016a, 2016b; Takamura et al., 2015), Nd model ages (Milisenda et al., 1988, 1994) and Sr model ages (Crawford and Oliver, 1969), the detritus of the metasediments in the CHC were derived from unidentified Archean to Proterozoic source terrains of  $3.2\text{--}2.0\text{ Ga}$  in age, and peak metamorphism occurred around  $610\text{--}550\text{ Ma}$  (Kröner et al., 1994; Hölzl et al., 1991, 1994; Sajeev et al., 2010; Santosh et al., 2014; He et al., 2016a, 2016b). Baur et al. (1991) and Hölzl et al. (1994) obtained zircon upper intercept ages around  $1900\text{--}1800\text{ Ma}$  for orthogneisses, which were interpreted as crystallization ages of the protoliths. On the other hand, Kröner et al. (1987, 2003) identified lead loss and zircon growth events at  $1100\text{--}750\text{ Ma}$ . Sajeev et al. (2003, 2007) also proposed  $1400\text{ Ma}$  and  $530\text{ Ma}$  thermal events in the CHC, although Sajeev et al. (2007) pointed out that the  $1100\text{ Ma}$  and  $1400\text{ Ma}$  ages require reexamination. Sajeev et al. (2010) has given evidence of  $1.7\text{ Ga}$  age clusters, episodes of zircon growth at  $1.04\text{--}0.83\text{ Ga}$  and two generations of overgrowths in zircon at  $569\pm 5$  and

551±7 Ma in quartz-saturated granulites. Their results also indicate that the Archean sediments of the CHC have undergone repeated thermal events. On the other hand, Hölzl et al. (1994) reported ages 610–550 Ma of monazite, indicating the existence of thermal events older than 550 Ma. Malaviarachchi and Takasu (2011) identified three types of internal textures in monazite: unzoned, core-rim-type zoned, and mesh-like zoned types. Moreover, they indicated three age ranges of 613–561 Ma (Group I), 728–619 (Group II) Ma, and 516–460 Ma (Group III).

Several crustal evolution models on Sri Lanka have been proposed based on the petrology, structural geology, and geochronology around the CHC. A model defined that the Wannai, Highland, and Vijayan Complexes were discrete terranes (Vitanage, 1972, 1985), and proposed that the Wannai and Highland Complexes collided at first and subsequently thrust over the Vijayan Complex (Vitanage, 1972; Voll and Kleinschrodt, 1991; Kröner and Jaeckel, 1994; Kriegsman, 1995; Kehelpannala, 1997, 2004). On the other hand, Sajeev et al. (2010) suggested that ultra hot collisional orogeny took place in the area of Sri Lanka in the process of assembly of Gondwana. Sajeev et al. (2010) further explained that the CHC was superheated by basaltic underplating followed by fast extensional exhumation. In the model proposed by Santosh et al. (2014), the crustal evolution of Sri Lanka relates to a double-sided subduction in the Neoproterozoic age, and the Wannai Complex to the west and the Vijayan Complex to the east correspond to continental arc in collision along the Highland Complex. The double-sided subduction model further suggests that the Highland complex is an accretionary belt as well as the collisional suture (Santosh et al., 2014). He et al. (2016a) suggested that in the early to late Neoproterozoic bimodal magmatic suite in Sri Lanka, active convergent margin magmatism has taken place repeatedly. These studies denied the previous model prior to Sajeev et al. (2010).

In contrast to the detailed studies on the Central Highland Complex (CHC) noted above, the Southwestern Highland Complex (SWHC) has not been well studied, and the thermal events of the SWHC are not yet well understood. However, the location of the SWHC has been regarded to be close to the West Gondwana fragments of Madagascar and South India (Dissanayake and Chandrajith, 1999), and, thus, the SWHC is a critical place to give a clear view of multiple thermal history and relationship among West Gondwana fragments. As mentioned by Parrish (1990), age dating using monazite is one of the most suitable methods to clarify multiple thermal histories. In fact, mineral assemblages and textures of metamorphic rocks in Gondwana fragments were overprinted by Pan-African thermal events, but internal textures of monazite record older thermal events.

Zircon is a common accessory mineral in nature. It can survive in many geo-environmental processes without changing the chemistry and textures. Zircon present in many rock types, thus, several types of zircon can be observed: igneous zircon, metamorphic zircon, hydrothermal zircon, kimberlitic and mantle-related zircon, and impact related zircon. Metamorphic zircon forms under a range of different metamorphic processes: precipitation from melt during anatexis (Roberts and Finger, 1997), sub-solidus nucleation and Si released by metamorphic breakdown reactions of major silicates (Fraser et al., 1997) and accessory phases (Pan, 1997), precipitation from aqueous metamorphic fluids (Williams et al., 1996), recrystallization of protolith zircon (Black et al., 1986). As the Earth's timekeeper (Harley et al., 2007) zircon behave as a reliable fingerprint of the isotopic character. Zircon behavior in during the crustal process is not passive but must be interpreted carefully in its petrological, mineralogical and geological context, and in the light of all possible lines of evidence (Harley et al., 2007). Textural relation should be taken into extra attention as one of the most important aspects.

Metamorphism changes internal textures of zircons: the preserved internal textures of detrital zircon, particularly igneous oscillatory zoning, are progressively changed into convoluted, blurred, and thickened. Then the dominant texture is transgressive patches and lobes across all pre-existing textures (Figure 2). More detail classification with several types of textures was established by Vavra et al. (1996): detrital core (dc), and overgrowth patterns such as fir-tree texture (abbreviated as ft), radial zoning (rd), peripheral zones (sd), resorption (rs), euhedral faces (eu), and planer banded zoning (bd) (Figure 2).

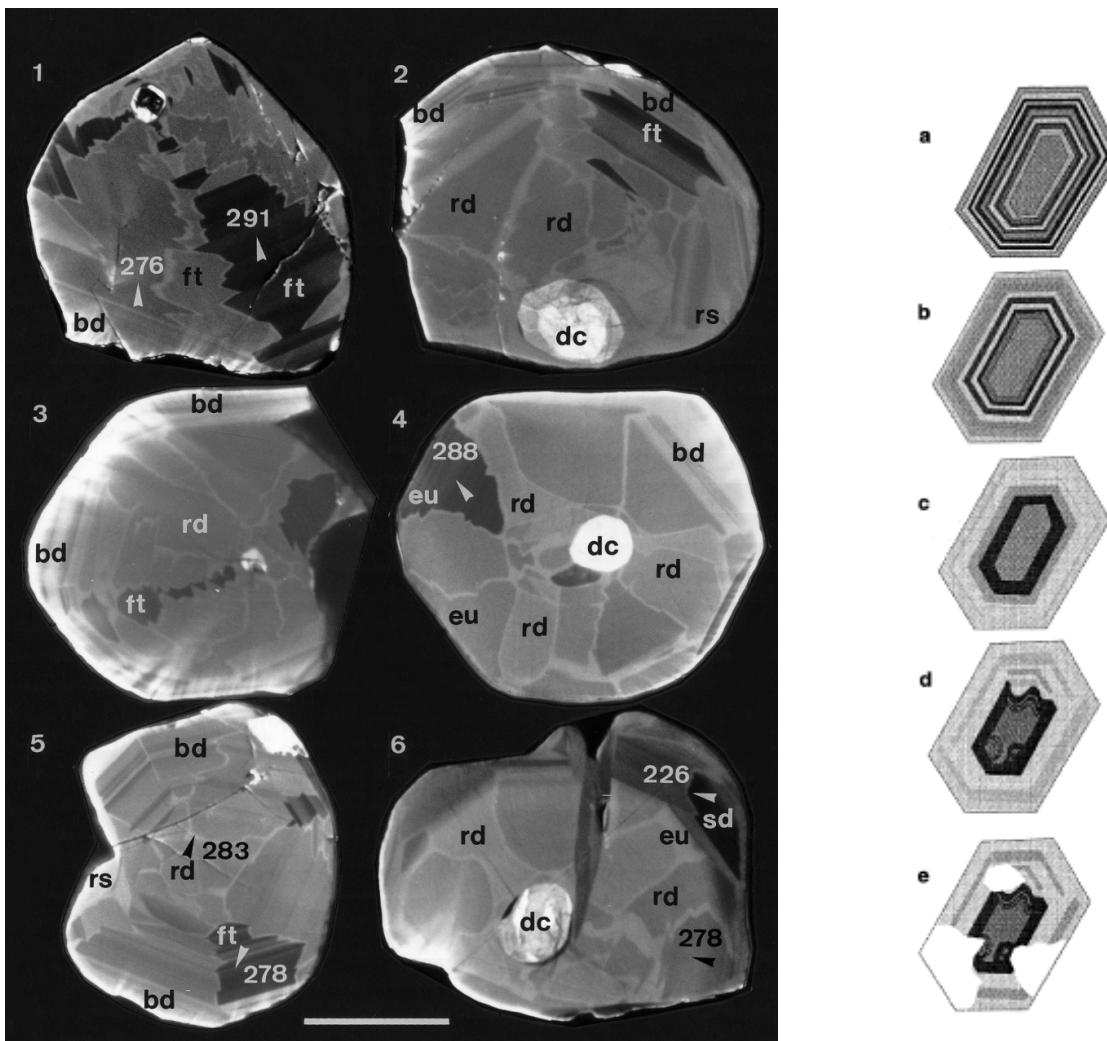


**Figure 2.** Detrital core (dc) and over growth patterns of metamorphic zircons which were proposed by Vavra et al., 1996 as: rd; radial sector zoning, ft; fir-tree sector zoning, bd; planer growth banding, rs; resorption, eu; euhedral surfaces, sd; discrete peripheral zones. Pidgeon et al., 1998 used a schematic diagram to explain the changes from igneous oscillatory zoning into transgressive lobes and patches in zircon (a-e).

The other most common but minor mineral that formed during different magmatic or metamorphic events is monazite. Monazite is used for age dating for the study on the various stages of metamorphism, because its Th-U-Pb composition depends on genetic age. Monazite age dating has been carried out successfully throughout the last decade using the electron probe microanalyzer (Suzuki and Adachi, 1991, 1994; Suzuki et al., 1994; Cocherie et al., 1998). The most recent electron microprobe analyzer, a field-emission type equipment, such as JEOL JXA-8530F at Department of Geology, Shimane University, has high spatial resolution ability, enables us to distinguish different domains within a monazite more precisely than before, and is used as a powerful tool to clarify the processes through which the zircon-bearing metamorphic rocks were formed.

## **I-1 SIGNIFICANCE AND PURPOSE OF THE STUDY**

The petrological studies of the Highland Complex have shown the mineral assemblages formed by the latest stage granulite facies metamorphism, and proved that the effect of the final metamorphic event was intensive, and the mineral assemblages and textures formed by metamorphism before then have been overprinted significantly. Such phenomena have been widely known in many high-grade metamorphic terrains, and have also been observed in Sri Lankan metamorphic terrain. The crustal evolution in the CHC has repeatedly been investigated using geological, structural geological, petrological and chronological methods, including zircon and monazite geochronology. However, geochronology on the metamorphic rocks in the SWHC and thermal structure of the SWHC area have not been studied well, and the relation between the SWHC and the CHC and other Gondwana crustal blocks has not been fully understood. Thus, only speculative models on the evolution of the Sri Lanka have been proposed.

For further understanding of the geological, petrological, and chronological properties of the SWHC and elucidation of the crustal evolution process of the Sri Lanka, internal textures the zircon and monazite will give us a clue, because internal textures of these minerals preserve well the thermal process. The evidence given by the internal textures of zircon and monazites and synchronized geochronology will contribute to understand the thermal history of the SWHC, to clarify the relation between the SWHC and CHC, and to construct more realistic crustal evolution model of the Sri Lanka.

The ages of early Pan-African thermal events in the South India have been reported as  $1802\pm 16$  Ma (Bartlett et al., 1998) and 1793 Ma (Choudhary et al., 1992), and Paquette et al. (1994) reported  $1679\pm 04$  Ma in Androyan Complex of Madagascar. The Rb-Sr isochron ages of 484–440 Ma given from biotite, feldspar, and garnet from metamorphic rocks in South India, have been considered to represent Post-Pan-African thermal events (Choudhary et al., 1992; Unnikrishnan-Warrier et al., 1995; Unnikrishnan-Warrier, 1997). According to the Gondwana reconstruction, the SWHC is much closer to South Indian KKB and Androyan Complex of Madagascar. Previous studies have a gap of data and knowledge, especially in the SWHC. These chronological data plays an important role to establish the Gondwana linkage between these crustal units.

Therefore, in the present doctoral thesis study, internal textures within zircons and monazite from metamorphic rocks in the SWHC have been investigated in detail, in the light of a classification scheme of internal textures of this mineral (e.g., Vavra et al., 1996; Pidgeon et al., 1998; and Corfu et al., 2003), and ages of zircon were determined using U-Pb data to clarify the repeated thermal events in the SWHC. Monazites were investigated in detail, and the chemical U-Th-total Pb isochron method (CHIME; Suzuki et al., 1991; Suzuki and Adachi, 1991) was applied to determine the ages of the internal domains. The analyzed results of the zircon and monazite have to be consistent with the petrology of the



metamorphic rocks. Thus, the metamorphic temperatures of the studied samples of zircon and monazite-bearing metamorphic rocks were examined using biotite-garnet geothermometer for biotite-garnet gneiss, and clarified thermal structure of the SWHC. Finally, multi-thermal process and evolution of the SWHC and CHC, Sri Lanka, and significance of the SWHC for understanding Gondwana supercontinent are discussed.

## II. STUDY AREA AND GEOLOGY

### II-1. STUDY AREA

The study area is situated in the south-west of Sri Lanka (Figure 3). It extends from lower boundary of Gampaha to lower part of the Kalutara district, and east end is limited by the boundary of Ratnapura district. The west end is demarcated by the Indian Ocean.

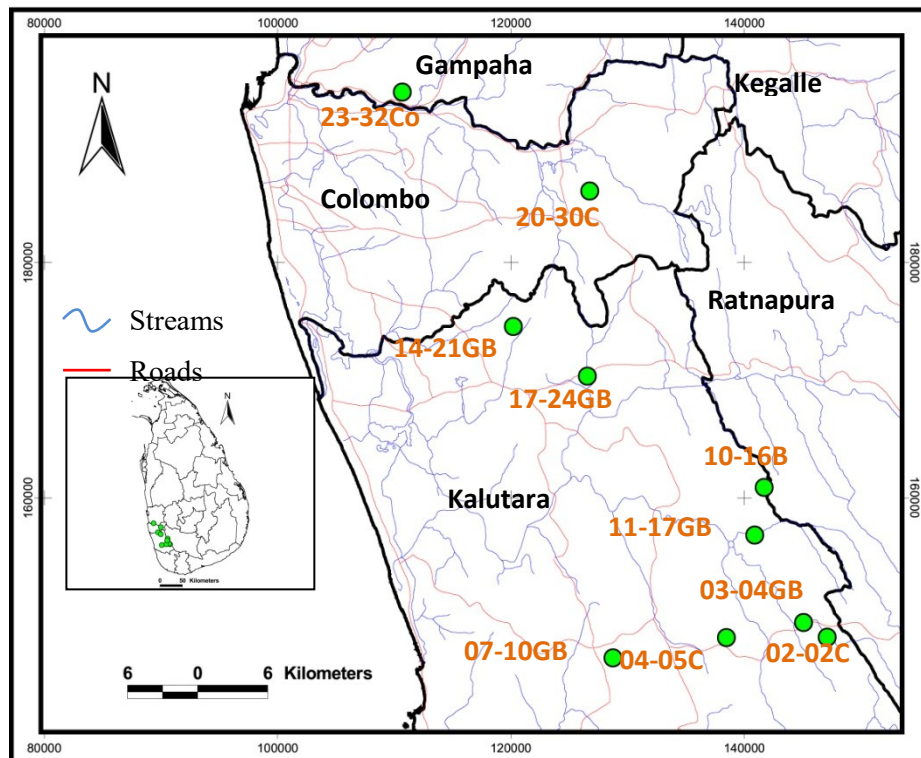


**Figure 3.** Location map of the samples of study area showing the major roads, district boundaries and drainage patterns. (Sri Lankan coordinate system is used) (modified after geological maps of the Geological Survey and Mines Bureau of Sri Lanka)

The area is the most populated area on the island and almost all the area is urbanized. However, closer to the Ratnapura district it is moderately populated urban area and low-moderately populated semi-rural area.

## II-2. GEOLOGY OF SOUTHWESTERN HIGHLAND COMPLEX AND STUDY AREA

High-grade rocks of Neoproterozoic Wannu and Highland Complexes are locally overlain by Quaternary sediments of the western coastal plain. The Proterozoic metamorphic rock descriptions of the SWHC and the study area can be found in geological maps of the Geological Survey and Mines Bureau of Sri Lanka; geology data from 1:100000, geology map sheets 16 and 19.

Gneisses in the north and west of the study area, in general, comprise banded, streaky and distorted migmatitic granodiorite, tonalite, and granitoid gneisses, predominantly hornblende-bearing calc-alkaline orthogneisses with interlayered much more mafic gneisses. These are intruded throughout by pink potash-feldspar-bearing melts. Charnockitic relicts are common. Paragneisses, together with minor layers of the lithologies listed above, are more common in the southern eastern part of the area, and include calc-silicate gneisses, extensive late-stage addition of K-rich melts hampers the recognition of the protoliths. The addition of extensive melts is most common around Ambagaspitiya where they crop out as thick replacive sheets, repeated by folding. These melts obscure the Wannu-Highland Complex boundary.

The oldest rocks in the area are the mainly paragneissic lithologies of the Highland Complex that crop out over much of the southern and eastern part of the area. Here a sequence of paragneisses-calc gneisses, rare marbles, quartzites and quartz-schists, biotite-bearing quartzofeldspathic rocks and garnet-biotite-sillimanite-graphite gneisses (formerly termed 'khondalites') are interlayered with each other and with more massive charnockitic gneisses probably of both para- and ortho-gneissic origin. 'Charnockitisation' is indicated to be of more than one stage. These high-grade rocks have Nd model ages between 2.8–2.0 Ga for their protoliths, and attained metamorphic temperatures approaching 900 °C much later,

between 610-500 Ma (e.g., Kröner et al., 1987; Santosh et al., 2014; He et al., 2016a, 2016b; Takamura et al., 2015). Pressures are lower in this area about 4–5kbar than elsewhere in the CHC, and this has permitted the late stage syn to post D3 deformations either alkali feldspar or cordierite bearing crustal melts to form, some of these S-type melts locally contain sillimanite.

The area consists of few major structural sinforms and antiforms with several shear zones: e.g. Pugoda, Siyabalape sinforms, and Oruwela, Hanwella antiforms. Kalutara-Matara shear zone and Hiduma-Weligama shear zone. All most all the rock bands foliated N-NW and in the northeast of the area is foliated to N-NE directions.

Lithological variation coupled with tropical weathering. This has given rise to a strongly featured topography of ridges and valleys, generally striking NNW-SSE and often highlighting map-scale folds within the metasediments. Ridge-forming rocks those used particularly to trace the regional structures depend on of the percentage of quartz, with quartzites, quartz-rich layer-parallel pegmatites and quartz-rich granitoids being the most resistant. The least resistant rocks are the calc-gneisses, marbles, garnetiferous biotite-sillimanite gneisses, and hornblende-bearing gneisses, which form negative features resulting in very poor exposure in the valley bottoms. Lithological layering is everywhere parallel to foliation, with abundant evidence of extreme flattening and stretching of individual compositional layers. Tight to isoclinal intrafolial folds are common. All indications are that as elsewhere in Sri Lanka, the stratigraphy is tectonic, being produced primarily during D1 and D2 deformations. A uniform and powerful sub-horizontal stretching lineation are defined by flattened quartz ribbons, mafic mineral aggregates, and small fold-hinges, the structural pattern is strongly controlled by the last phase fo deformation-D3 which gives NNW-SSE oriented tight to isoclinal folds of earlier D2 recumbent nappes. These early nappes are best developed by poorly exposed as a series of imbricate thrusts around Pugoda. Limbs of the D3

folds are flattened and sheared and commonly marked by anastomosing shear zones. The most important of these is the Kuliypitiya-Yatiantota-Pelmadulla deformation zone which parallels the Highland escarpment in the map sheet and marks a fundamental structural break which extends some 100 km NNW-SSE across this and adjacent map sheets. Close inspection of the D3 synforms which appear to be double plunging shows that many have limbs which comprise extremely attenuated refolded 'hook' folds. The axial trace of such folds is at a small angle to the lithological layering within the folds. Attenuation is most obvious on eastern limbs and increases towards the Kuliypitiya-Yatiantota-Pelmadulla deformation zone in the east of the study area. The map-scale outcrop pattern strongly supports the hypothesis that locally (and perhaps regionally) the marbles and calc-silicates act as weak zones (possibly even detachment zone) focussing ductile deformation and producing large-scale folds of the intervening lithologies (Geological Survey and Mines Bureau of Sri Lanka: Geology Sheet 16, 1996; Geology Sheet 19, 2000).

Geological map of Geological and Mines Bureau (Geological Survey and Mines Bureau of Sri Lanka: Geology Sheet 16, 1996; Geology Sheet 19, 2000), Sri Lanka, shows many categories of above major rock types (Figures 4 and 5). Using the graphic software, six rock types (charnockitic gneiss, garnet-biotite gneiss, cordierite gneiss, hornblende-bearing gneiss, quartzite, marble/ calc gneiss) were redrawn in Figure 6 for better understandings.

### **II-3. SAMPLE LOCALITY**

The samples were collected from roadside outcrops, and some samples were collected from rock quarries. The sampled locations can be accessed easily by main and minor roads of the area. Figures 4, 5, and 6 show the sample positions plotted on the geological map after Geological Survey and Mines Bureau of Sri Lanka: Geology Sheet 16 (1996) and Geology Sheet 19 (2000).

Four samples are shown in Figure 4 (Geology sheet 16). The location of 23-32Co shows cordierite gneiss on the map with the general foliation of NNW-SSE. The location of 20-30C shows mainly garnet-biotite gneiss rocks. However, the rocks were interlayered with charnockitic gneisses. The foliation is the NNE-SSW direction. 14-21GB and 17-24GB are generally found the garnet-biotite rich locality and the foliation plains follow the general regional foliation (NNW-SSE).

The other six samples shown in Figure 5 are 10-16B, 11-17GB, 03-04GB, 02-02C, 04-05C, and 07-10GB. Figure 5 is a combination of the Geology sheets 16 and 19 published by Geological Survey and Mines Bureau of Sri Lanka. The whole area follows the general regional foliation. Rock types are interlayered as described in the general geology of the area. However, hornblende-bearing gneissic layer found in this area and one sample (10-16B) was collected. Other samples are general garnet-biotite gneisses and charnockitic gneisses which are locally interlayered.

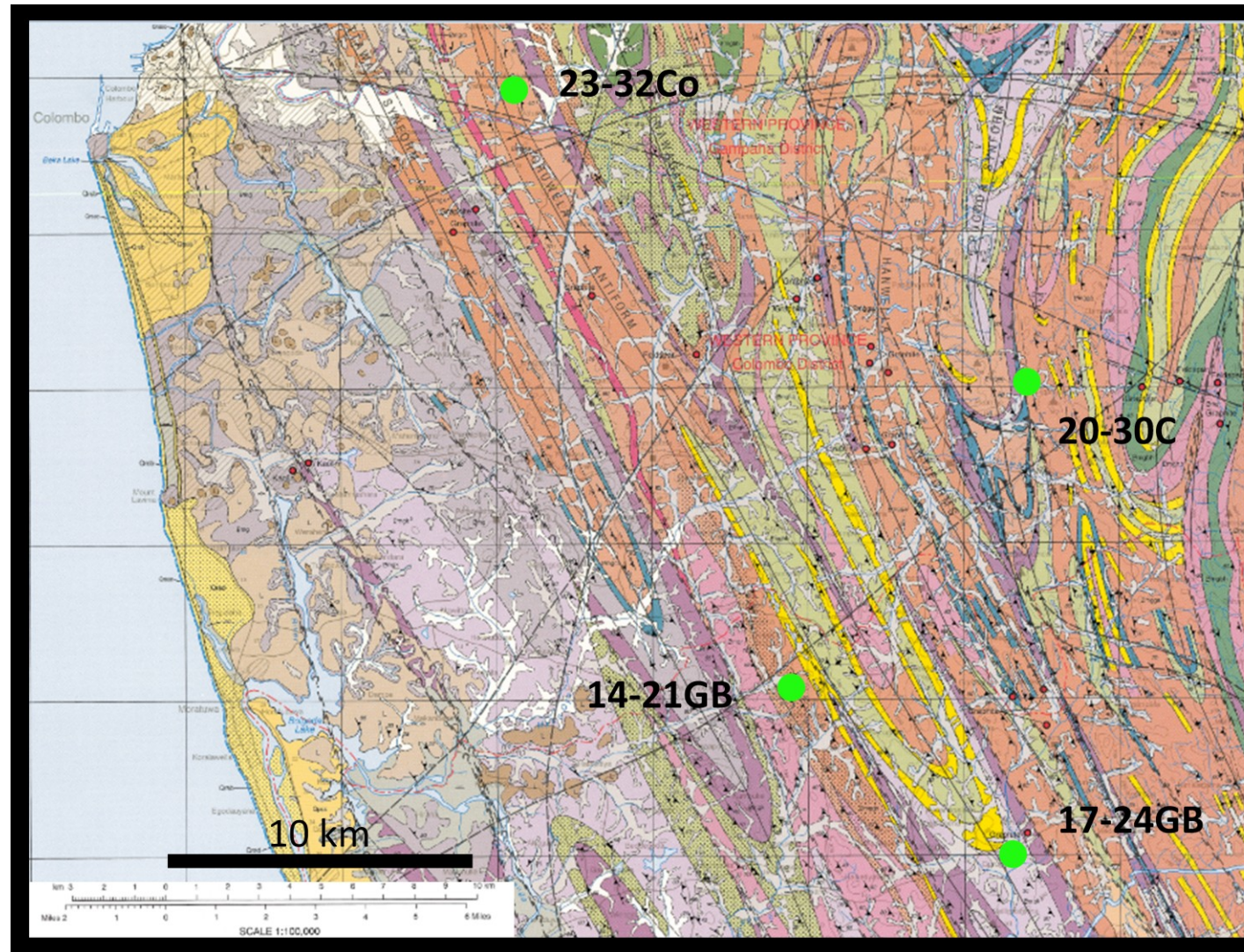


**Figure. 4** Geology Map of the studied sample area (modified after geological maps of the Geological Survey and Mines Bureau of Sri Lanka; geology data from 1:100000, geology map sheets 16 and 19)

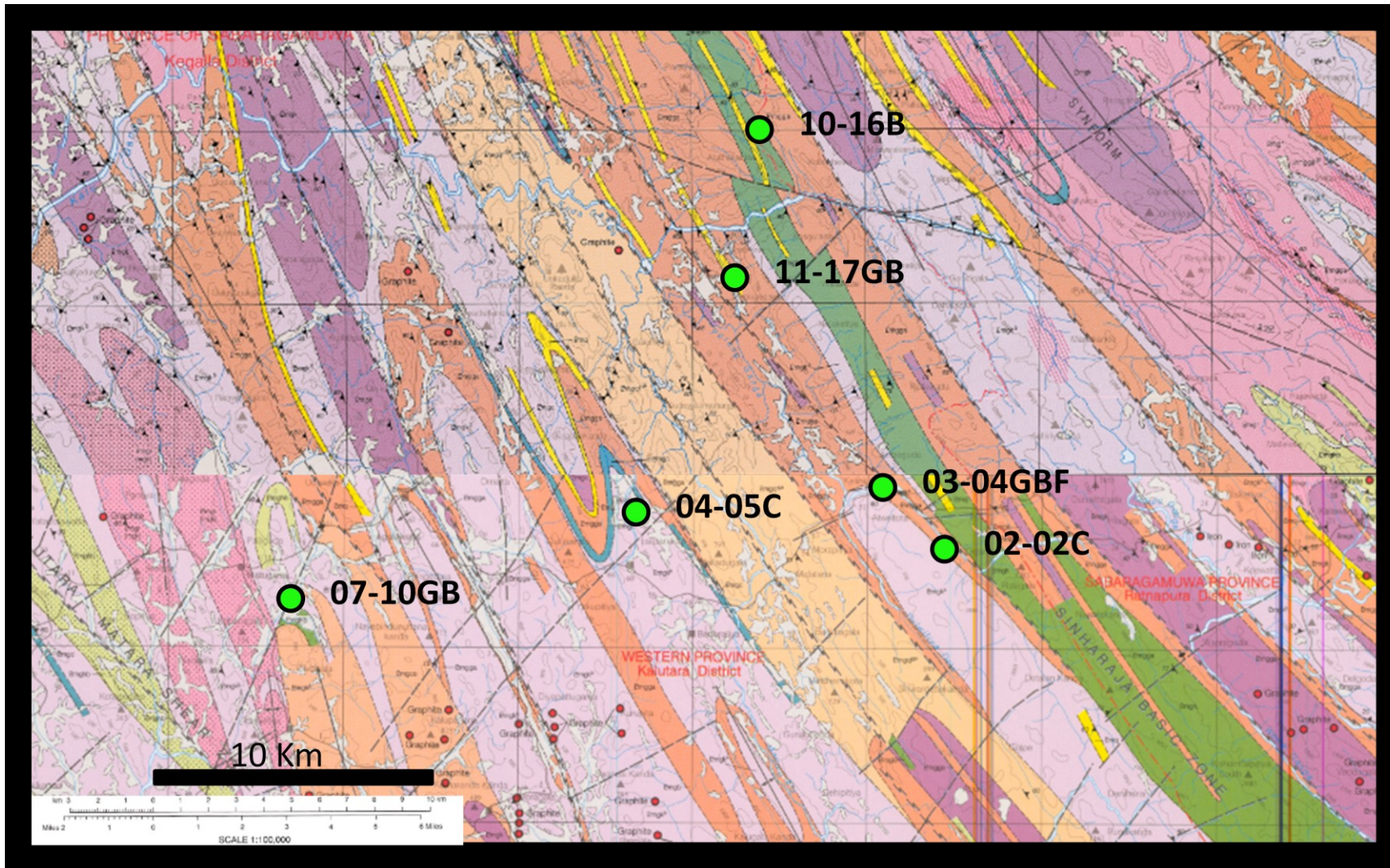


**Figure. 5** Geology Map of the studied sample area (modified after geological maps of the Geological Survey and Mines Bureau of Sri Lanka; geology data from 1:100000, geology map sheets 16 and 19)



EXPLANATION OF SYMBOLS

SUPERFICIAL DEPOSITS

	Laterite: discontinuous caps
	Sandy, lateritic gravel

QUATERNARY - RECENT AND PLEISTOCENE DEPOSITS

	Alluvium: sand, silt or clay
	Stiff brown or blue-grey organic rich clays, "paddy clays"
	Lagoonal and estuarine deposits: organic rich silts and clays includes lake and marsh deposits
	Beach sand: <sup>1</sup> etc. indicates older ? Holocene beach ridges
	Dune sand
	Beachrock: planar beds of calcareous cemented beach sand of past and present shorelines, often including heavy minerals
	Grey and White Sands: unconsolidated bleached sands, in part dune sands (4) for silica sand resource)
	Unconsolidated brown and grey coastal sands = ?Grey and White Sands

PROTEROZOIC METAMORPHIC ROCKS (no stratigraphic order implied)

*Lithologies principally (but not exclusively) of the Wannu Complex and associated Kadugannuwa Complex*

	Granite gneiss: massive leucocratic quartzofeldspathic gneisses, quartz >20%, few mafics, <sup>kt</sup> indicates late-stage alkali feldspar
	Pegmatitic granitoid gneiss: distinctive quartz-rich, leucocratic, white or pink, pegmatite-layered gneiss produced by deformation, usually ridge-forming
	Alkali feldspar granite/gneiss/migmatite: unfoliated to foliated late-stage K-feldspar-rich intrusions and melts, includes Ambagasptiya type

The Legend of the Geology Maps

	Hornblende-biotite gneiss: massive to compositionally layered grey gneiss with quartz >20% plagioclase and garnet < ca 10%; tonalite composition
	Biotite-hornblende gneiss: medium to dark grey gneiss, plagioclase > K-feldspar; quartz <15%; quartz monzodiorite to leucodiorite composition
	Undifferentiated Proterozoic gneisses: poorly exposed under thick residual soils

*Lithologies principally (but not exclusively) of the Highland Complex*

	Garnet-sillimanite-biotite gneiss ± graphite: pelitic schist or gneiss often cordierite bearing
	Garnet-sillimanite-biotite gneiss ± graphite: pelitic schist or gneiss
	Quartzites: pure coarse-grained ridge-forming quartzites locally with <5% each of sillimanite, kaolinised feldspar or biotite
	Marble, usually coarse-grained and dolomitic, locally high calcite marble present
	Calc-gneisses and / or granulites: calc-silicate gneisses with very variable mineralogy
	Cordierite gneiss: granoblastic, with cordierite >15%, and K-feldspar, biotite, quartz, ± sillimanite, garnet usually present
	Undifferentiated charnockitic biotite gneisses: extensive sequences of charnockitic-looking grey gneisses usually lacking hypersthene, though commonly with boudinaged orthopyroxene-bearing mafic layers; but may include some paragneisses
	Charnockitic gneisses: restricted outcrops, often ridge-forming; typically coarse-grained with characteristic brown or green greasy lustre; may lack hypersthene. Includes patchy <i>in situ</i> charnockites as well as partially retrogressed, bleached 'ex-charnockites', stipple indicates local charnockitisation

Late-stage intrusives (in general younger than 550 Ma)

	Pegmatites: simple quartz-feldspar pegmatites with magnetite and/or allanite
	Vein quartz: usually transparent to milky, high-purity, massive to lenticular

<sup>kt</sup> indicates extensive pink potash-rich veins and melts in any lithological unit

EXPLANATION OF LINE AND STRUCTURAL SYMBOLS

	Approximate or inferred geological boundary or contact
	Geological boundary, between superficial deposits and solid formations
	Geological boundary, concealed
	Fault, inferred from air photographs (tick shows downthrow side)
	Shear zone, inferred from air photographs (arrows denote shear sense where known)
	Axial trace of antiform, and plunge
	Axial trace of synform, and plunge
	Overtured antiform
	Overtured synform
	Strike and dip of foliation (generally parallel to compositional layering)
	Azimuth and plunge of lineation
	Azimuth and plunge of minor fold
	Thrust or shear with thrust sense probable
	Thrust inferred
	Structure, form or trend lines, from air photographs
	Mineral occurrence
	Extent of mineral resource, i.e. silica sand, gravel (or limits of patchy gravel spread)

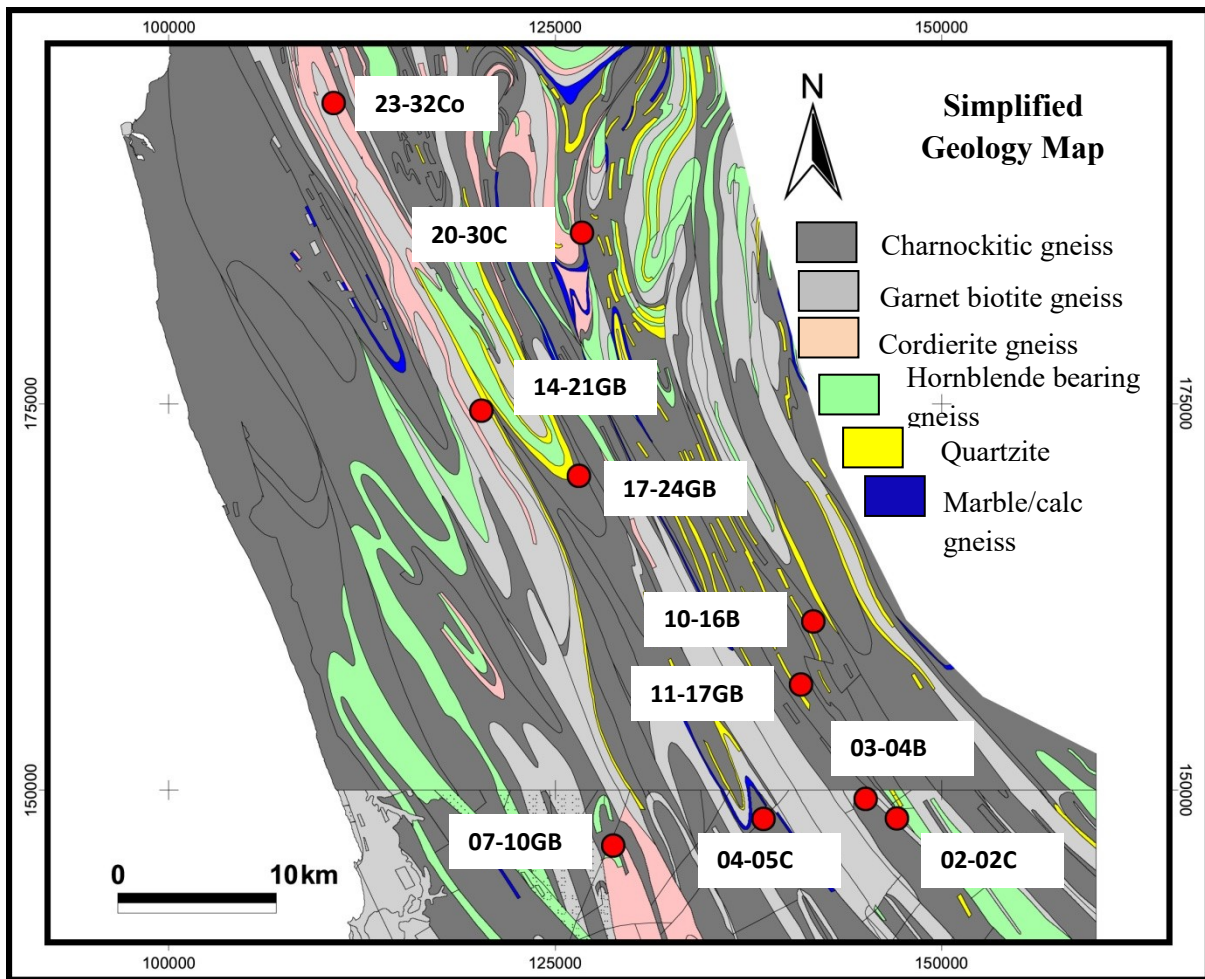









**Figure 6.** Simplified Geology Map of the studied sample area (modified after geological maps of the Geological Survey and Mines Bureau of Sri Lanka; geology data from 1:100000, geology map sheets 16 and 19)







### III. SAMPLES

Twenty-four rock samples were collected from natural rock outcrops. Based on preliminary petrographic study on zircon showing diverse internal textures, ten gneiss samples were selected for detailed study: five garnet-biotite gneiss samples (17-24GB, 14-21GB, 07-10GB, 11-17GB, and 03-04GB), one garnet-biotite-cordierite gneiss sample (23-32Co), one hornblende-bearing charnockitic gneiss sample (10-16B), and three charnockitic gneiss samples (04-05C, 02-02C, and 20-30C). Three thinsections of each sample were prepared during the thinsection observations. The maps in Figures 1, 3, 4, 5, and 6 only show the locations of these studied ten samples. Due to extremely sporadic distribution of zircon lack of zircon, quartzite samples were not used in the present study. Charnockitic gneisses also contained a subtle amount of zircons. Therefore, several charnockitic gneisses were rejected in the present study. Table 1 shows the used sample number and respective major rock types with the images of the samples.

**Table 1** Studied rock samples.

Sample Number	Major rock type	Images of the Sample and the Locations
17-24GB	Garnet biotite gneiss	

22-23Co	Cordierite bitotite gneiss		
02-02C	Charnockitic gneiss		
14-21GB	Garnet biotite gneiss		
07-10GB	Garnet-biotite gneiss		

04-05C	Charnockitic gneiss		
20-30C	Chanrnockitic gneiss		
11-17GB	Garnet-biotite sillimanite gneiss		
03-04GB	Garnet bitotite gneiss		

10-16B	Hornblende bearing gneiss		
--------	------------------------------	--	--

## **IV. METHODS**

### **IV-1. PETROGRAPHY**

Petrographic study of thinsections of the samples was carried out using an optical microscope and electron images by electron microprobe analyzer to identify minerals, to determine mineral assemblages and to evaluate igneous and metamorphic properties of the textures.

### **IV-2. CHEMICAL ANALYSIS OF MINERALS AND OBSERVATIONS OF INTERNAL TEXTURES OF ZIRCON AND MONAZITE USING ELECTRON MICROPROBE ANALYZER**

Chemical compositions of zircons in thin sections were determined using a JEOL JXA-8530F electron microprobe analyzer (EMPA) at Shimane University, operated at an accelerating voltage of 15 kV, with a beam current of 20 nA and beam diameter of 1  $\mu\text{m}$ . The standard materials used were natural wollastonite for Si and Ca, synthetic  $\text{TiO}_2$  for Ti, synthetic spinel for Al and Mg, synthetic  $\text{Cr}_2\text{O}_3$  for Cr, synthetic  $\text{Ca}_3\text{V}_2\text{O}_8$  for V, synthetic hematite for Fe, synthetic MnO for Mn, synthetic NiO for Ni, synthetic  $\text{ZrO}_2$  for Zr, synthetic  $\text{Y}_2\text{Al}_5\text{O}_{12}$  for Y,  $\text{K}_2\text{O}\cdot\text{TiO}_2\cdot\text{P}_2\text{O}_5$ -glass for K and P, and synthetic  $\text{HfO}_2$  for Hf.; The CHIME isochron method (Suzuki et al., 1991; Suzuki and Adachi, 1991) was applied for the age determination of monazite, using “working standard” technique by Kato et al. (2005). By this technique, natural monazites were calibrated using well-characterized primary oxide standards of U, Th and Pb, and are usable as working standard only with measurement of X-ray intensities of U, Th and Pb. In the present study, natural Sri Lankan monazites with  $\text{UO}_2 = 1.682$ ,  $\text{ThO}_2 = 6.93$ , and  $\text{PbO} = 0.261$  wt.%, and with  $\text{UO}_2 = 0.512$ ,  $\text{ThO}_2 = 15.890$ , and  $\text{PbO} = 0.401$  wt.% were used working standards for U and Th, respectively. The standard

materials used for Y and Pb were synthetic  $Y_2Al_5O_{12}$  and natural PbS, respectively. The compositions of natural Sri Lankan monazites were determined at Tsukuba Research Departments, National Museum of Nature and Science, Japan. The abundances of U, Th, Pb, and Y were measured using an accelerating voltage of 15 kV, a beam current of 200 nA, and a beam diameter of 3–10  $\mu\text{m}$ . The X-ray interferences of  $ThM\zeta_{1,2}$  and  $YL\gamma$  on  $PbM\alpha$ , and  $ThM\gamma$  on  $UM\beta$  were corrected along with the background interference corrections, using dwell time of 200 seconds in both peak and background positions. The ZAF method was used for data correction for all elements.

Internal textures of zircon were examined using back-scattered electron (BSE) images and cathodoluminescence (CL) images. The CL images were obtained using a panchromatic cathodoluminescence system attached to the JEOL JXA-8530F EMPA.

### **IV-3. LASER ABLATION INDUCTIVELY COUPLED PLASMA MASS SPECTROMETRY (LA-ICP-MS) ANALYSIS FOR ZIRCON**

For the chronological analyses of zircon using Laser Ablation Inductively Coupled Plasma Mass Spectrometry (LA-ICP-MS), zircon grains were separated using heavy liquid from crushed fine rock fragments below 200  $\mu\text{m}$  in size, and finally handpicked. The separated zircon grains were mounted in epoxy resin, and polished by diamond paste until they were thinned approximately half of the original thickness. The LA-ICP-MS analyses were carried out using an Agilent 7500 Series LA-ICP-MS equipment in Hiroshima University. The analytical procedure is summarized in Katsube et al. (2012), and the data reduction was done using Pepi-AGE software (Dunkl et al., 2008). The software program Isoplot 4.15 based on Ludwig (2008) was used to represent the U-Pb Concordia plots and calculate the weighted average of ages.



#### IV-4. U-Th-TOTAL Pb ISOCHRONAL ANALYSIS FOR MONAZITE

Monazite includes radioactive elements as U and Th. They are chemically stable for the environment such as heat. It is considered that these radioactive elements have not moved in the rock since the mineral particle crystallized. Radioactive elements such as U gradually undergo radioactive decay and generate Pb as a nuclide. The initial amount of Pb to assumed as constant or negligible. Quantitative analyses of U, Th, and Pb at many points were taken and make an isochron plot. The following equation shows the U-Th-total Pb and apparent age ( $\tau$ ) relationship.

$$TotalPb = Pb_{initial} + Th\{\exp(\lambda_{232}\tau) - 1\} + U\left\{\frac{137.88 \exp(\lambda_{238}\tau) + \exp(\lambda_{235}\tau)}{138.88} - 1\right\}$$

Where,  $\lambda_{232}$ ,  $\lambda_{238}$ , and  $\lambda_{235}$  represent the decay constants.

Preparation of sample should be in a Pb-free environment in any possible way. This is because of the lower amount of Pb content in monazite can be easily contaminated. In this study, the thin-sections were carbon coated and then observed the BSE images and chemical composition maps on U, Th, Pb, and Y to identify the possible domains.

For the analyses of U, Th, Pb, and Y, special EPMA conditions were applied for the X-Ray beam current, peak and background count time, and matrix corrections. The beam current, diameter, and peak and background count time were selected as 200 nA, 3  $\mu$ m, and 100–200 s, respectively. The ZAF matrix correction method was used with fixed other elements (Si, P, Ca, La, Ce, Pr, Nd, Sm, Gd, Dy). The average pelite monazite values were used for the fixed elements as recommended by Pyle (2001) and Pyle et al. (2005).

Considering the possible interferences (Fig. 5) as described by Scherre et al. (2000), X-Ray types for Th, Pb and U were selected as  $ThM\alpha$ ,  $PbM\alpha$ , and  $UM\beta$ , respectively. The interferences were corrected as  $ThM\zeta_{1,2}$  and  $YL\gamma$  on  $PbM\alpha$ , and  $ThM\gamma$  on  $UM\beta$ . X-Ray

detectors of the EPMA for Th-U and Pb are Gass-flow proportional counter (PETJ) and Xe-filled proportional counter (PETH), respectively.

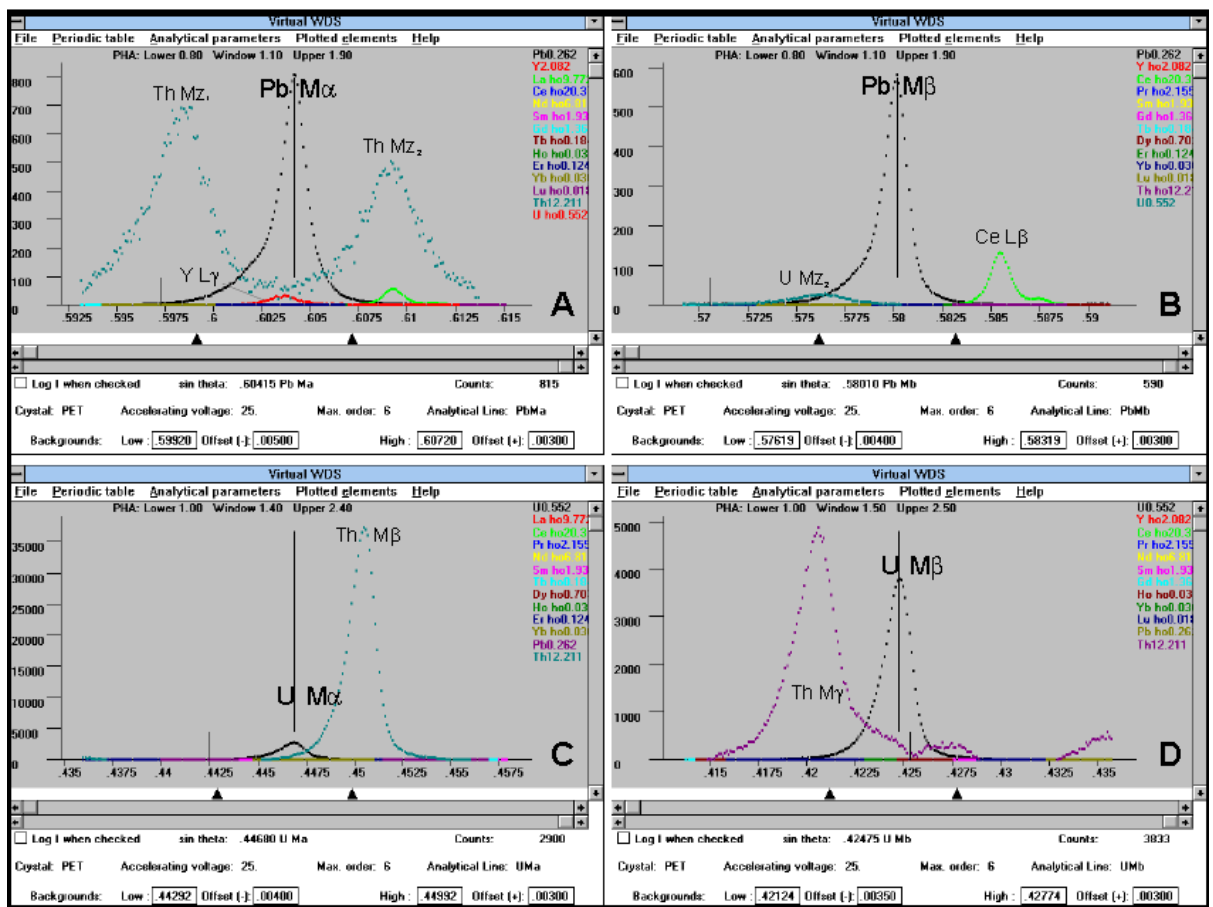


**Figure 7.** Peak overlap simulations applying the program VIRTUAL WDS by Reed and Buckley (1996) (modified after Scherrer et al., 2000). The figure visualizes the critical interferences relevant to Th-U-Pb dating of monazite with the EPMA. (A) Y and Th interference on PbM $\alpha$ . (B) U and Ce interference in PbM $\beta$ . (C) Th interference on UM $\alpha$ . (D) Th interference on UM $\beta$ .

The background positions for background interference corrections were done according to the Pyle et al. (2005). The examples of background positions for  $UM\beta$  and  $PbM\alpha$  were shown in Figure 8.

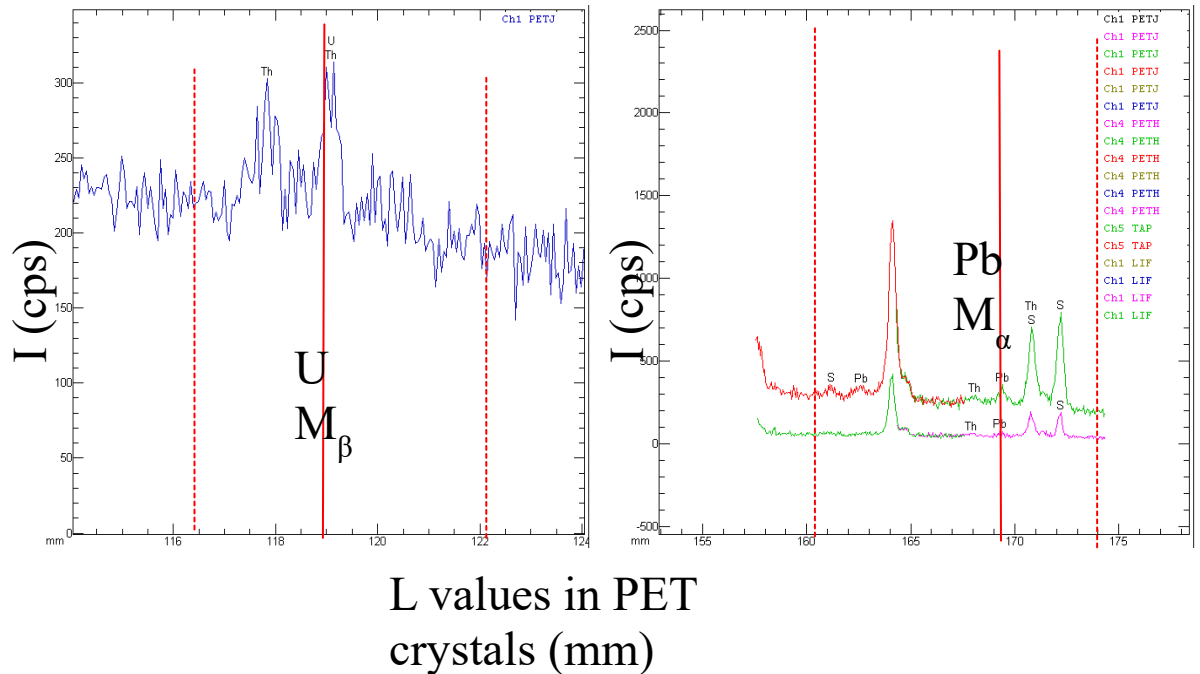


**Figure 8.** Background interference corrections.

Quantitative analyses were carried out after fixing the machine conditions for each identified domains in monazite. Age calculation was done using isochron plots and CHIME software installed in EPMA. The weighted average of apparent age method, Suzuki and Adachi method (Suzuki et al., 1991; Suzuki and Adachi, 1991), and Montel method (Montel et al., 1996) were used to calculate the ages. In the Suzuki and Adachi method, the isochron is plotted assuming that the common Pb and partial loss of Pb are detectable, where the interception value is taken into considerations. In the Montel method, the isochron is plotted assuming that the common Pb is negligible and partial loss of Pb has not occurred, where the regression line is forced through the zero. Suzuki and Adachi method is effectively applied for larger monazite grains, thick zones, and larger domains, whereas, Montel method can be applied to the smaller monazite grains, thin zones, and smaller domains.

## V. RESULTS

### V-1. SAMPLE DESCRIPTION AND PETROGRAPHY

Twenty-four rock samples were collected from natural rock outcrops. Based on the preliminary petrographic study, six gneiss samples with monazite as accessory mineral were selected for detailed study: five garnet-biotite gneiss samples (17-24GB, 14-21GB, 07-10GB, 11-17GB, and 03-04GB), one garnet-biotite-cordierite gneiss sample (23-32Co), one hornblende-bearing charnockitic gneiss sample (10-16B), and three charnockitic gneiss samples (04-05C, 02-02C, and 20-30C). Mineral assemblages and abundances of the minerals in these samples are summarized in Table 2.

The mineral assemblage of the garnet-biotite gneiss is garnet + biotite + plagioclase + K-feldspar ± cordierite ± sillimanite + quartz + magnetite ± rutile ± spinel ± ilmenite ± calcite. Garnet occurs as porphyroblasts, and three modes of occurrences were recognized: (1) inclusion-free first generation garnet (Figure 9a); (2) inclusion-bearing first generation garnet (Figure 9b, c, d, and g); and (3) second generation garnet (Figure 9h). Most of the garnet porphyroblasts lack compositional zoning. However, some garnets in 11-17GB contain inclusion-rich cores and inclusion-poor rims (Figure 9c). Sample 14-21GB contains cordierite as a reaction product. Zircon and monazite are present as accessory minerals in all five samples of garnet-biotite gneiss (Figure 9a). Their grain sizes range from 50 to 150 μm and from 50 to 500 μm, respectively, and their abundances are characteristically high in quartz- and biotite-rich samples. Most of the zircons occur around biotite layers, and as inclusions within biotite (Figure 9i). Most of those zircons linearly occur along the foliation of biotite, and biotite grains in the biotite layer are rather large in size (0.2–2 mm). Cordierite and sillimanite are characteristic minerals in the matrices of 14-21GB and 11-17GB, respectively

(Table.2). Monazite occurs mainly in the matrix (Figure 9a d, and f) and as inclusions in garnet (Figure 9e).

**Table 2.** Mineral assemblages of selected samples

Sample No.	Location	Major and minor minerals										Accessory minerals						
		Grt	Bt	Kfs	Pl	Opx	Cpx	Hbl	Crd	Sil	Qtz	Ap	Mnz	Zrn	Mag	Rt	Ilm	Spl
Garnet-biotite gneiss																		
17-24GB	80°06'32.4"E 06°43'55.0"N	⊙	⊙	⊙	○	×	×	×	×	×	⊙	△	△	△	△	△	△	×
14-21GB	80°03'06.0"E 06°46'12.0"N	⊙	⊙	⊙	⊙	×	×	×	△	×	⊙	△	△	△	△	△	△	×
07-10GB	80°07'45.4"E 06°30'55.9"N	⊙	⊙	⊙	⊙	×	×	×	×	×	⊙	△	△	△	△	△	△	×
11-17GB	80°14'20.2"E 06°36'35.7"N	⊙	⊙	⊙	○	×	×	×	×	⊙	⊙	△	△	△	△	△	△	×
03-04GB	80°16'37.3"E 06°32'34.5"N	⊙	⊙	⊙	○	×	×	×	×	×	⊙	△	△	△	△	△	△	×
Garnet-biotite-cordierite gneiss																		
23-32Co	80°06'10.8"E 06°56'54.9"N	○	⊙	○	○	×	×	×	⊙	×	○	△	△	△	○	△	△	○
Hornblende-bearing charnockitic gneiss																		
10-16B	80°14'46.7"E 06°38'48.3"N	⊙	×	△	△	⊙	⊙	⊙	×	×	△	△	△	△	△	△	△	×
Charnockitic gneiss																		
04-05C	80°13'01.6"E 06°31'52.7"N	○	○	○	⊙	○	⊙	×	×	×	○	△	△	△	△	△	△	×
02-02C	80°17'42.9"E 06°31'53.9"N	×	×	○	○	⊙	⊙	×	×	×	○	△	△	△	△	△	△	×
20-30C	80°06'38.3"E 06°52'26.7"N	×	⊙	○	⊙	⊙	⊙	×	×	×	○	△	△	△	△	△	△	×

⊙abundant; ○common; △ occasional; ×absent.

Ap, apatite; Bt, biotite; Cpx, clinopyroxene; Crd, cordierite; Grt, garnet; Hbl, hornblende; Ilm, ilmenite; Kfs, K-feldspar; Mag, magnetite; Mnz, monazite; Opx, orthopyroxene; Pl, plagioclase; Qtz, quartz; Rt, rutile; Sil, sillimanite; Spl, Spinel; Zrn, zircon.

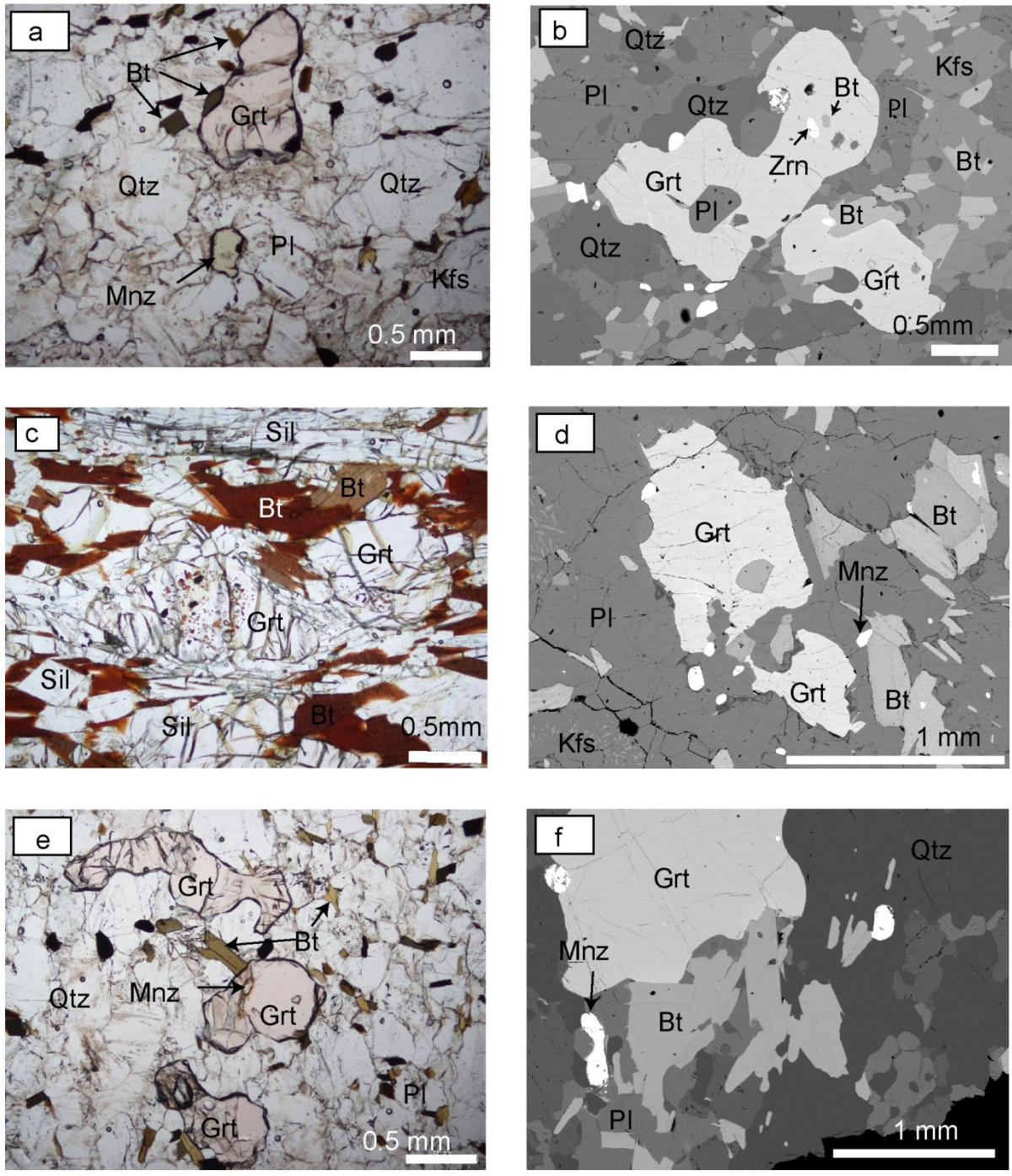


**Figure 9.** Representative petrographic images. (a), (c), and (e) are optical microscopic images in plane-polarized light, and (b), (d) and (f) are back-scattered electron (BSE) images. (a) inclusion-free garnet porphyroblast and matrix monazite (17-24GB). (b) inclusion-bearing porphyroblastic garnet (17-24GB). (c) garnet porphyroblasts with inclusion-rich cores and inclusion-poor rims (11-17GB). (d) garnet porphyroblast and monazite in matrix (23-32Co). (e) garnet with monazite inclusions (17-24GB). (f) garnet porphyroblast in matrix (03-04GB).

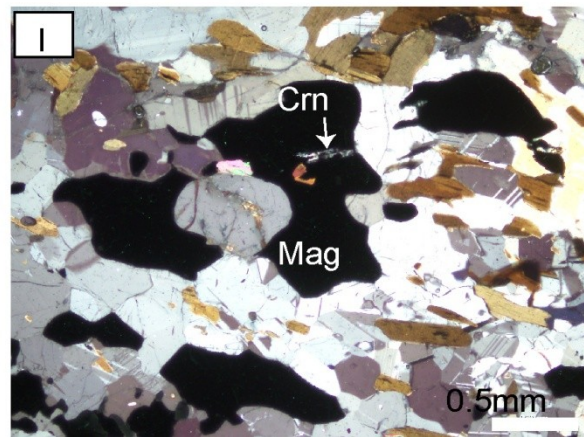
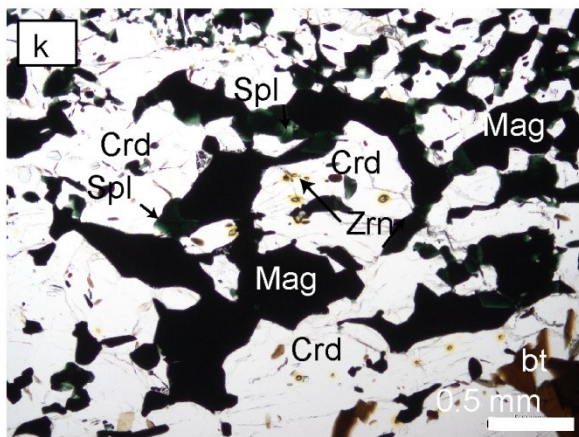
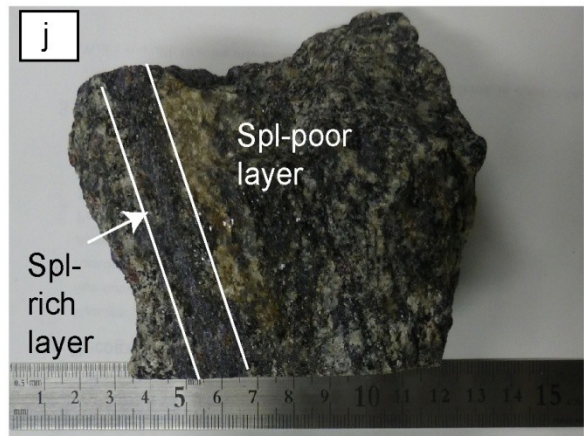
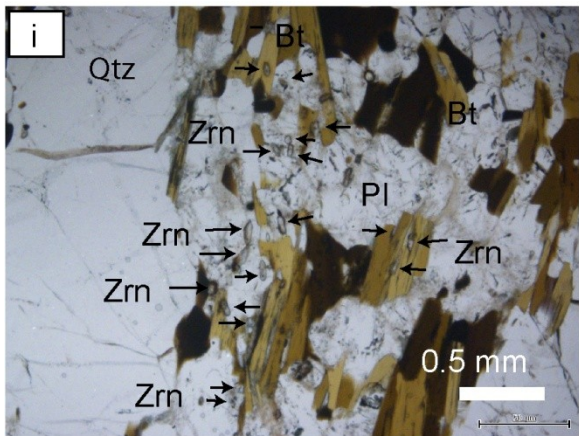
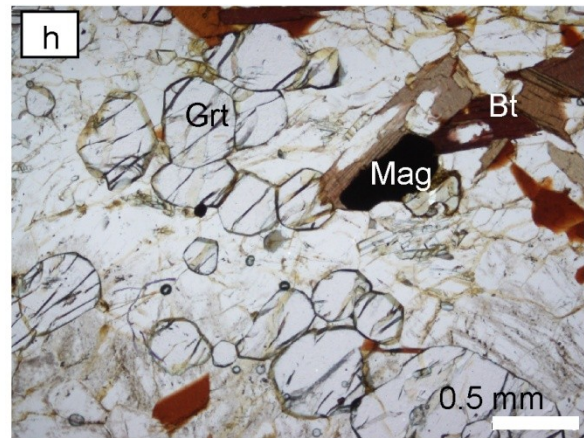
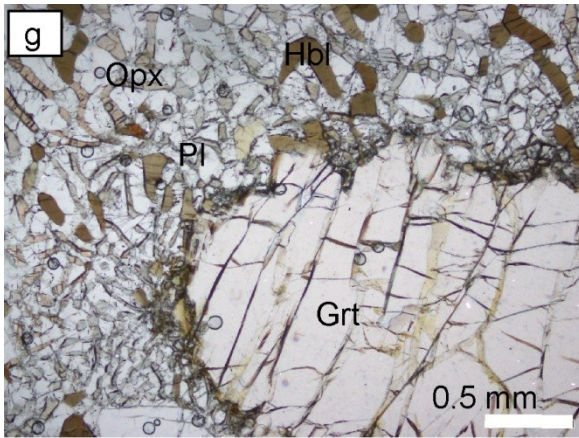


**Figure 9 (cont.).** Representative petrographic images. (g), (h), (i), and (k) are optical microscopic images in plane-polarized light, (l) is ptical microscopic images in cross-polarized light, and (j) is a hand specimen image. (g) reaction texture of garnet breakdown (10-16B). (h) second generation garnet (11-17GB). (i) zircon around biotite layer and zircon inclusions in biotite (07-10GB). (j) spinel-rich and spinel-poor layers in garnet-biotite-cordierite gneiss (23-32Co). (k) fine-grained zircon inclusions in cordierite (23-32Co). (l) corundum inclusions in magnetite (23-32Co).



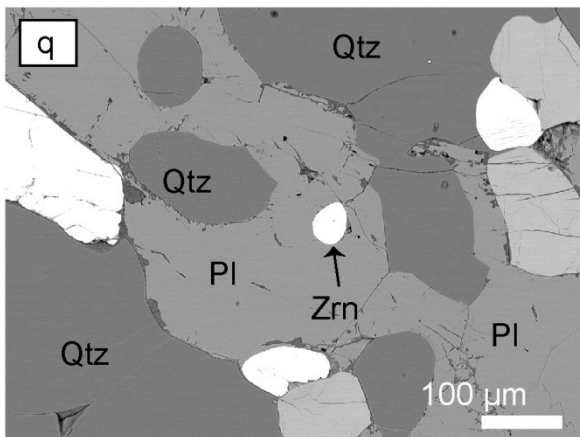
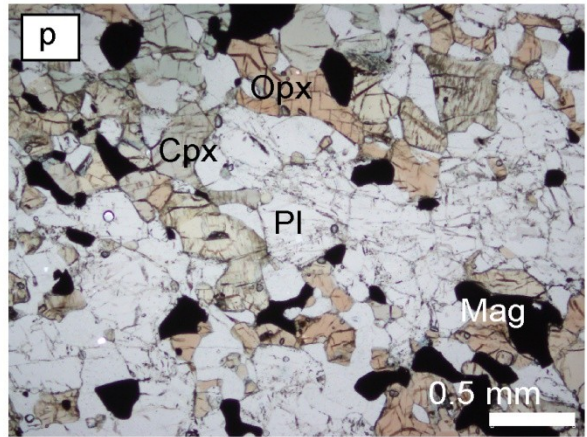
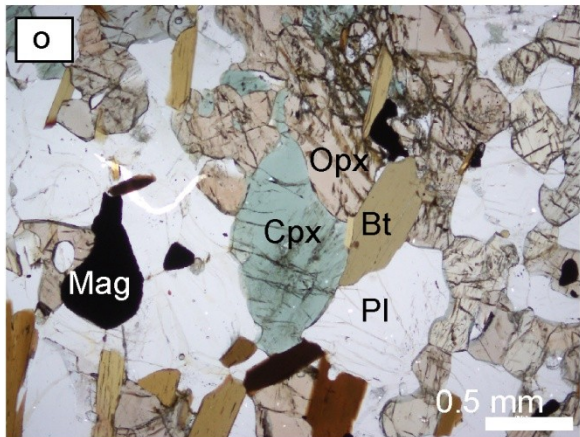
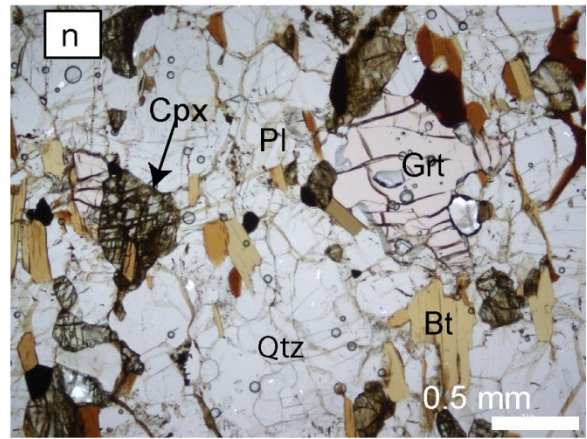
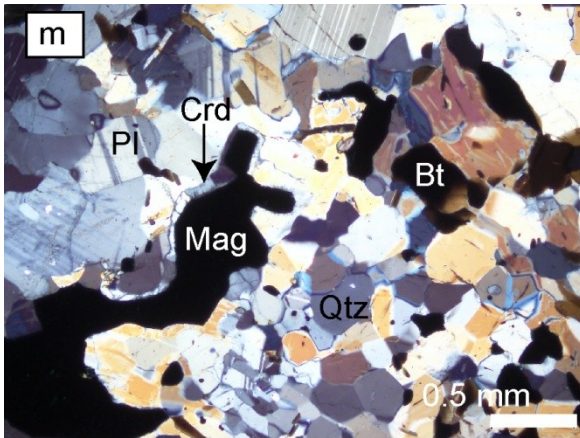


**Figure 9 (cont.).** Representative petrographic images. (n), (o), and (p) are optical microscopic images in plane-polarized light, and (m) is optical microscopic images in cross-polarized light. (q) is back-scattered electron (BSE) images. (k) reaction texture of magnetite + spinel + quartz  $\leftrightarrow$  cordierite (23-32Co). (l) garnet + biotite + clinopyroxene assemblage (04-05C). (m) The typical mineral assemblage of biotite-bearing charnockitic gneiss (20-30C). (n) The typical mineral assemblage of charnockitic gneiss without biotite (02-02C). (o) zircon inclusions in plagioclase (17-24GB).

The garnet-biotite-cordierite gneiss (22-32Co) in the study area consists of thin spinel-rich and extremely quartz-poor layers with the assemblage cordierite + plagioclase + magnetite + spinel  $\pm$  corundum, and spinel-poor layers with garnet + biotite + K-feldspar + plagioclase + quartz  $\pm$  magnetite  $\pm$  spinel (Figure 9j). In the former, cordierite occurs as a recrystallized phase. Zircon and monazite occur as fine (10  $\mu$ m) inclusions within cordierite (Figure 9k), and their abundances in garnet-biotite-cordierite gneiss are greater than that in garnet-biotite gneiss. Some magnetites contain corundum inclusions (Figure 9l). In the latter, coarse-grained cordierite is replaced by pinite. Antiperthite and an assemblage produced by the reaction of magnetite + spinel + quartz  $\leftrightarrow$  cordierite were observed in both layers (Figure 9m).

The mineral assemblage of the hornblende-bearing charnockitic gneiss (10-16B) is garnet + orthopyroxene + clinopyroxene + hornblende + anorthite  $\pm$  quartz, where hornblende and garnet occur as coarse-grained porphyroblasts. Garnet reacts with clinopyroxene, and breaks down to an assemblage of orthopyroxene + plagioclase (Figure 9g). Zircon and monazite grains are very fine (10  $\mu$ m) and/or rare.

The mineral assemblage of the charnockitic gneiss is clinopyroxene + orthopyroxene  $\pm$  biotite  $\pm$  garnet + K-feldspar + anorthite + quartz  $\pm$  magnetite. Samples 04-05C and 20-30C contain garnet (Figure 9n) and biotite (Figure 9o), respectively, whereas the other charnockitic gneisses do not (Figure 9p). Zircon is rare and fine-grained. Some zircon grains occur as inclusions within plagioclase (Figure 9q). Monazite is also rare.

## V-2. MINERAL CHEMISTRY OF REPRESENTATIVE MINERALS

### V-2-1. CHEMICAL COMPOSITION OF GARNET

The occurrence of garnet was described already. Examples of analysis positions and quantitative data are shown in Figure 8 and Table 3. Garnets are solid solutions of grossular-almandine-pyrope (Grs-Alm-Prp) series except for grossular garnets in 10-16B which is richer in (Sps) component. Garnets in all the samples are chemically homogeneous. Representative traverse lines for line analysis and chemical compositions are shown in Figures 10 and 11. Garnet compositions in garnet-biotite gneiss are Prp<sub>18-35</sub>Alm<sub>61-72</sub>Grs<sub>0-7</sub>. Garnet compositions in garnet-biotite-cordierite gneiss are Prp<sub>28.7</sub>Alm<sub>67.4</sub>Grs<sub>3.8</sub>. Garnet compositions in charnockitic gneiss are Prp<sub>18.0</sub>Alm<sub>66.6</sub>Grs<sub>10.7</sub>. In contrast, garnet compositions in hornblende-bearing charnockitic gneiss (10-16B) are Prp<sub>27.2</sub>Alm<sub>0.0</sub>Grs<sub>48.9</sub>Sps<sub>19.5</sub>.

The representative garnet chemical compositions in Table 3 show the  $X_{\text{mg}}$  [Mg/(Mg+Fe+Ca+Mn)] values of 0.12–0.24 in the garnet-biotite gneiss, 0.12 in the garnet-biotite-cordierite gneiss, and 0.29 in the charnockitic gneiss with garnet.

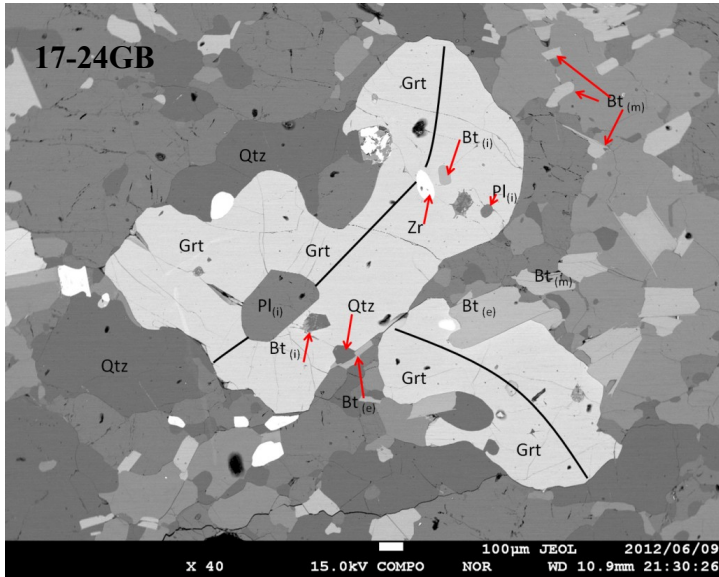
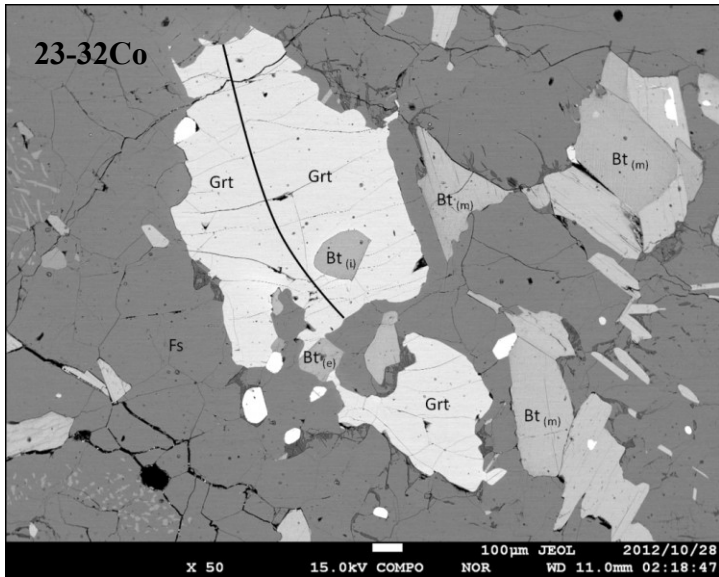
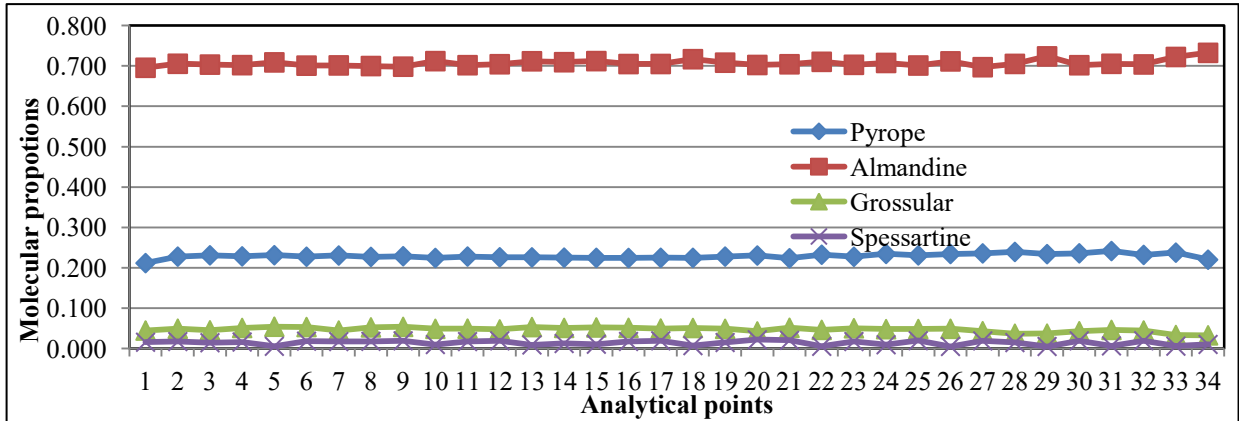


**Figure 10.** Analysis positions in garnet grains from 17-24GB and 23-32 Co samples. These two figures are representative examples of selecting three types of biotites: (1) Bt (i) – biotite as inclusions; (2) Bt (e) – biotite at edges of garnets; (3) Bt (m) – biotite in matrix.



**A**



**B**

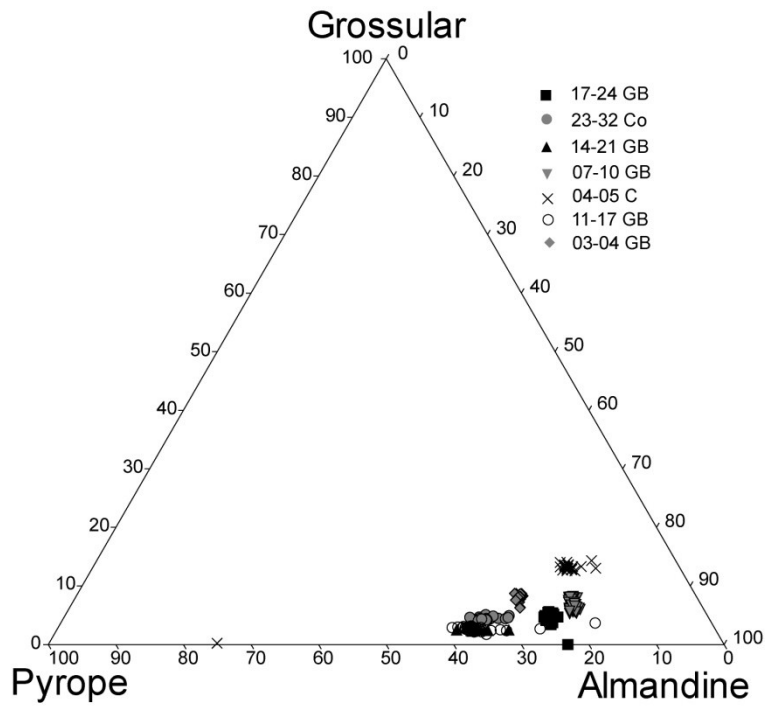


**Figure 11.** Variations of garnets in garnet-biotite gneiss and garnet-bearing cordierite gneiss. A. The variation of the end member components of the garnet according to the Figure 10 17-24GB. B. Grossular:pyrope:almandine-ratios (mol. %) in garnet for different samples.

**Table 3** Representative garnet chemical compositions

Sample no	17-24GB	14-21GB	07-10GB	11-17GB	03-04GB	04-05C	23-32Co	10-16B
SiO <sub>2</sub>	38.77	38.66	38.39	39.20	39.03	37.95	39.59	39.85
TiO <sub>2</sub>	0.01	0.01	0.01	0.01	0.03	0.02	0.00	0.06
Al <sub>2</sub> O <sub>3</sub>	21.47	21.73	21.27	22.02	21.69	20.99	22.93	22.15
Cr <sub>2</sub> O <sub>3</sub>	0.00	0.03	0.02	0.03	0.03	0.05	0.02	0.00
FeO	31.87	29.59	31.88	29.27	29.99	30.32	29.12	23.03
MnO	0.32	0.27	1.35	0.42	0.63	1.35	0.00	0.99
MgO	5.61	9.13	4.57	9.20	6.73	4.49	6.96	7.20
CaO	1.77	0.87	2.32	1.00	2.90	4.32	1.32	7.19
Na <sub>2</sub> O	0.05	0.01	0.01	0.02	0.01	0.01	0.03	0.00
K <sub>2</sub> O	0.03	0.01	0.00	0.01	0.00	0.36	0.00	0.01
Total	99.91	100.31	99.82	101.18	101.04	99.87	99.97	100.48
Oxygen	12							
Si	3.045	2.987	3.040	2.992	3.017	3.013	3.047	3.037
Ti	0.001	0.001	0.001	0.001	0.002	0.001	0.000	0.004
Al	1.988	1.978	1.985	1.982	1.976	1.964	2.080	1.989
Cr	0.000	0.002	0.001	0.002	0.002	0.003	0.001	0.000
Fe	2.094	1.912	2.111	1.883	1.939	2.013	1.874	1.467
Mn	0.021	0.018	0.090	0.028	0.041	0.091	0.000	0.064
Mg	0.657	1.052	0.540	1.044	0.775	0.530	0.799	0.818
Ca	0.149	0.072	0.197	0.082	0.240	0.367	0.109	0.587
Na	0.007	0.002	0.002	0.003	0.002	0.002	0.004	0.000
K	0.003	0.001	0.000	0.001	0.000	0.036	0.000	0.000
Total cation	7.965	8.024	7.967	8.017	7.993	8.021	7.915	7.966
Fe <sup>+3</sup>	0.000	0.057	0.000	0.047	0.004	0.025	0.000	0.000
Fe <sup>+2</sup>	2.094	1.855	2.111	1.836	1.935	1.988	1.874	1.467
End members (mol%)								
Almandine	71.7	61.9	71.8	61.4	64.7	66.6	67.4	0.0
Pyrope	22.8	35.1	18.4	34.9	25.9	18.0	28.7	27.3
Grossular	4.9	0.0	6.6	0.4	7.7	10.7	3.8	48.9
Spessartine	1.5	0.6	3.1	0.9	1.4	3.0	0.0	19.6
Andradite	0.0	2.9	0.1	2.3	0.3	1.4	0.1	2.1
Uvarovite	0.0	0.1	0.1	0.1	0.1	0.2	0.1	3.0
$X_{Mg}^*$	0.24	0.24	0.12	0.24	0.18	0.13	0.29	

\* $X_{Mg}^* = Mg/(Ca+Fe+Mg+Mn)$  atomic ratio

## V-2-2. CHEMICAL COMPOSITION OF BIOTITE

The occurrence of biotite is in a wide range. They occur as inclusions in garnet, matrix, and edge to the garnet. In the quantitative analysis, biotites at the edge and in the matrix were selected. Representative analysis positions and quantitative data are shown in Figure 12 and Tables 4 and 5.

In all studied samples, Mg/(Mg+Fe)-atomic ratios ( $X_{Mg}$ ) in biotites vary in a range between 0.4 and 0.5.  $X_{Mg}$ -values of 14-21GB, and 11-17GB biotites are about 0.5. Since the backscattered electron images and the quantitative data do not show significant chemical variations, biotite can be regarded as homogeneous in composition. Figure 12a shows the representative mineral assemblage of garnet and biotite in 17-24GB. The chemical compositions of biotites with four modes of occurrences are shown in Table 5. The Bt1 biotite, in the garnet, has chemical composition with  $X_{Mg}$  of 0.62 and TiO<sub>2</sub> content of 6.85 wt.%. The Bt2 and Bt3 biotites occurring at the edges of the garnets had  $X_{Mg}$ -values of 0.64–0.56 and TiO<sub>2</sub> content of 4.8–5.6 wt.%. The Bt4, matrix biotite, showed  $X_{Mg}$ -values of 0.58 and TiO<sub>2</sub> content of 4.39 wt.%.

Figure 12b shows the representative mineral assemblage of garnet and biotite in the 23-32Co garnet-biotite-cordierite gneiss. The chemical compositions are shown in Table 5. The Bt5 biotite, inclusions in the garnet, has  $X_{Mg}$  of 0.67 and TiO<sub>2</sub> of 4.97 wt.%. Bt6 biotites occurring at the edges of the garnets had  $X_{Mg}$  of 0.56 and TiO<sub>2</sub> of 2.63 wt.%. The Biotite in the matrix, Bt7, had  $X_{Mg}$  of 0.62, and the TiO<sub>2</sub> of 5.2 wt.%.

Figure 12c shows the mineral assemblage of garnet and biotite in garnet-biotite gneiss 14-21GB. The chemical compositions are shown in Table 5. The Bt8 biotite, inclusions in the garnet, has  $X_{Mg}$  of 0.73 and TiO<sub>2</sub> of 7.76 wt.%. The Bt9 biotite occurring at the edges of the garnets has  $X_{Mg}$  of 0.64 and TiO<sub>2</sub> of 5.21 wt.%.

In garnet-biotite gneiss 07-10GB (Figure 12d), Bt10 biotite occurring at the edges of the garnets had  $X_{Mg}$  of 0.52 and  $TiO_2$  5.07 wt.%, and Bt11 biotite occurring in the matrix had  $X_{Mg}$  value and  $TiO_2$  content of are 0.49 and 5.16 wt.%, respectively (Table 5).

In the charnockitic gneiss 04-05C (Figure 12e), Bt12 biotite occurring at the edges of the garnets has  $X_{Mg}$ -value of 0.49 and  $TiO_2$  content of 5.51 wt.%, and the Bt13 biotite occurring in the matrix had  $X_{Mg}$  of 0.46 and  $TiO_2$  content of 5.74 wt.% (Table 5).

Figure 12f shows the mineral assemblage of garnet and biotite in garnet-biotite gneiss 11-17GB. The chemical compositions are shown in Table 5. The used biotites (Bt14) presence at the edges of the garnets with  $X_{Mg}$  of 0.68 and  $TiO_2$  of 5.33 wt.%.

In the garnet-biotite gneiss 03-04GB (Figure 12g), Bt15 biotite occurring at the edges of the garnets has  $X_{Mg}$  of 0.6 and  $TiO_2$  content of 5.42 wt.%, and Bt16 biotite occurring in the matrix-had  $X_{Mg}$  of 0.59 and  $TiO_2$  content of 5.85 wt.% (Table 5).



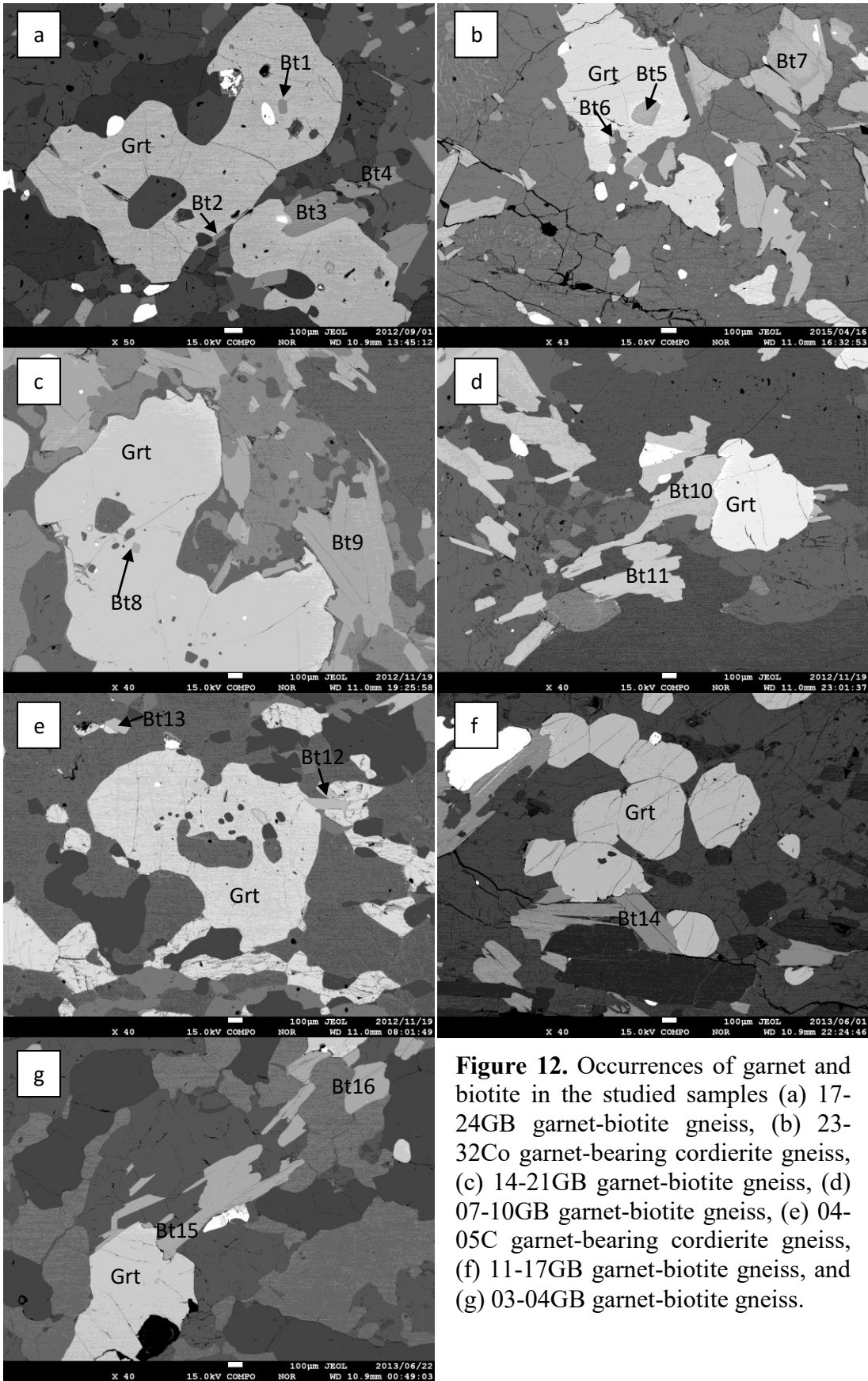


**Figure 12.** Occurrences of garnet and biotite in the studied samples (a) 17-24GB garnet-biotite gneiss, (b) 23-32Co garnet-bearing cordierite gneiss, (c) 14-21GB garnet-biotite gneiss, (d) 07-10GB garnet-biotite gneiss, (e) 04-05C garnet-bearing cordierite gneiss, (f) 11-17GB garnet-biotite gneiss, and (g) 03-04GB garnet-biotite gneiss.

**Table 4.** Average biotite chemical compositions for each sample\*

Sample no	17-24GB	14-21GB	07-10GB	11-17GB	03-04GB	04-05C	23-32Co
SiO <sub>2</sub>	36.90	37.85	35.68	36.56	35.56	36.16	36.75
TiO <sub>2</sub>	5.74	5.19	5.34	5.27	5.55	5.64	5.16
Al <sub>2</sub> O <sub>3</sub>	15.98	15.62	15.80	15.36	15.22	13.84	16.00
Cr <sub>2</sub> O <sub>3</sub>	0.05	0.06	0.04	0.06	0.02	0.07	0.02
FeO	16.55	14.45	20.06	14.19	16.59	21.27	16.54
MnO	0.01	0.02	0.03	0.02	0.02	0.02	0.12
MgO	12.21	16.29	9.28	16.14	14.00	11.18	16.14
CaO	0.01	0.00	0.00	0.01	0.00	0.00	0.04
Na <sub>2</sub> O	0.09	0.09	0.05	0.10	0.06	0.03	0.07
K <sub>2</sub> O	9.91	9.76	9.88	9.61	9.59	9.85	8.37
Total	97.46	99.33	96.17	97.32	96.60	98.09	99.21
Oxygen	22						
Si	5.455	5.411	5.44	5.346	5.310	5.443	5.283
Ti	0.610	0.558	0.61	0.580	0.624	0.639	0.558
Al	2.799	2.632	2.84	2.647	2.678	2.456	2.712
Cr	0.004	0.007	0.00	0.006	0.002	0.008	0.003
Fe	2.002	1.728	2.56	1.736	2.072	2.678	1.990
Mn	0.003	0.002	0.00	0.003	0.002	0.003	0.014
Mg	2.720	3.470	2.11	3.518	3.116	2.508	3.457
Ca	0.001	0.001	0.00	0.002	0.001	0.001	0.006
Na	0.027	0.026	0.02	0.029	0.018	0.009	0.020
K	1.853	1.781	1.92	1.793	1.827	1.892	1.537
Total cation	15.474	15.615	15.50	15.658	15.649	15.637	15.579
$X_{Mg}^{**}$	0.425	0.530	0.316	0.532	0.458	0.344	0.494

\*Average values for each mineral grain were further averaged for each rock sample.

\*\*  $X_{Mg} = Mg/(Mg + Fe)$  atomic ratio.

**Table 5.** Representative biotite chemical compositions

Sample no	17-24GB			14-21GB		07-10GB		11-17GB		03-04GB		23-32Co		04-05C		
	Bt1	Bt2	Bt3	Bt4	Bt8	Bt9	Bt10	Bt11	Bt14	Bt15	Bt16	Bt5	Bt6	Bt7	Bt12	Bt13
SiO <sub>2</sub>	36.59	37.13	36.61	36.64	36.78	36.59	35.96	36.09	37.62	35.09	35.28	37.35	38.00	36.41	36.04	35.67
TiO <sub>2</sub>	6.85	4.88	5.60	4.39	7.76	5.21	5.07	5.16	5.33	5.42	5.85	4.97	2.63	5.20	5.51	5.74
Al <sub>2</sub> O <sub>3</sub>	14.97	15.95	16.08	16.30	16.05	15.28	15.58	15.61	16.02	15.08	15.19	16.31	17.72	17.10	13.62	13.72
Cr <sub>2</sub> O <sub>3</sub>	0.06	0.00	0.14	0.00	0.06	0.03	0.10	0.05	0.02	0.00	0.00	0.01	0.03	0.00	0.10	0.11
FeO	14.10	13.95	16.23	15.43	11.28	14.97	18.99	19.86	13.58	16.70	16.59	15.27	18.59	14.73	20.98	21.79
MnO	0.00	0.00	0.00	0.03	0.00	0.02	0.02	0.06	0.02	0.01	0.05	0.03	1.29	0.06	0.02	0.00
MgO	13.03	13.93	11.85	12.40	17.08	15.27	11.93	10.94	16.22	14.06	13.62	17.93	13.35	13.61	11.57	10.72
CaO	0.00	0.00	0.04	0.00	0.00	0.00	0.00	0.00	0.00	0.00	0.00	0.02	0.53	0.00	0.00	0.00
Na <sub>2</sub> O	0.33	0.06	0.11	0.08	0.42	0.10	0.07	0.08	0.07	0.04	0.07	0.06	0.09	0.07	0.03	0.01
K <sub>2</sub> O	9.55	9.89	10.16	9.71	9.13	9.43	9.99	9.76	10.08	9.79	9.79	6.50	4.12	10.02	9.92	9.85
Total	95.48	95.80	96.81	94.97	98.57	96.90	97.71	97.61	98.95	96.19	96.43	98.43	96.35	97.19	97.78	97.62
Oxygen	22															
Si	5.452	5.497	5.438	5.507	5.226	5.386	5.370	5.406	5.388	5.280	5.289	5.310	5.531	5.341	5.441	5.417
Ti	0.768	0.543	0.626	0.496	0.830	0.577	0.569	0.582	0.574	0.613	0.660	0.531	0.288	0.573	0.625	0.655
Al	2.629	2.784	2.815	2.888	2.688	2.650	2.742	2.755	2.703	2.674	2.684	2.732	3.040	2.957	2.423	2.456
Cr	0.006	0.000	0.017	0.000	0.007	0.004	0.011	0.006	0.002	0.000	0.000	0.001	0.003	0.000	0.012	0.013
Fe	1.757	1.727	2.016	1.939	1.341	1.843	2.372	2.488	1.626	2.101	2.080	1.815	2.263	1.807	2.648	2.768
Mn	0.000	0.000	0.000	0.003	0.000	0.003	0.003	0.007	0.002	0.002	0.006	0.003	0.159	0.007	0.003	0.001
Mg	2.894	3.074	2.624	2.778	3.619	3.350	2.656	2.443	3.462	3.155	3.044	3.800	2.898	2.977	2.604	2.427
Ca	0.000	0.000	0.006	0.000	0.000	0.001	0.000	0.000	0.000	0.000	0.000	0.003	0.082	0.000	0.000	0.000
Na	0.095	0.018	0.031	0.023	0.117	0.027	0.020	0.024	0.018	0.011	0.020	0.017	0.025	0.019	0.010	0.003
K	1.816	1.869	1.926	1.862	1.656	1.771	1.904	1.865	1.841	1.879	1.873	1.178	0.765	1.874	1.911	1.909
Total cation	15.418	15.511	15.498	15.495	15.483	15.610	15.646	15.577	15.616	15.715	15.656	15.390	15.055	15.554	15.677	15.649
$X_{Mg}^*$	0.622	0.640	0.566	0.589	0.730	0.645	0.528	0.495	0.680	0.600	0.594	0.677	0.561	0.622	0.496	0.467

\* $X_{Mg}$  = Mg/(Ca+Fe+Mg+Mn) atomic ratio

### V-2-3. CHEMICAL COMPOSITIONS OF PYROXENE AND AMPHIBOLE

The representative chemical compositions of orthopyroxene (Opx), clinopyroxene (Cpx), hornblende (Hbl) are shown in Tables 6, 7 and 8, respectively. The occurrences are shown in Figure 13.

The compositions of orthopyroxenes can be identified as basically hypersthene composition.

The clinopyroxene composition can be identified as  $\text{Ca}_{0.87}(\text{Mg}_{0.7}\text{Fe}_{0.3})\text{Si}_{1.97}\text{O}_6$ .

Amphiboles present in 10-16B shows the chemical composition of  $[\text{Na}_{0.6}\text{Ca}_{1.5}\text{Mg}_{3.1}\text{Fe}_{1.4}\text{Al}_{0.5}][\text{Al}_{2.1}\text{Si}_{6.1}]_{\Sigma 8.2}\text{O}_{22}(\text{OH})_2$ .

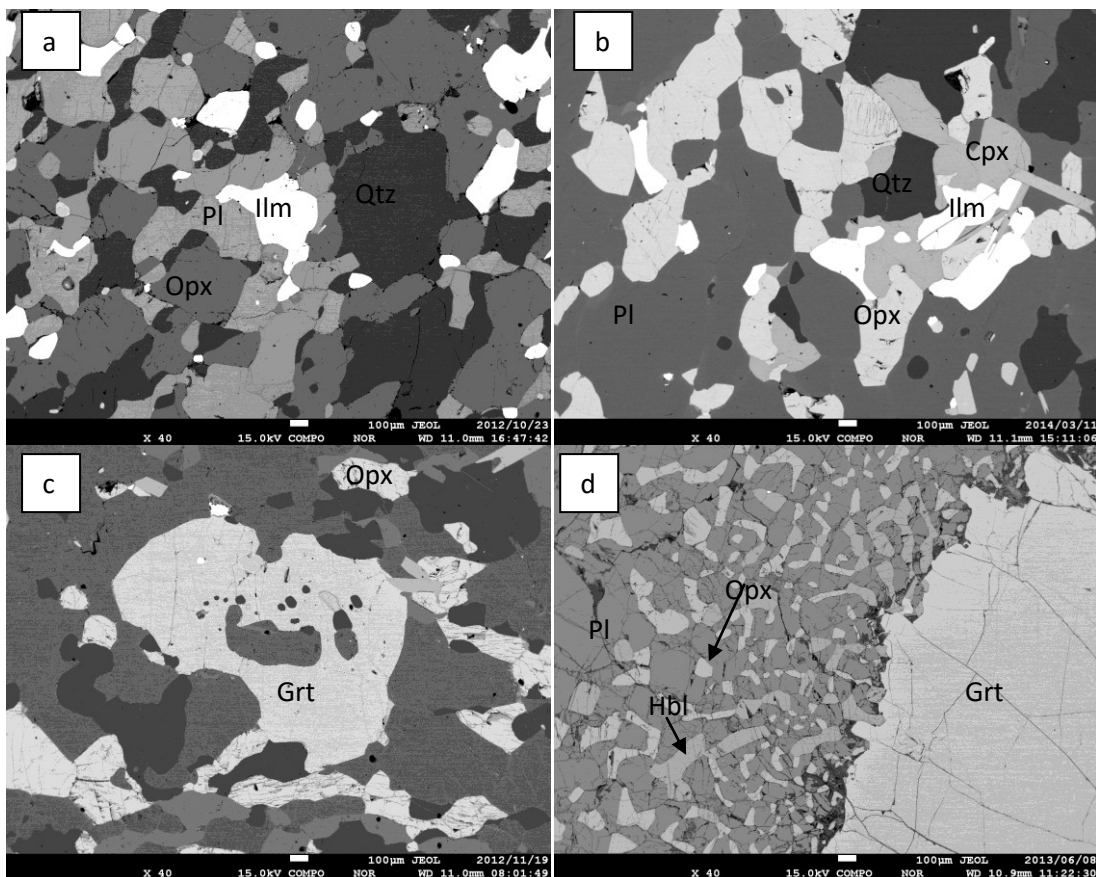


**Figure 13.** Backscattering images of orthopyroxene, clinopyroxene and hornblende in the samples 02-02C (a), 20-30C (b), 04-05C (c), and 10-16B (d).

**Table 6.** Representative chemical compositions of orthopyroxene in the samples 02-02C, 20-30C, 04-05C and 10-16B.

Sample No.	02-02C	20-30C	04-05C	10-16B
SiO <sub>2</sub>	54.78	51.82	49.28	52.56
TiO <sub>2</sub>	0.06	0.06	0.15	0.00
Al <sub>2</sub> O <sub>3</sub>	1.03	0.85	1.11	2.72
Cr <sub>2</sub> O <sub>3</sub>	0.00	0.00	0.11	0.00
FeO	21.04	27.25	34.07	23.73
MnO	0.88	0.33	0.23	0.43
MgO	22.14	18.25	14.66	20.61
CaO	0.47	0.36	0.51	0.35
Na <sub>2</sub> O	0.03	0.02	0.00	0.00
K <sub>2</sub> O	0.03	0.00	0.00	0.00
Total	100.44	98.94	100.12	100.40
Oxygen 6				
Si	2.012	1.994	1.946	1.956
Ti	0.002	0.002	0.005	0.000
Al	0.044	0.038	0.052	0.119
Cr	0.000	0.000	0.003	0.000
Fe	0.646	0.877	1.125	0.738
Mn	0.027	0.011	0.008	0.014
Mg	1.212	1.047	0.863	1.143
Ca	0.018	0.015	0.022	0.014
Na	0.002	0.001	0.000	0.000
K	0.001	0.000	0.000	0.000
Total	3.966	3.985	4.022	3.984

**Table 7.** Representative chemical composition of clinopyroxene in the sample 20-30C.

	20-30C
SiO <sub>2</sub>	51.98
TiO <sub>2</sub>	0.13
Al <sub>2</sub> O <sub>3</sub>	1.53
Cr <sub>2</sub> O <sub>3</sub>	0.00
FeO	10.90
MnO	0.10
MgO	12.53
CaO	21.54
Na <sub>2</sub> O	0.41
K <sub>2</sub> O	0.00
Total	99.12
Oxygen 6	
Si	1.971
Ti	0.004
Al	0.068
Cr	0.000
Fe	0.346
Mn	0.003
Mg	0.709
Ca	0.875
Na	0.030
K	0.000
Total	4.006

**Table 8.** Representative chemical composition of hornblende in the sample 10-16B.

	10-16B
SiO <sub>2</sub>	42.12
TiO <sub>2</sub>	1.28
Al <sub>2</sub> O <sub>3</sub>	16.37
Cr <sub>2</sub> O <sub>3</sub>	0.08
FeO	11.53
MnO	0.22
MgO	14.25
CaO	9.49
Na <sub>2</sub> O	2.40
K <sub>2</sub> O	0.78
Total	98.53
Cations per O <sub>22</sub> (OH) <sub>2</sub>	
Si	6.083
Ti	0.139
Al	2.787
Cr	0.009
Fe	1.393
Mn	0.027
Mg	3.068
Ca	1.469
Na	0.672
K	0.144
Total	15.789

### **V-3. CHEMICAL COMPOSITION, MORPHOLOGY, DETRITAL CORES AND OVERGROWTHS, INTERNAL TEXTURES AND CHRONOLOGY OF ZIRCON**

#### **V-3-1. CHEMICAL COMPOSITION OF ZIRCON**

Representative EMPA data of zircons in each sample are listed in Table 9. Due to scarcity and fine grain size, chemical analysis of zircon in the hornblende-bearing charnockitic gneiss (10-16B) was not possible. The Zr, Hf and Si contents of zircons from all samples except for 10-16B are essentially the same. The UO<sub>2</sub> and ThO<sub>2</sub> contents vary in the ranges of 0–0.5 wt.% and 0–0.1 wt.%, respectively. Lead and Y contents are below the detection limits of the EMPA (Table 9).

There is no difference in Zr, Hf and Si contents between the bright and dark zones in BSE images of individual zircons. However, some darker zones in zircons in 11-17GB are poorer in Zr and Si, and contain minor amounts of Ca, Al and Y (Figure 14(a)). Those elemental variations in the darker zones are mainly due to alteration or metamictization. Due to the altered or metamictized areas of zircons, errors of analytical data of zircons in 07-10GB and 11-17GB (Table 9) are rather large.

**Table 9.** Variation of chemical compositions and average composition of zircon from each rock sample (bdl; below detection limit)

Garnet-biotite gneiss										
17-24GB			14-21GB		07-10GB		11-17GB		03-04GB	
	Range	Av.(s.d.)	Range	Av.(s.d.)	Range	Av.(s.d.)	Range	Av.(s.d.)	Range wt.%	Av.(s.d.)
	<i>n</i> = 209		<i>n</i> = 23		<i>n</i> = 105		<i>n</i> = 26		<i>n</i> = 23	
SiO <sub>2</sub>	33.51-34.67	34.18(60)	33.72-34.24	33.91(21)	30.20-34.07	32.66(133)	29.78-34.98	61.86(168)	34.13-39.32	34.74(103)
ZrO <sub>2</sub>	63.04-65.57	64.55(60)	63.39-64.72	64.19(52)	54.16-65.31	61.60(379)	52.62-64.54	1.52(21)	57.24-64.61	63.49(149)
HfO <sub>2</sub>	0-1.67	0.94(27)	1.18-1.61	1.35(16)	1.05-1.97	1.48(21)	1.01-1.81	33.63(381)	0.77-1.59	1.17(23)
UO <sub>2</sub>	bdl	bdl	0.02-0.09	0.06(3)	0-0.50	0.17(17)	bdl	bdl	bdl	bdl
ThO <sub>2</sub>	bdl	bdl	0-0.008	0.001(3)	0-0.25	0.03(6)	bdl	bdl	bdl	bdl
PbO	bdl	bdl	bdl	bdl	0-0.04	0.01(9)	bdl	bdl	bdl	bdl
Y <sub>2</sub> O <sub>3</sub>	bdl	bdl	0-0.03	0.01(1)	bdl	bdl	bdl	bdl	bdl	bdl
Total		99.67		99.52		95.97		97.20		99.44
Cations per 4 oxygens										
Si		1.04(1)		1.02(1)		1.00(13)		1.12(20)		1.06(3)
Zr		0.94(2)		0.95(1)		0.91(21)		0.86(22)		0.93(3)
Hf		0.01(1)		0.01(1)		0.01(1)		0.01(1)		0.01(1)
Garnet-biotite-cordierite gneiss			Charnockitic gneiss							
23-32 Co			04-05C		02-02C		20-30C			
	Range	Av.(s.d.)	Range	Av.(s.d.)	Range	Av.(s.d.)	Range	Av.(s.d.)		
	<i>n</i> = 162		<i>n</i> = 41		<i>n</i> = 48		<i>n</i> = 50			
SiO <sub>2</sub>	33.49-33.79	33.67(12)	33.65-34.41	33.94(22)	33.62-33.95	33.82(12)	33.48-34.66	34.17(25)		
ZrO <sub>2</sub>	63.34-64.56	63.83(55)	60.58-65.94	64.61(126)	62.19-64.10	62.62(37)	64.30-64.19	65.25(47)		
HfO <sub>2</sub>	1.39-1.54	1.45(7)	0.86-1.77	1.39(23)	1.16-1.37	1.22(9)	0.76-1.56	1.20(16)		
UO <sub>2</sub>	0.01-0.10	0.04(4)	0-0.38	0.10(11)	bdl	bdl	bdl	bdl		
ThO <sub>2</sub>	bdl	bdl	bdl	bdl	bdl	bdl	bdl	bdl		
PbO	0-0.01	0.01(1)	0-0.27	0.04(7)	bdl	bdl	bdl	bdl		
Y <sub>2</sub> O <sub>3</sub>	0.01-0.14	0.08(6)	bdl	bdl	bdl	bdl	bdl	bdl		
Total		99.04		100.30		97.67		100.71		
Cations per 4 oxygens										
Si		1.04(3)		1.03(2)		1.03(1)		1.03(1)		
Zr		0.94(3)		0.96(8)		0.95(1)		0.96(1)		
Hf		0.01(1)		0.01(1)		0.01(1)		0.01(1)		

\* Values in parentheses are standard deviations

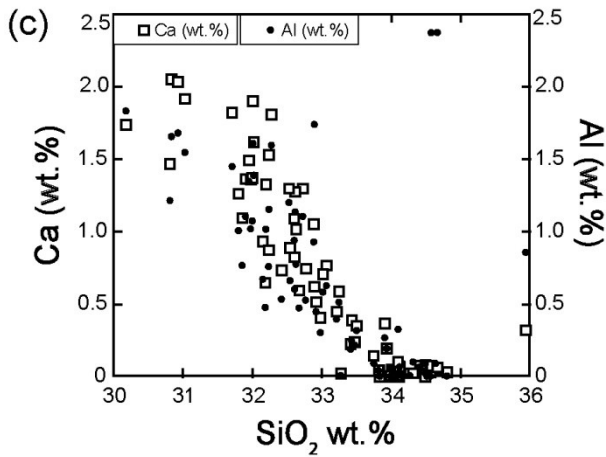
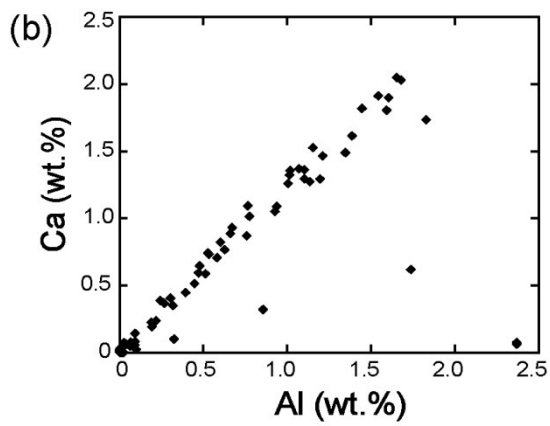
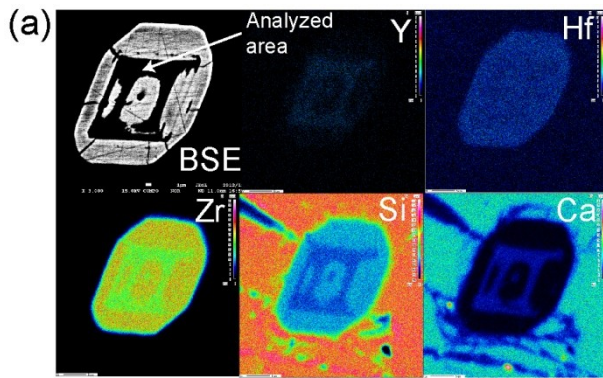


**Figure 14.** Chemistry of altered or metamictized area of zircon. (a) BSE image and elemental distribution maps for Y, Hf, Zr, Si, and Ca; (b) Al (wt.%)–Ca (wt.%) relation; (c) Ca (wt.%) and Al (wt.%) contents against SiO<sub>2</sub> (wt.%).



### **V-3-2. MORPHOLOGY OF ZIRCONS**

Zircons in the four rock types show a wide variety of morphology, abundances of detrital cores and internal textures, as summarized in Table 10.

As Corfu et al. (2003) indicated, zircon morphology reflects its formation process. Zircon grains with the lower length/width ratios are typical in metamorphic rocks, whereas zircons formed at magmatic temperatures or under hydrothermal conditions show higher length/width ratios. Length/width ratios of 200 zircon grains measured in thin-section of garnet-biotite-gneiss, charnockitic gneiss, hornblende-bearing charnockitic gneiss and charnockitic gneiss range mostly between 1.0 and 1.5, and are less than 3.0 (Table 10). However, in the garnet-biotite-gneiss samples of 07-10GB and 03-04GB, the ratios attained in a range between 4.0 and 4.5 (Table 10; Figure 15). The abundance of euhedral zircons (0–24 % of the analyzed zircons) is less than that of subhedral and anhedral zircons (17–100 % and 0–83 %, respectively) (Table 10). The subhedral and anhedral shapes are due to resorption.

### **V-3-3. ABUNDANCES OF DETRITAL CORE IN ZIRCON IN EACH ROCK TYPE**

In the garnet-biotite gneiss samples of 17-24GB, 14-21GB, 07-10GB, 11-17GB, and 03-04GB, abundances of the detrital cores in zircons distribute in a range between 30 % (17-24GB) and 80 % (07-10GB). In these samples, 22 % (03-04GB) to 50 % (17-24GB) of the detrital cores in zircons show oscillatory zoning, and 88 % (03-04GB) to 50 % (17-24GB) of the detrital cores have transgressive textures. However, in the sillimanite-bearing garnet-biotite gneiss (11-17GB), almost all detrital cores show transgressive textures.

In the garnet-biotite-cordierite gneiss (23-32Co), 47% of the analyzed zircon grains show detrital cores, in which 21% of them bear oscillatory zonings, and 26% of them show transgressive textures. Larger grains in the matrix and fine inclusions in the recrystallized

cordierite are two major occurrences of the zircon in this sample. Fine zircon inclusions rarely show detrital cores.

In the hornblende-bearing charnockitic gneiss (10-16B), 20% of the analyzed zircon grains show detrital cores. None of them bears oscillatory zoning, and the all of them have transgressive textures.

In the charnockitic gneiss, the abundances of the detrital cores of zircons are 36 %, 33 % and 42 % of the analyzed zircon grains for 04-05C, 02-02C, and 20-30C, respectively. The detrital cores of 04-05C and 02-02C lack oscillatory zoning, and only 2 % of zircons in the 20-30C had the detrital cores showing oscillatory zoning. Instead, the detrital cores of the zircons in the charnockitic gneiss essentially have transgressive textures.

**Table 10.** Abundances of zircon with detrital core and internal textures

Sample No.	Mineral assemblage	Length to width ratio of zircon (%)					External morphology of zircon (%)			Abundance of zircon with detrital core (%)			Abundance of internal textures (%)			
		1.0-1.5	1.5-2.0	2.0-2.5	2.5-3.0	4.0-4.5	Euhedral form	Subhedral form	Anhedra form by resorption	Total	With oscillatory zoning	Without oscillatory zoning	Radial growth	Planner banded zones	Darker seam around detrital core	Fir-tree
17-24GB	Grt+Bt+Kfs+Pl+Qtz	43	43	5	10	0	4	43	53	28	14	14	74	37	0	2
14-21GB	Grt+Bt+Kfs+Pl+Crd+Qtz	100	0	0	0	0	7	19	74	73	23	50	100	36	9	14
07-10GB	Grt+Bt+Kfs+Pl+Qtz	44	26	19	7	4	0	17	83	77	47	30	85	11	9	1
11-17GB	Grt+Bt+Kfs+Pl+Sil+Qtz	64	21	7	7	0	5	36	59	57	0	57	36	43	21	0
03-04GB	Grt+Bt+Kfs+Pl+Qtz	68	14	11	5	3	24	52	25	54	22	32	11	60	22	3
22-32Co	Grt+Bt+Kfs+Pl+Crd+ Qtz+ Spl	67	17	11	6	0	5	37	53	47	21	26	98	0	0	0
10-16B	Grt+Bt+Kfs+Pl+Opx+Cpx+ Hbl+Qtz	100	0	0	0	0	4	30	67	20	0	20	20	0	0	0
04-05C	Grt+Bt+Kfs+Pl+Cpx+Qtz	87	13	0	0	0	14	43	43	36	0	36	100	45	0	18
02-02C	Kfs+Pl+Opx+Cpx+Qtz	100	0	0	0	0	8	51	35	33	0	33	100	0	0	0
20-30C	Bt+Kfs+Pl+Opx+Cpx+Qtz	55	45	0	0	0	0	100	0	42	2	40	96	22	0	0

Abbreviation follows the Table 2 and accessory minerals ( $\pm$ Ap $\pm$ Mnz $\pm$ Zrn $\pm$ Mag $\pm$ Rt $\pm$ Ilm) are common for all the samples

\* Zircons with length to width ratios in a range of 3.0–4.0 have not been observed.

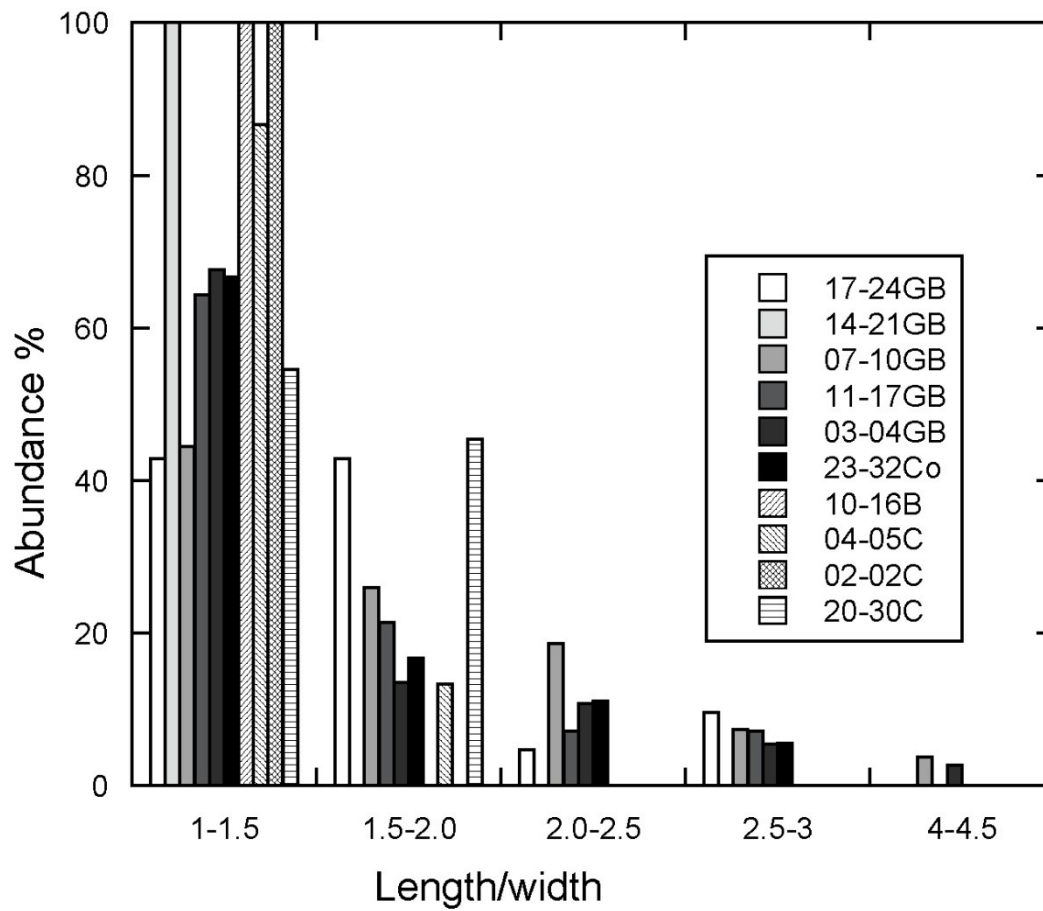


**Figure 15.** Length to width ratios of zircon grains from the Southwestern Highland Complex

#### **V-3-4. INTERNAL TEXTURES: DETRITAL CORES AND OVERGROWTHS**

Internal textures of 200 zircon grains in the thin sections of all rock types and forty-eight separated zircon grains from garnet-biotite gneiss are characterized as follows.

##### **V-3-4-1. GARNET-BIOTITE GNEISS (17-24GB, 14-21GB, 07-10GB, 11-17GB, AND 03-04GB).**

As shown in Figure 16, the BSE and CL images of most of the zircons from garnet-biotite gneiss show the presence of detrital zircon cores and overgrowths. Doubled core-bearing grains also show several overgrowths (Figure 16 CL7).

Detrital zircon cores occur as rounded (Figure 16 CL1, CL2, Nos. 5 and 6) and euhedral to subhedral shapes (Figure 16 No. 3, CL4, CL7, CL8, CL9, CL10, CL11, Nos. 12 and 13). Rounded and euhedral to subhedral detrital cores with truncated and/or undulated outlines (Figure 16 CL4 and CL11) show evidence of resorption. The detrital cores show transgressive internal textures (Figure 16 CL1, Nos. 3, 5, 6, CL8, CL10, CL11, Nos. 12 and 13) or oscillatory zoning (Figure 16 CL2, CL4, CL7, and CL9).

The overgrowths with two stages (Figure 16 CL9, CL11, Nos. 12 and 13), three stages (Figure 16 CL1 and CL4), and four stages (Figure 16 CL2 and CL10) are observed. In rare cases, five stages of zircon growth were recognized in the BSE images (Figure 16 No. 6). The volumes of the overgrowths on the detrital cores are generally less than those of the detrital cores (Figure 16 CL1 and CL2). The thicker overgrowths than the cores observed in some zircons (Figure 16 Nos. 5, 6, CL10, and CL11) are due to the plane of sectioning.

The first stage overgrowths completely or partially overlay the detrital cores, and commonly lack internal metamorphic texture (Figure 16 CL1, CL2, CL4, and No. 6). However, the first stage overgrowths in some zircons have banded zoning (bd) (Figure 16 CL1, No. 5, CL9, and CL10), and the banding is truncated (Figure 16 No. 5). Such

occurrence of the first stage overgrowth suggests that a resorption event occurred after the formation of the first stage overgrowth. In some grains, the first stage overgrowths show sector zoning (Figure 16 CL9), and the second and third stage overgrowths have peripheral zoning (Figure 16 CL2). Although the surface of each overgrowth in most zircons was resorped, the second stage overgrowths in some zircons with three to five successive overgrowths are overlain by the third stage overgrowth with sharp boundary (Figure 16 CL1, CL2, CL4, and No. 6). The third stage overgrowths are peripheral.

The zircons without detrital cores have metamorphic internal textures such as fir-tree texture (ft), radial growth (rd), and a planar banded (bd) zones (Figure 16 CL14).

Garnet-biotite gneiss

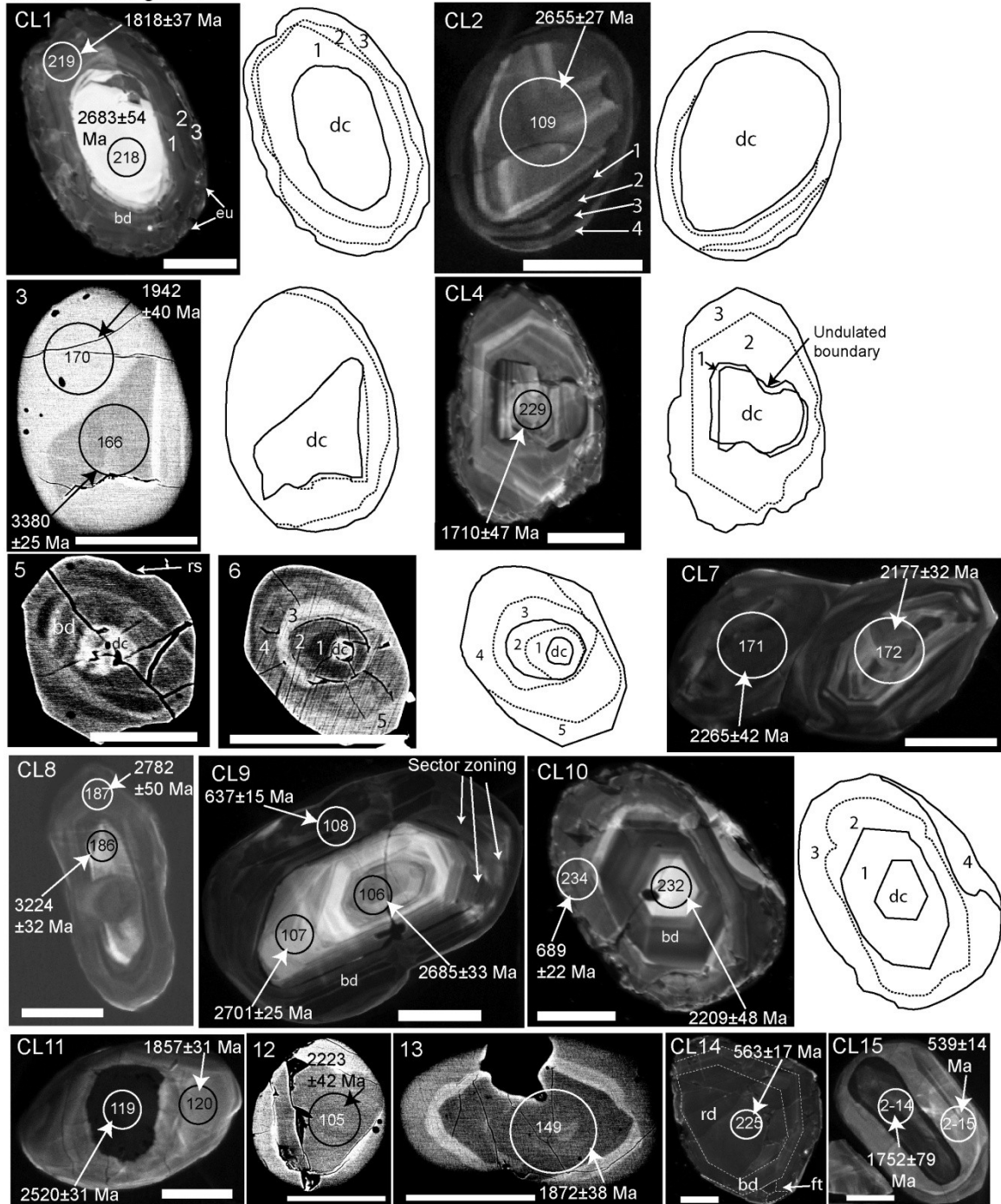


**Figure 16.** Cathodoluminescence images (CL1, CL2, CL4, CL7-CL11, CL14, and CL15) and backscattered electron images (Nos. 3, 5, 6, 12, and 13) of representative zircon grains. Scale bars are 50  $\mu\text{m}$ . dc: detrital core, eu: euhedral surface, sd: peripheral zone, bd: planar banded pattern, ft: fir-tree texture, rd: radial zone. CL1: rounded with transgressive zoning and three overgrowths. CL2: rounded detrital core with oscillatory zoning and four overgrowths. No. 3: subhedral detrital core with transgressive zoning. CL4: subhedral detrital core with oscillatory zoning. No. 5: detrital core with two overgrowths; the second overgrowth cuts the planar banding of the first. No. 6: rounded detrital core with transgressive zoning and five overgrowths demarcated by fracture-truncated boundaries. CL7: doubled core and overgrowths. CL8-CL11, Nos. 12 and 13, CL14 and CL15: zircon grains showing cores with different ages and overgrowths.

#### **V-3-4-2. GARNET-BIOTITE-CORDIERITE GNEISS (23-32CO).**

Well-defined detrital cores were not observed in zircons from the garnet-biotite-cordierite gneiss sample. The zircons consist of euhedral core part (bright part in the BSE images of Figure 17 Nos. 1, 2, and 3) and growth zones. Four to five growth stages were recognized, as shown in Figure 17 Nos. 1 and 3, even though the zircons are fine-grained (<50  $\mu\text{m}$ ). In most zircon grains, the latest growth zone had large volume. All growth zones bore no internal texture. Radial fractures were recognized in the later stage growth zones (Figure 17 Nos. 1 and 3). The morphology of the zircons is comparable to the shapes of the core part and each growth zone. Resorption changed euhedral morphology into subhedral one.

#### **V-3-4-3. HORNBLLENDE-BEARING CHARNOCKITIC GNEISS (10-16B) AND CHARNOCKITIC GNEISS (04-05C, 02-02C, AND 20-30C).**

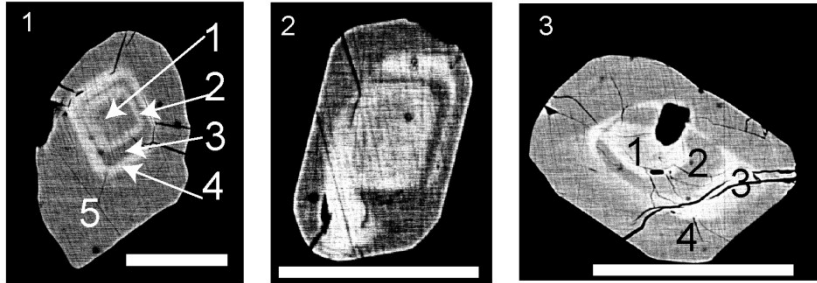
Most of the zircons in these rock types are fine-grained (<50  $\mu\text{m}$ ), but some of them reach about 200  $\mu\text{m}$  in length. Rounded external forms are due to resorption. Some zircons contain radial fractures (Figure 17 Nos. 5, 6, and 7). Zircon grains with about 200  $\mu\text{m}$  in length consist of internal texture-free cores and rims or growth zones, but lack detrital cores (Figure 17 Nos. 4 and 5). Fine-grained subhedral zircon less than 100  $\mu\text{m}$  in diameter have rounded or skeletal detrital cores containing well-rounded inclusions and/or voids (Figure 17 Nos. 5, 6, and 7). The overgrowths lack internal textures.

Zircons in the 04-05C lack detrital cores. Although growth zoning is indistinct in the BSE images (Figure 17 No. 8), the CL images reveal complex sector zoning and three sub-stages of zircon growth (Figure 17 CL8). In this case, the core of the grain (core 1 in Figure 17 CL8) may have been generated at the earliest (probably magmatic) stage of zircon crystallization, followed by the second stage and third stage overgrowths (zones 2 and 3 in



CL8, respectively). The first, second and third stage zircons have fir-tree texture (ft), radial growth (rd) and a planar banded zone (bd), respectively.

Garnet-biotite-cordierite gneiss



Hornblende-bearing charnockitic gneiss and charnockitic gneiss

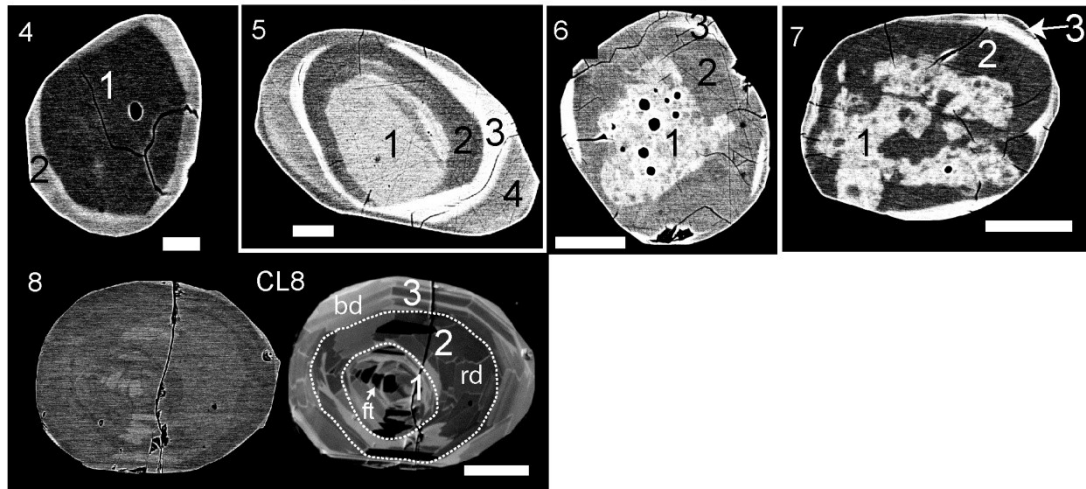


**Figure 17.** Cathodoluminescence image (CL8) and backscattered electron images (Nos. 1-8) of representative zircon grains. Scale bars are 20  $\mu\text{m}$ . bd: planar banded pattern, ft: fir-tree texture, rd: radial zone. Nos. 1, 2, and 3: euhedral grains with several zoning in garnet-biotite-cordierite gneiss. No. 4: a grain from charnockitic gneiss lacking a detrital core. No. 5: a grain from charnockitic gneiss with four growth zonings. No. 6: well-rounded and fine-grained zircon in the detrital core. No. 7: skeletal detrital core. No. 8 and CL8: a grain with three sub-stages defined by fir-tree texture, radial zone, and planar banding.

### **V-3-5. GEOCHRONOLOGY AND INTERNAL TEXTURES OF ZIRCON**

According to the wide variation of internal textures in zircons, two samples of the garnet-biotite gneiss were chosen for the geochronological study. Separated zircon grains are translucent and colorless to pale pink in color. The length to width ratios vary from 1.0 to about 4. Chronological analyses were performed at 82 positions in total of 48 zircon grains from 17-24GB, and 93 positions in total of 55 zircon grains from 07-10GB. The U-Pb analytical results are given in Tables 11 and 12. The analyses points of all the grains are shown in Figures of Appendix 01 and 02. Some analysis positions are indicated in the BSE and CL images of zircons in Figure 16. To obtain clear chronological values, the Th/U ratios were examined. In 07-10GB, zircons with ages of ~3.2–1.8 Ga have Th/U ratios of >0.2, whereas the most of the zircons with the ages less than 1800 Ma have Th/U ratios of <0.1 (Figure 18a). On the other hand, in the zircons of 17-24GB, Th/U ratios were categorized into three groups such as <0.1, 0.1–3.0, and >0.3. The concordance values are used to define the age groups of the detrital cores and overgrowths. The upper and lower intercepts are estimated using discordia array in the Concordia plots. According to the internal textures (Figure 17) and concordance ages (Tables 11 and 12; Figure 18), the ages of zircons in the garnet-biotite gneisses can be categorized into six ranges of 3380–3224 Ma, 2726–2668 Ma (Figure 18b), 2600–2500 Ma (Figure 18b), 2223–2177 Ma (Figure 18b), 1900–1700 Ma (Figure 18b) and 630–500 Ma (Figure 18c), as described below.

#### **V-3-5-1. ZIRCONS IN THE 07-10GB GARNET-BIOTITE GNEISS**

A subhedral and transgressive detrital core of zircon in 07-10GB, shown in Figure 16 No. 3, gave the oldest  $^{207}\text{Pb}/^{206}\text{Pb}$  age of  $3380\pm 25$  Ma (Figure 18b). The transgressive and oscillatory zoned detrital cores of zircons also show old  $^{207}\text{Pb}/^{206}\text{Pb}$  ages (Figure 18):  $3224\pm 32$  Ma for CL8;  $2701\pm 25$ – $2655\pm 27$  Ma for CL1, CL2 and CL9;  $2520\pm 31$  Ma for CL11;

2265±42–2177±32 Ma for CL7, CL10 and No. 12; and 1872±38 and 1710±47 Ma for No. 13 and CL4 respectively, with discordance <10% (Figure 18b).

The grain shown in Figure 8 CL8 has overgrowth with the  $^{207}\text{Pb}/^{206}\text{Pb}$  age of 2782±50 Ma on the subhedral and transgressive detrital core with the  $^{207}\text{Pb}/^{206}\text{Pb}$  age of 3224±32 Ma. The grains shown in Figure 16 CL1 and CL9 have overgrowths with the  $^{207}\text{Pb}/^{206}\text{Pb}$  age of 1818±37 Ma and  $^{206}\text{Pb}/^{238}\text{U}$  age of 637±15 Ma, respectively. The overgrowth of the grain shown in Figure 16 CL11 gave the  $^{207}\text{Pb}/^{206}\text{Pb}$  age of 1857±31 Ma. In the case of CL10 in Figure 18 gave the age of 689±22 Ma, and the analysis position covers both overgrowths 2 and 3, and the age data is not regarded as a unique value.

The detrital core-free zircon grains having metamorphic internal textures gave the  $^{206}\text{Pb}/^{238}\text{U}$  age of 630–500 Ma (Figure 18c). Such zircons have the length to width ratio of ~1.0. A zircon of the CL14 in Figure 16, having  $^{206}\text{Pb}/^{238}\text{U}$  age of 563±17 Ma, is a representative one.

### **V-3-5-2. ZIRCONS IN 17-24GB**

Figure 16 No. 15 shows an example of a zircon in 17-24GB, in which the detrital core gave an age of 1752±79 Ma and an overgrowth of 539±14 Ma in age. The zircons with Th/U ratio <0.1 in Concordia diagram (Figure 17d) are concentrated around ~550 Ma, and the weighted mean  $^{206}\text{Pb}/^{238}\text{U}$  age is 558±12 Ma (MSWD = 10) (Figure 18e), which corresponds to that of the latest zircon and overgrowth formation. The most of the zircons with Th/U ratios of 0.1–0.3 are discordant (Figure 18f). However, some of them show concordance around 1.8 Ga. The upper and lower intercepts are 1893±43 and 515±56 Ma, respectively (Figure 18f). The plots of zircons with Th/U ratio >0.3 in Concordia diagram (Figure 18g) are mostly concentrated into age around 1.8 Ga, and the weighted mean  $^{207}\text{Pb}/^{206}\text{Pb}$  age is

1865±59 Ma (MSWD = 28), which corresponds to the age of the detrital cores, although the most of the spots in Concordia diagram are discordant (Figure 18g).

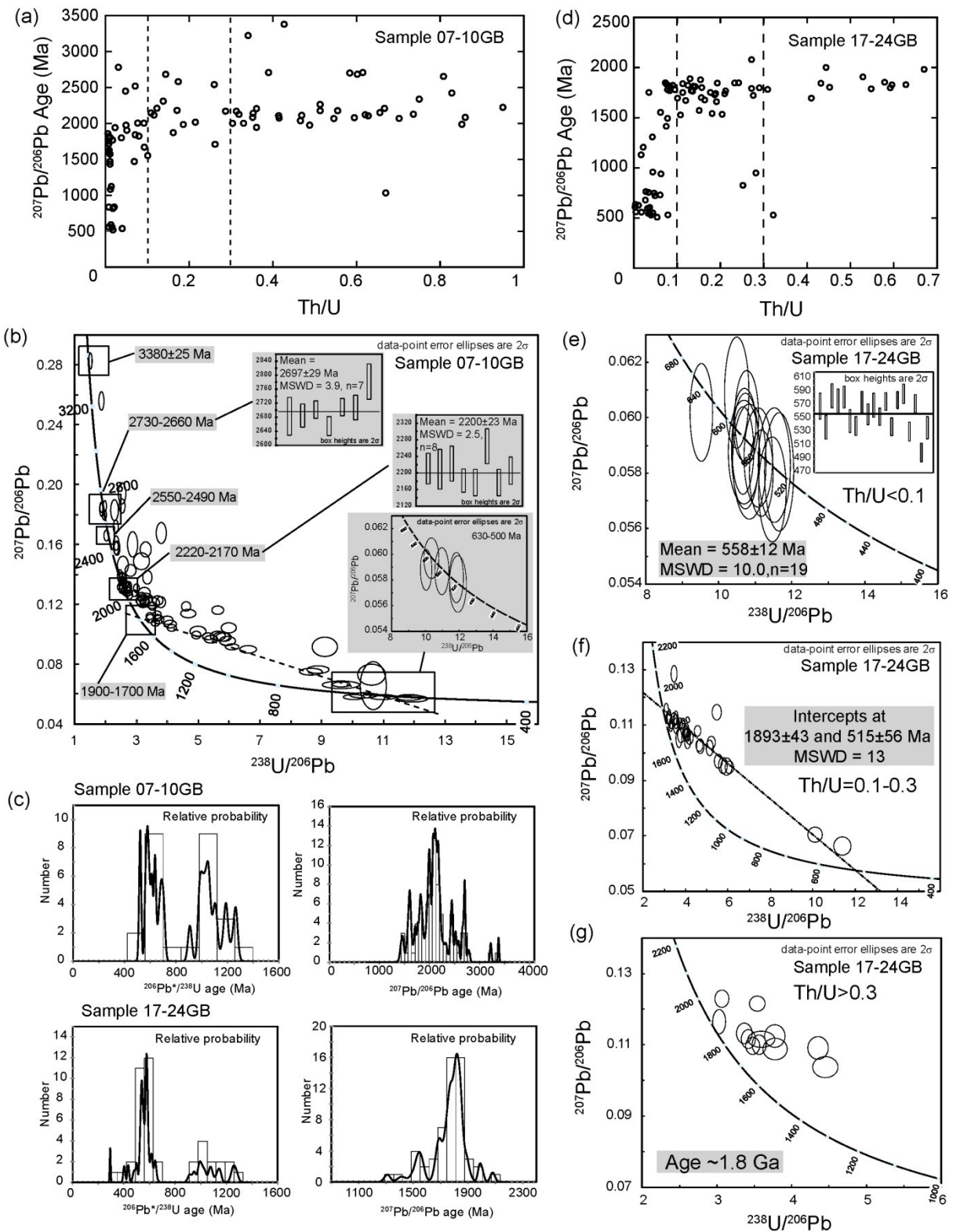


**Figure 18.** (a) Th/U variation with  $^{207}\text{Pb}/^{206}\text{Pb}$  ages (Ma) in 07-10GB. (b) Concordia diagram of zircons from 07-10GB. (c) Relative probability diagrams of zircon population (d) Th/U variation with  $^{207}\text{Pb}/^{206}\text{Pb}$  ages (Ma) in 17-24GB. (e) Concordia diagram of zircons at positions having Th/U ratio < 0.1 in 17-24GB. (f) Concordia diagram of zircons at positions having Th/U ratio of 0.1-0.3 (g) Concordia diagram of zircons at positions having Th/U ratio > 0.3.

**Table 11.** 17-24GB zircon data

Grain	Spot	$^{238}\text{U}/^{206}\text{Pb}^* \pm 2\sigma$	$^{207}\text{Pb}^*/^{206}\text{Pb}^* \pm 2\sigma$	$^{206}\text{Pb}^*/^{238}\text{U} \text{ age} \pm 2\sigma(\text{Ma})$	$^{207}\text{Pb}^*/^{235}\text{U} \text{ age} \pm 2\sigma(\text{Ma})$	$^{207}\text{Pb}^*/^{206}\text{Pb}^* \text{ age} \pm 2\sigma(\text{Ma})$	Th/U	Disc. <sup>(1)</sup> (%)	L/W
1	5	3.43±0.12	0.1114±0.0019	1651±50	1727±32	1822±31	0.090	4.7	3.8
	6	3.32±0.12	0.1120±0.0019	1699±53	1760±33	1833±31	0.076	3.6	
	7	3.45±0.11	0.1124±0.0019	1639±47	1729±30	1839±31	0.113	5.5	
2	8	10.83±0.38	0.0584±0.0017	569±19	565±20	546±65	0.034	-0.8	1.5
3	9	3.55±0.12	0.1099±0.0023	1601±48	1688±34	1798±39	0.290	5.4	1.4
	10	3.28±0.11	0.1107±0.0023	1716±50	1759±33	1811±39	0.084	2.5	
	11	3.79±0.13	0.1066±0.0022	1511±46	1610±33	1741±39	0.189	6.5	
4	15	5.96±0.20	0.0963±0.0018	1001±31	1190±27	1553±36	0.062	18.9	5.6
5	16	11.50±0.39	0.0647±0.0014	538±18	583±18	764±45	0.028	8.4	4.2
6	17	10.53±0.34	0.0644±0.0016	585±18	621±19	756±54	0.034	6.2	4.2
	18	10.69±0.35	0.0588±0.0015	577±18	573±19	559±58	0.018	-0.6	
7	19	4.17±0.14	0.1058±0.0020	1385±43	1526±31	1728±35	0.187	10.2	3.4
	20	6.56±0.24	0.0895±0.0028	914±32	1074±32	1414±61	0.075	17.5	
8	21	4.05±0.12	0.1064±0.0018	1423±38	1555±27	1739±32	0.210	9.2	5.6
	22	4.68±0.15	0.1026±0.0022	1249±35	1413±29	1671±39	0.120	13.2	
9	2-5	3.68±0.11	0.1055±0.0028	1551±43	1625±34	1722±50	0.276	4.8	2.8
10	2-6	4.08±0.11	0.1071±0.0018	1413±34	1554±26	1751±31	0.113	10.0	3.0
	2-7	3.94±0.13	0.1114±0.0022	1457±42	1613±31	1823±37	0.079	10.7	
11	2-8	10.57±0.31	0.0642±0.0021	583±16	618±21	749±71	0.047	6.0	1.8
12	2-9	3.85±0.09	0.1096±0.0020	1489±32	1619±25	1792±33	0.272	8.7	1.6
13	2-10	3.60±0.15	0.1117±0.0019	1582±58	1690±37	1828±31	0.596	6.8	2.2
	2-11	3.32±0.08	0.1108±0.0016	1695±36	1749±24	1813±26	0.138	3.1	
14	2-12	12.94±0.58	0.0847±0.0019	480±21	653±24	1308±43	0.043	36.1	4.1
	2-13	14.37±0.49	0.0634±0.0016	434±14	483±16	722±54	0.049	11.3	
15	2-14	11.29±0.36	0.1072±0.0045	547±17	850±31	1752±79	0.035	55.3	1.7
	2-15	11.46±0.31	0.0574±0.0016	539±14	533±16	508±61	0.054	-1.1	
16	2-19	4.35±0.11	0.1093±0.0026	1333±31	1519±28	1788±44	0.548	13.9	1.5
17	2-20	3.45±0.11	0.1286±0.0024	1640±48	1842±33	2079±34	0.272	12.3	3.2
	2-21	10.71±0.31	0.0588±0.0017	575±16	572±18	561±65	0.005	-0.5	
18	2-22	15.54±0.61	0.0710±0.0021	402±15	496±19	958±63	0.044	23.4	1.0
	2-23	11.08±0.32	0.0586±0.0015	557±16	556±16	552±56	0.044	-0.2	
19	2-24	4.02±0.10	0.1082±0.0022	1433±34	1574±27	1769±37	0.133	9.9	1.7
	2-25	6.06±0.16	0.0950±0.0018	985±25	1169±23	1527±36	0.108	18.6	
	2-26	3.99±0.10	0.1079±0.0019	1443±31	1578±24	1764±33	0.136	9.4	
20	2-30	10.81±0.36	0.0621±0.0021	570±18	593±21	679±72	0.027	3.9	1.5
21	2-31	3.42±0.08	0.1118±0.0021	1654±34	1732±25	1829±35	0.628	4.8	2.1
22	2-32	3.06±0.08	0.1230±0.0020	1821±40	1906±26	2001±29	0.444	4.7	1.9
	2-33	4.56±0.12	0.1081±0.0016	1279±31	1474±24	1767±28	0.212	15.2	
23	2-34	3.81±0.08	0.1082±0.0017	1504±28	1617±21	1769±30	0.083	7.6	3.3
	2-35	6.30±0.18	0.0933±0.0023	949±25	1129±26	1494±48	0.078	19.0	
24	2-36	3.47±0.08	0.1099±0.0020	1631±32	1705±23	1798±33	0.592	4.6	2.6
	2-37	9.95±0.26	0.0773±0.0014	618±15	740±17	1130±36	0.017	19.8	
25	2-42	3.78±0.13	0.1090±0.0025	1515±47	1630±35	1782±43	0.309	7.6	2.4
	2-43	3.23±0.08	0.1128±0.0025	1741±37	1789±28	1846±40	0.233	2.8	
26	2-44	3.54±0.09	0.1128±0.0020	1603±34	1710±25	1845±33	0.193	6.7	3.4
27	2-45	11.16±0.27	0.0580±0.0013	553±13	549±14	530±49	0.040	-0.8	1.7
	2-46	5.53±0.15	0.0972±0.0020	1071±28	1250±26	1572±40	0.151	16.7	
28	2-47	4.18±0.13	0.1088±0.0019	1382±37	1547±27	1780±31	0.078	11.9	2.0
	2-48	21.51±0.54	0.0607±0.0014	293±7	334±10	628±50	0.011	13.9	
29	2-49	10.70±0.26	0.0598±0.0011	576±13	580±13	595±40	0.032	0.7	1.0

Pb\*: Radiogenic Pb

<sup>(1)</sup> Discordancy defined as  $[(^{207}\text{Pb}^*/^{235}\text{U} \text{ age}) / (^{206}\text{Pb}^*/^{238}\text{U} \text{ age}) - 1] \times 100$  (%)

**Table 11. (Continued)**

Grain	Spot	$^{238}\text{U}/^{206}\text{Pb}^* \pm 2\sigma$	$^{207}\text{Pb}^*/^{206}\text{Pb}^* \pm 2\sigma$	$^{206}\text{Pb}^*/^{238}\text{U} \text{ age} \pm 2\sigma(\text{Ma})$	$^{207}\text{Pb}^*/^{235}\text{U} \text{ age} \pm 2\sigma(\text{Ma})$	$^{207}\text{Pb}^*/^{206}\text{Pb}^* \text{ age} \pm 2\sigma(\text{Ma})$	Th/U	Disc. <sup>(1)</sup> (%)	L/W
30	2-53	3.19±0.09	0.1130±0.0018	1758±45	1799±28	1848±29	0.242	2.4	2.9
	2-54	11.48±0.30	0.0804±0.0032	538±13	686±24	1206±81	0.022	27.4	
	2-55	9.51±0.26	0.0602±0.0014	644±17	637±17	611±53	0.003	-1.1	
	2-56	3.73±0.09	0.1107±0.0018	1532±33	1653±24	1811±29	0.142	7.9	
31	2-57	3.03±0.07	0.1167±0.0028	1840±37	1871±29	1906±44	0.529	1.7	1.1
	2-58	10.65±0.25	0.0588±0.0013	578±13	575±14	561±49	0.005	-0.6	
32	2-59	5.22±0.16	0.1039±0.0019	1130±31	1341±26	1695±34	0.101	18.6	1.9
33	2-60	4.00±0.12	0.1072±0.0021	1438±40	1570±30	1752±37	0.177	9.2	2.0
34	2-61	3.54±0.08	0.1217±0.0017	1605±34	1775±24	1982±25	0.670	10.6	2.2
35	2-62	10.48±0.27	0.0609±0.0016	588±15	598±17	636±59	0.004	1.7	1.6
36	2-63	4.65±0.13	0.1029±0.0017	1256±32	1421±26	1677±32	0.164	13.1	2.0
	2-67	3.30±0.08	0.1100±0.0018	1708±38	1750±25	1800±29	0.157	2.4	
37	2-68	3.36±0.08	0.1133±0.0024	1678±37	1757±28	1854±39	0.579	4.8	3.7
	2-69	3.56±0.08	0.1102±0.0022	1595±31	1687±25	1803±37	0.452	5.8	
38	2-70	5.47±0.17	0.1149±0.0023	1083±31	1381±28	1878±37	0.154	27.5	2.6
	2-71	5.76±0.17	0.0957±0.0024	1032±28	1210±27	1542±48	0.181	17.2	
	2-72	5.13±0.13	0.1019±0.0023	1149±27	1340±26	1660±43	0.191	16.6	
39	2-73	4.08±0.11	0.1042±0.0021	1414±36	1532±27	1700±37	0.156	8.4	1.3
40	2-74	3.07±0.08	0.1156±0.0020	1817±43	1851±28	1889±31	0.130	1.9	2.9
	2-75	3.54±0.09	0.1114±0.0021	1606±36	1702±26	1822±35	0.125	6.0	
41	2-79	11.78±0.31	0.0580±0.0027	525±13	526±22	530±106	0.322	0.2	1.6
	2-80	11.64±0.33	0.0581±0.0017	531±14	531±17	532±67	0.079	0.0	
42	2-81	10.11±0.28	0.0707±0.0022	608±16	686±21	949±65	0.282	12.7	1.3
	2-82	5.92±0.21	0.0953±0.0026	1006±34	1187±32	1534±52	0.204	18.0	
43	2-83	10.76±0.27	0.0600±0.0014	573±14	579±15	605±51	0.037	1.1	1.7
	2-84	11.39±0.34	0.0666±0.0027	543±16	601±23	826±88	0.252	10.7	
44	2-85	12.39±0.36	0.0636±0.0020	500±14	544±18	730±67	0.061	8.7	1.3
45	2-86	11.51±0.37	0.0583±0.0017	537±17	538±18	542±65	0.037	0.1	1.4
	2-87	9.60±0.53	0.0704±0.0031	639±34	710±36	940±93	0.063	11.1	
46	2-91	3.89±0.19	0.1087±0.0027	1475±64	1604±45	1779±46	0.095	8.8	2.0
47	2-92	3.46±0.12	0.1130±0.0021	1636±49	1731±33	1848±35	0.073	5.8	1.6
48	2-93	3.78±0.11	0.1127±0.0026	1515±41	1657±32	1843±42	0.432	9.4	2.5
	2-94	4.45±0.14	0.1039±0.0024	1307±37	1462±31	1695±43	0.410	11.8	

Pb\*: Radiogenic Pb

<sup>(1)</sup> Discordancy defined as  $[(^{207}\text{Pb}^*/^{235}\text{U} \text{ age})/(^{206}\text{Pb}^*/^{238}\text{U} \text{ age})-1] \times 100$  (%)

**Table 12.** 07-10GB zircon data

Grain Spot	$^{238}\text{U}/^{206}\text{Pb}^* \pm 2\sigma$	$^{207}\text{Pb}^*/^{206}\text{Pb}^* \pm 2\sigma$	$^{206}\text{Pb}^*/^{238}\text{U}$ age $\pm 2\sigma$ (Ma)	$^{207}\text{Pb}^*/^{235}\text{U}$ age $\pm 2\sigma$ (Ma)	$^{207}\text{Pb}^*/^{206}\text{Pb}^*$ age $\pm 2\sigma$ (Ma)	Th/U	Disc. <sup>(1)</sup> (%)	L/W	
1	205	3.71±0.14	0.1104±0.0021	1537±51	1654±35	1806±35	0.011	7.6	2.4
	206	3.25±0.15	0.1282±0.0031	1729±69	1891±45	2074±43	0.415	9.4	
	207	3.25±0.11	0.1233±0.0027	1728±53	1857±36	2005±40	0.077	7.5	
2	208	2.68±0.08	0.1322±0.0030	2043±55	2086±35	2128±41	0.736	2.1	1.1
	209	3.79±0.12	0.122±0.0030	1510±42	1719±34	1985±45	0.186	13.9	
3	210	11.91±0.41	0.0577±0.0018	520±17	519±19	518±72	0.018	-0.1	1.7
	211	10.34±0.36	0.0597±0.0013	595±20	594±19	591±46	0.013	-0.2	
4	212	5.74±0.21	0.099±0.0024	1036±35	1237±31	1606±45	0.007	19.4	1.4
	213	5.81±0.20	0.0985±0.0023	1025±33	1224±30	1596±44	0.007	19.5	
	214	8.65±0.30	0.0755±0.0019	706±23	803±24	1083±51	0.012	13.8	
5	218	2.28±0.11	0.1833±0.0059	2341±91	2529±54	2683±54	0.144	8	1.6
	219	3.45±0.11	0.1111±0.0022	1642±45	1721±31	1818±37	0.008	4.8	
6	220	2.33±0.07	0.1723±0.0036	2298±54	2451±33	2581±36	0.174	6.7	1.5
	221	4.08±0.16	0.1073±0.0021	1414±51	1556±37	1754±37	0.008	10.0	
7	222	5.62±0.16	0.1166±0.0024	1055±28	1371±27	1905±38	0.051	29.9	1.5
	223	2.52±0.08	0.1387±0.0029	2156±59	2184±35	2211±37	0.123	1.3	
	224	4.93±0.13	0.1002±0.0020	1190±29	1356±26	1627±38	0.009	13.9	
8	225	10.96±0.34	0.0587±0.0015	563±17	561±17	556±55	0.016	-0.2	1.2
9	229	5.99±0.20	0.1048±0.0026	996±31	1246±31	1710±47	0.262	25.2	1.6
	230	5.62±0.20	0.0994±0.0024	1055±35	1254±31	1612±45	0.009	18.8	
	231	5.41±0.18	0.0974±0.0021	1094±34	1267±29	1574±42	0.011	15.8	
10	232	3.34±0.12	0.1385±0.0037	1689±55	1935±41	2209±48	0.667	14.5	1.4
	233	2.77±0.09	0.127±0.0025	1990±59	2023±35	2057±36	1.431	1.6	
	234	8.87±0.29	0.077±0.0022	689±22	799±24	1122±57	0.014	16.1	
	235	5.93±0.21	0.0962±0.0026	1005±34	1193±32	1552±52	0.101	18.7	
11	105	2.45±0.07	0.1396±0.0034	2209±56	2216±35	2223±42	0.950	0.3	1.2
12	106	1.87±0.06	0.1836±0.0037	2760±72	2717±37	2685±33	0.602	-1.6	1.6
	107	1.85±0.05	0.1854±0.0028	2784±61	2736±30	2702±25	0.584	-1.7	
	108	9.63±0.24	0.067±0.0013	637±15	683±16	837±42	0.021	7.2	
13	109	1.95±0.05	0.1802±0.0029	2671±59	2662±30	2655±27	0.808	-0.3	1.3
14	110	3.19±0.07	0.1213±0.0022	1760±36	1861±25	1976±32	0.488	5.7	2.5
	111	3.67±0.10	0.1115±0.0017	1552±39	1671±27	1824±28	0.080	7.7	
15	112	10.6±0.37	0.0737±0.0057	581±20	683±43	1033±164	0.670	17.4	1.5
16	113	2.52±0.08	0.131±0.0022	2154±57	2133±32	2112±30	0.469	-1.0	1.3
17	114	2.67±0.07	0.1279±0.0020	2052±46	2061±28	2070±29	0.702	0.4	1.5
	115	2.64±0.06	0.1287±0.0022	2069±39	2074±25	2080±30	0.595	0.3	
18	119	2.02±0.06	0.1662±0.0030	2596±64	2554±33	2520±31	0.071	-1.6	1.4
	120	3.67±0.11	0.1136±0.0019	1554±42	1688±28	1857±31	0.006	8.6	
19	121	11.82±0.34	0.0582±0.0016	523±15	526±17	537±60	0.040	0.5	2.0
20	122	2.54±0.07	0.1364±0.0022	2140±48	2161±28	2182±28	0.171	1.0	1.3
21	123	2.59±0.07	0.1291±0.0021	2104±49	2094±28	2085±28	0.86	-0.5	2.1
	124	2.49±0.06	0.1306±0.0024	2179±45	2142±27	2107±32	0.628	-1.7	
	125	2.93±0.07	0.1278±0.0019	1892±38	1978±24	2068±27	0.546	4.5	
22	126	2.86±0.13	0.1604±0.0069	1931±79	2200±59	2460±75	2.865	13.9	2.1
	127	2.34±0.08	0.1601±0.0051	2290±68	2379±44	2456±55	2.548	3.9	
23	131	3.67±0.15	0.1231±0.0027	1554±58	1754±40	2002±40	0.330	12.9	2.5
	132	4.99±0.21	0.1025±0.0028	1177±45	1363±38	1669±51	0.093	15.8	
24	133	2.52±0.06	0.136±0.0024	2157±44	2168±27	2177±32	0.555	0.5	1.4
25	134	2.67±0.06	0.1339±0.0020	2049±39	2100±24	2150±27	0.656	2.5	1.6
26	135	2.74±0.06	0.1308±0.0020	2004±38	2056±24	2108±27	0.414	2.6	1.4
27	136	9.61±0.49	0.0669±0.0021	638±31	683±30	836±66	0.008	7.1	1.8
	137	10.03±0.28	0.0588±0.0013	613±16	601±17	558±49	0.008	-1.9	

Pb\*: Radiogenic Pb

<sup>(1)</sup> Discordancy defined as  $[(^{207}\text{Pb}^*/^{235}\text{U} \text{ age}) / (^{206}\text{Pb}^*/^{238}\text{U} \text{ age}) - 1] \times 100$  (%)



**Table 12. (Continued)**

Grain	Spot	$^{238}\text{U}/^{206}\text{Pb}^* \pm 2\sigma$	$^{207}\text{Pb}^*/^{206}\text{Pb}^* \pm 2\sigma$	$^{206}\text{Pb}^*/^{238}\text{U} \text{ age} \pm 2\sigma(\text{Ma})$	$^{207}\text{Pb}^*/^{235}\text{U} \text{ age} \pm 2\sigma(\text{Ma})$	$^{207}\text{Pb}^*/^{206}\text{Pb}^* \text{ age} \pm 2\sigma(\text{Ma})$	Th/U	Disc. <sup>(1)</sup> (%)	L/W
28	138	3.29±0.15	0.157±0.0042	1711±70	2056±48	2423±47	0.828	20.2	2.1
	139	5.32±0.16	0.099±0.0019	1111±31	1291±27	1605±36	0.009	16.2	
29	140	10.67±0.34	0.0663±0.0132	577±18	628±99	816±483	0.018	8.8	1.3
30	144	2.74±0.08	0.1317±0.0032	2007±52	2064±34	2121±43	0.621	2.8	1.4
	145	2.46±0.06	0.1321±0.0022	2201±43	2162±26	2126±30	0.319	-1.8	
31	146	3.99±0.15	0.11±0.0024	1441±49	1593±36	1800±41	0.038	10.5	1.9
32	147	3.52±0.10	0.1193±0.0024	1613±40	1763±29	1945±36	0.361	9.3	1.6
33	148	2.65±0.07	0.1335±0.0021	2066±46	2106±28	2145±28	0.109	1.9	1.4
34	149	4.68±0.20	0.1145±0.0024	1248±48	1498±38	1872±38	0.162	20	1.7
35	150	2.73±0.09	0.1291±0.0022	2013±56	2049±32	2085±30	0.352	1.8	1.6
36	151	1.97±0.05	0.1862±0.0028	2645±55	2681±28	2709±25	0.615	1.4	1.6
37	152	3.14±0.13	0.123±0.0026	1783±63	1886±39	2001±38	0.304	5.7	1.8
	153	2.57±0.06	0.1355±0.0019	2116±40	2144±24	2171±25	0.287	1.3	
	157	2.5±0.06	0.1354±0.0022	2169±44	2169±26	2169±28	0.313	0.0	
38	158	3.15±0.21	0.1493±0.0048	1778±103	2051±66	2338±56	0.750	15.4	1.5
	159	4.14±0.12	0.105±0.0018	1395±37	1527±27	1715±32	0.008	9.4	
39	160	3.28±0.19	0.1242±0.0030	1713±88	1855±55	2017±43	0.215	8.2	1.1
40	161	9.09±0.34	0.0921±0.0054	673±24	888±42	1470±116	0.069	31.9	2.5
	162	6.09±0.18	0.0921±0.0018	980±26	1144±24	1470±38	0.011	16.7	
41	163	2.99±0.08	0.1314±0.0022	1858±45	1983±29	2117±30	0.116	6.8	2.1
	164	3.52±0.19	0.1213±0.0029	1613±76	1777±50	1976±43	0.049	10.2	
42	165	2.53±0.08	0.1861±0.0039	2149±57	2449±35	2708±35	0.390	14.0	2.0
43	166	1.5±0.04	0.283±0.0045	3293±73	3347±32	3380±25	0.427	1.6	1.5
	170	4.61±0.12	0.119±0.0026	1266±29	1541±27	1942±40	0.023	21.7	
44	171	2.8±0.15	0.1431±0.0034	1969±92	2117±54	2265±42	0.513	7.5	2.4
	172	2.51±0.07	0.136±0.0024	2158±50	2168±29	2177±32	0.513	0.4	
45	173	3.43±0.10	0.1126±0.0018	1649±41	1736±27	1842±29	0.071	5.3	2.1
46	174	2.51±0.07	0.1332±0.0019	2165±54	2153±29	2141±25	0.353	-0.6	1.3
47	175	3.17±0.11	0.1256±0.0025	1766±54	1894±35	2038±36	0.466	7.3	1.5
48	176	2.55±0.14	0.1469±0.0048	2132±101	2224±59	2310±58	0.138	4.3	2.4
49	177	3.34±0.12	0.1233±0.0023	1689±52	1835±35	2004±34	0.092	8.6	3.4
50	178	3.2±0.17	0.1222±0.0033	1752±80	1862±52	1988±49	0.852	6.3	3
51	179	2.34±0.05	0.1595±0.0024	2293±43	2377±25	2450±26	0.048	3.7	2.4
52	183	3.79±0.14	0.1683±0.0057	1509±49	1993±45	2541±58	0.260	32.1	1.9
	184	6.61±0.23	0.0904±0.0021	908±30	1076±28	1434±45	0.011	18.5	
53	185	2.37±0.08	0.1581±0.0038	2268±62	2358±37	2436±41	1.303	3.9	2.0
54	186	1.86±0.06	0.2563±0.0051	2774±75	3042±38	3224±32	0.341	9.7	2.6
	187	2.52±0.10	0.1946±0.0058	2156±72	2494±47	2782±50	0.031	15.7	
55	188	2.56±0.10	0.1383±0.0026	2127±75	2168±41	2206±33	0.361	1.9	2.2
	189	3.61±0.11	0.1082±0.0017	1578±44	1662±29	1769±30	0.017	5.3	

Pb\* : Radiogenic Pb

<sup>(1)</sup> Discordancy defined as  $[(^{207}\text{Pb}^*/^{235}\text{U} \text{ age})/(^{206}\text{Pb}^*/^{238}\text{U} \text{ age})-1] \times 100$  (%)

## **V-4. CHEMICAL COMPOSITION, INTERNAL TEXTURES AND CHRONOLOGY OF MONAZITE**

### **V-4-1. INTERNAL TEXTURES AND CHEMICAL COMPOSITIONS OF MONAZITE**

Internal textures of more than 100 grains of monazite in the six samples were categorized into four types, based on the observation of their backscattered electron (BSE) images: core-rim zoned (Figure 19a, b, and c), inherited core-bearing (Figure 19d, e, and f), complexly zoned (Figure 19g), and oscillatory zoned (Figure 19h) types. Especially, the oscillatory zoned monazites were rare in the studied samples. Core rim zoned monazites show the distinguishable core area and thin rim area. Inherited core-bearing monazites can be identified as the core fraction is remarkably stand out respect to other area. Complexly zoned monazites have several internal cores and several darker and brighter areas. The grains showing repeated darker and brighter banded features are recognized as oscillatory zoned monazites. The element distributions of U, Th, Pb and Y in the monazite grains were analyzed to find chemical variations in the internal textures of monazites shown in the BSE images (Figure 19).

The CHIME dating of internal domains and zones in three core-rim zoned type monazite grains, three inherited core-bearing type monazite grains, and one grain for each complex zoned and oscillatory zoned monazites, were performed (Tables of analyses of monazite in Figure 19a, b, c, d, e, f, g, and h are attached in Appendix 03). The PbO against  $\text{ThO}_2^*$  diagrams of each domain and zone within the analyzed monazites are shown along with isochron ages, where  $\text{ThO}_2^*$  is the recalculated  $\text{ThO}_2$  which corresponds to measured  $\text{ThO}_2$  plus  $\text{ThO}_2$  equivalent of measured  $\text{UO}_2$  (Suzuki et al., 1991; Suzuki and Adachi, 1991). Summary of U-Th-total Pb isochron age data for monazite domains are shown in Table 13.

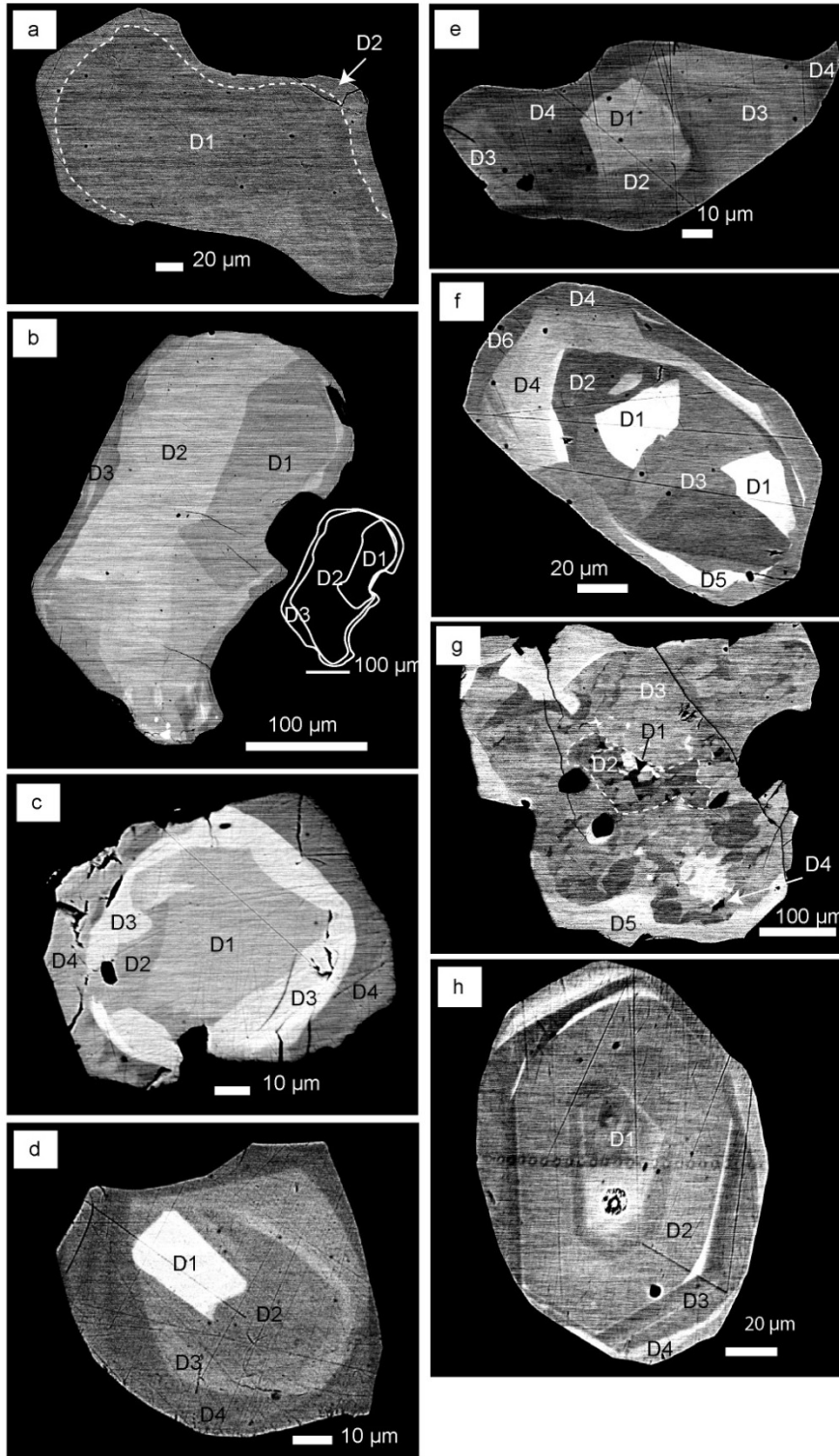


**Figure 19.** BSE images of monazites. (a), (b), and (c) core-rim zoned monazite. (d),(e), and (f) inherited core-bearing monazite. (g) complexly zoned monazite. (h) oscillatory zoned monazite.

**Table 13.** Summary of U-Th-total Pb isochron age data for monazite domains

Internal textures	Grains	Domains	Weighted average of apparent ages (Ma)	Suzuki and Adachi method (Ma)	Montel Method (Ma)	Age group
(1) Core-rim zoned	Figure 19a	D1	503±5	521±32	503±25	Group III
		D2	456±6	451±27	458±19	Group IV
	Figure 19b	D1	533±3	527±24	533±22	Group III
		D2	534±2	523±25	533±14	Group III
		D3	500±5	493±27	498±22	Group III
	Figure 19c	D1	522±8		517±43	Group III
		D2	525±22	485±85	525±34	Group III
		D3	467±10		468±50	Group IV
		D4	481±60		450±150	Group IV
	(1) Inherited core bearing zoned	Figure 18d	D1	512±5		512±09
D2			481±30	550±46	488±40	Group III
D3			467±6		468±18	Group IV
D4			467±15		469±34	Group IV
Figure 19e		D1	472±6		472±17	Group IV
		D2	452±18	517±36	449±44	Group IV
		D3	462±6		462±19	Group IV
		D4	433±6		433±14	Group IV
Figure 19f		D1	1787±22		1788±30	Group I
		D2	1783±97	1802±91	1766±140	Group I
	D3	526±14		529±41	Group III	
	D4	471±21	529±74	481±42	Group III	
	D5	496±13		495±69	Group III	
	D6	436±15		434±59	Group IV	
(1) Complexly zoned	Figure 19g	D1	1679±35	1648±186	1686±186	Group I
		D2	662±68	803±99	679±99	Group II
		D3	508±8		507±49	Group III
		D4	499±12	527±69	503±55	Group III
		D5	458±16		458±64	Group IV
(1) Oscillatory zoned	Figure 19h	D1-D4	467±7	452±27	470±45	Group IV

#### V-4-2. CORE-RIM ZONED MONAZITE

An anhedral core-rim zoned type monazite from garnet-biotite gneiss (17-24GB), shown in Figure 19a, is ~200  $\mu\text{m}$  in size, and represents the simple zoning, where D1 core is rimmed by D2, ~10  $\mu\text{m}$  in thickness. The D1 core is more abundant in U and Y (Figure 20a-1 and a-4, respectively) but slightly poorer in Th than the D2 rim (Figure 20a-2). As shown in a PbO against  $\text{ThO}_2^*$  diagram (Figure 21) and Table 13, the D1 and D2 have isochron ages (Suzuki and Adachi method) of  $521 \pm 32$  (intercept:  $c = -0.01128$ ) and  $451 \pm 27$  Ma ( $c = 0.00307$ ), respectively, and weighted average of apparent ages (abbreviated as WAVG ages) of  $503 \pm 5$  and  $457 \pm 6$  Ma, respectively (Table 13). The D1 and D2 have isochron ages (Montel method) of  $503 \pm 25$  and  $458 \pm 19$  Ma, respectively (Figure 23a; Table 13).

An anhedral monazite from 17-24GB shown in Figure 16b is more than 300  $\mu\text{m}$  in size, and consists of three zones, D1, D2, and D3. The D2 is brighter in the BSE image (Figure 19b) and richer in Th than the D1 and D3 (Figure 20b-2). The U and Y contents of the D3 are slightly less than those of the D1 and D2 (Figure 20b-1 and b-4). The PbO against  $\text{ThO}_2^*$  diagram (Figure 22) shows isochron ages (Suzuki and Adachi method) of  $527 \pm 24$  ( $c = 0.00122$ ),  $523 \pm 25$  ( $c = 0.00519$ ) and  $493 \pm 27$  Ma ( $c = 0.00081$ ), and WAVG ages of  $533 \pm 3$ ,  $534 \pm 2$ , and  $500 \pm 5$  Ma for the D1, D2, and D3, respectively (Table 13). According to Montel method the D1, D2, and D3 show isochron ages of  $533 \pm 14$ ,  $533 \pm 22$ , and  $498 \pm 22$  Ma (Figure 23b).

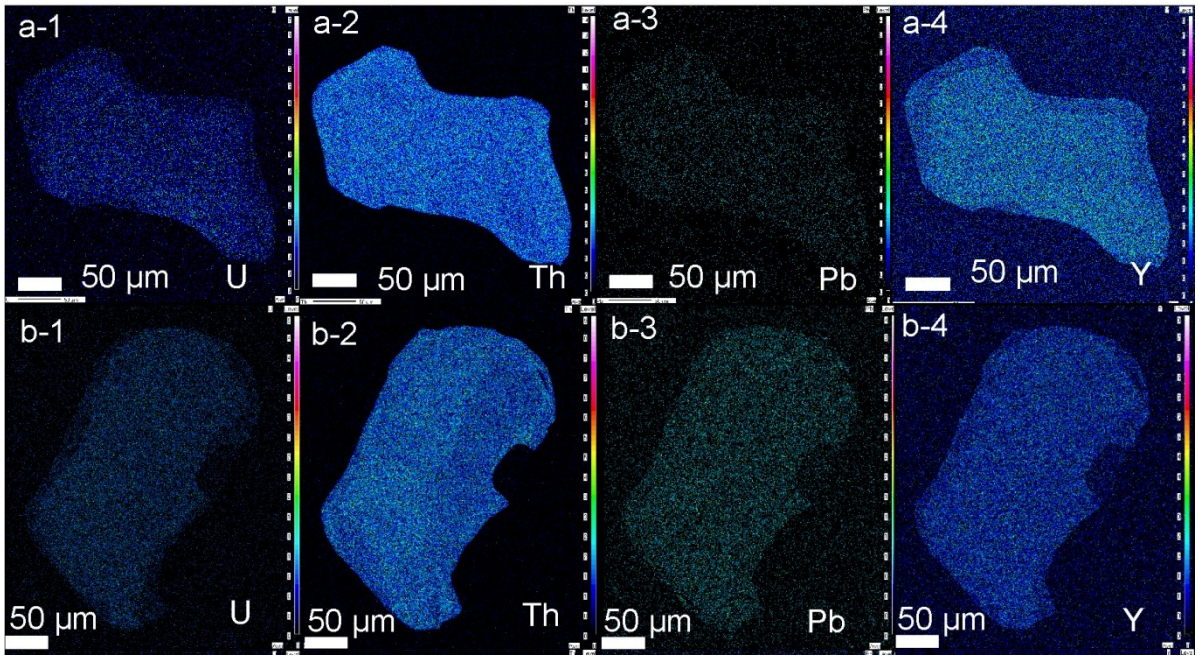


**Figure 20.** X-ray map images showing the distribution of U, Th, Pb, and Y in the core-rim zoned monazites (a-1, a-2, a-3, a-4; b-1, b-2, b-3, b-4).

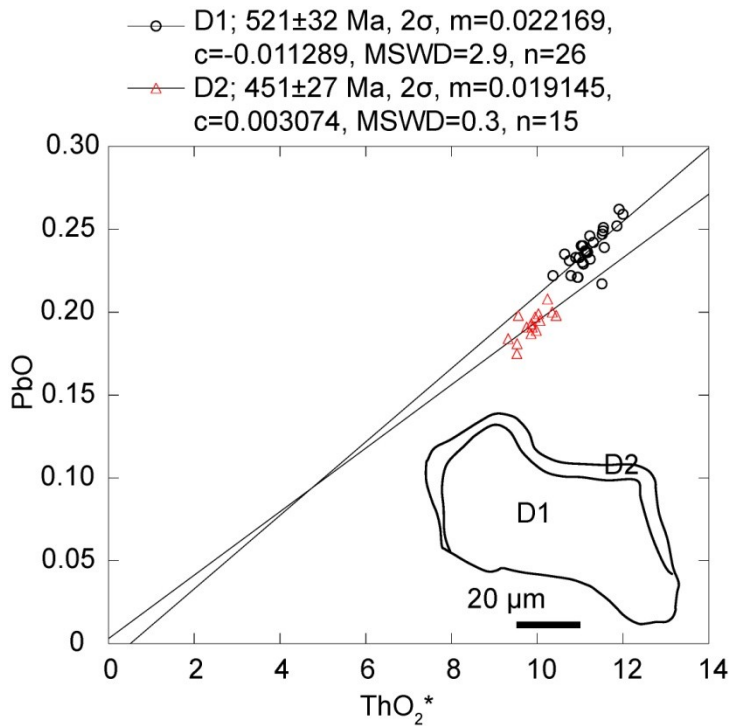


**Figure 21.**  $\text{ThO}_2^*$ -PbO diagrams showing U-Th-total Pb isochrons and determined isochron ages (Suzuki and Adachi method)

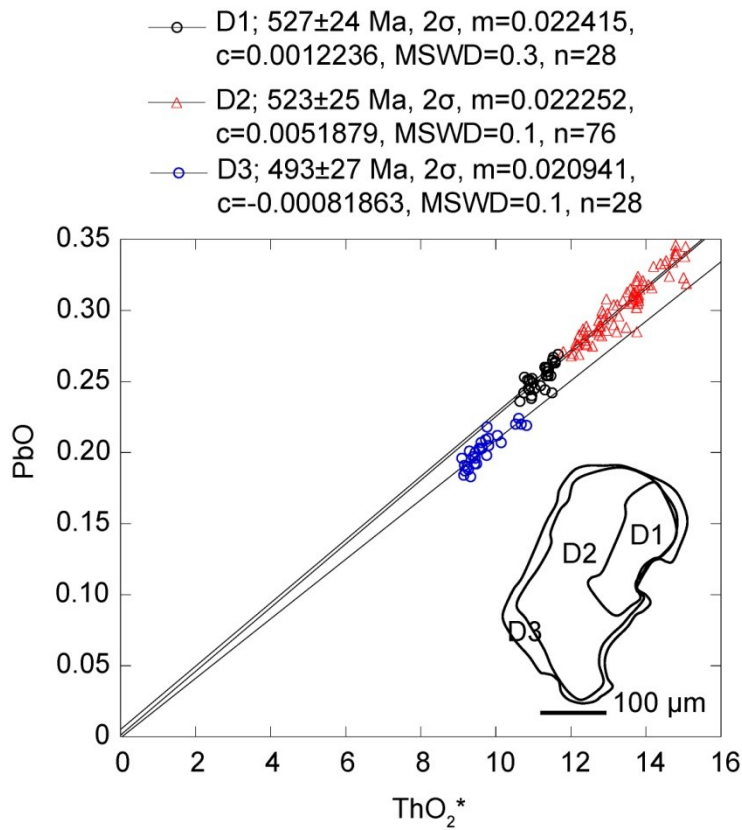


**Figure 22.**  $\text{ThO}_2^*$ -PbO diagrams showing U-Th-total Pb isochrons and determined isochron ages (Suzuki and Adachi method)

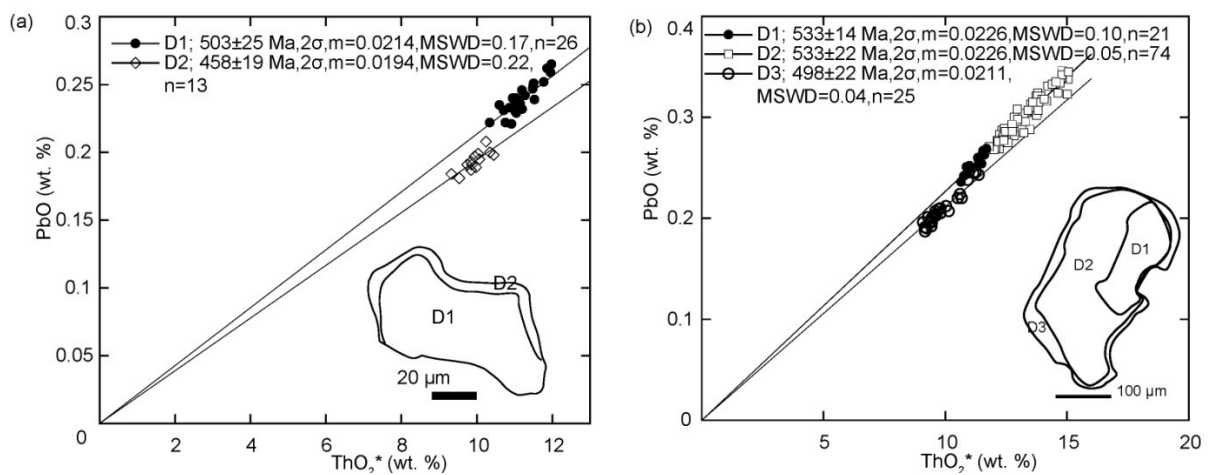


**Figure 23.**  $\text{ThO}_2^*$ -PbO diagrams showing U-Th-total Pb isochrons and determined isochron ages (Montel method)

In a monazite in the garnet-biotite-cordierite gneiss (23-32Co), the core consisting of D1 and D2 and overgrowths of D3 and D4 are recognized in the BSE image of the grain (Figure 19c). The D1 and D2 are richer in U and Y than the D3 and D4 (Figure 24c-1 and c-4, respectively); D3 is richer in Th than the D1, D2, and D4 (Figure 24c-2), and more dominant in Pb than D4 (Figure 24c-3); and D4 tends to be rich in Y as well as D1, although its content is variable (Figure 24c-4). The D1 to D4 also shows  $485\pm 85$  Ma ( $c = 0.00029$ ) in isochron age (Suzuki and Adachi method), respectively (Figure 25). The D1 and D2 are  $522\pm 8$  Ma and  $525\pm 22$  Ma in WAVG age, respectively (Table 13). The WAVG ages of the D3 and D4 are  $467\pm 10$  and  $481\pm 60$  Ma, respectively (Table 13). The D1 and D2 are  $517\pm 43$  and  $525\pm 34$  Ma in isochron age (Montel method), respectively (Figure 26c). On the other hand, the D3 and D4 yield isochron ages (Montel method) of  $468\pm 50$  and  $450\pm 150$  Ma, respectively, although the latter has a remarkably large error.



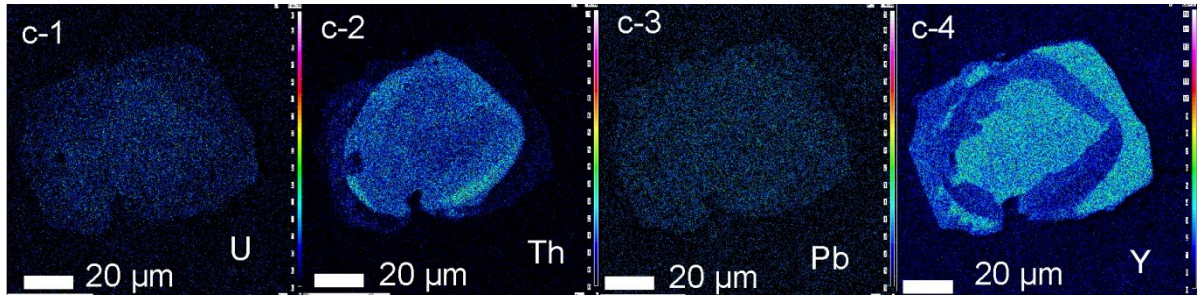


**Figure 24.** X-ray map images showing the distribution of U, Th, Pb, and Y in the core-rim zoned monazites (c-1, c-2, c-3, c-4).

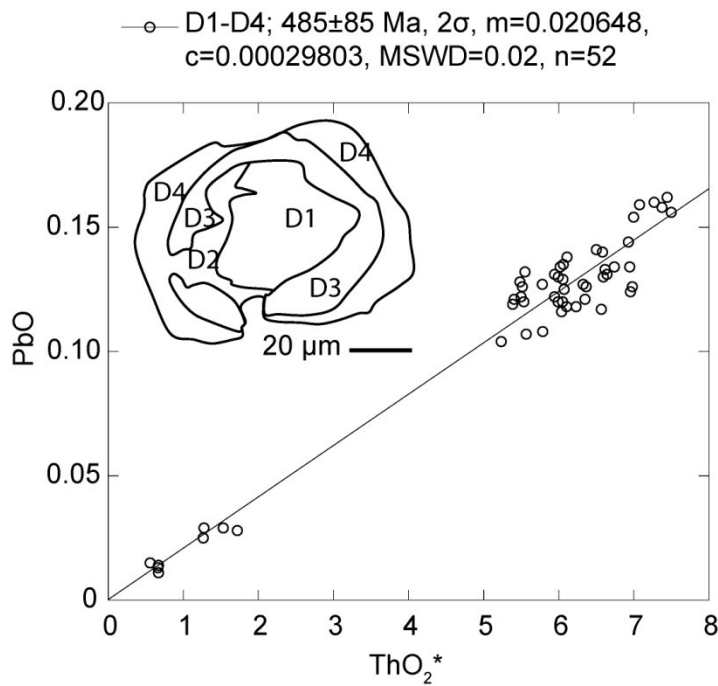


**Figure 25.** ThO<sub>2</sub>\*-PbO diagrams showing U-Th-total Pb isochrons and determined isochron ages (Suzuki and Adachi method)

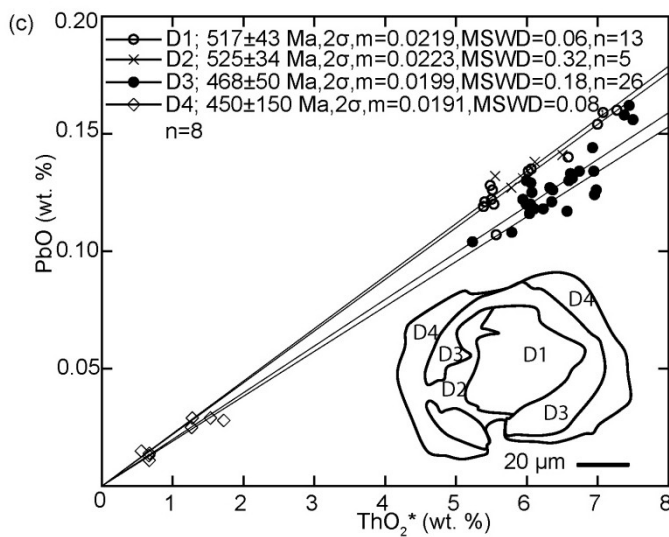


**Figure 26.** ThO<sub>2</sub>\*-PbO diagrams showing U-Th-total Pb isochrons and determined isochron ages (Montel method)

### V-4-3. INHERITED CORE-BEARING MONAZITE

Three grains of the inherited core-bearing monazite from garnet-biotite gneiss are subhedral in form and fine in size (50–100  $\mu\text{m}$ ), where two of them are from 17-24GB, and one from 11-17GB.

The monazite from 17-24GB shown in Figure 19d has D1 peripheral core and D2, D3 and D4 zones. In the monazite in Figure 19e, a peripheral core consisting of the D1 and D2 and D3 domains is overgrown by the D4 zone. The monazite in Figure 19f consists of a core made up of D1, D2 and D3 domains and three overgrowth zones of D4, D5, and D6. In the monazite shown in Figure 19d, the core D1 is characterized by higher U, Th and Pb contents than the zones D2, D3, and D4 (Figure 27d-1, d-2 and d-3, respectively); the zone D2 is higher in U and Y and lower in Th than the zone D3 (Figure 27d-1 and d-4, respectively); the D3 is the richer in Th than D4 (Figure 27d-2) but poorest in U and Y among the zones (Figure 27d-1 and d-4, respectively); and the D4 is characterized by rather high U and Y (Figure 27d-1 and d-4, respectively) but low Th and Pb contents among the zones (Figure 27d-2 and d-3, respectively). The D1 to D4 domains show the isochron age (Suzuki and Adachi method) of  $550\pm 46\text{Ma}$  ( $c = -0.02721$ ) and WAVG ages of  $512\pm 5$ ,  $481\pm 30$ ,  $467\pm 6$ , and  $467\pm 15$  Ma, respectively (Figure 28; Table 13). The D1 domain shows the isochron age (Montel method) of  $512\pm 9$  Ma, and the D2, D3, and D4 zones yield younger isochron ages (Montel Method) of  $488\pm 40$ ,  $468\pm 18$ , and  $469\pm 34$  Ma, respectively (Figure 31d; Table 13).

In the monazite from 17-24GB shown in Figure 19e, D1 and D2 domains consisting of the peripheral core is characteristically richer in U and Th (Figure 27e-1 and e-2, respectively), D3 is the poorest in U, Th, Pb and Y (Figure 27e-1, e-2, e-3, and e-4, respectively), and D4 is characteristically rich in Y (Figure 27e-4). The D1, D2, D3, and D4 yield isochron ages (Suzuki and Adachi method) of  $517\pm 36$  Ma ( $c = -0.02484$ ) (WAVG ages of  $472\pm 6$ ,  $452\pm 18$ ,  $462\pm 6$ , and  $433\pm 6$  Ma) (Figure 29; Table 13). According to the Montel

method the D1, D2, D3, and D4 yield isochron ages of  $462\pm 19$ ,  $472\pm 14$ ,  $449\pm 44$ , and  $433\pm 14$  Ma, respectively, indicating all domains have more or less similar age values (Figure 31e; Table 13).

In the monazite of Figure 19 from 11-17GB, the peripheral core is characterized by the D1 domain rich in Th and Pb (Figure 27f-2 and f-3, respectively), D2 in U, Pb, and Y (Figure 27f-1, f-3 and f-4, respectively), and D3 in U and Th (Figure 27f-1 and f-2, respectively). The D4 and D5 zones are characterized by rather high Th content (Figure 27f-2). The D6 is poor in U, Th, Pb, and Y (Figure 27f-1, f-2, f-3 and f-4, respectively). The PbO against  $\text{ThO}_2^*$  diagram shown in Figure 30 and Table 13 show the isochron age (Suzuki and Adachi method) of  $1802\pm 30$  Ma ( $c = -0.00712$ ) for the D1 and D2;  $529\pm 41$  Ma ( $c = -0.01413$ ) for D3 to D6. The PbO against  $\text{ThO}_2^*$  diagram shown in Figure 31f and Table 13 show the isochron ages (Montel method) of  $1788\pm 30$  and  $1766\pm 140$  Ma, and WAVG ages of  $1787\pm 22$  and  $1783\pm 97$  Ma for the D1 and D2, respectively; isochron age of  $529\pm 41$  Ma and WAVG age of  $526\pm 14$  Ma for the D3; and  $481\pm 42$ ,  $495\pm 69$  and  $434\pm 59$  Ma in isochron ages (Montel method) and  $471\pm 21$ ,  $496\pm 13$  and  $436\pm 15$  Ma in WAVG age for the D4, D5 and D6, respectively.

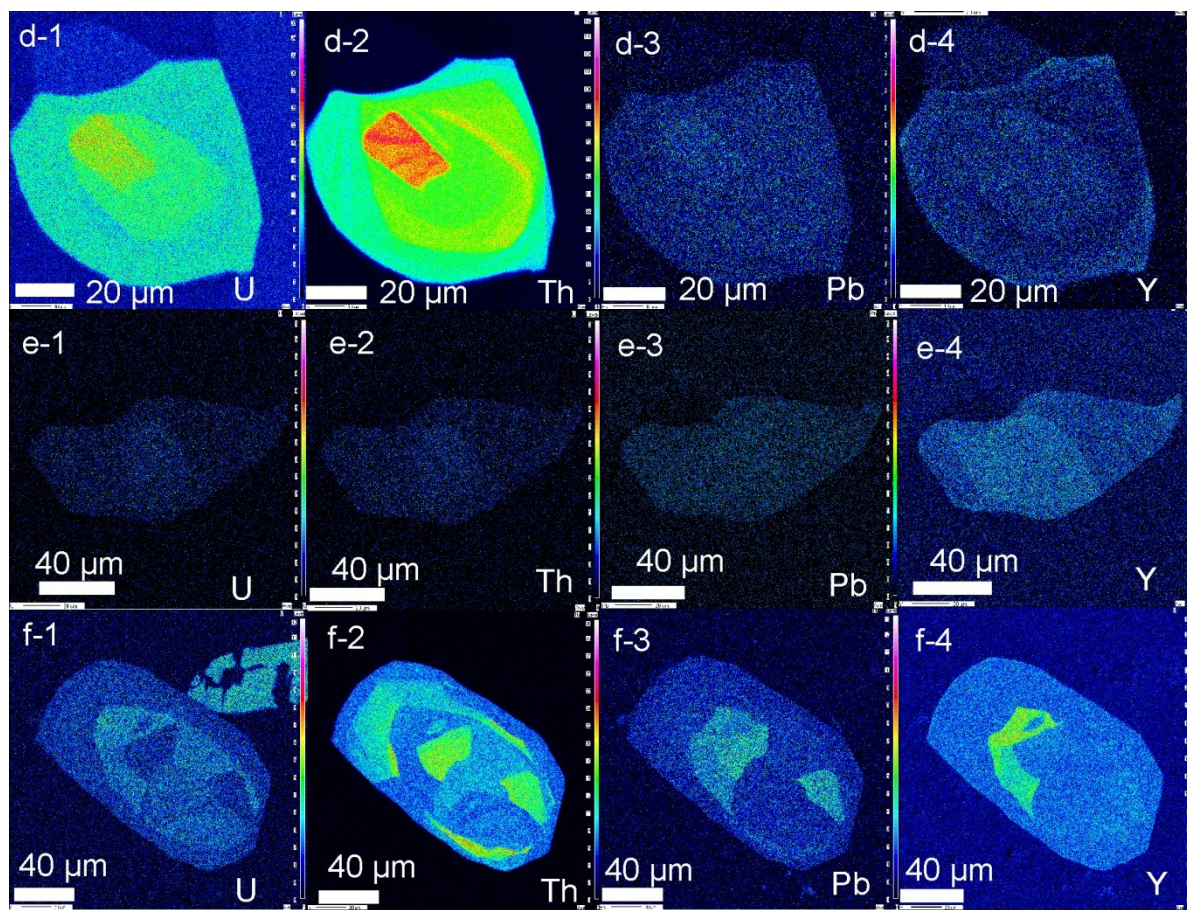


**Figure 27.** X-ray map images showing the distribution of U, Th, Pb, and Y in the inherited core-bearing type monazites (d-1, d-2, d-3, d-4; e-1, e-2, e-3, e-4; f-1, f-2, f-3, f-4).

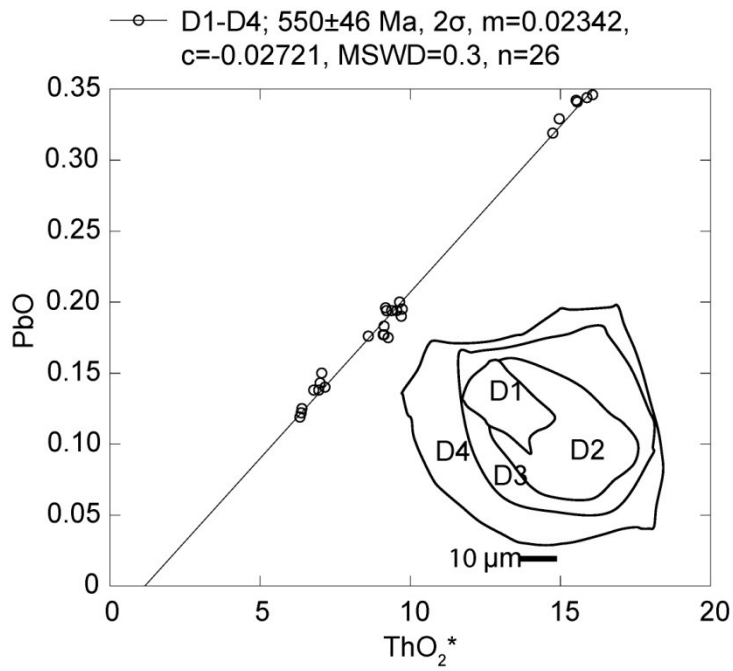


**Figure 28.** ThO<sub>2</sub>\*-PbO diagrams showing U-Th-total Pb isochrons and determined isochron ages (Suzuki and Adachi method)

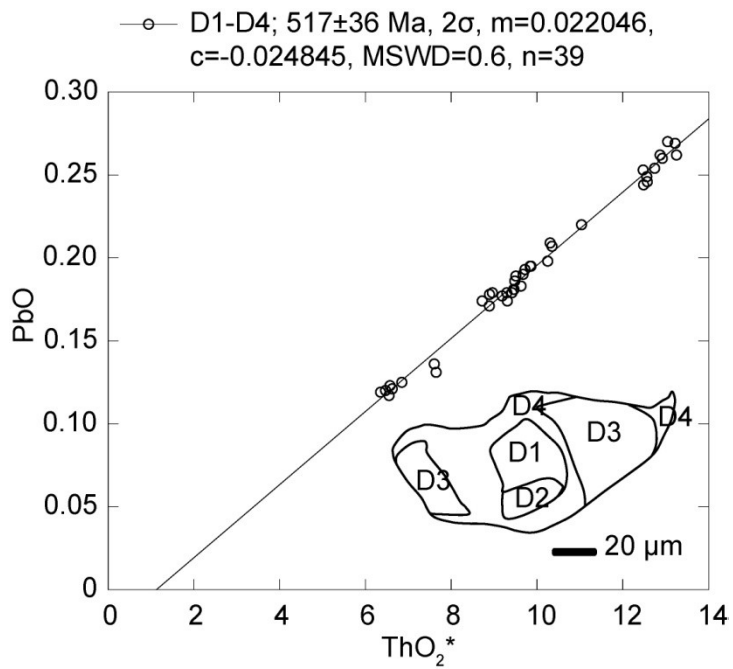


**Figure 29.** ThO<sub>2</sub>\*-PbO diagrams showing U-Th-total Pb isochrons and determined isochron ages (Suzuki and Adachi method)

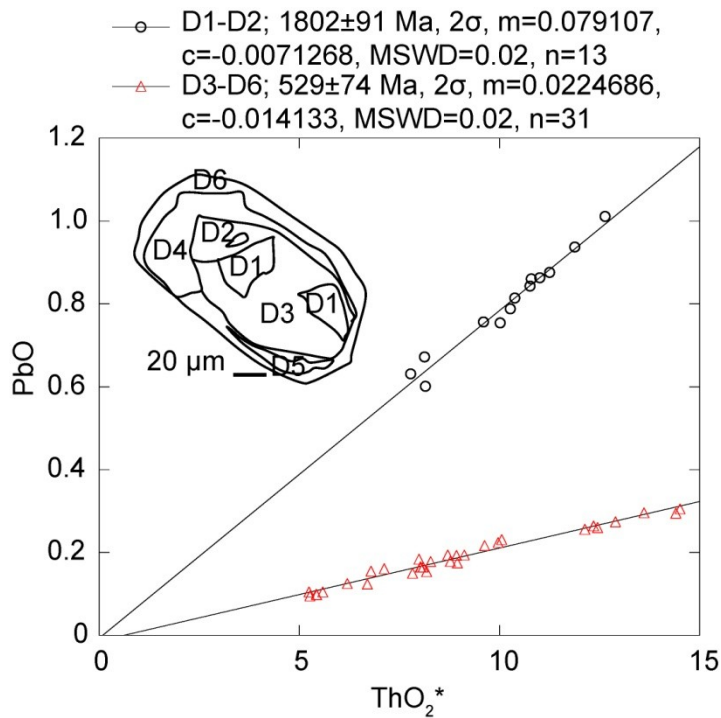


**Figure 30.**  $ThO_2^*$ -PbO diagrams showing U-Th-total Pb isochrons and determined isochron ages (Suzuki and Adachi method)

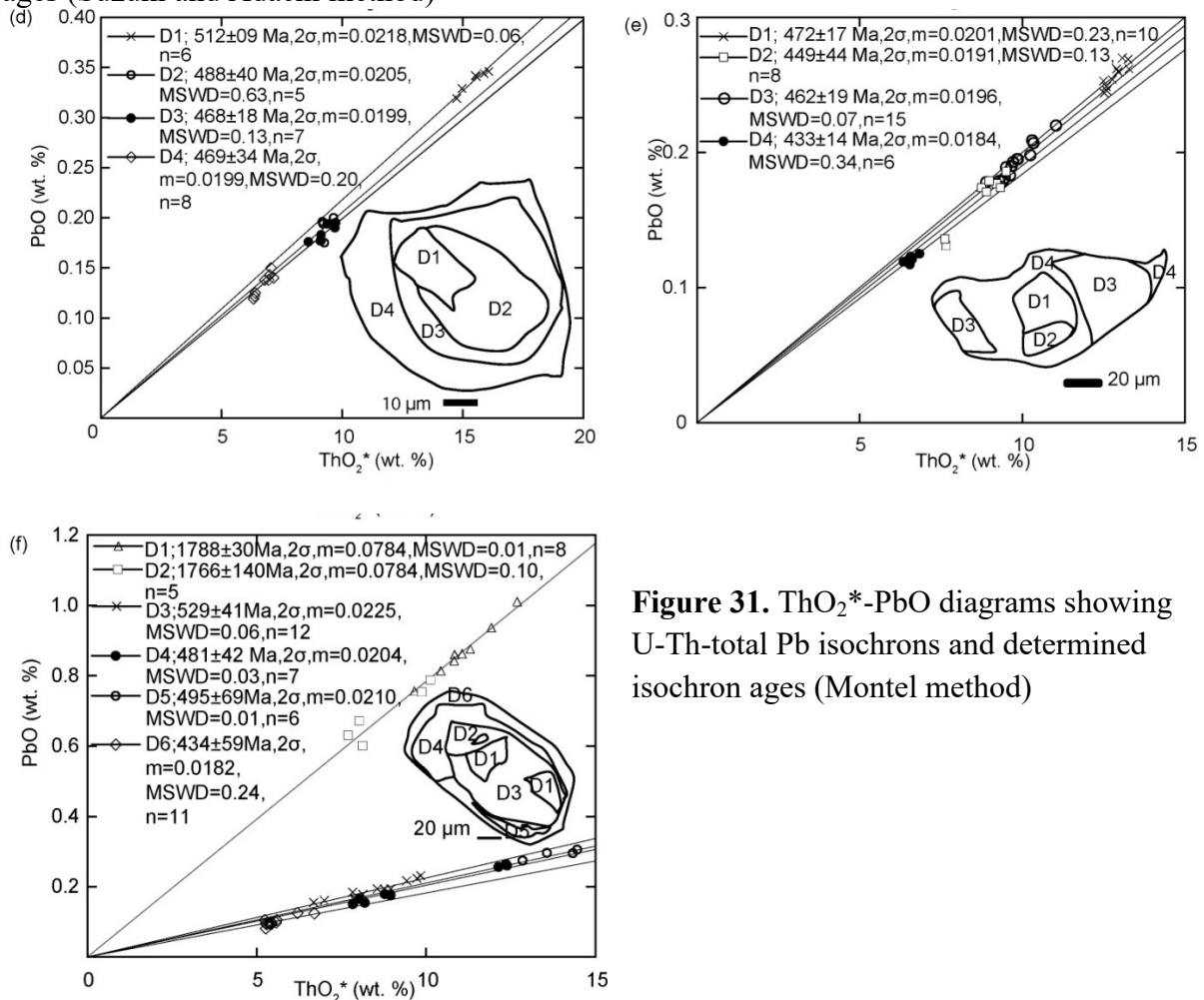


**Figure 31.**  $ThO_2^*$ -PbO diagrams showing U-Th-total Pb isochrons and determined isochron ages (Montel method)

#### V-4-4. COMPLEXLY ZONED MONAZITE

The complexly zoned monazite grains from the garnet-biotite gneiss are anhedral in form, significantly resorped, and relatively larger in size (500  $\mu\text{m}$ ). As shown by BSE image of a grain from 14-21GB (Figure 19g), internal texture is very complex and difficult to identify all sectors and zones. The complex occurrences of the brighter and darker zones in the BSE images are characteristic in the main part, which is rimmed by thin (10–20  $\mu\text{m}$ ) latest overgrowth zones. In the complexly zoned main part, quartz grains are included. In this study, the complex internal textures were categorized into five domains, based on the BSE image (Figure 19g) and the determined age for each domain (Figure 29): D1 is the remarkably dark zone; D2 covers the D1; D3 is an overgrowth zone on the D2; D4 domains distribute outermost region of the D3 zone, and D5 is the outermost zone of the grain. The PbO against  $\text{ThO}_2^*$  diagram drawn according to Suzuki and Adachi method (Figure 32) and Table 13 show the oldest isochron age of  $1648 \pm 186$  Ma ( $c = 0.00800$ ) and  $803 \pm 99$  Ma ( $c = -0.04251$ ) for the D2;  $527 \pm 69$  Ma ( $c = -0.00859$ ) for the D3-D5. The PbO against  $\text{ThO}_2^*$  diagram drawn according to Montel method (Figure 33g) and Table 13 show the oldest isochron age of  $1686 \pm 186$  Ma and WAVG age of  $1675 \pm 35$  Ma for the D1 domain; isochron age of  $679 \pm 99$  Ma and WAVG age of  $662 \pm 68$  Ma for the D2; isochron ages of  $507 \pm 49$  and  $503 \pm 55$  Ma and WAVG ages of  $507.8 \pm 7.7$  and  $499 \pm 12$  Ma for the D3 and D4, respectively; and  $458 \pm 64$  Ma in isochron age and  $458 \pm 16$  Ma in WAVG age for the D5.

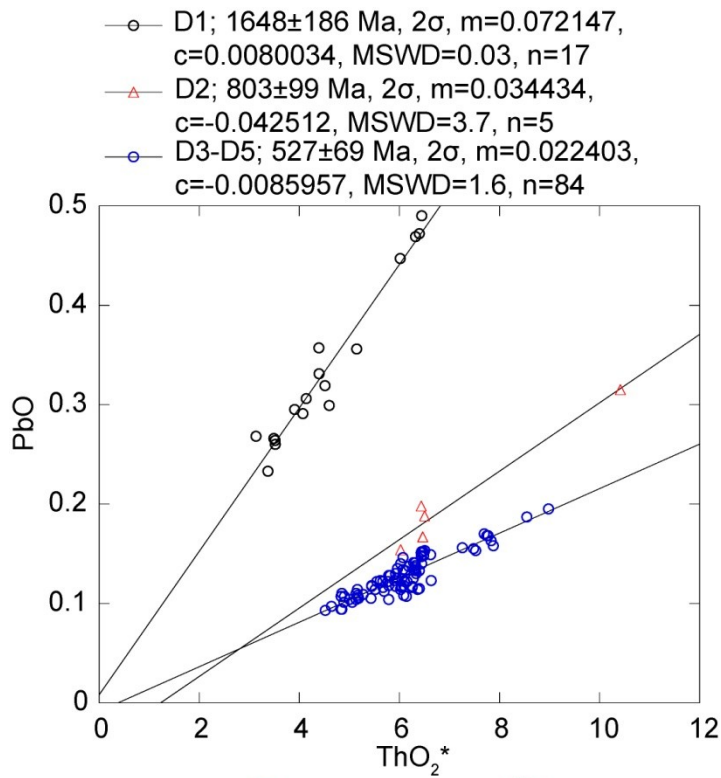


**Figure 32.**  $\text{ThO}_2^*$ -PbO diagrams showing U-Th-total Pb isochrons and determined isochron ages (Suzuki and Adachi method)

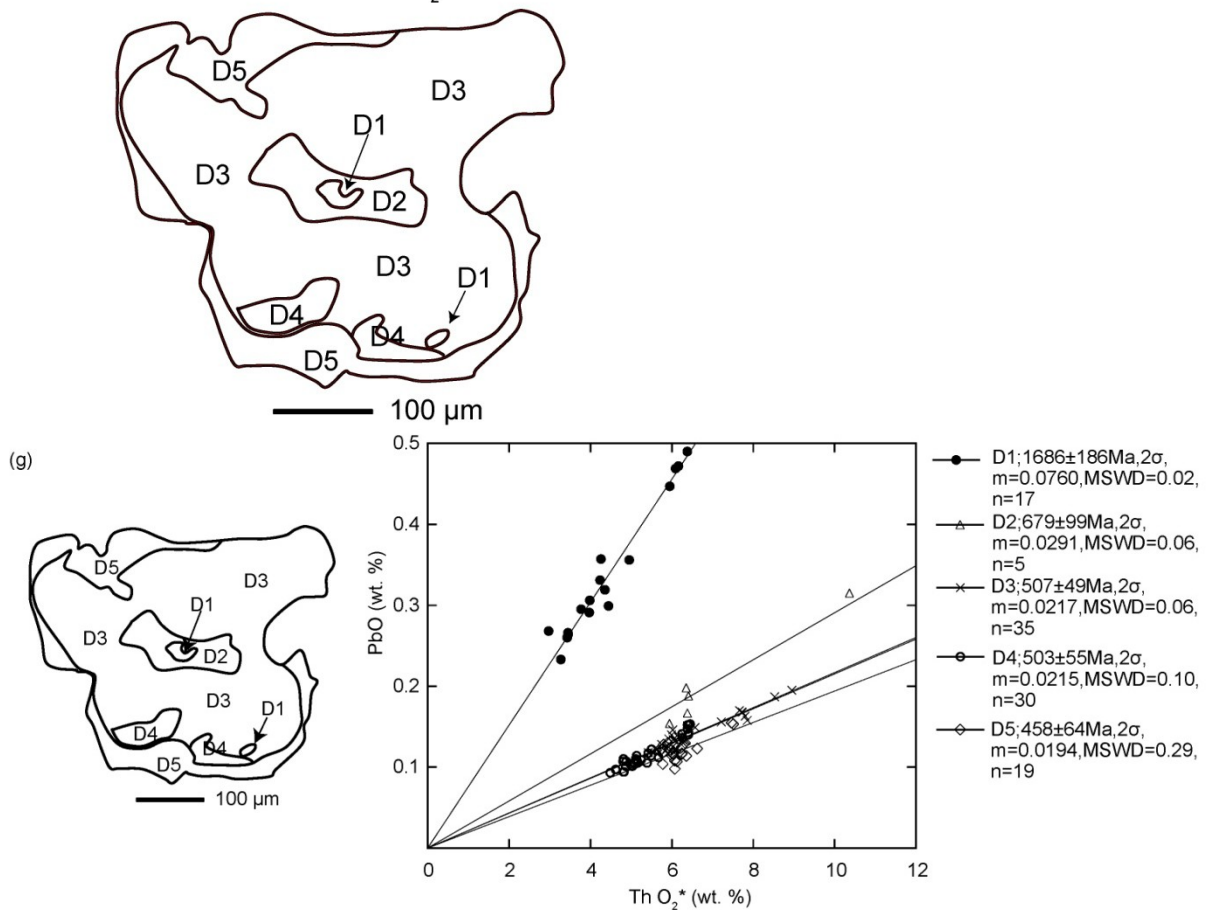


**Figure 33**  $\text{ThO}_2^*$ -PbO diagrams showing U-Th-total Pb isochrons and determined isochron ages (Montel method)



#### V-4-5. OSCILLATORY ZONED MONAZITE

Figure 19h represents the BSE image of an oscillatory zoned monazite from garnet-biotite gneiss (07-10GB). The grain is euhedral to subhedral in form and fine in size (100  $\mu\text{m}$ ). In the BSE image, alternating brighter and darker growth zones show different thicknesses. The surface of each generation shows euhedral to slightly resorped subhedral shapes. The internal texture is categorized into a core D1 and three overgrowths of D2, D3, and D4 (Figure 19h). The core and D2 zone are thicker than the overgrowth zones of D3 and D4. As shown by the PbO against  $\text{ThO}_2^*$  diagram drawn according to Suzuki and Adachi method and Montel method in Figure 34 and 35h, one age group of  $452 \pm 27$  Ma ( $c = 0.00741$ ),  $470 \pm 45$  Ma in isochron age, respectively, and  $467 \pm 8$  Ma in WAGV age is given for the D1, D2, D3, and D4.

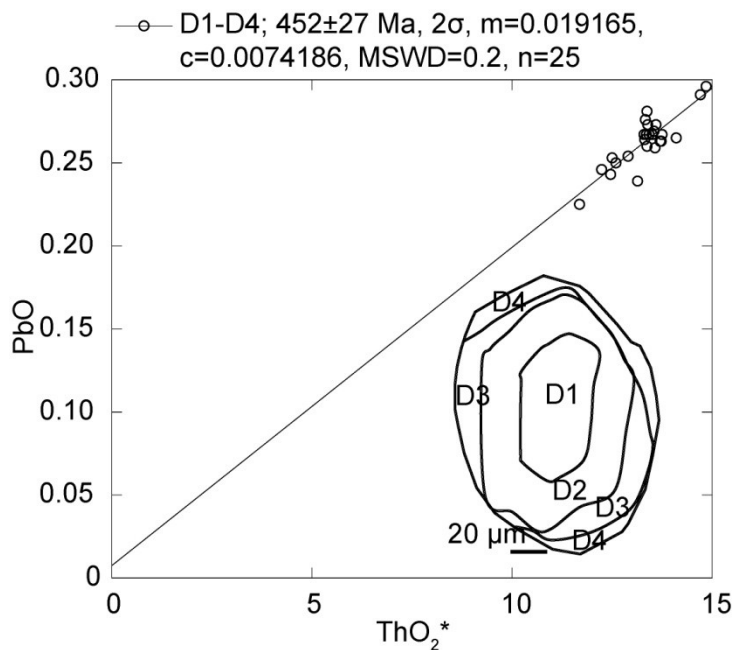


**Figure 34.**  $\text{ThO}_2^*$ -PbO diagrams showing U-Th-total Pb isochrons and determined isochron ages (Suzuki and Adachi method)

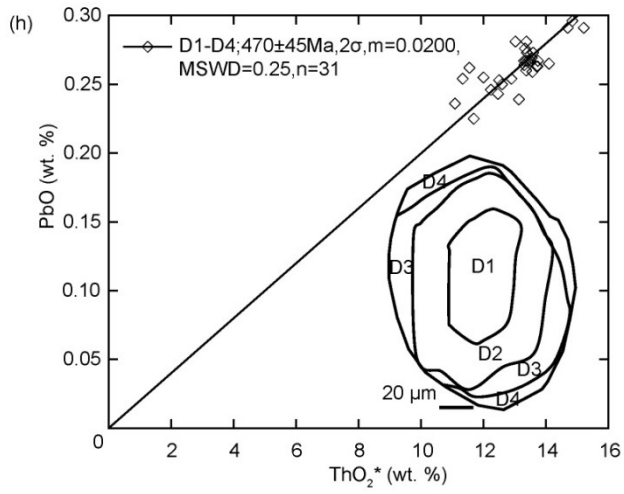


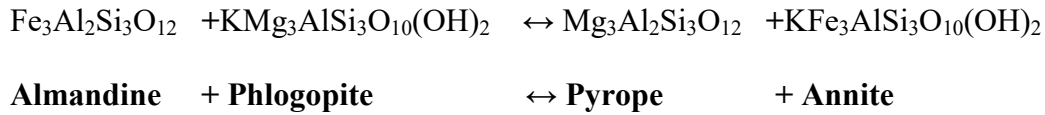
**Figure 35.** ThO<sub>2</sub>\*-PbO diagrams showing U-Th-total Pb isochrons and determined isochron ages (Montel method)

## VI. DISCUSSION

### VI-1. GEOTHERMAL CONDITIONS OF HOST ROCKS

Petrology of metamorphic rocks in the Central Highland Complex (CHC) and Southwestern Highland Complex (SWHC) has repeatedly been investigated in efforts to clarify the evolution of the major crustal units in Sri Lanka. Katz (1973) regarded the Highland Series (CHC) and Southwestern Group (SWHC) metamorphic rocks as Barrovian-type facies series and Abukuma-type facies series, respectively, based on their mineral assemblages. Nevertheless, Perera (1984) suggested that the change in bulk chemical composition resulted in the differing mineral assemblages between the Highland Series and the SWHC. Faulhaber and Raith (1991) estimated metamorphic pressures and temperature gradients in the southern part of Sri Lanka. By applying the garnet-biotite geothermometer and the estimated metamorphic pressures after Faulhaber and Raith (1991), Sajeev and Osanai (2005) proposed a thermal gradient with the highest temperature ( $>850\text{ }^{\circ}\text{C}$ ) in the CHC and gradually decreased temperature ( $<700\text{ }^{\circ}\text{C}$ ) towards the SWHC. Dharmapriya et al. (2014) described the spinel + quartz assemblages of spinel- and cordierite-bearing garnet-sillimanite-biotite-graphite gneiss in the SWHC are non-Ultra High Temperature (UHT) assemblage because of Zn and  $\text{Fe}^{+3}$  possibly incorporate into spinel under high oxidizing conditions, and estimated the maximum temperature for the rock sample as  $870\text{--}900\text{ }^{\circ}\text{C}$  (Dharmapriya et al., 2014). To compare the metamorphic temperature of the SWHC to the CHC, closure temperatures of seven samples containing garnet and biotite were calculated, using the conventional geothermometric method (Ferry and Spear, 1978).

In this study, following equilibrium was build based on the mineral assemblages, textures, and mineral chemistry:



The garnet-biotite geothermometer estimates temperature at equilibrium condition using Fe and Mg partition coefficient between garnet and biotite. For temperature calculation, two experimental equilibrium constant and temperature relationships were used. First method is by ideal mixing model for garnet and biotite after Ferry and Spear (1978):  $\ln K_D = (2109/T) - 0.782$ . The second one is by non-ideal mixing model for garnet and biotite after Perchuk and Lavrentéva (1983):  $\ln K_D = (3948/T) - 2.87$ .

In the calculation of equilibrium temperature, I followed analytical protocol of the Spear (1991) and Spear and Florence (1992) to estimate the peak equilibrium conditions: In this protocol garnet and biotite included within feldspar and quartz without other mineral inclusions were selected for analysis to minimize the potential retrograde Fe-Mg exchange and maximize the potential for retaining peak equilibrium  $K_D$  (garnet-biotite). Moreover, Sajeev and Osanai (2005) avoided applying the geothermometer to biotite and garnet in contact each other to minimize the effect of retrograde metamorphic process. I also followed their method. Petrographic observation and microprobe line-scan analyses of garnet and biotite were done to ensure the mineral contact condition and the chemical homogeneity. The garnets from the garnet-biotite gneiss, garnet-biotite-cordierite gneiss, and charnockitic gneiss with garnet were used in calculation of equilibrium temperature. However, the garnets in hornblende-bearing charnockitic gneiss were not used due to higher grossular content.

### **Application of garnet-biotite geotherm for garnet-biotite gneiss 17-24GB**

Figure 12a shows the mineral assemblage of garnet and biotite in the garnet-biotite gneiss 17-24GB. Three types of occurrences of biotites are observed: biotite inclusions in garnet, which is designated as Bt1; biotite at the edge of garnet, designated as Bt2 and Bt3; and biotite in the matrix, designated as Bt4. However, B4 biotites are not in contact with garnet. The representative equilibrium temperatures of garnet and Bt1 was given as  $629 \pm 11$  °C by applying ideal mixing model after Ferry and Spear (1978) and as  $611 \pm 8$  °C by non-ideal mixing model after Perchuk and Lavrentéva (1983). The representative temperatures of garnet and Bt2 are given as  $584 \pm 10$  °C by ideal mixing model and as  $587 \pm 7$  °C by non-ideal mixing model, whereas the representative equilibrium temperatures of garnet and Bt3 are  $716 \pm 12$  °C by the ideal mixing model and as  $654 \pm 8$  °C by non-ideal mixing model. The representative equilibrium temperatures of garnet and Bt4 are calculated as  $660 \pm 11$  °C by the ideal mixing model and as  $627 \pm 8$  °C by non-ideal mixing model.

**Table 14** Calculated equilibrium temperature (°C) by garnet and biotite in 17-24GB

Sample	kbar	Representative equilibrium temp. by ideal mixing model after Ferry and Spear (1978)	Representative equilibrium temp. by non-ideal mixing model after Perchuk and Lavrentéva (1983)
Bt1	2-10	629±11	611±8
Bt2	2-10	584±10	587±7
Bt3	2-10	716±12	654±8
Bt4	2-10	660±11	627±8

### **Application of garnet-biotite geotherm for garnet-biotite cordierite gneiss 23-32Co**

Figure 12b shows the mineral assemblage of garnet and biotite in garnet-biotite-cordierite gneiss. Three modes of occurrences of biotites were observed: biotite inclusions in garnet, designated as Bt5; biotite at the edge of garnet, designated as B6; and biotite in the matrix, designated as B7. Biotites (B7) are not in contact with garnet. The representative equilibrium temperatures of garnet and Bt5 are given as  $631 \pm 11$  °C by the ideal mixing model and  $612 \pm 8$  °C by non-ideal mixing model. The representative equilibrium

temperatures of garnet and Bt6 are calculated as  $868 \pm 14$  °C by the ideal mixing model  $722 \pm 9$  °C by non-ideal mixing model. The representative temperatures of garnet and Bt7 are  $733 \pm 12$  °C by the ideal mixing model and  $662 \pm 8$  °C by non-ideal mixing model.

**Table 15** Calculated equilibrium temperature (°C) by garnet and biotite in 23-32Co

Sample	kbar	Representative equilibrium temp. by ideal mixing model after Ferry and Spear (1978)	Representative equilibrium temp. by non-ideal mixing model after Perchuk and Lavrentéva (1983)
Bt5	2-10	631±11	612±8
Bt6	2-10	868±14	722±9
Bt7	2-10	733±12	662±8

### Application of garnet-biotite geotherm for garnet-biotite gneiss 14-21GB

Figure 12c shows the mineral assemblage of garnet and biotite in garnet-biotite gneiss (14-21GB). Two modes of occurrences of biotites were observed: biotite inclusions in garnet, designated as Bt8; and biotite at the edge of garnet, designated as Bt9. The representative equilibrium temperatures of garnet and Bt5 are given as  $640 \pm 11$  °C by the ideal mixing model and  $617 \pm 8$  °C by non-ideal mixing model. The representative equilibrium temperatures of garnet and Bt6 are calculated as  $825 \pm 13$  °C by the ideal mixing model  $704 \pm 8$  °C by non-ideal mixing model.

**Table 16** Calculated equilibrium temperature (°C) by garnet and biotite in 14-21GB

Sample	kbar	Representative equilibrium temp. by ideal mixing model after Ferry and Spear (1978)	Representative equilibrium temp. by non-ideal mixing model after Perchuk and Lavrentéva (1983)
Bt8	2-10	640±11	617±8
Bt9	2-10	825±13	704±8

### Application of garnet-biotite geotherm for garnet-biotite gneiss 07-10GB

Figure 12d shows the mineral assemblage of garnet and biotite in the garnet-biotite gneiss 07-10GB. Two types of occurrences of biotites are observed: biotite at the edge of garnet, designated as Bt10; and biotite in the matrix, designated as Bt11. Biotites (B11) are not in contact with garnet. The representative equilibrium temperatures of garnet and Bt10

was given as  $703 \pm 12$  °C by applying ideal mixing model after Ferry and Spear (1978) and as  $648 \pm 8$  °C by non-ideal mixing model after Perchuk and Lavrentéva (1983). The representative temperatures of garnet and Bt11 are given as  $764 \pm 12$  °C by ideal mixing model and as  $677 \pm 8$  °C by non-ideal mixing model.

**Table 17** Calculated equilibrium temperature (°C) by garnet and biotite in 07-10GB

Sample	kbar	Representative equilibrium temp. by ideal mixing model after Ferry and Spear (1978)	Representative equilibrium temp. by non-ideal mixing model after Perchuk and Lavrentéva (1983)
Bt10	2-10	703±12	648±8
Bt11	2-10	764±12	677±8

#### **Application of garnet-biotite geotherm for charnockitic gneiss 04-05 C**

Figure 12e shows the mineral assemblage of garnet and biotite in charnockitic gneiss. Two modes of occurrences of biotites were observed: biotite at the edge of garnet, designated as B12; and biotite in the matrix, designated as B13. Biotites (B13) are not in contact with garnet. The representative equilibrium temperatures of garnet and Bt12 are given as  $710 \pm 12$  °C by the ideal mixing model and  $651 \pm 8$  °C by non-ideal mixing model. The representative equilibrium temperatures of garnet and Bt13 are calculated as  $868 \pm 14$  °C by the ideal mixing model  $722 \pm 9$  °C by non-ideal mixing model.

**Table 18** Calculated equilibrium temperature (°C) by garnet and biotite in 04-05C

Sample	kbar	Representative equilibrium temp. by ideal mixing model after Ferry and Spear (1978)	Representative equilibrium temp. by non-ideal mixing model after Perchuk and Lavrentéva (1983)
Bt12	02-10	710±12	651±8
Bt13	02-10	764±13	677±8

#### **Application of garnet-biotite geotherm for garnet-biotite gneiss 11-17GB**

Figure 12f shows the mineral assemblage of garnet and biotite in garnet-biotite gneiss. One mode of occurrences of biotites was observed: biotite at the edge of garnet, designated as B14. The representative equilibrium temperatures of garnet and Bt14 are given as  $555 \pm 10$  °C by the ideal mixing model and  $571 \pm 7$  °C by non-ideal mixing model.

**Table 19** Calculated equilibrium temperature (°C) by garnet and biotite in 11-17GB

Sample	kbar	Representative equilibrium temp. by ideal mixing model after Ferry and Spear (1978)	Representative equilibrium temp. by ideal mixing model after Ferry and Spear (1978)
Bt14	2-10	555±10	571±7

**Application of garnet-biotite geotherm for garnet-biotite gneiss 03-04GB**

Figure 12g shows the mineral assemblage of garnet and biotite in garnet-biotite gneiss. Two modes of occurrences of biotites were observed: biotite at the edge of garnet, designated as B15; and biotite in the matrix, designated as B16. Biotites (B16) are not in contact with garnet. The representative equilibrium temperatures of garnet and Bt15 are given as  $717 \pm 12$  °C by the ideal mixing model and  $655 \pm 8$  °C by non-ideal mixing model. The representative equilibrium temperatures of garnet and Bt16 are calculated as  $729 \pm 12$  °C by the ideal mixing model  $660 \pm 8$  °C by non-ideal mixing model.

**Table 20** Calculated equilibrium temperature (°C) by garnet and biotite in 03-04GB

Sample	kbar	Representative equilibrium temp. by ideal mixing model after Ferry and Spear (1978)	Representative equilibrium temp. by ideal mixing model after Ferry and Spear (1978)
Bt15	02-10	717±12	655±8
Bt16	02-10	729±12	660±8



Tables 21 show a summary of the average of calculated  $K_D$  values and estimated representative equilibrium temperature for the samples in this study.

**Table 21** Average  $K_D$  values and Estimated equilibrium temperature ( $T$ ) for the Fe-Mg exchange between garnet and biotite

Sample no	17-24GB	14-21GB	07-10GB	11-17GB	03-04GB	04-05GB	23-32Co
n	24	13	64	10	14	24	28
$K_D$	3.872	3.651	3.227	3.657	3.762	3.553	3.267
$\ln K_D$	1.354	1.295	1.172	1.297	1.325	1.268	1.184
T (°C) Sp (by ideal mixing model)	737±13	765±14	831±15	764±14	751±14	779±14	824±15
T (°C) Per (by non-ideal mixing model)	683±9	696±9	726±9	696±9	689±9	703±9	723±9
Average	710±11	730±12	778±12	730±12	720±12	741±12	774±12

Sp: Ferry and Spear (1978), Per: Perchuk and Lavrentéva (1983)

As described already, the typical petrographic characteristics formed by the metamorphism are (1) formation of orthopyroxene and porphyroblastic garnet (Fig. 9a, b, c, d, and g) in prograde metamorphism (Perera, 1987, 1994); (2) breakdown of garnet (Fig. 9g) in the isothermal decompression stage before reaching the peak temperature (Perera, 1987, 1994); and (3) crystallization of secondary garnet (Fig. 9h) in the isobaric cooling stage (Perera, 1987, 1994). According to the estimated equilibrium temperatures using biotite-garnet assemblages, the calculated average temperature for porphyroblastic garnets in the sample 11-17GB is ~764 °C, whereas the secondary garnet in the same sample gave the temperature of ~550 °C. This difference of temperatures between the porphyroblastic garnets and the secondary garnets suggests that formation of porphyroblastic garnet and breakdown of garnet has taken place at temperatures of 850–750 °C and the secondary garnet formation by retrograde isobaric cooling process at ~550 °C. Such difference of estimated metamorphic temperatures was only observed in the zircons from the granulite facies metamorphic rocks in

the study area. This may indicate the existence of several thermal events or repeated thermal events during the final metamorphic event. The thin peripheral overgrowths in zircon grains may have been formed by this final metamorphic event.

Based on the present results, contour lines of temperature can be drawn as shown in Figure 36. Sajeev and Osanai (2005) also proposed distribution of metamorphic temperatures of whole Southwest Highland Complex including the same area as this study. Sajeev and Osanai (2005) used average temperatures from four conventional thermometers as Thompson (1979), Ferry and Spear (1978), Perchuk and Lavrenteva (1983), and Perchuk et al. (1985). However, their conclusions were derived using the results from three samples which were not sufficient in amount to establish contour map for the SWHC. In this study, I analyzed seven samples, and, by combining Sajeev and Osanai (2005), the metamorphic temperature contour map in Figure 36 is more reliable and accurate. According to this result, eastern and southern areas tend to show higher temperatures, which is similar to that by Sajeev and Osanai (2005) but more complicated. This complication is because of the rocks are highly interlayered. Thermal gradients can be constructed smoothly in contact metamorphic terrains. However, the high grade terrains, like the SWHC suffered mostly regional metamorphism, collisional deformations, and interlayered rocks, give rather complicated thermal gradients which should be taken into consideration of thermal structure in these regions.

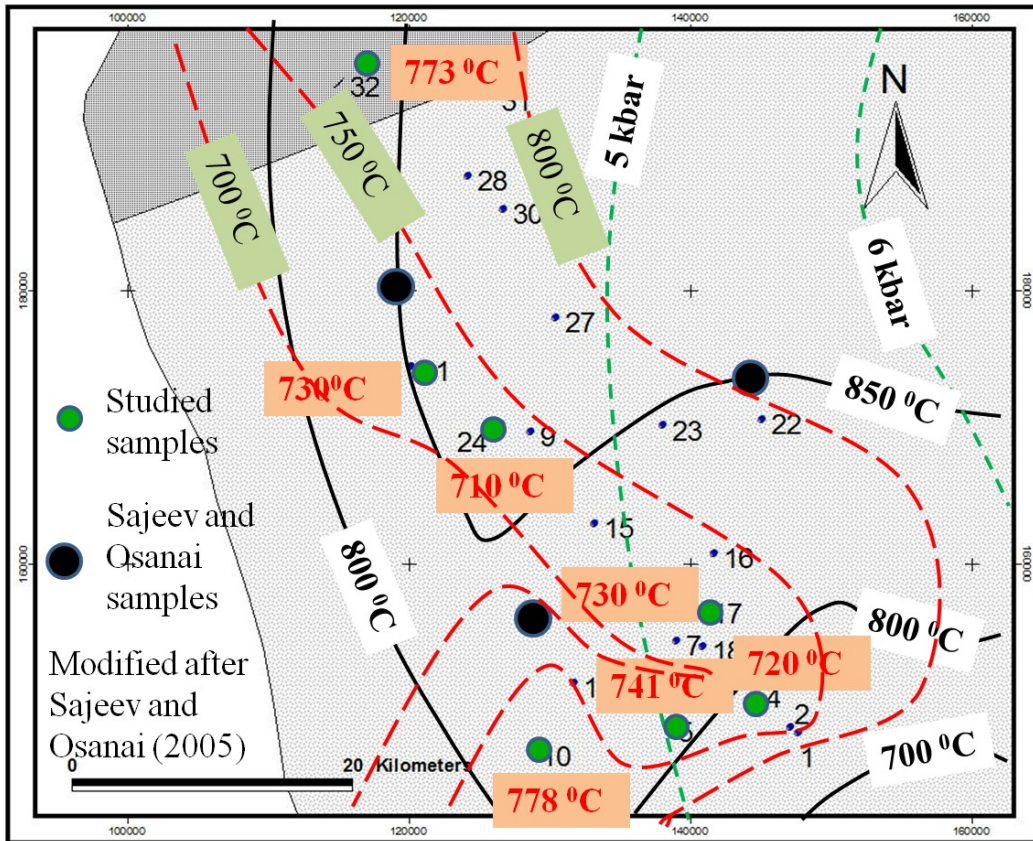


**Figure 36.** Distribution of metamorphic temperatures in the studied area which is the same as the study area by Sajeev and Oşanai (2005). Red lines indicate the current study. Black colored contours indicate the contours proposed by Sajeev and Oşanai (2005). Green contouring is according to the Faulharber and Raith (1991) study for pressure

## VI-2. SOURCE OF DETRITAL CORES OF ZIRCON

Many studies have shown relations between the metamorphic  $P$ - $T$  conditions in high-grade metamorphic terrains and their U-Pb chronological data (e.g. Harley et al., 2007). Zircon is, in many cases, only mineral keeping age information even though they have repeatedly subjected thermal events. According to Harley et al. (2007), there are two main reasons why only zircon can provide the age information on the thermal histories. First, the metamorphic or igneous temperatures are higher than the diffusional closure temperatures for many minerals (Cherniak and Watson, 2000). Hence, U and Pb contents (or U/Pb-ratio) in rutile, Ar isotope contents in mica, and even Sm and Nd contents in garnet record only the later stage or post-peak metamorphism histories. Second, if temperatures of thermal events are extremely high, partial melting takes place in rocks containing hydrous minerals like mica and amphibole (Sawyer, 2001).

On the basis of above recognition, several studies on the origin of the detrital cores of zircons from the Highland Complex have been studied by now. The U-Pb zircon dating of 3.2–2.0 Ga by Kröner et al. (1987) indicates that the detrital cores of zircons from the CHC were derived from an Archean source. Such an Archean source has also been proposed based on Nd model ages of 3.0–2.2 Ga (Milisenda et al., 1988, 1994) and Sr model ages of 2.5–2.0 Ga (Crawford and Oliver, 1969). Recent studies (e.g., Santosh et al., 2014; He et al., 2016a, 2016b; Takamura et al., 2015) also confirmed that the origin of the detrital cores of CHC zircons is attributed to the Neoproterozoic-Paleoproterozoic crustal source. In the present study, the oscillatory zoned and transgressive detrital cores of zircons from the SWHC gave the oldest ages of 3380–3220 Ma, indicating the detrital zircons in the SWHC also originated from a Paleoproterozoic source, as well as the case of the CHC.

It has been known that rounded and/or truncated shapes of primary igneous zircons in sedimentary rocks indicate long-distance sedimentary transport (Vavra et al., 1996), whereas

subhedral to euhedral detrital cores and aggregated detrital cores suggest limited transport distance from the source (Jocelyn and Pidgeon, 1974). The detrital cores of zircons from the garnet-biotite gneiss in the study area are commonly rounded or subhedral to euhedral in form, and show oscillatory zoning of magmatic origin. Such occurrences of the detrital cores of zircons in the garnet-biotite gneiss of the SWHC suggest two modes of transportation processes for the detrital cores in zircons: the first is proximal to the depositional basin, and the second lay in a more distal setting.

The results of the present study also show the ages of detrital cores ranging from 3.3–1.7 Ga. The ages of the detrital cores can be categorized into five ranges of 3380–3220 Ma (range 1), 2730–2660 Ma (range 2), 2550–2490 Ma (range 3), 2220–2170 Ma (range 4), and 1900–1700 Ma (range 5). As schematically shown in Figure 37, the ages of the detrital cores in the range 2, 2726–2668 Ma, are similar to those of the first overgrowths of CL8 in Figure 12. Thus, the detrital cores with ages in the range 1 are considered to have been subjected to a thermal event in the range 2. The detrital cores with ages in the range 4 (2220–2170 Ma) are likewise regarded to have been subjected to a thermal event and got younger ages. The detrital cores, except for those with ages in the range 5 (1900–1700 Ma) have Th/U ratios more than 0.3, indicating that they are essentially igneous in origin. On the other hand, most of the detrital cores with ages of the range 5 have Th/U of >0.3 or 0.3–0.1, indicating the igneous or metamorphic property. However, the detrital cores with Th/U ratio less than 0.1 also gave ages of ~1.8 Ga (Fig. 18; Tables 11 and 12), which may indicate an age of a metamorphic event, because the Th/U ratios less than 0.1 are most likely to have occurred in the metamorphic process (Hoskin and Schaltegger, 2003). Moreover, the first overgrowths giving ages in the range 5 occur on the detrital cores with ages in the ranges 1, 2, and 3 (3380–2490 Ma) (Fig. 16 CL1, No. 3, and CL11). Therefore, the ages in the range 5, 1900–1700 Ma, are regarded as ages of a metamorphic event. Baur et al. (1991) and Hölzl et

al. (1994) also recognized zircon upper intercept ages around 1900–1700 Ma for orthogneisses in the CHC, although they interpreted these as the crystallization ages of the protoliths.

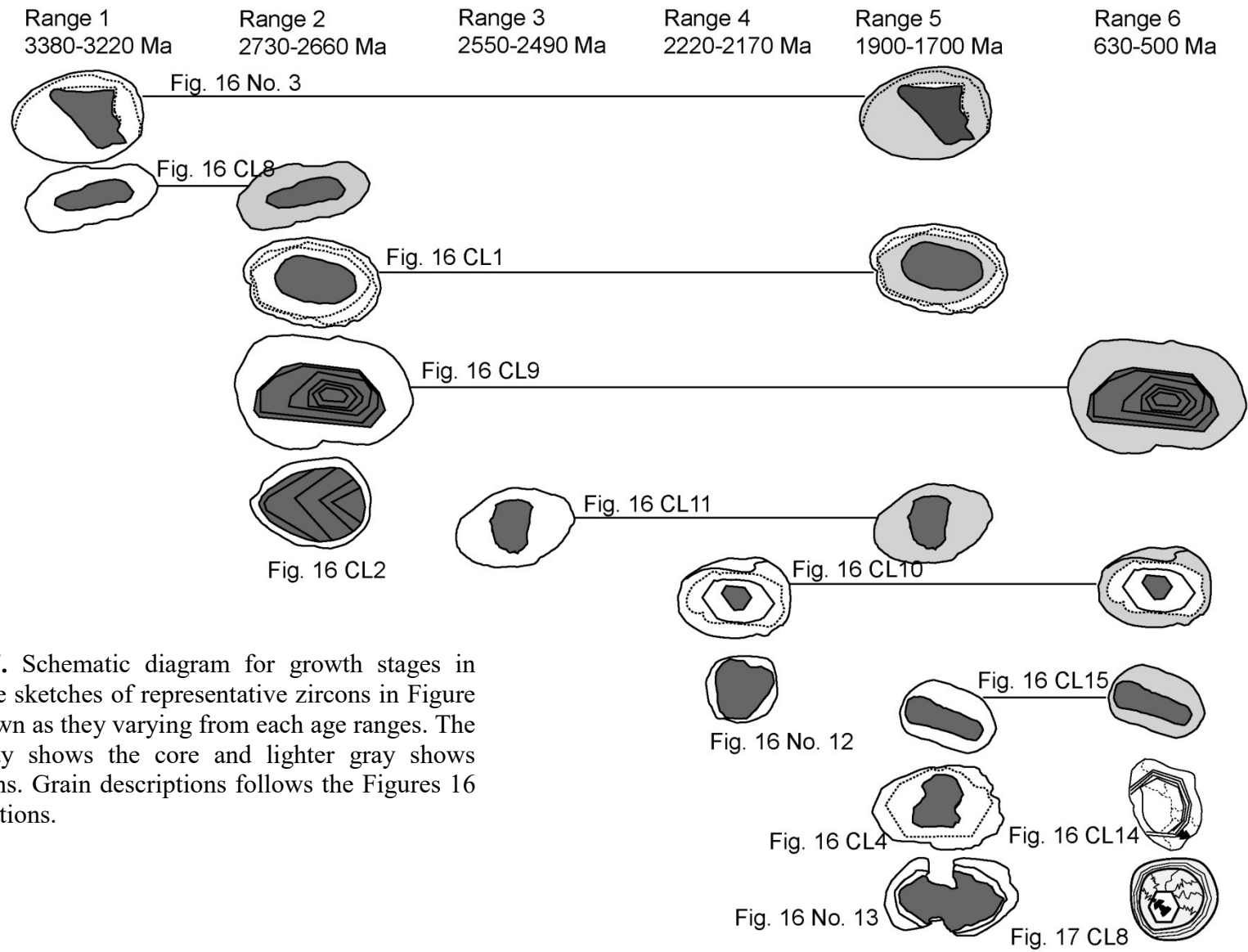


**Figure 37.** Schematic diagram for growth stages in zircon. The sketches of representative zircons in Figure 16 are shown as they vary from each age ranges. The darker gray shows the core and lighter gray shows overgrowths. Grain descriptions follows the Figures 16 and 17 captions.

In spite of the metamorphism by later stage thermal events, the detrital cores in zircons from the garnet-biotite gneiss preserved oscillatory zoning. This fact suggests that the metamorphic temperature was not high enough to modify or eliminate this zoning. At the same time, the detrital cores also show transgressive zoning which is regarded to have been formed by thermal events, because transgressive lobes and patches in igneous zircons with oscillatory zoning are formed by thermal events (e.g., Pidgeon, 1992; Vavra et al., 1996; Pidgeon et al., 1998; Hoskin and Black, 2000; Corfu et al., 2003). The reason for the presence of both detrital cores with preserved oscillatory zoning and transgressive zoning in the same rock samples may be due to local disequilibrium condition or local difference of thermal diffusion rate. In the sillimanite-bearing garnet-biotite gneiss (11-17GB), an abundance of the detrital core with oscillatory zoning is extremely low, and all of those detrital cores show transgressive textures, suggesting higher temperature conditions that may have converted the primary oscillatory zoning to the transgressive textures. Moreover, the zircons in charnockitic gneisses also have mainly transgressive textures. Since pyroxene-bearing charnockitic gneisses were subjected to the granulite facies metamorphism, the detrital core zircons with oscillatory zoning have changed to those with transgressive textures.

### **VI-3. FORMATION OF OVERGROWTHS AND INTERNAL TEXTURES OF ZIRCON**

The age data of the overgrowths can also be categorized into the several ranges, as well as the ages of the detrital cores. Finally, the age data of both detrital cores and overgrowths can be categorized into six ranges, as shown in Figure 37: the range 1 of 3380–3220 Ma; the range 2 of 2730–2660 Ma; the range 3 of 2550–2490 Ma; the range 4 of 2220–2170 Ma; the range 5 of 1900–1700 Ma; and the range 6 of 630–500 Ma.



According to the age data of the overgrowths on the detrital cores of zircons, the first overgrowths clearly show ages of the range 2 (2730–2660 Ma) (Fig. 16 CL8), the range 5 (1900–1700 Ma) (Fig. 16 CL1, No. 3, and CL11) and the range 6 (630–500 Ma) (Fig. 16 CL9 and CL15). The second stage overgrowths gave ages of the range 5 (1900–1700 Ma). Therefore, there are the first overgrowths giving younger ages of the ranges 5 and 6 than other first overgrowths with the older ages of the range 2. Based on the relation between the overgrowths and determined ages, it is supposed that the initial chemical compositions of both the detrital core and overgrowth zircons were changed to those giving younger ages by the latest stage thermal events that have been suggested by recent studies (Santosh et al., 2014; He et al., 2016a, 2016b). Such repeated thermal events contributed to form fourth or fifth overgrowths observed in zircon grains, and to generate the youngest zircon grains giving ages of the range 6 (630–500 Ma). The Th/U ratios of the zircons with ages in the range 6 are less than 0.1, indicating that these zircons are the latest metamorphic product. The fir-tree, radial, and planar banded internal textures in the zircons from the garnet-bearing region and the biotite-bearing region in the charnockitic gneiss (04-05C) are considered to have been formed during the latest thermal events, as well as those in garnet-biotite gneiss (Fig. 37). Previous studies on zircons from the CHC also identified this age group as the latest metamorphic event in the region (Kröner et al., 1994; Hölzl et al., 1991, 1994; Sajeev et al., 2010; Santosh et al., 2014; He et al., 2016a, 2016b). Zircons, lacking detrital cores, in the hornblende-bearing charnockitic gneiss and charnockitic gneisses are regarded to be metamorphic origin. This interpretation may be supported by the fact that the zircons showing internal textures in the charnockitic gneiss have only metamorphic internal textures.

#### **VI-4. INTERNAL TEXTURES AND CHRONOLOGY OF MONAZITE**

Internal textures of monazite in metamorphic rocks record growth process of monazite subjected to thermal events, and, thus, are important to elucidate the thermal history of the metamorphic rocks. In the study on monazites from the metamorphic rocks in the CHC, Malaviarachchi and Takasu (2011) identified three types of internal textures in the monazites, such as core-rim zoned, unzoned, and mesh-like zoned types, and indicated three age ranges of 728–619 Ma (Group II), 613–561 Ma (Group I), and 516–460 Ma (Group III). The result in the present study indicated that monazites in the metamorphic rocks of the SWHC in Sri Lanka have various internal textures, which can be categorized into four types: the core-rim zoned type, inherited core-bearing type, complexly zoned type, and oscillatory-zoned type. The core-rim zoned type monazite was common in the CHC and SWHC, but the unzoned type and mesh-like zoned type monazites were not observed in the SWHC. However, I newly defined three types of internal textural categories: inherited-core-bearing, complexly zoned, and oscillatory-zoned types. Finding of the inherited core-bearing type and complexly zoned type monazites are important, because, in monazites in these types, the core domains gave isochron ages of 1830–1648 Ma which is older than the data by Malaviarachchi and Takasu (2011).

According to the isochron ages of all the domains and zones in the present study, four distinct age groups can be proposed: group I defined by ages of 1830–1648 Ma, group II of 803±99 Ma and 679±99 Ma, group III of 550–485 Ma, and group IV of 470–430 Ma. The ages of each group according to Suzuki and Adachi method and Montel method are shown in Table 22. The two isochron methods do not show significant differences within the error ranges.

**Table 22** Four age groups according to the monazite isochron ages

Group	Suzuki and Adachi method (Suzuki and Adachi, (1991))	Montel Method (Montel et al., 1996)
I	1830–1648 Ma	1766±140 and 1788±30 Ma
II	803±99 Ma	679±99 Ma
III	550–485 Ma	533±22 and 481±42 Ma
IV	470–430 Ma	472±17 and 433±14 Ma

As described already, ages of the groups I, II, and III in the present study were obtained from the core domains and inner core zones, whereas the group IV ages were mainly given from rim zones of the monazites by means of Montel method. The group II ages of the SWHC monazite in this study coincide with the group II ages by Malaviarachchi and Takasu (2011), 778–619 Ma. I obtained the group II ages from the complexly zoned monazites, while Malaviarachchi and Takasu (2011) got their data from the unzoned core-rim type monazites. The groups III and IV ages in the present study, which were given from the rim zones of all kinds of monazites, seem to coincide with the group III ages, 516–460 Ma, of the mesh-like zoned monazite by Malaviarachchi and Takasu (2011). After all, the internal textures in monazite in the SWHC show evidence of at least four stages of thermal events, which would be common in the CHC. Thus, the ages of monazites in the SWHC and CHC essentially show common features. A minor difference of the age data between the SWHC and CHC may be due to local variations of thermal events, which caused somewhat different growth processes of monazites in each metamorphic rock.

In this study, I got ages of the group I (1830–1648 Ma) in inherited-core-bearing type and complex zoned type monazites from the garnet-biotite gneisses. These ages may imply either magma emplacement ages or depositional ages of sediments. The ages close to the group I ages (1830–1648 Ma) in this study have been reported by several studies on the CHC using zircon-geochronology. Sajeev et al. (2010) interpreted 1.7 Ga age clusters in quartz-

saturated granulites from the CHC as episodes of zircon growth in the source region of the protolith sediments. The upper intercept ages around 1.9–1.8 Ga (Baur et al., 1991; Hölzl et al., 1994) for zircon were interpreted as crystallization ages of protoliths of orthogneisses in the CHC. Therefore, the result in the present study is consistent with the published results on zircons in metamorphic rocks from the CHC, and proves that the detrital monazites were crystallized by thermal event at around 1.7 Ga.

## **VI-5. AGES OF MULTITHERMAL EVENTS DETERMINED ZIRCON AND MONAZITE CHROLOGICAL DATA**

This study on SWHC and previous studies on the CHC showed that zircon growth took place during 1900–1700 Ma of the range 5. This age range corresponds to the crustal formation age of the CHC which was recognized by Baur et al. (1991) and Hölzl et al. (1994) using zircon upper intercept ages for orthogneisses in the CHC. However, the overgrowth of the age range 5 (1900–1700 Ma) found in this study have never been reported not only from SWHC but also CHC, and is new finding. The overgrowths in the age range 5 essentially show Th/U ratios less than 0.1. Therefore, it is concluded that the SWHC has formed during 1900–1700 Ma and finally suffered the metamorphism in the range 6 (630–500 Ma) together with the CHC.

Monazite U-Th-Pb dating can be used in conjugation with zircon geochronology to define the metamorphic events. Formation of monazite and presence of overgrowths in zircon with Th/U ratios less than 0.1 show their metamorphic origin. However, the chronological studies on monazites in the Sri Lankan basement, especially the SWHC, are few. As discussed above, the group I (1830–1648) in inherited-core-bearing type and complex zoned type monazites from the garnet-biotite gneisses may imply either magma emplacement ages or depositional ages of sediments, and is considered that the detrital monazites were crystallized by thermal event at around 1.7 Ga. The ages of the group III (550–485 Ma) correspond to the stage of the most prominent thermal event recorded in the region. The previous chronological studies of both zircon and monazite in the CHC confirmed that this age group corresponds to the peak metamorphic event in the region (Kröner et al., 1994; Hölzl et al., 1991, 1994; Sajeev et al., 2010; Santosh et al., 2014; He et al., 2016a, 2016b). The groups III and IV defined in this study, 550–485 and 470–430 Ma, respectively, can be identified as post-peak thermal events. Such young ages have also been reported by

chronological studies on zircons from the CHC, and have been interpreted to represent youngest thermal events (Hözl et al., 1994; Sajeev et al., 2003, 2007; Malaviarachchi and Takasu, 2010; He et al., 2016a, 2016b). However, as indicated in this study, most of these younger ages are recorded near and in the rim area of the monazites. According to Ayers et al. (1999), such growth patterns can be interpreted as later resetting of monazites due to the longer heating period in the event of peak metamorphism. In this process, monazite crystals grew by Ostwald ripening to form rims and by coalescence, during which smaller crystals may move with grain boundaries by recrystallizing and reset the isotopic system. In this study, it can be assumed that the ages of the group IV at least represent the latest stage of the post-peak thermal events.

To understand the evolution of the Sri Lanka using geological, petrological and chronological data, two crustal evolution models have been proposed by now. One model proposed and developed by Vitanage (1972), Voll and Kleinschrodt (1991), Kröner and Jaeckel (1994), Cooray (1994), Kriegsman (1995) and Kehelpannala (1997, 2004) explained that two collisions had taken place. In this model, the first collision was assumed to have taken place in the age range of 1900–1700 Ma, because Baur et al. (1991) and Hözl et al. (1994) recognized age range of 1900–1700 Ma using zircon upper intercept ages for orthogneisses in the CHC; and the second collision caused the high-grade metamorphism in 630–500 Ma. In addition, the present study found the overgrowth of 1900–1700 Ma in zircons from the metamorphic rocks from the SWHC, which has never been reported not only from SWHC but also CHC, and is new knowledge. The overgrowths in age range 5 of 1900–1700 Ma essentially shows Th/U ratios less than 0.1. Therefore, it is considered that the SWHC has formed during 1900–1700 Ma and finally suffered the 630–500 Ma metamorphism together with the CHC. If the crustal model by Vitanage (1972) and others is assumed, following interpretation may be possible: detrital cores of the range 1 (3380–3220

Ma) to range 4 (2220–2170 Ma) were overgrown by thermal events in the range 5 (1900–1700 Ma) and range 6 (630–500 Ma); and the thermal event of the range 5 correspond to metamorphism by the first collision prior to the high-grade metamorphism in 630–500 Ma caused by the second collision in the crustal model.

On the other hand, recent studies on the CHC (e.g., Santosh et al., 2014; He et al., 2016a, 2016b) lead to a new interpretation of the evolution of the Highland Complex in terms of polyphase deformation relating to repeated thermal events during 630–520 Ma. However, the results of the present study on the internal textures and the age data of the detrital cores and overgrowths in zircons from the metamorphic rocks in the SWHC show complex evolution process of the high-grade basement of the SWHC, and seem to be consistent with the first crustal model than the recent crustal models for CHC.

## VI-6. RECONSTRUCTION OF TECTONOTHERMAL HISTORY OF THE SWHC

The estimated equilibrium temperatures calculated using the garnet-biotite Fe-Mg exchange geothermometry, monazite age data, and U-Pb zircon geochronology give important facts to clarify the evolution of the history of the SWHC.

The data is summarized into a map as shown in Figure 38, to show the relationship between sample localities and the chronological data.

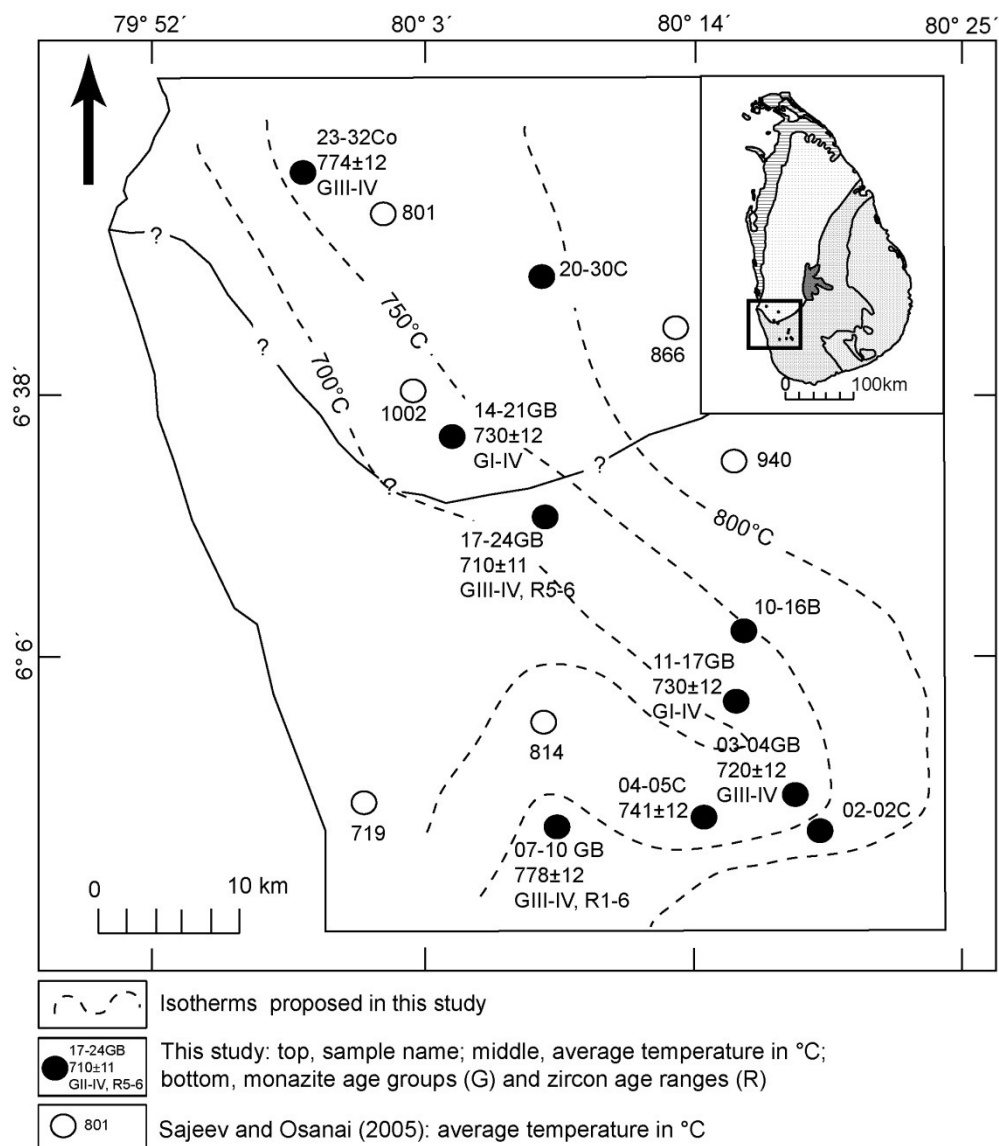


**Figure 38.** The summarized data plotted on the map to show the relationship of the temperature, monazite ages, and zircon ages.



A geographical relationship among Sri Lanka, South India, Madagascar and Antarctica in Gondwana supercontinent has been proposed by Kriegsman (1993), Grunow et al. (1996), and Dissanayake and Chandrajith (1999), as shown in Figure 39. According to their model, the SWHC is closely related to Kerala Khondolite Belt (KKB) in South India and Androyan Complex of Madagascar. The result in the present study and the published data in KKB monazite by Santosh et al. (2005), shown in  $\text{ThO}_2^*$ -PbO (wt.%) diagram of Figure 40, prove a close relationship between the SWHC and the KKB: in this diagram, the plots of PbO (wt.%) against  $\text{ThO}_2^*$  (wt.%) of the SWHC monazites with ages of 1788–1689 Ma;  $1766 \pm 140$ ;  $1788 \pm 30$  Ma and of 679–434 Ma form upper and lower trends, respectively, and the trends by the data of the KKB monazites with 1967–1759 Ma and 563–515 Ma (Santosh et al., 2005) are the same as those of the SWHC monazites. Moreover, the ages of early Pan-African thermal events in the South India have been reported as  $1802 \pm 16$  Ma (Bartlett et al., 1998) and 1793 Ma (Choudhary et al., 1992), and Paquette et al. (1994) reported  $1679 \pm 04$  Ma in Androyan Complex of Madagascar (Figure 39). Therefore, the SWHC, the KKB, and the Androyan Complex give similar ages of early Pan-African thermal events. On the other hand, the ages of 760–550 Ma given from zircons and monazite of the CHC have been interpreted in terms of Pan-African metamorphism with multiple thermal events (Kröner et al., 1994; Hölzl et al., 1991, 1994; Sajejev et al., 2010; Santosh et al., 2014; He et al., 2016a, 2016b). The Rb-Sr isochron ages of 484–440 Ma given from biotite, feldspar, and garnet from metamorphic rocks in South India, have been considered to represent Post-Pan-African thermal events (Choudhary et al., 1992; Unnikrishnan-Warrier et al., 1995; Unnikrishnan-Warrier, 1997). Thus, the lower trend in Figure 40 is interpreted to correspond to Pan-African and Post-Pan-African thermal events.

After all, the close relationship between the SWHC and other Gondwana fragments in the proposed model on Gondwana supercontinent can be confirmed by the chronological data in the present study and the published data.

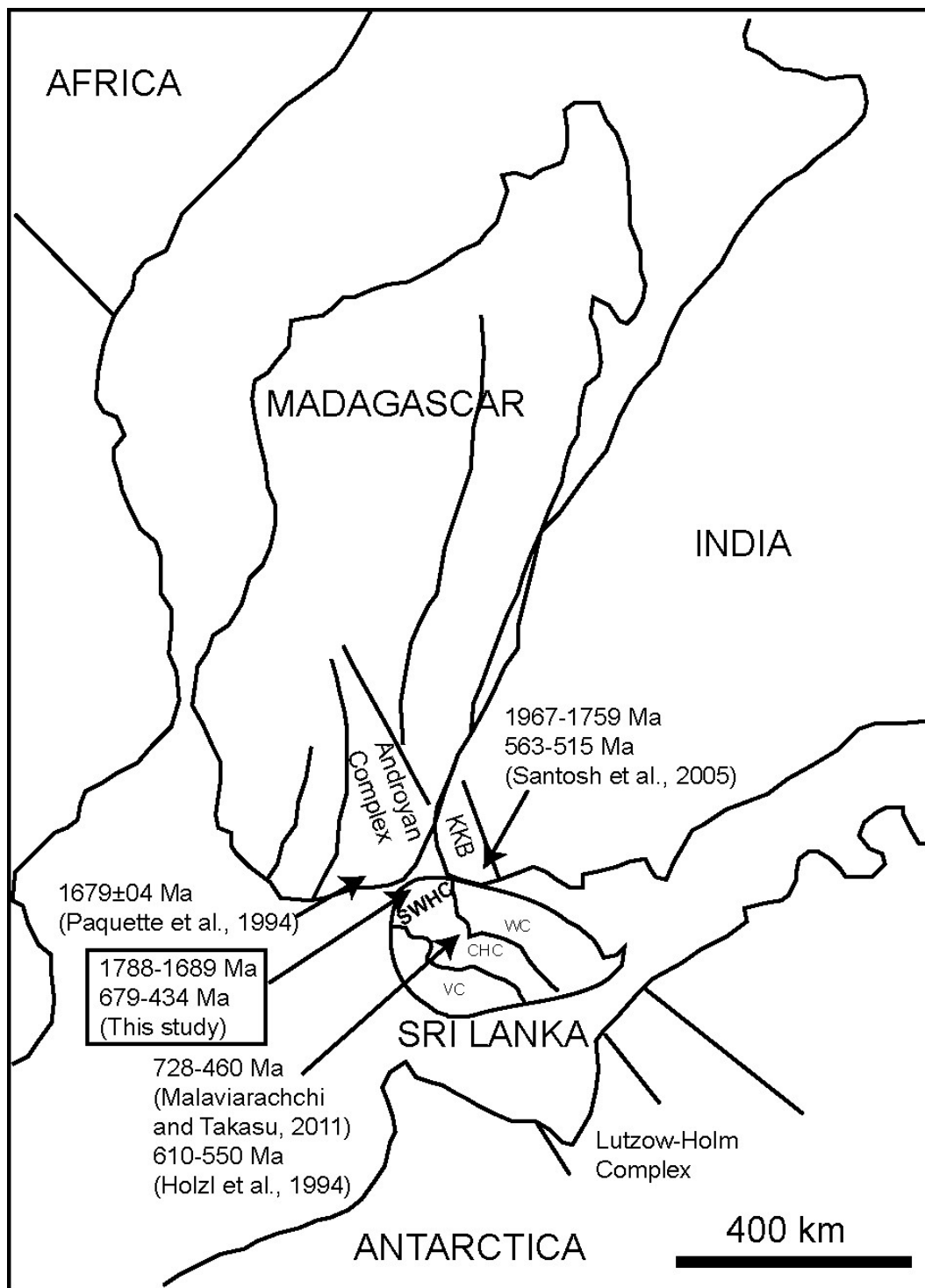


**Figure 39.** The position of Sri Lanka in Gondwana (modified after Dissanayake and Chandrajith, 1999). CHC, Central Highland Complex; KKB, Kerala Khondalite Belt; SWHC, South Western Highland Complex; VC, Vijayan Complex; WC, Wanni Complex.

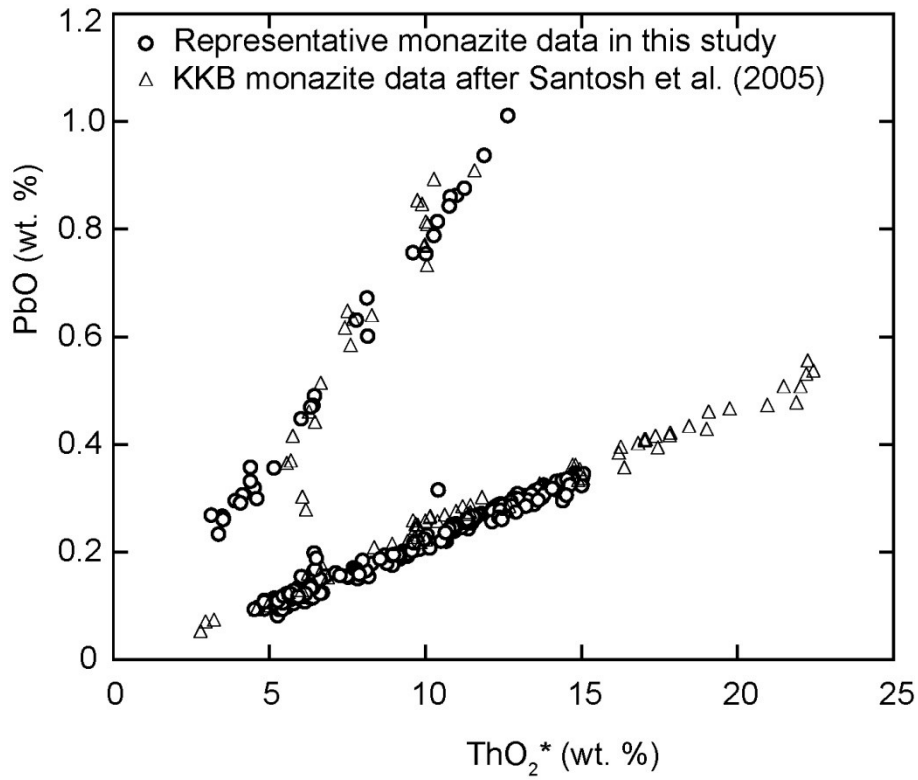


**Figure 40.** PbO-ThO<sub>2</sub>\* relation of zircons from the metamorphic rocks from the Southwestern Highland Complex and Kerala Khondolite Belt (KKB) in South India.

## VII. CONCLUSIONS

The SWHC in Sri Lanka is a critical place to give a clear view of multiple thermal history and relationship among West Gondwana fragments. Thus, the present author has investigated systematically the internal textures and chronology of zircons and monazites from the garnet-biotite gneiss, garnet-biotite-cordierite gneiss, hornblende-bearing charnockitic gneiss, and charnockitic gneiss in the SWHC. Moreover, thermal structure in the SWHC was reconstructed based on the present petrological study to examine the consistency among the internal textures of zircon and monazite, chronology and geothermal structure in the SWHC, CHC and other crustal units in the Sri Lanka.

Zircons from the garnet-biotite gneiss consist of the detrital zircon cores and overgrowths. The detrital zircon cores are rounded or euhedral to subhedral in shape, and show transgressive internal textures or oscillatory zoning. The overgrowths with two to five growth stages were recognized. In the garnet-biotite-cordierite gneiss sample, the zircons consisted of euhedral core part (not detrital core) and four to five growth zones lacking internal texture. Most of the zircons in the hornblende-bearing charnockitic gneiss and charnockitic gneiss are fine-grained and rounded in form, and have cores (not detrital core) and rims lacking internal textures. A few of them consist of rounded or skeletal detrital cores containing inclusions and/or voids and overgrowths with two or three generations. In some zircons, the overgrowths of the first, second and third generations exhibit fir-tree texture (ft), radial growth (rd) and a planar banded zone (bd), respectively. The ages of the detrital cores can be categorized into five ranges of 3380–3220 Ma, 2730–2660 Ma, 2550–2490 Ma, 2220–2170 Ma, and 1900–1700 Ma. The first overgrowths show several different ranges of ages: 2730–2660 Ma; 1900–1700 Ma; and 630–500 Ma. In the period of 630–500 Ma, fourth

or fifth overgrowths and the latest grains of zircons were generated. The overgrowths giving the ages in the range of 630–500 Ma have typical metamorphic internal textures.

The BSE images, element distributions, and CHIME age data of monazites in the garnet-biotite gneiss and garnet-biotite-cordierite gneiss from the SWHC, Sri Lanka, show several domains and zones even in one monazite grain. The internal domains and zones within monazites were categorized into four types: core-rim zoned, inherited core-bearing, complexly zoned, and oscillatory-zoned types. Among those categories, inherited core-bearing, complexly zoned, and oscillatory-zoned types are newly found for Sri Lankan monazites by the present study. The determined ages are grouped into five clusters: group I of 1830–1648 Ma,  $1766\pm 140$  Ma,  $1788\pm 30$  Ma; group II of  $803\pm 99$  Ma,  $679\pm 99$  Ma; group III of ages in a range between 550–485 Ma,  $533\pm 22$  –  $481\pm 42$  Ma; and group IV of ages in a range between 470–430 Ma,  $472\pm 17$  –  $433\pm 14$  Ma. The areas of rims of monazites show younger ages (533–434 Ma). The core areas of the inherited core-bearing type and complexly zoned type monazites gave oldest age values of the group I, whereas the rims and zones in the rim area show younger ages of the groups III and IV. Some monazite grains provided a wide variation in age (e.g., complexly zoned monazite). However, the Group II to IV can be considered as one group or thermal event within the error ranges of the ages.

Two possible interpretations are proposed here: 1) The detrital cores of the age range 1 to age range 5 were overgrown by thermal events in the age range 6, implying the overgrowth was formed as a single collisional event 2) The detrital cores of the age range 1 to age range 4 were overgrown by thermal events in the age ranges 5 and 6, meaning overgrowths giving ages in the ranges 5 and 6 are due to two collisional events. The results of this study show that the earlier thermal events in the ages of 3.4–1.7 Ga are attributed to complex metamorphic processes in the SWHC, and seem to be consistent with the crustal model by Vitanage (1972), Voll and Kleinschrodt (1991), Kröner and Jaeckel (1994), Cooray (1994), Kriegsman (1995)

and Kehelpannala (1997, 2004) and others than the recent crustal models for CHC (e.g., Sajeev et al., 2010; Santosh et al., 2014; He et al., 2016a, 2016b).

According to the results on the thermal history of the SWHC in this study and the published chronological data of the KKB in South India and Androyan Complex in Madagascar, the SWHC shows a close geochronological relationship with the KKB in South India and Androyan Complex. The synchronized studies of internal textures and geochronology of monazites are required to evaluate tectonic setting and evolution of the Gondwana amalgamation among those crustal blocks.

## REFERENCES

- Ayers, J.C., Miller, C., Gorisch, B. and Millerman, J. (1999) Textural development of monazite during high-grade metamorphism: Hydrothermal growth kinetics, with implications for U, Th-Pb geochronology. *American Mineralogist*, 84, 1766–1780.
- Bartlett, J.M., Dougherty-Page, J.S., Harris, N.B.W., Hawkesworth, C.J. and Santosh, M. (1998) The application of single zircon evaporation and Nd model ages to the interpretation of polymetamorphic terrains: an example from the Proterozoic mobile belt of south India. *Contributions to Mineralogy and Petrology*, 131, 181–195.
- Baur, A., Kröner, A., Todt, W., Liew, T.C., Williams, I.S. and Hofmann, A.W. (1991) U-Pb isotopic systematics of zircons from prograde and retrograde transition zones in high-grade orthogneisses, Sri Lanka. *The Journal of Geology*, 99, 527–545.
- Berger, A.R. and Jayasinghe, N.R. (1976) Precambrian Structure and chronology in the Highland Series of Sri Lanka. *Precambrian Research*, 3, 559–576.
- Black, L.P., Williams, I.S. and Compston, W. (1986) Four zircon ages from one rock: the history of a 3930 Ma-old granulite from Mount Sones, Enderby Land, Antarctica. *Contribution to Mineralogy and Petrology*, 94, 427–437.
- Cherniak, D.J. and Watson, E.B. (2000) Pb diffusion in zircon. *Chemical Geology*, 172, 5–24.
- Choudhary, A.K., Harris, N.B.W., Van Calsteren, P. and Hawkesworth, C.J. (1992) Pan-African charnockite formation in Kerala, South India. *Geological Magazine*, 129, 257–264.
- Cocherie, A., Legendre, O., Peucat, J.J. and Kouamelan, A.N. (1998): Geochronology of polygenetic monazites constrained by in situ electron microprobe Th-U-total lead determination: Implications for lead behavior in monazite. *Geochimica Cosmochimica Acta*, 62, 2475–2497.



- Cooray, P.G. (1994) The Precambrian of Sri Lanka: a historical review. *Precambrian Research*, 66, 3–16.
- Corfu, F., Hanchar, M.J., Hoskin, P.W.O. and Kinny, P. (2003) Atlas of Zircon Textures. *Reviews in Mineralogy and Geochemistry*, 53-1, 469–500.
- Crawford, A.R. and Oliver, R.L. (1969) The Precambrian geochronology of Ceylon. *Geological Society of Australia*, 2, 283–316.
- Dharmapriya, P.L., Malaviarachchi, S.P.K., Galli, A., Su, B., Subasinghe, N.D., Dissanayake, C.B., Nimalsiri, T.B. and Zhu, B. (2014) P–T evolution of a spinel+quartz bearing khondalite from the Highland Complex, Sri Lanka: implications for non-UHT metamorphism. *Journal of Asian Earth Sciences*, 95, 99–113.
- Dissanayake, C.B. and Chandrajith, R. (1999) Sri Lanka-Madagascar Gondwana linkage: Evidence for a Pan-African mineral belt. *The Journal of Geology*, 107, 223–235.
- Dunkl, I., Mikes, T., Simon, K. and von Eynatten, H. (2008) Brief introduction to the Windows program Pepita: data visualization, and reduction, outlier rejection, calculation of trace element ratios and concentrations from LA-ICP-MS data. In Sylvester, P., ed., *Laser Ablation ICP-MS in the Earth Sciences: Current practices and outstanding issues*. Mineralogical Association of Canada Short Course, 40, 334–340.
- Faulhber, S. and Raith, M. (1991) Geothermometry and geobarometry of highgrade rocks: a case study on garnet-pyroxene granulites in southern Sri Lanka. *Geological Magazine*, 55, 33–56.
- Ferry, J. M. and Spear, F. S. (1978) Experimental calibration of the partitioning of Fe and Mg between biotite and garnet. *Contributions to Mineralogy and Petrology*, 66, 113–117.
- Fraser, G., Ellis, D. and Eggins, S. (1997) Zirconium abundance in granulite-facies minerals, with implications for zircon geochronology in high-grade rocks. *Geology*, 25, 607–610.

- Geological Survey and Mines Bureau of Sri Lanka (1996) Geological Map of Sri Lanka  
Colombo-Ratnapura: Geological Survey Department of Sri Lanka. Scale 1:100000,  
Sheet No. 16.
- Geological Survey and Mines Bureau of Sri Lanka (2000) Geological Map of Sri Lanka  
Aluthgama-Galle: Geological Survey Department of Sri Lanka. Scale 1:100000, Sheet  
No. 19.
- Grunow, A., Hanson, R. and Wilson, T. (1996) Were aspects of Pan-African deformation  
linked to Iapetus opening? *Geology*, 24, 1063–1066.
- Harley, S.L., Kelly, N.M. and Möller, A. (2007) Zircon behavior and the thermal histories of  
mountain chains. *Elements*, 3, 25–30.
- He, X., Santosh., M., Tsunogae, T. and Malaviarachchi, S.P.K. (2016a) Early to late  
Neoproterozoic magmatism and magma mixing-mingling in Sri Lanka: Implications for  
convergent margin processes during Gondwana assembly. *Gondwana Research*, 32,  
151–180.
- He, X., Santosh., M., Tsunogae, T., Malaviarachchi, S.P.K. and Dharmapriya, P.L. (2016b)  
Neoproterozoic arc accretion along the ‘eastern suture’ in Sri Lanka during Gondwana  
assembly. *Precambrian Research*, 279, 57–80.
- Hoffman, P.F. (1999) The break-up of Rodinia, birth of Gondwana, true polar wander and  
Snowball Earth. *Journal of African Earth Sciences*, 28, 17–33.
- Hoskin, P.W.O. and Black, L.P. (2000) Metamorphic zircon formation by solid-state  
recrystallization of protolith igneous zircon. *Journal of Metamorphic Geology*, 18, 423–  
439.
- Hoskin, P.W.O. and Schaltegger, U. (2003) The composition of zircon and igneous and  
metamorphic petrogenesis. *Reviews in mineralogy and geochemistry*, 53, 27–62.

- Hözl, S., Köhler, H., Kröner, A., Jaekel, P. and Liew, T.C. (1991) Geochronology of the Sri Lankan basement. Geological Survey Department of Sri Lanka, Professional Papers, 5, 236–257.
- Hözl, S., Hofmann, A.W., Todt, W. and Köhler, H. (1994) U-Pb geochronology of the Sri Lankan basement. *Precambrian Research*, 66, 123–149.
- Jocelyn, J. and Pidgeon, R.T. (1974) Examples of twinning and parallel growth in zircon from some Precambrian granites and gneisses. *Mineralogical Magazine*, 39, 587–594.
- Kato, T., Cho, D. and Suzuki, K. (2005) Determination of interference correction factors and preparation of standard materials using “working standard” technique for CHIME dating. *Bulletin of Nagoya University Museum*, 21, 43–49.
- Katsube, A., Hayasaka, Y., Sakaguchi, A. and Takahashi, Y. (2012) U-Pb zircon dating using Nd-YAG (213 nm) Laser ablation-ICP-MS, and evaluating the consistency with SHRIMP dating. *Journal of Geological Society of Japan*, 118, 762–767.
- Katz, M. B. (1973) The Precambrian Metamorphic rocks of Ceylon: A Reply. *Geologische Rundschau*, 347–350.
- Kehelpannala, K.V.W. (1997) Deformation of a high-grade Gondwana fragment, Sri Lanka. *Gondwana Research*, 1, 47–68.
- Kehelpannala, K.V.W. (2004). Arc accretion around Sri Lanka during the assembly of Gondwana. *Gondwana Research*, 7(4S), 41–46.
- Kriegsman, L. (1993) Geodynamic evolution of the Pan-African lower crust in Sri Lanka. *Geological Ultraiectnia*, 114, 208.
- Kriegsman, L. (1995) The Pan-African events in East Antarctica: a review from Sri Lanka and the Mozambique Belt. *Precambrian Research*, 75, 263–277.

- Kröner, A., Williams, I.S., Compston, W., Baur, N., Vitanage, P.W. and Perera, L.R.K. (1987) Zircon ion microprobe dating of high-grade rocks in Sri Lanka. *The Journal of Geology*, 95, 775–791.
- Kröner, A., Cooray, P.G. and Vitanage, P.W. (1991) Lithotectonic subdivision of the Precambrian basement in Sri Lanka. In: A. Kröner (Editor), *The Crystalline Crust of Sri Lanka, Part I. Summary of Research of the German-Sri Lankan Consortium*. Geological Survey Department, Sri Lanka, Professional Papers, 5, 5–21.
- Kröner, A. and Jaeckel, P. (1994) Zircon ages from the Wannai Complex, Sri Lanka. *Journal of Geological Society of Sri Lanka*, 5, 4–57.
- Kröner, A., Jaeckel, P. and Williams, I.S. (1994) Pb-loss patterns in zircons from a high-grade metamorphic terrain as revealed by different dating methods; U-Pb and Pb-Pb ages for igneous and metamorphic zircons from northern Sri Lanka. *Precambrian Research*, 66, 151–181.
- Kröner, A., Kehelpannala, K.V.W. and Hegner, E. (2003) Ca. 750-1100 Ma magmatic events and Grenville-age deformation in Sri Lanka: relevance for Rodinia supercontinent formation and dispersal, and Gondwana. *Journal of Asian Earth Sciences*, 22, 279–300.
- Kröner, A., Rojas-Agramonte, Y., Kehelpannala, K.V.W., Zack, T., Hegner, E., Geng, H.Y., Wong, J. and Barth, M. (2013) Age, Nd–Hf isotopes, and geochemistry of the Vijayan Complex of eastern and southern Sri Lanka: a Grenville-age magmatic arc of unknown derivation. *Precambrian Research*, 234, 288–321.
- Ludwig, K.R. (2008) User's manual for isoplot 3.70. *A Geochronological Toolkit for Microsoft Excel*. Berkeley Geochronology Center Special Publication, 4, 76.
- Mathavan, V., Prame, W.K.B.N. and Cooray, P.G. (1999) Geology of the high grade Proterozoic terrains of Sri Lanka and the assembly of Gondwana: an update on recent developments. *Gondwana Research*, 2, 237–250.

- Mathavan, V. and Fernando, G.W.A.R. (2001) Reactions and textures in grossular–wollastonite–scapolite calc-silicate granulites from Maligawila, Sri Lanka. *Lithos*, 59, 217–232.
- Malaviarachchi, S.P.K. and Takasu, A. (2011) Electron microprobe dating of Monazites from Sri Lanka: implications on multiple thermal events related to Gondwana. *Journal of the Geological Society of Sri Lanka*, 14, 81–90.
- Milisenda, C.C., Liew, T.C., Hofmann, A.W. and Kröner, A. (1988) Isotopic mapping of age provinces in Precambrian high-grade terrains, Sri Lanka. *The Journal of Geology*, 96, 608–615.
- Milisenda, C.C., Liew, T.C., Hofmann, A.W. and Kröner, A. (1994) Nd isotopic mapping of the Sri Lanka basement; update and additional constraints from Sr isotopes. *Precambrian Research*, 66, 95–110.
- Montel, J.M., Foret, S., Veschambre, M., Nicollet, C. and Provost, A. (1996) Electron microprobe dating of monazite. *Chemical Geology*, 131, 37–53.
- Pan, Y. (1997) Zircon- and monazite-forming metamorphic reactions at Manitouwadge, Ontario. *Canadian Mineralogist*, 35, 105–118.
- Paquette, J.L., Nedelec, A., Moine, B. and Rakotondrazafy, M. (1994) U–Pb, single zircon Pb-evaporation, and Sm–Nd isotopic study of a granulite domain in SE Madagascar. *The Journal of Geology*, 102 (5), 523–538.
- Parrish, R.R. (1990) U–Pb dating of monazite and its application to geological problems. *Canadian Journal of Earth Sciences*, 27, 1431–1450.
- Perchuk, L. L. and Lavrenteva, I. V. (1983) Experimental investigation of exchange equilibria in the system cordierite-garnet-biotite. *Advance in physical geochemistry*, 3, 199–239.

- Perera L. R. K. (1984) Co-existing Almandine – A Key to the Metamorphic History of Sri Lanka. *Precambrian Research*, 25, 349–364.
- Perera, L.R.K. (1987) Petrogenesis of granulite-facies metamorphic rocks in Sri Lanka. Unpublished M.Phil thesis, University of Peradeniya, 124.
- Perera, L.R.K. (1994) P-T-t path vs. isotopic ages in correlations, anti-correlations and pseudo-correlations of regional metamorphic terrains: A case study from Sri Lanka. *Journal of the Geological Society of Sri Lanka*, 5, 27–40.
- Pidgeon, R.T. (1992) Recrystallisation of oscillatory zoned zircon: some geochronological and petrological implications. *Contributions to Mineralogy and Petrology*, 110, 463–472.
- Pidgeon, R.T., Nemchin, A.A. and Hitchen, G.J. (1998) Internal structures of zircons from Archaean granites from the Darling Range batholiths: implications for zircon stability and the interpretation of zircon U-Pb ages. *Contributions to Mineralogy and Petrology*, 132, 288–299.
- Pyle, J.M. (2001) Distribution of select trace elements in pelitic metamorphic rocks: pressure, temperature, mineral assemblage, and reaction-history controls. Ph.D. dissertation, Rensselaer Polytechnic Institute.
- Pyle, J.M., Spear, F.S., Wark, D.A., Daniel, C.G. and Storm, L.C. (2005) Contributions to precision and accuracy of monazite microprobe ages. *American Mineralogist*, 90, 547–577.
- Reed, S.J.B. and Buckley, A. (1996) Virtual WDS. *Mikrochim. Acta [Suppl.]*, 13, 479–483.
- Roberts M.P. and Finger F. (1997) Do U-Pb zircon ages from granulite reflect peak metamorphic conditions? *Geology*, 25, 319–322.

- Sajeev, K., Osanai, Y., Suzuki, S. and Kagami, H. (2003) Geochronological evidence for multistage-metamorphic events in ultrahigh-temperature granulites from Central Highland Complex, Sri Lanka. *Polar Geoscience*, 16, 137–148.
- Sajeev, K. and Osanai, Y. (2005) Thermal gradients in the Sri Lankan granulite terrane: a garnet-biotite thermometric approach. *Journal of Metamorphic Geology*, 23, 383–397.
- Sajeev, K., Osanai, Y., Connolly, J.A.D., Suzuki, S., Ishioka, J., Kagami, H. and Rino, S. (2007) Extreme crustal metamorphism during a Neoproterozoic event in Sri Lanka: a study of dry mafic granulites. *The Journal of Geology*, 115, 563–582.
- Sajeev, K., Williams, I.S. and Osanai, Y. (2010) Sensitive high-resolution ion microprobe U–Pb dating of prograde and retrograde ultrahigh-temperature metamorphism as exemplified by Sri Lankan granulites. *Geology*, 38, 971–974.
- Santosh, M., Collins, A. S., Morimoto, T. and Yokoyama, K. (2005) Depositional constraints and age of metamorphism in southern India: U-Pb chemical (EPMA) and isotopic (SIMS) ages from the Trivandrum Block. *Geological Magazine*, 142, 255–268.
- Santosh, M., Tsunogae, T., Malaviarachchi, S.P.K., Zhang, Z., Ding, H., Tang, L. and Dharmapriya, P.L. (2014) Neoproterozoic crustal evolution in Sri Lanka: Insights from petrologic, geochemical and zircon U-Pb and Lu-Hf isotopic data and implications for Gondwana assembly. *Precambrian Research*, 255, 1–29.
- Sawyer, E.W. (2001) Melt segregation in the continental crust: distribution and movement of melt in anatectic rocks. *Journal of Metamorphic Geology*, 18, 291–309.

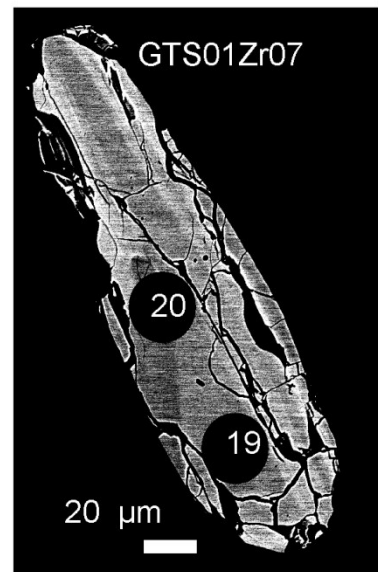
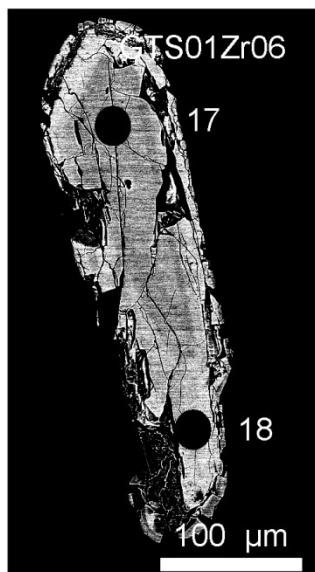
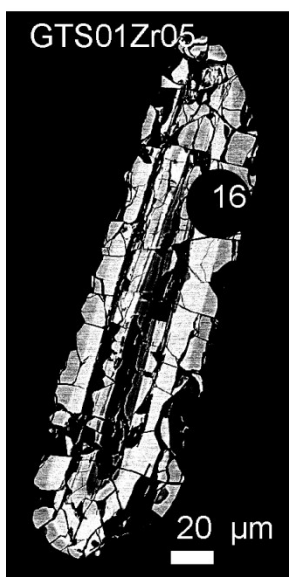
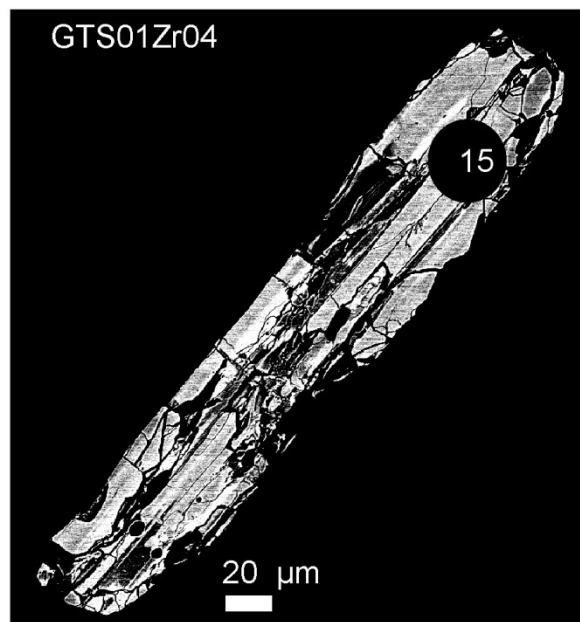
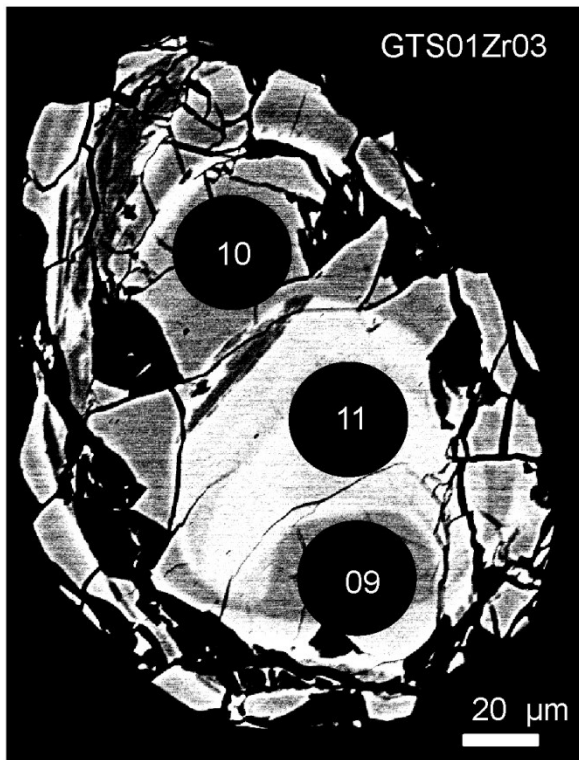
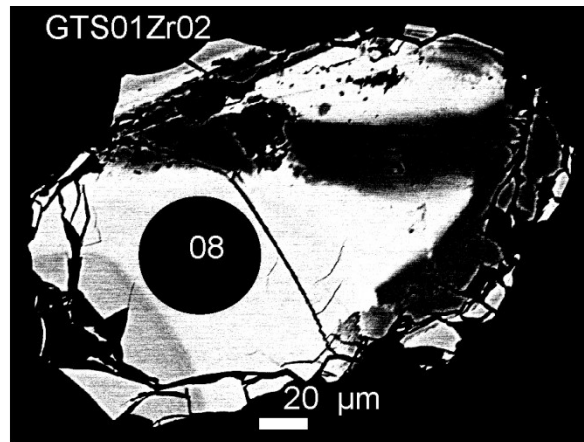
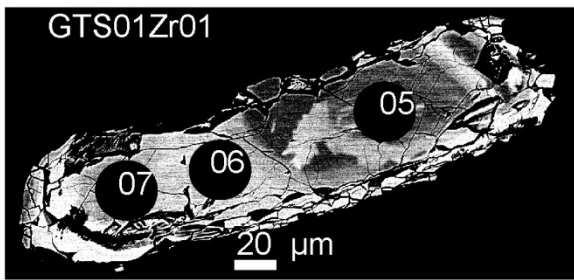
- Scherrer, N.C., Engi, M., Gnos, E., Jakob, V. and Liechti A. (2000) Monazite analysis; from sample preparation to microprobe age dating and REE quantification. *Schweizerische Mineralogische und Petrographische Mitteilungen (Swiss Bulletin of Mineralogy and Petrology)*, 80, 93–105.
- Suzuki, K. and Adachi, M. (1991) Precambrian provenance and Silurian metamorphism of the Tsubonosawa paragneiss in the South Kitakami terrane, northeast Japan, revealed by the chemical Th-U-total Pb isochron ages of monazite, zircon, and xenotime. *Geochemical Journal*, 25, 357–376.
- Suzuki, K., Adachi M. and Tanaka T. (1991) Middle Precambrian provenance of Jurassic sandstone in the Mino terrane, central Japan: evidence from an electron microprobe Th-U total Pb monazite study. *Sedimentary Geology*, 75, 141–147.
- Takamura, Y., Tsunogae, T., Santosh, M., Malaviarachchi, S.P.K. and Tsutsumi, Y. (2015) Petrology and zircon U-Pb geochronology of metagabbro from the Highland Complex, Sri Lanka: Implications for the correlation of Gondwana suture zones. *Journal of Asian Earth Sciences*, 113, 826–841.
- Thompson, A.B. (1979) Mineral reactions in pelitic rocks: II. calculation of some P-T-X (Fe-Mg) phase relations. *American Journal of Science*, 26, 849–872.
- Unnikrishnan-Warrier, C. (1997) Isotopic signature of Pan-African rejuvenation in the Kerala Khondalite Belt, southern India: implications for East Gondwana reassembly. *Journal of the Geological Society of India*, 50, 179–190.
- Unnikrishnan-Warrier, C., Santosh, M. and Yoshida, M. (1995) First report of Pan-African Sm-Nd and Rb-Sr mineral ages from regional charnockites of southern India. *Geological Magazine*, 132, 253–260.
- Vavra, G., Gebauer, D., Schmid, R. and Compston, W. (1996) Multiple zircon growth and recrystallization during polyphase Late Carboniferous to Triassic metamorphism in

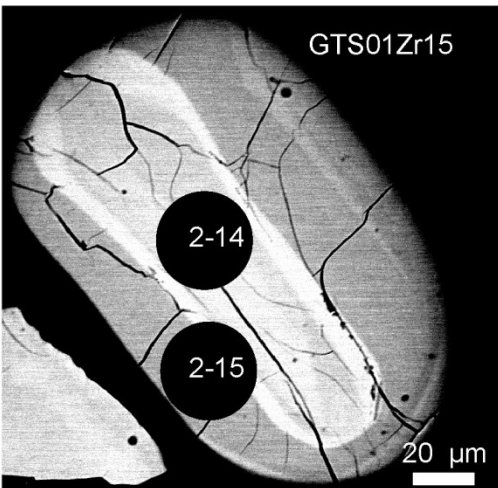
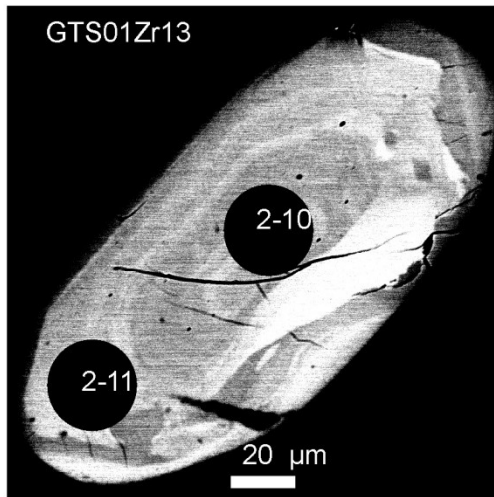
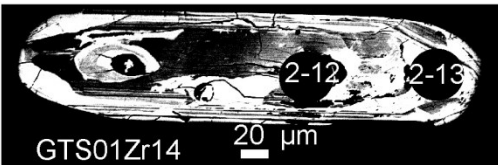
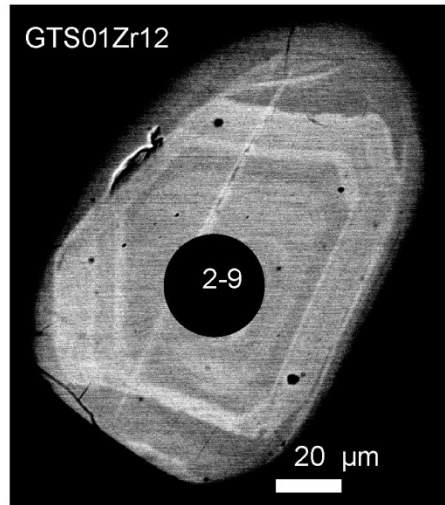
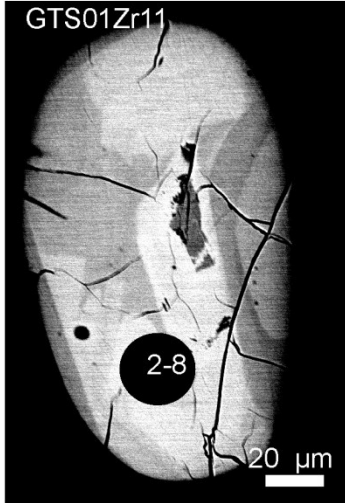
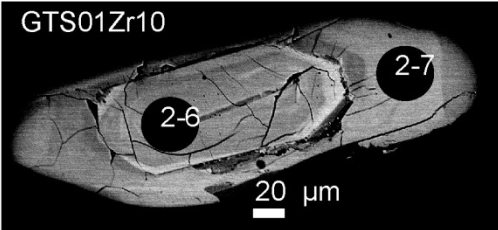
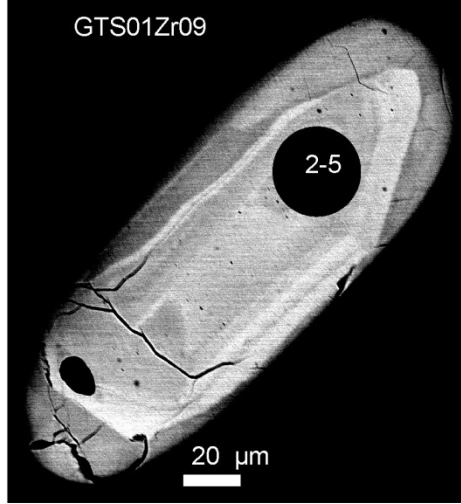
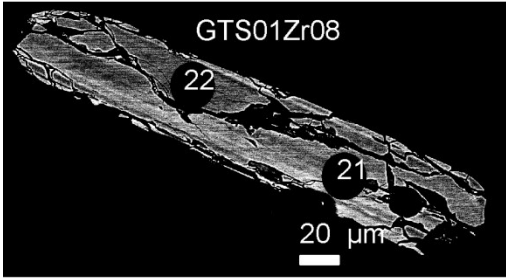


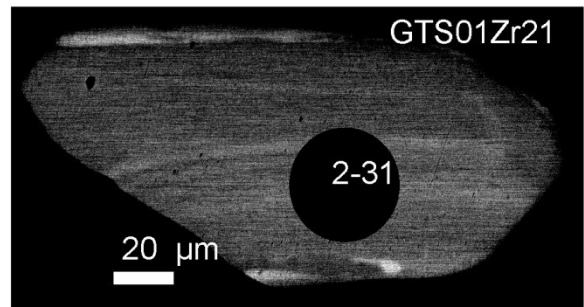
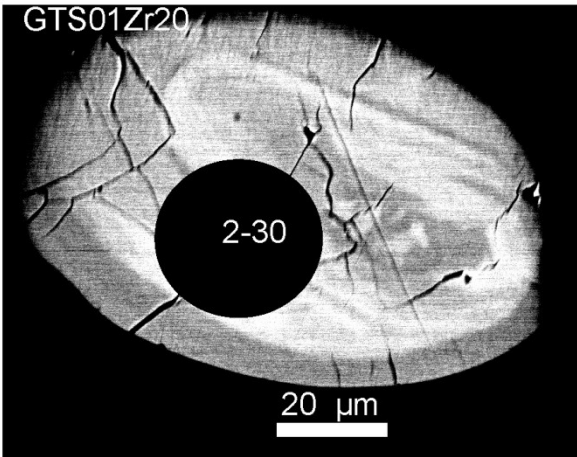
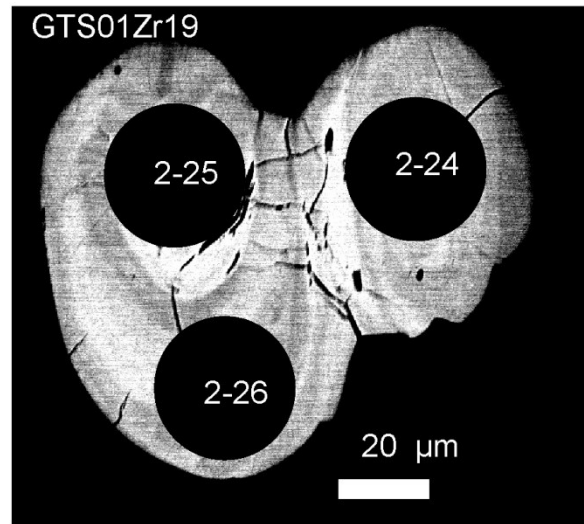
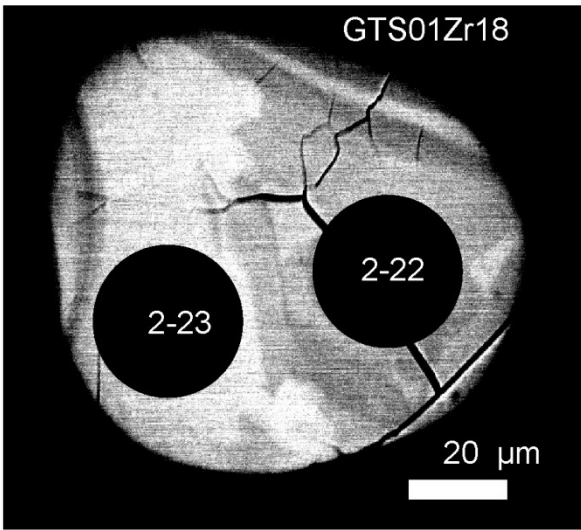
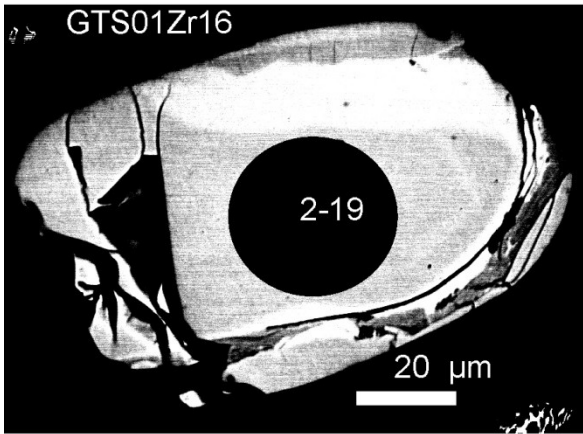
- granulites of the Ivrea Zone (Southern Alps): An ion microprobe (SHRIMP) study. *Contributions to Mineral Petrology*, 33, 247–255.
- Vitanage, P.W. (1972) Post-Precambrian uplift and regional neotectonic movements in Ceylon. 24th International Geological Congress. Montreal, Section 3, 642–654.
- Vitanage, P.W. (1985) Tectonics and mineralization in Sri Lanka. *Bulletin of the Geological Society of Finland*, 57, 157–168.
- Voll, G. and Kleinschrodt, R. (1991) Sri Lanka: Structural, magmatic and metamorphic development of a Gondwana fragment. Geological Survey Department, Sri Lanka, Professional Paper 5, 22–52.
- Williams, I.S., Buick, I.S. and Cartwright, I. (1996) An extended episode of early Mesoproterozoic fluid flow in the Reynolds Range, central Australia. *Journal of Metamorphic Geology*, 14, 29–47.

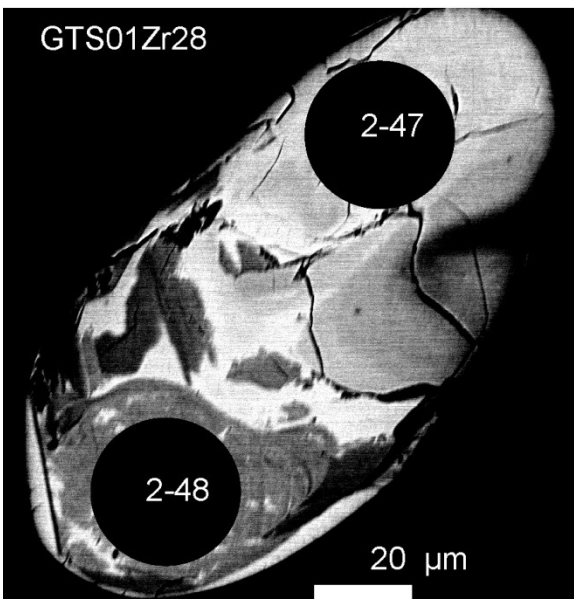
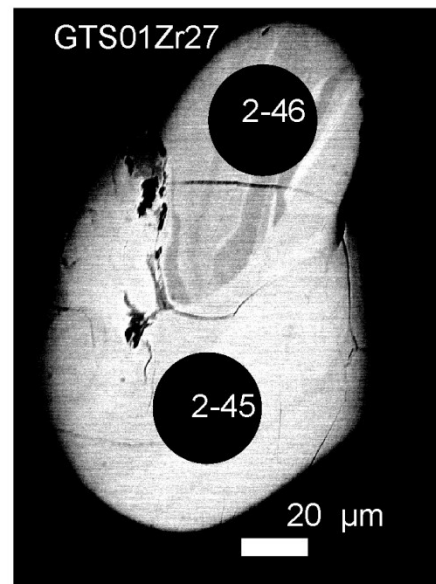
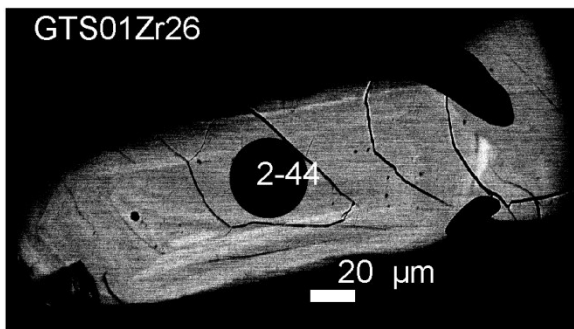
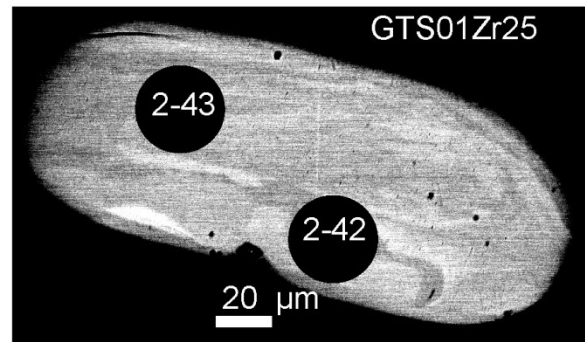
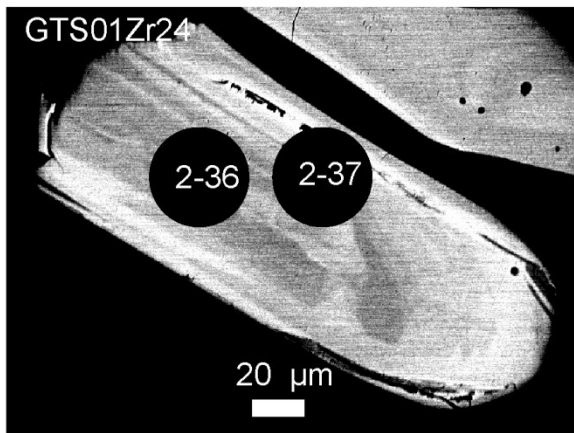
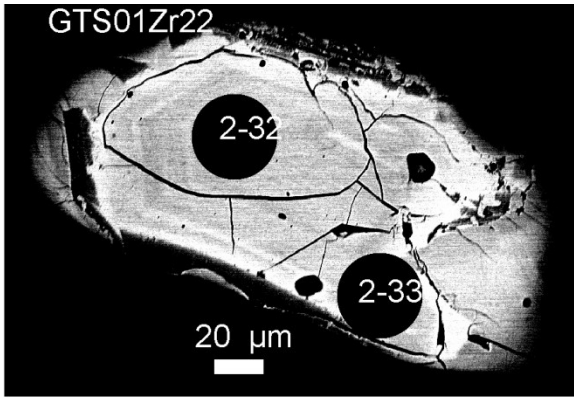
APPENDICES

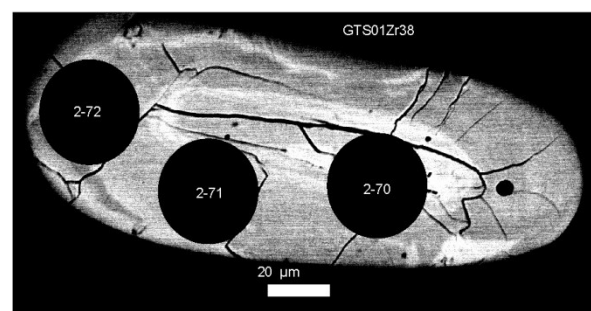
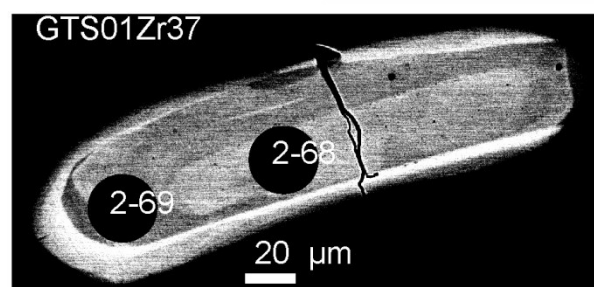
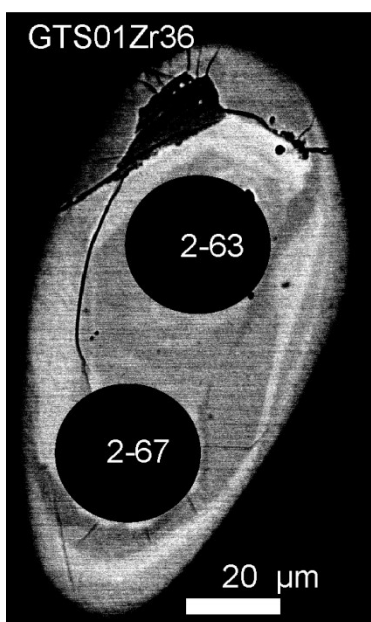
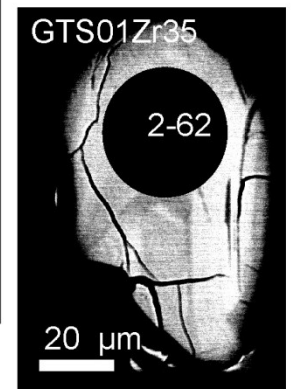
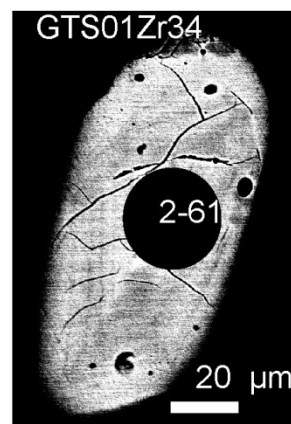
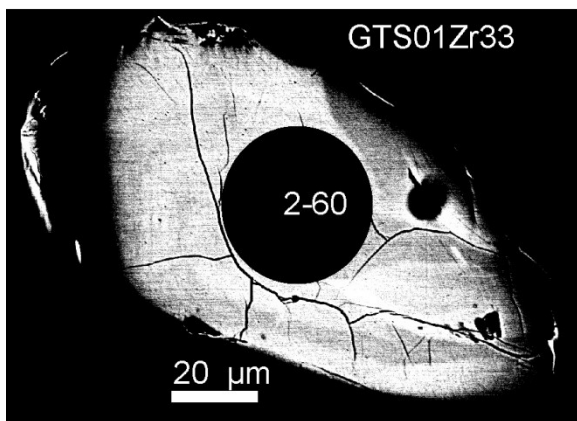
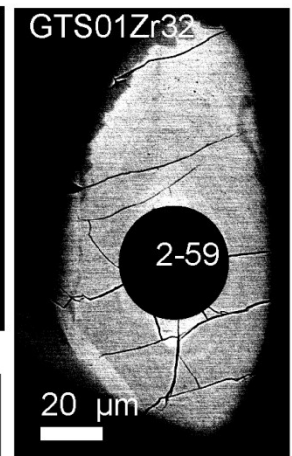
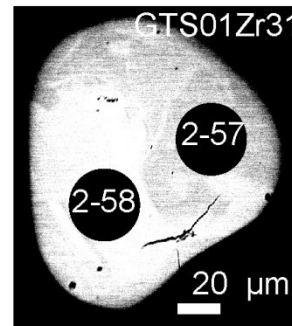
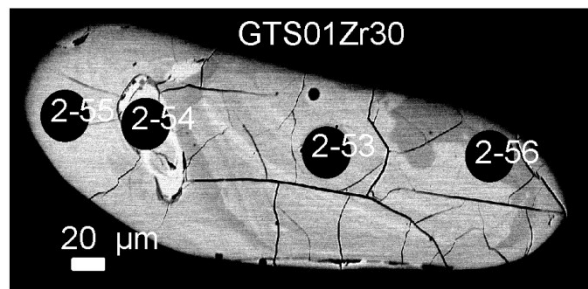
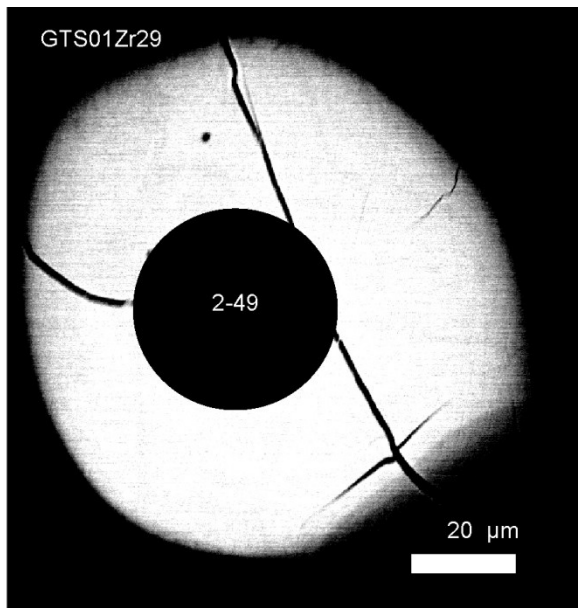
APPENDIX 01 (Zircon from 17-24GB)

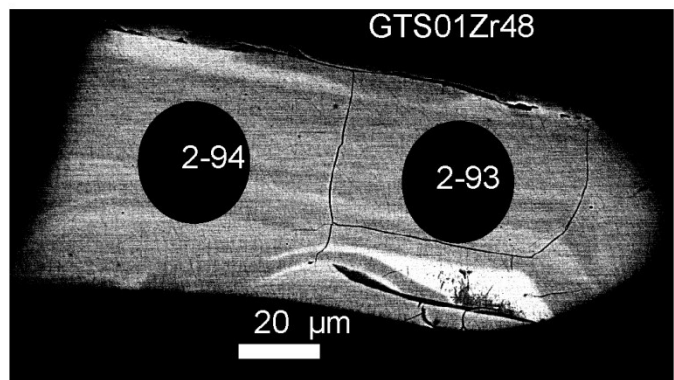
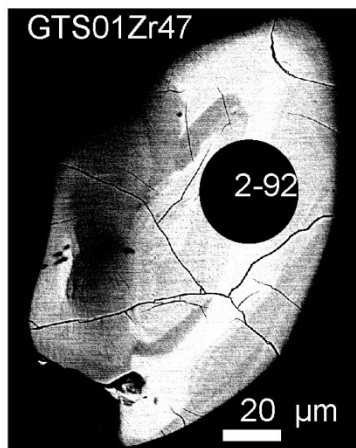
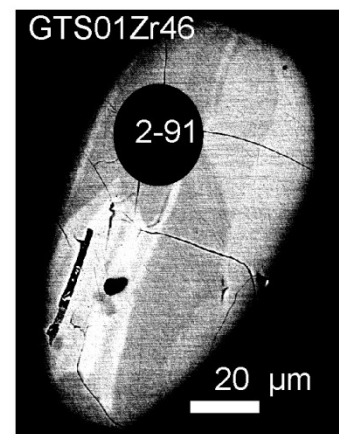
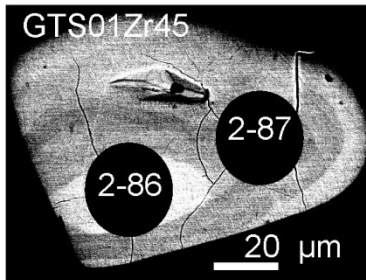
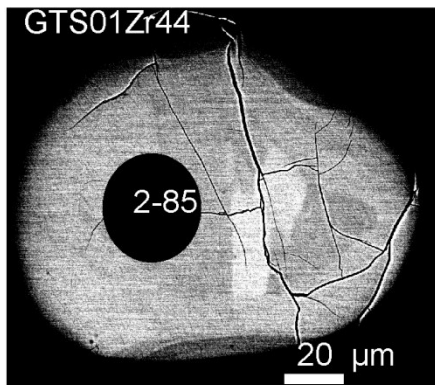
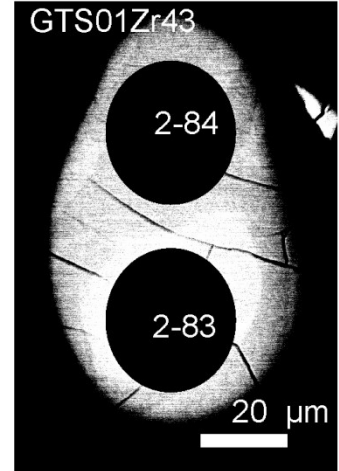
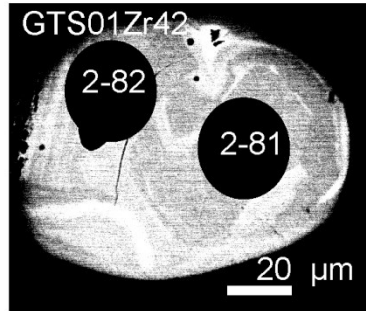
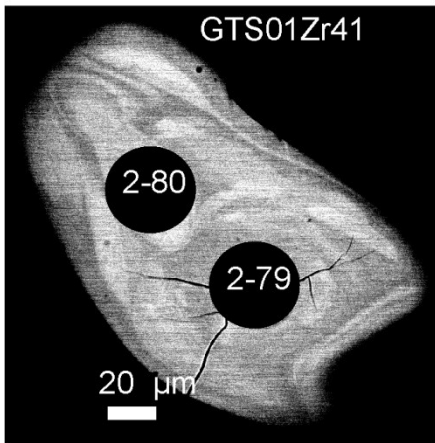
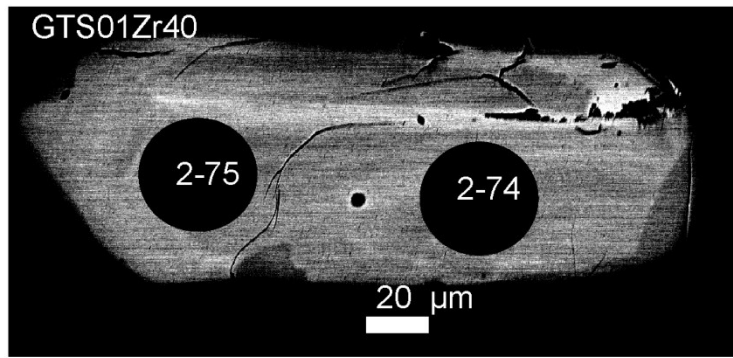
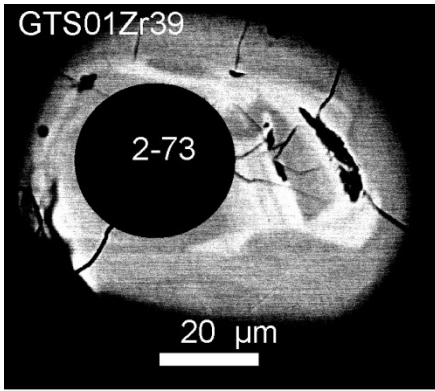




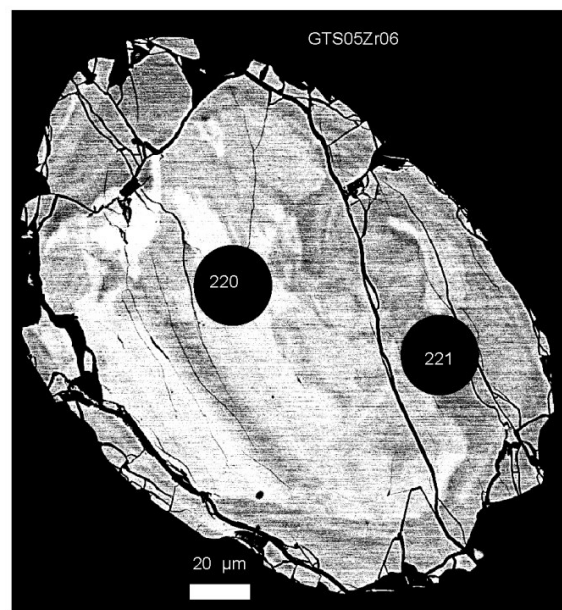
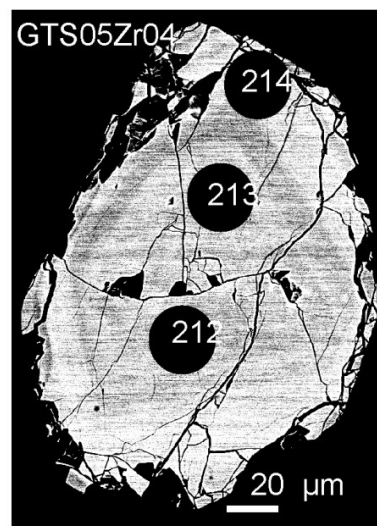
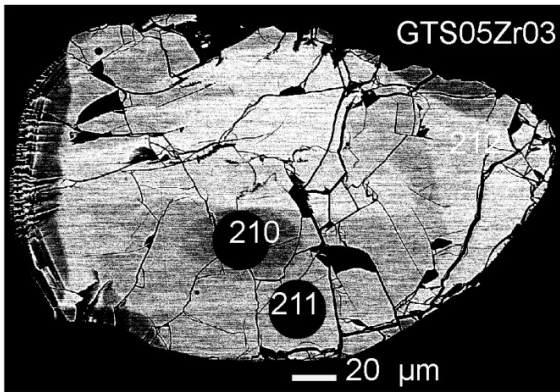
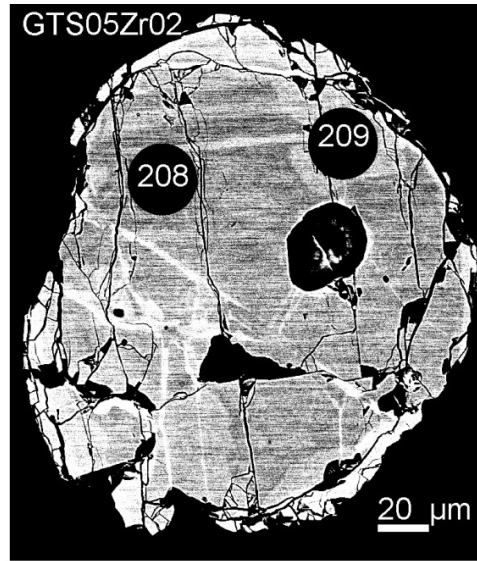
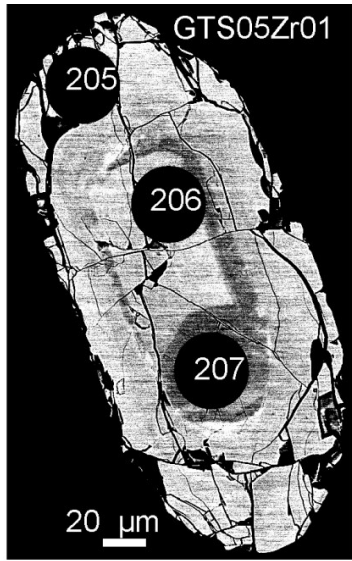




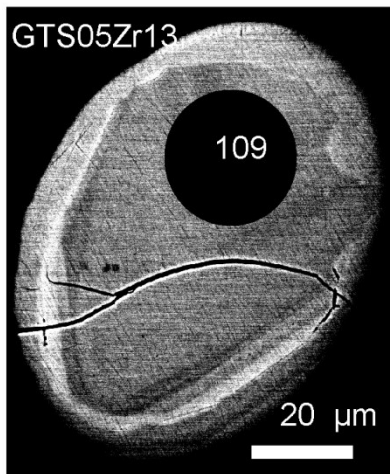
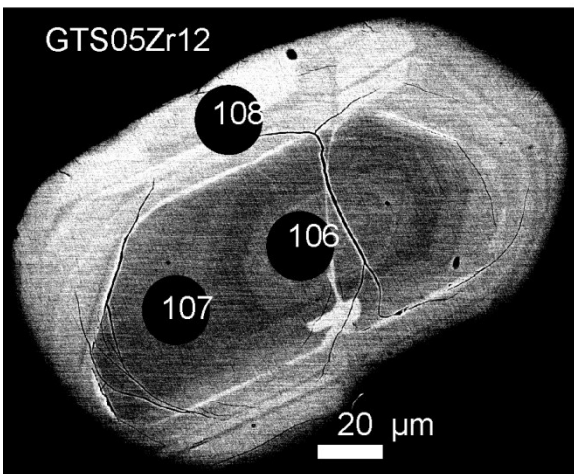
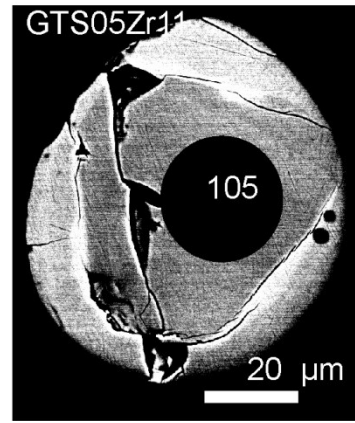
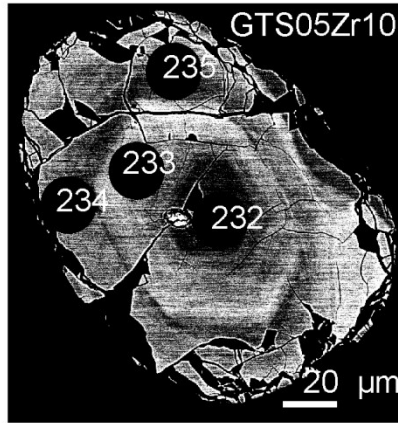
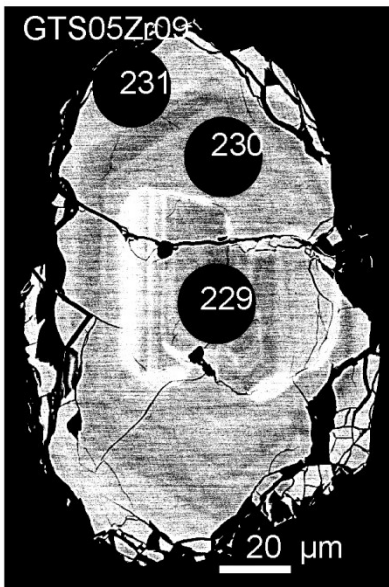
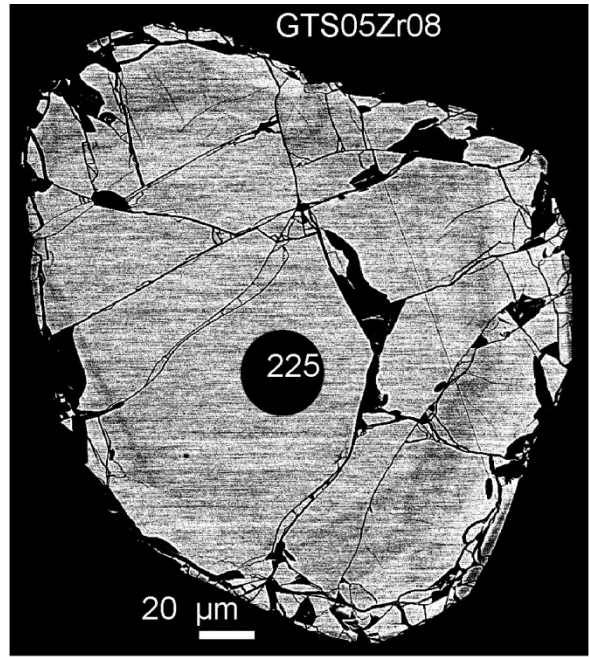
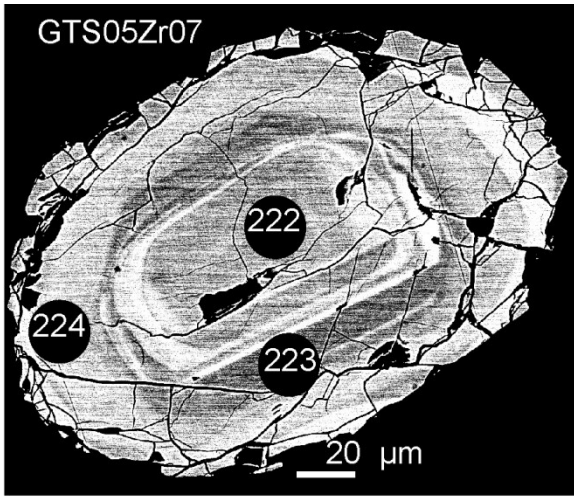


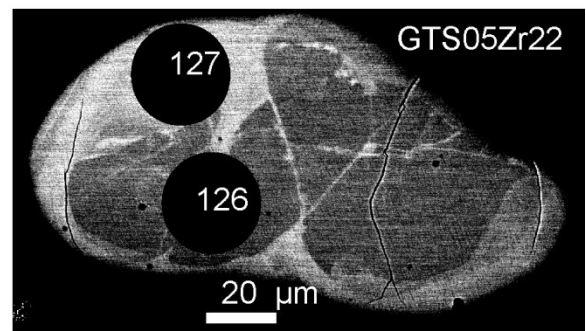
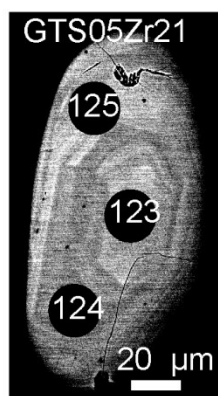
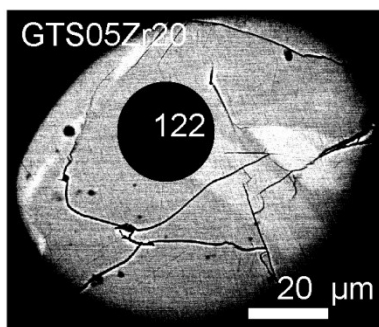
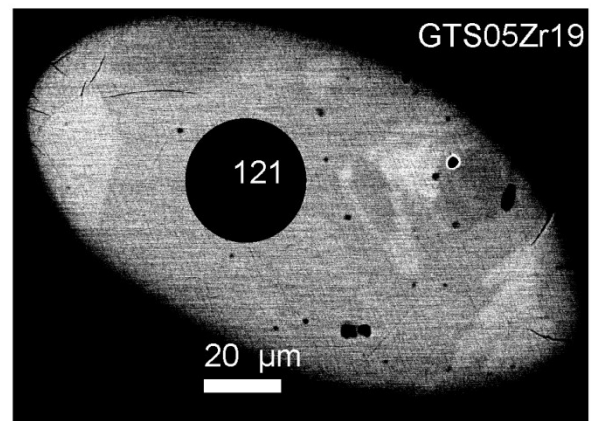
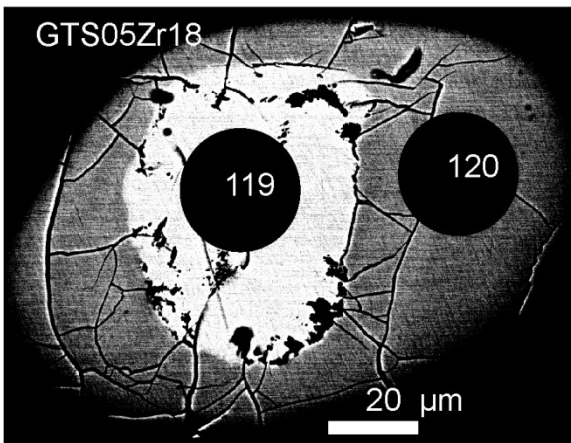
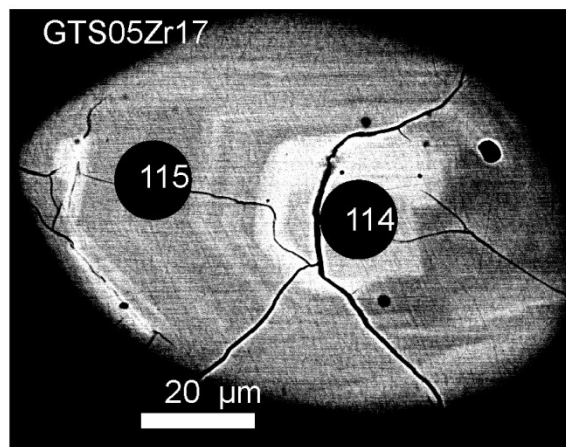
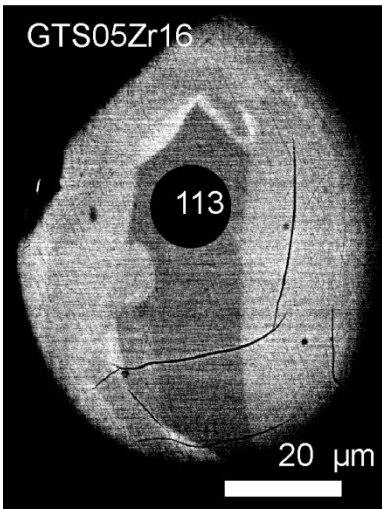
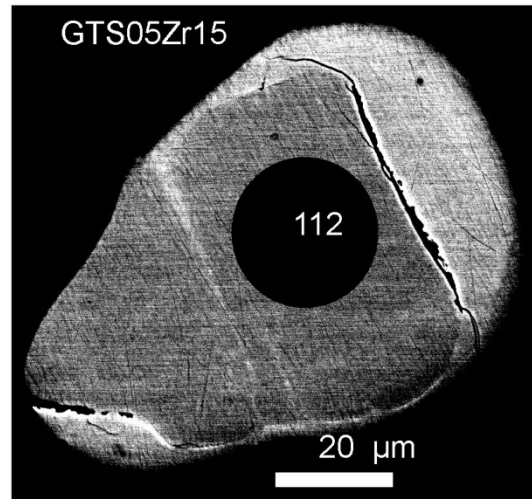
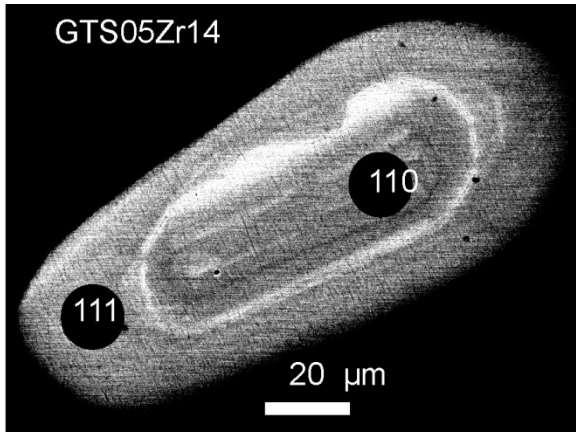


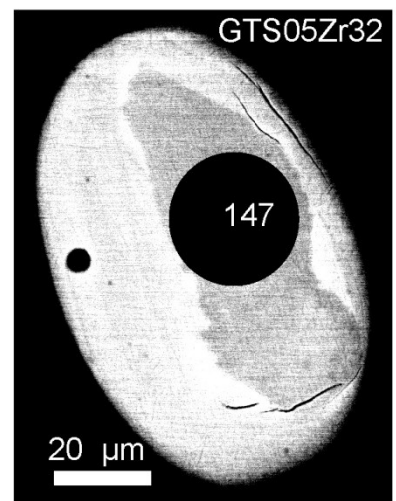
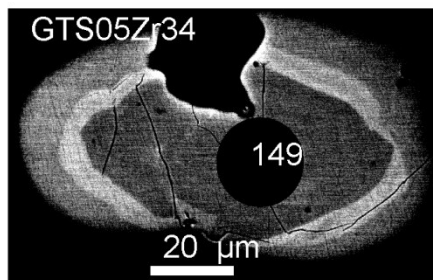
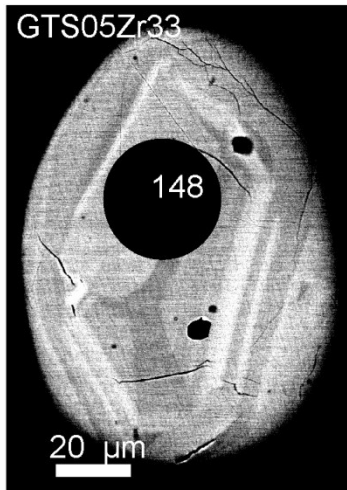
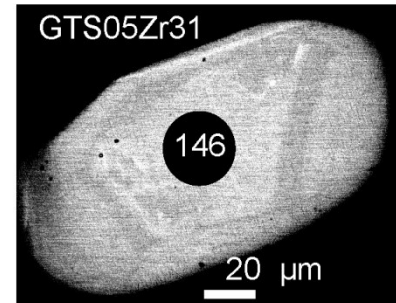
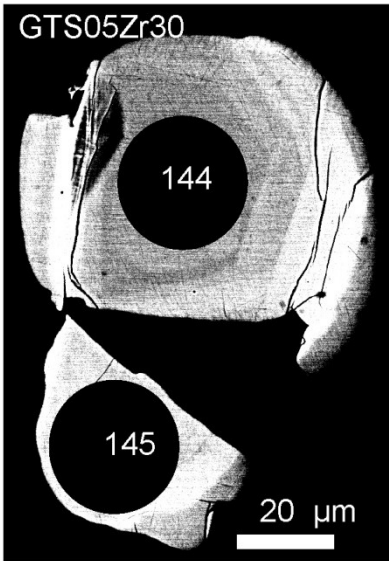
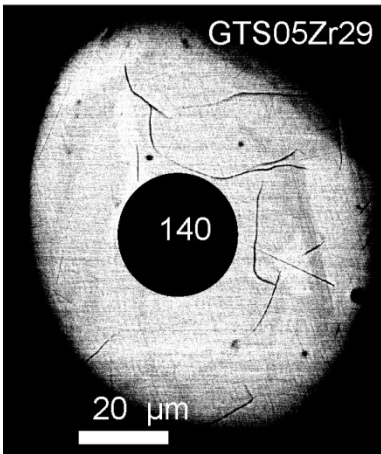
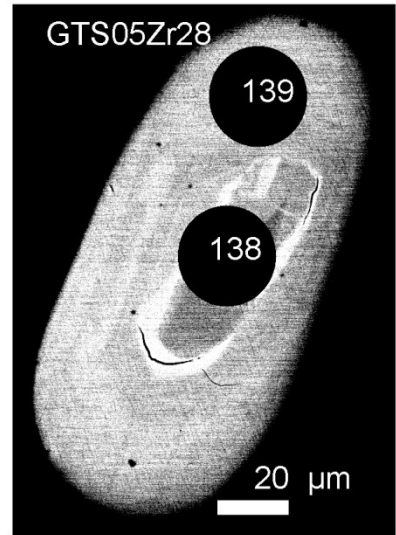
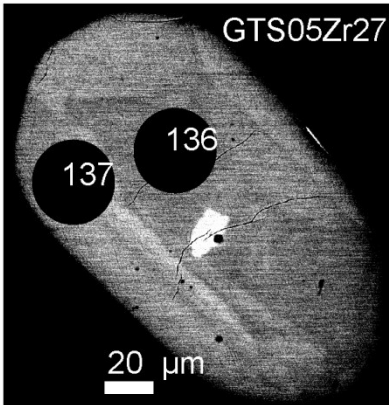
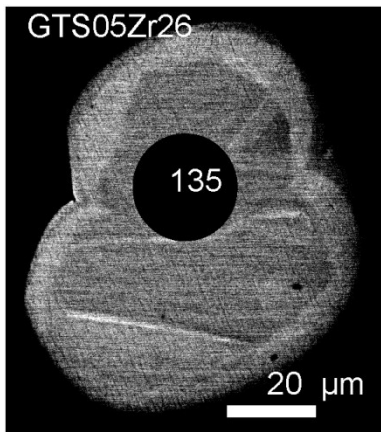
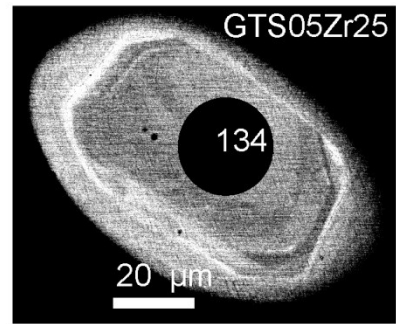
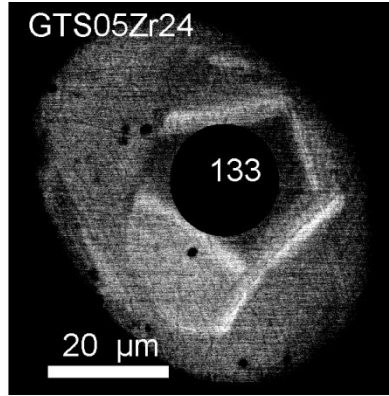
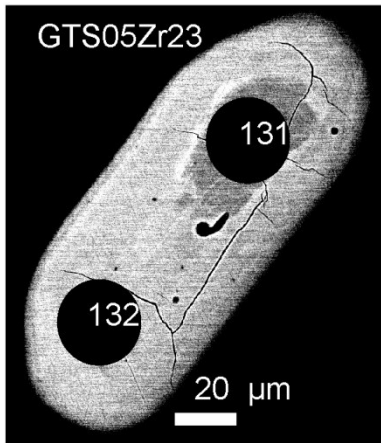
APPENDIX 02 (Zircon from 07-10GB)

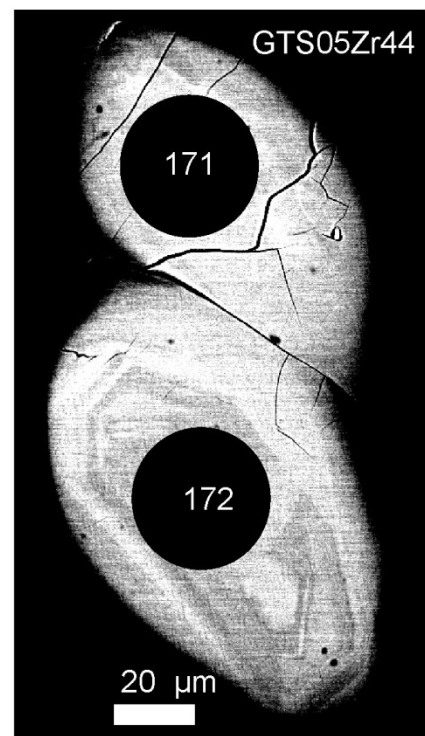
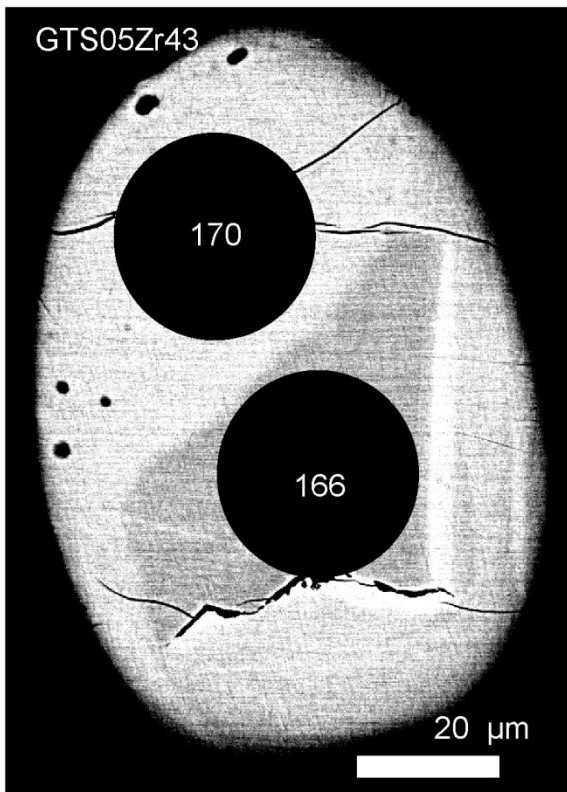
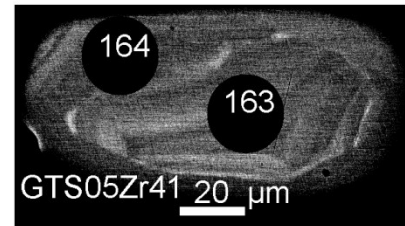
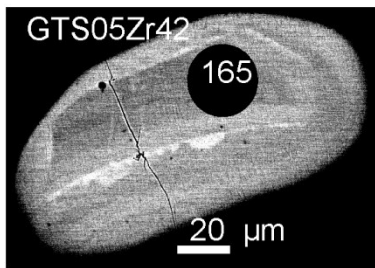
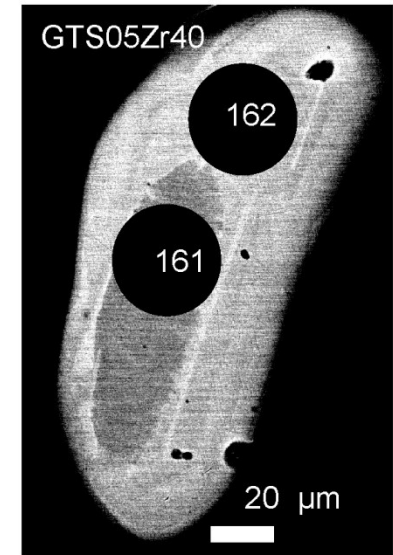
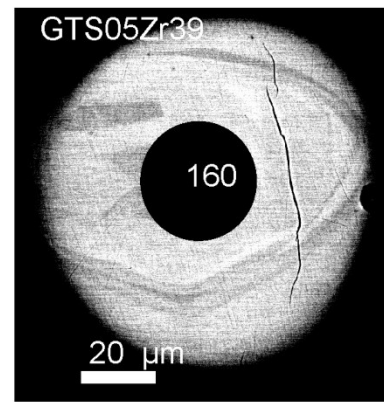
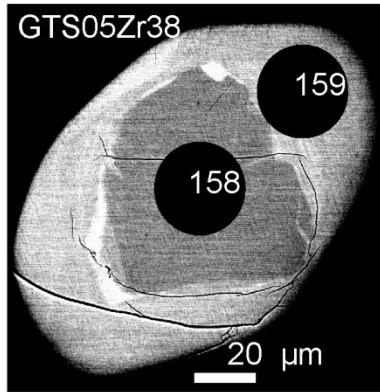
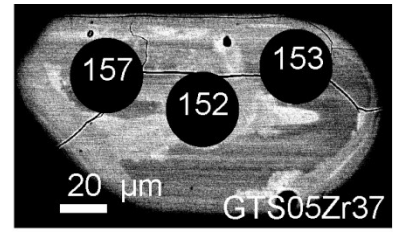
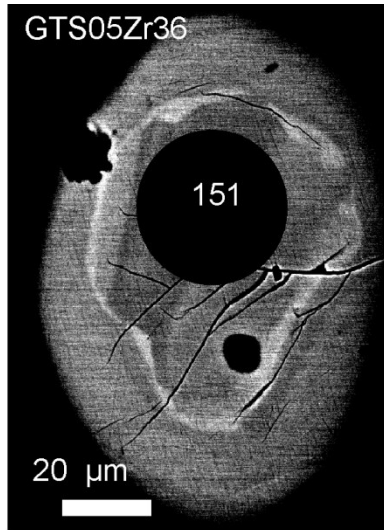
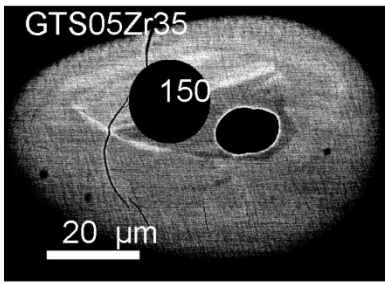


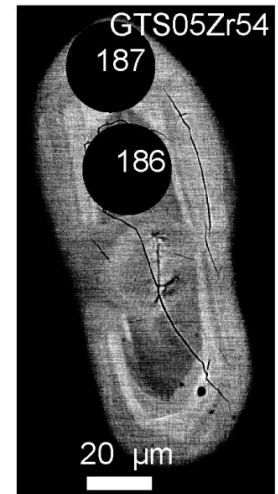
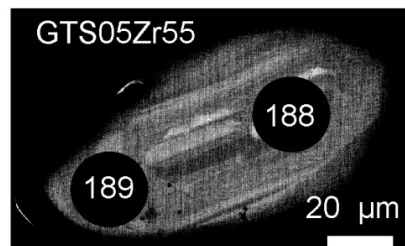
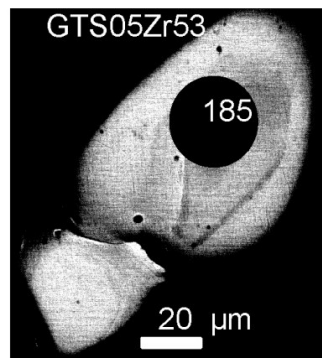
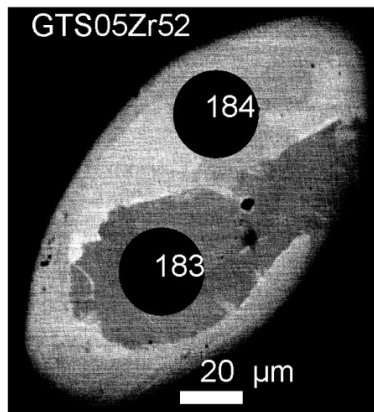
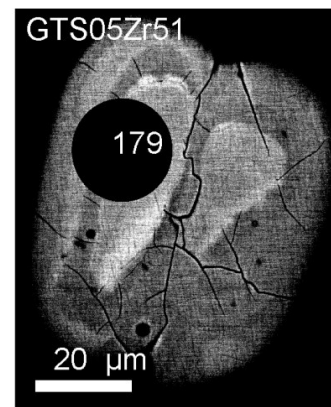
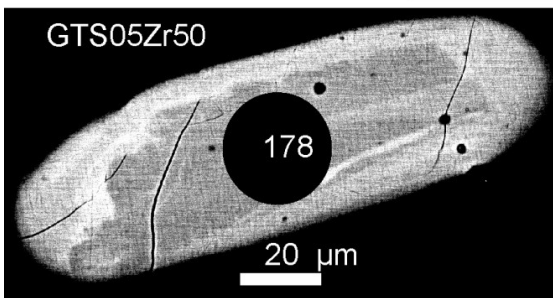
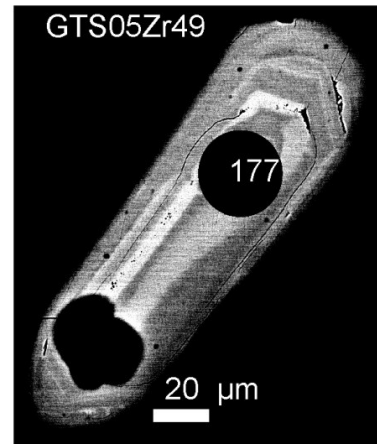
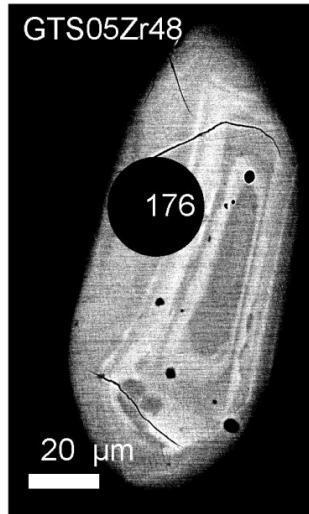
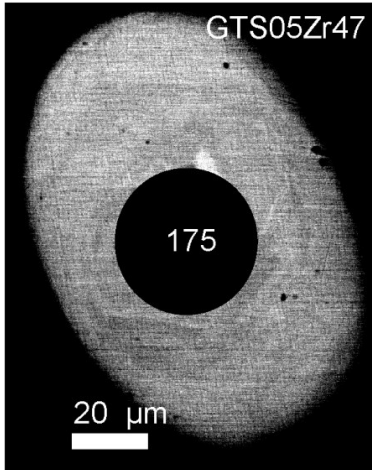
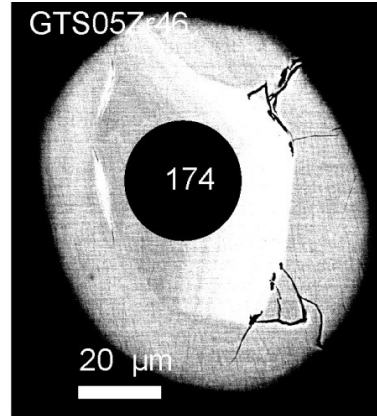
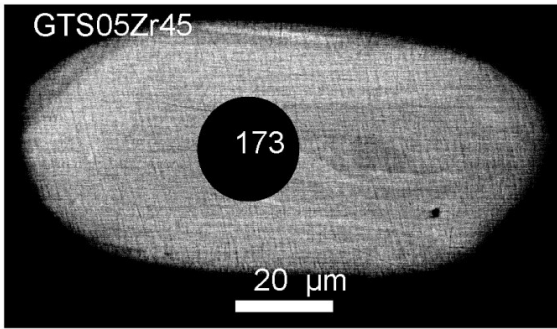












## APPENDIX 03

Table 1. U, Th, and Pb compositions of the grain in Figure 19a.

D1	ThO <sub>2</sub>	Th count error %	UO <sub>2</sub>	U count error %	PbO	Pb count error %	Age (Ma)	Age error Ma	ThO <sub>2</sub> *
1	8.785	0.15	0.685	0.94	0.229	1.25	488	7.7	11.049
2	8.739	0.15	0.670	0.95	0.233	1.23	500	7.8	10.954
3	8.769	0.15	0.651	0.97	0.221	1.28	477	7.7	10.921
4	9.052	0.15	0.619	1.01	0.237	1.21	502	7.9	11.098
5	9.015	0.15	0.608	1.03	0.230	1.24	491	7.9	11.025
6	8.683	0.15	0.661	0.96	0.233	1.22	504	7.9	10.868
7	8.727	0.15	0.661	0.96	0.221	1.28	477	7.7	10.912
8	9.042	0.15	0.654	0.97	0.232	1.23	487	7.7	11.204
9	8.765	0.15	0.604	1.03	0.222	1.28	486	8.0	10.761
10	8.931	0.15	0.638	0.99	0.240	1.19	511	7.9	11.040
11	9.037	0.15	0.639	0.98	0.236	1.21	498	7.8	11.149
12	8.936	0.15	0.657	0.96	0.236	1.21	500	7.8	11.108
13	8.929	0.15	0.686	0.94	0.246	1.17	517	7.8	11.196
14	8.982	0.15	0.771	0.85	0.239	1.20	488	7.2	11.530
15	8.942	0.15	0.769	0.86	0.247	1.17	506	7.4	11.484
16	8.814	0.15	0.815	0.82	0.251	1.15	513	7.3	11.508
17	8.669	0.15	0.789	0.84	0.242	1.19	505	7.4	11.277
18	8.519	0.15	0.900	0.76	0.249	1.16	510	7.1	11.494
19	8.541	0.15	1.033	0.68	0.259	1.12	510	6.7	11.955
20	8.476	0.15	1.025	0.69	0.262	1.12	519	6.9	11.864
21	7.670	0.16	0.886	0.77	0.235	1.22	521	7.6	10.598
22	7.704	0.16	0.910	0.75	0.231	1.24	507	7.4	10.712
23	8.450	0.15	0.573	1.07	0.222	1.27	505	8.4	10.344
24	7.814	0.16	0.949	0.73	0.240	1.21	515	7.3	10.951
25	8.439	0.15	1.009	0.70	0.252	1.16	504	6.9	11.774
26	8.365	0.16	1.093	0.66	0.265	1.11	520	6.8	11.978
D2									
1	8.590	0.15	0.223	2.20	0.184	1.50	465	12.4	9.325
2	9.577	0.14	0.122	3.24	0.189	1.45	446	15.8	9.979
3	9.929	0.14	0.095	3.70	0.208	1.34	478	18.8	10.242
4	9.443	0.15	0.179	2.53	0.199	1.39	467	13.5	10.033
5	9.580	0.14	0.148	2.86	0.195	1.41	456	14.6	10.067
6	8.780	0.15	0.229	2.16	0.181	1.51	447	11.8	9.534
7	9.563	0.14	0.268	1.89	0.198	1.39	447	10.5	10.446
8	9.580	0.14	0.109	3.49	0.197	1.40	467	17.6	9.939
9	9.596	0.14	0.046	5.35	0.191	1.44	461	25.5	9.748
10	9.519	0.15	0.099	3.70	0.187	1.47	447	17.8	9.845
11	9.542	0.14	0.100	3.67	0.191	1.44	456	18.0	9.871
12	9.479	0.15	0.113	3.42	0.193	1.43	461	17.1	9.851
13	10.041	0.14	0.091	3.79	0.200	1.38	456	18.4	10.341

The error propagation is determined by the mean square of U, Th, and Pb X-ray counting errors (%)

Table 2. U, Th, and Pb compositions of the grain in Figure 19b.

D1	ThO <sub>2</sub>	Th count		U count		Pb count		Age	Age error	ThO <sub>2</sub> *
		error %	UO <sub>2</sub>	error %	PbO	error %	(Ma)	Ma		
1	8.344	0.22	0.909	0.75	0.259	1.12	536	7.3	11.356	
2	8.422	0.22	0.924	0.74	0.254	1.13	520	7.1	11.483	
3	8.506	0.22	0.877	0.77	0.254	1.13	523	7.2	11.412	
4	8.592	0.22	0.932	0.73	0.269	1.08	541	7.2	11.680	
5	8.374	0.22	0.902	0.75	0.254	1.13	526	7.2	11.362	
6	8.526	0.22	0.913	0.75	0.267	1.09	543	7.3	11.551	
7	8.413	0.22	0.908	0.75	0.257	1.12	529	7.2	11.421	
8	8.556	0.22	0.919	0.74	0.263	1.10	533	7.2	11.601	
9	8.579	0.22	0.912	0.75	0.264	1.10	535	7.2	11.601	
10	8.536	0.22	0.873	0.77	0.260	1.11	535	7.3	11.428	
11	8.512	0.22	0.912	0.75	0.265	1.10	540	7.3	11.534	
12	8.427	0.22	0.890	0.76	0.257	1.12	531	7.3	11.376	
13	8.389	0.22	0.887	0.77	0.260	1.11	539	7.4	11.328	
14	8.207	0.22	0.847	0.79	0.249	1.15	532	7.5	11.013	
15	8.118	0.22	0.865	0.78	0.252	1.14	539	7.5	10.984	
16	8.088	0.22	0.851	0.79	0.244	1.17	526	7.5	10.907	
17	8.100	0.22	0.851	0.79	0.251	1.15	540	7.6	10.919	
18	8.129	0.22	0.825	0.81	0.251	1.15	543	7.7	10.862	
19	8.068	0.22	0.850	0.79	0.245	1.16	529	7.5	10.884	
20	8.068	0.22	0.813	0.82	0.242	1.18	529	7.7	10.762	
21	10.017	0.20	0.190	2.37	0.236	1.20	521	13.9	10.646	
D2										
1	9.605	0.20	0.963	0.72	0.289	1.01	531	6.7	12.796	
2	9.580	0.20	0.959	0.72	0.289	1.02	533	6.7	12.757	
3	9.526	0.20	0.956	0.72	0.285	1.02	528	6.7	12.693	
4	9.627	0.20	0.982	0.71	0.294	1.00	537	6.7	12.881	
5	9.721	0.20	0.95	0.72	0.298	0.99	544	6.7	12.869	
6	9.762	0.20	0.961	0.72	0.286	1.02	520	6.6	12.946	
7	9.816	0.20	1.004	0.70	0.304	0.98	544	6.6	13.142	
8	9.871	0.20	0.989	0.70	0.290	1.02	519	6.5	13.148	
9	10.220	0.20	1.045	0.67	0.308	0.97	529	6.3	13.682	
10	10.192	0.20	1.001	0.70	0.313	0.95	544	6.5	13.509	
11	9.481	0.21	0.868	0.77	0.285	1.03	542	7.1	12.357	
12	9.372	0.21	0.891	0.76	0.287	1.03	547	7.1	12.324	
13	9.200	0.21	0.914	0.74	0.283	1.03	544	7.0	12.228	
14	9.225	0.21	0.904	0.75	0.269	1.08	518	6.9	12.220	
15	9.265	0.21	0.884	0.76	0.276	1.06	532	7.0	12.194	
16	9.220	0.21	0.879	0.77	0.277	1.06	537	7.1	12.132	
17	9.643	0.20	0.843	0.79	0.276	1.06	522	7.0	12.436	
18	9.227	0.21	0.858	0.78	0.270	1.07	526	7.1	12.070	
19	9.989	0.20	0.98	0.71	0.304	0.98	540	6.6	13.236	
20	10.279	0.20	1.06	0.67	0.324	0.93	552	6.4	13.791	
21	10.191	0.20	1.017	0.69	0.305	0.98	529	6.4	13.561	
22	9.860	0.20	0.955	0.72	0.296	1.00	534	6.7	13.024	
23	10.253	0.20	1.052	0.67	0.321	0.93	549	6.4	13.739	
24	10.329	0.20	1.036	0.68	0.314	0.95	536	6.4	13.761	
25	10.254	0.20	1.07	0.66	0.309	0.96	527	6.2	13.799	
26	10.391	0.20	1.065	0.66	0.321	0.94	542	6.3	13.920	
27	10.285	0.20	1.056	0.67	0.321	0.94	547	6.4	13.784	
28	10.274	0.20	1.063	0.66	0.310	0.96	528	6.2	13.796	
29	10.195	0.20	1.052	0.67	0.313	0.96	538	6.4	13.681	
30	9.693	0.20	0.924	0.74	0.283	1.04	522	6.7	12.754	
31	10.177	0.20	1.048	0.67	0.306	0.97	527	6.3	13.649	
32	10.163	0.20	1.061	0.67	0.312	0.96	536	6.4	13.678	
33	10.406	0.20	1.076	0.66	0.318	0.94	535	6.2	13.971	
34	10.302	0.20	1.051	0.67	0.305	0.97	520	6.2	13.784	
35	10.251	0.20	1.075	0.66	0.311	0.96	529	6.3	13.813	
36	10.098	0.20	1.069	0.66	0.309	0.97	533	6.3	13.640	
37	10.741	0.20	1.137	0.63	0.333	0.91	539	6.1	14.508	
38	10.473	0.19	1.114	0.64	0.316	0.94	525	6.1	14.164	
39	10.207	0.19	1.098	0.65	0.315	0.95	535	6.2	13.845	
40	10.215	0.20	1.068	0.66	0.302	0.98	517	6.2	13.754	
41	11.107	0.20	1.186	0.61	0.338	0.90	529	5.8	15.036	
42	10.995	0.19	1.148	0.63	0.339	0.90	538	6.0	14.799	

43	10.917	0.19	1.169	0.62	0.340	0.89	540	5.9	14.790
44	10.521	0.19	1.113	0.64	0.331	0.91	547	6.2	14.209
45	10.998	0.19	1.147	0.63	0.346	0.88	549	6.0	14.798
46	11.082	0.19	1.185	0.61	0.323	0.93	507	5.7	15.008
47	10.784	0.19	1.089	0.65	0.333	0.91	544	6.2	14.392
48	10.926	0.19	1.168	0.62	0.342	0.89	543	6.0	14.796
49	11.112	0.19	1.193	0.61	0.345	0.88	538	5.9	15.065
50	10.962	0.19	1.133	0.63	0.334	0.91	534	6.0	14.716
51	10.114	0.19	1.049	0.67	0.315	0.95	545	6.4	13.590
52	10.896	0.19	1.101	0.65	0.335	0.90	541	6.1	14.544
53	9.993	0.20	0.893	0.76	0.308	0.97	558	7.0	12.952
54	11.031	0.19	1.086	0.65	0.324	0.93	521	6.0	14.629
55	10.325	0.20	1.052	0.67	0.307	0.97	523	6.3	13.811
56	10.328	0.19	1.129	0.64	0.318	0.94	531	6.1	14.069
57	10.022	0.20	1.043	0.67	0.288	1.02	503	6.2	13.478
58	10.023	0.20	1.018	0.69	0.307	0.97	539	6.5	13.396
59	9.613	0.20	0.972	0.71	0.300	0.99	549	6.8	12.833
60	9.270	0.20	0.933	0.73	0.279	1.05	531	6.9	12.361
61	9.861	0.20	1.032	0.68	0.296	1.00	524	6.4	13.280
62	9.283	0.21	0.934	0.73	0.281	1.04	534	6.9	12.378
63	9.253	0.20	0.955	0.72	0.289	1.01	547	6.9	12.417
64	8.943	0.21	0.927	0.74	0.268	1.08	525	7.0	12.014
65	9.530	0.21	0.996	0.70	0.282	1.04	517	6.6	12.830
66	8.830	0.21	0.897	0.75	0.271	1.07	540	7.1	11.802
67	9.380	0.20	0.967	0.71	0.275	1.06	514	6.6	12.584
68	9.250	0.21	0.972	0.71	0.286	1.02	539	6.8	12.470
69	9.072	0.21	0.933	0.73	0.276	1.05	533	6.9	12.163
70	9.662	0.21	1.001	0.70	0.298	0.99	540	6.6	12.979
71	9.484	0.21	0.984	0.70	0.293	1.01	540	6.7	12.744
72	9.275	0.20	0.943	0.73	0.277	1.05	525	6.8	12.399
73	9.490	0.21	0.984	0.70	0.286	1.03	527	6.7	12.750
74	9.754	0.21	1.048	0.67	0.285	1.03	507	6.3	13.226

---

D3

1	8.805	0.21	0.278	2.19	0.209	1.41	506	13.2	9.724
2	8.381	0.22	0.215	2.77	0.196	1.50	507	16.0	9.091
3	8.571	0.22	0.248	2.43	0.197	1.48	494	14.1	9.390
4	8.479	0.22	0.292	2.10	0.200	1.46	498	12.8	9.444
5	8.387	0.22	0.274	2.21	0.201	1.46	509	13.5	9.292
6	8.941	0.21	0.260	2.33	0.210	1.40	504	13.7	9.800
7	8.753	0.21	0.204	2.31	0.192	1.43	479	13.1	9.427
8	8.427	0.22	0.225	2.17	0.187	1.46	480	12.6	9.170
9	8.572	0.22	0.200	2.35	0.190	1.44	484	13.4	9.233
10	9.161	0.21	0.087	3.96	0.196	1.40	488	20.5	9.448
11	8.749	0.22	0.125	3.24	0.191	1.44	491	17.4	9.162
12	9.463	0.21	0.054	4.95	0.203	1.36	495	25.4	9.641
13	9.518	0.21	0.013	7.55	0.203	1.37	500	38.4	9.561
14	10.302	0.20	0.113	3.29	0.220	1.28	485	17.1	10.675
15	9.366	0.21	0.202	2.30	0.212	1.31	497	13.2	10.033
16	9.388	0.21	0.126	3.16	0.205	1.34	492	16.9	9.804
17	8.814	0.21	0.237	2.07	0.207	1.34	507	12.5	9.597
18	10.015	0.20	0.374	1.45	0.246	1.16	514	9.6	11.251
19	9.867	0.20	0.319	1.63	0.238	1.19	513	10.4	10.921
20	10.867	0.19	0.155	2.64	0.243	1.17	502	14.5	11.379
21	8.835	0.21	0.221	2.18	0.202	1.37	497	12.8	9.565
22	9.959	0.20	0.195	2.33	0.224	1.25	497	13.2	10.603
23	9.111	0.21	0.423	1.33	0.220	1.27	493	9.1	10.509
24	9.871	0.20	0.082	3.96	0.207	1.34	480	20.1	10.142
25	8.333	0.22	0.853	0.78	0.245	1.17	517	7.4	11.151

---

The error propagation is determined by the mean square of U, Th, and Pb X-ray counting errors (%)



Table 3. U, Th, and Pb compositions of the grain in Figure 19c.

D1	ThO <sub>2</sub>	Th count error %	UO <sub>2</sub>	U count error %	PbO	Pb count error %	Age (Ma)	Age error Ma	ThO <sub>2</sub> *
1	4.444	0.22	0.477	1.29	0.134	1.85	523	11.9	6.022
2	3.599	0.25	0.547	1.16	0.121	2.00	526	12.2	5.409
3	3.644	0.25	0.572	1.12	0.120	2.02	510	11.8	5.537
4	3.703	0.25	0.548	1.16	0.126	1.95	537	12.3	5.516
5	4.267	0.23	0.543	1.16	0.135	1.83	523	11.4	6.064
6	4.514	0.22	0.626	1.03	0.140	1.77	500	10.3	6.585
7	4.669	0.22	0.704	0.94	0.154	1.64	518	9.9	6.999
8	4.695	0.22	0.720	0.92	0.159	1.61	528	9.9	7.078
9	4.796	0.21	0.748	0.89	0.160	1.60	518	9.5	7.271
10	4.016	0.24	0.469	1.32	0.107	2.20	453	11.7	5.568
11	3.616	0.25	0.569	1.12	0.122	1.99	522	12.0	5.499
12	3.410	0.26	0.598	1.08	0.119	2.05	519	12.1	5.389
13	3.658	0.25	0.552	1.15	0.128	1.92	548	12.3	5.485
D2									
1	4.355	0.22	0.362	1.61	0.132	1.82	558	13.6	5.552
2	4.852	0.21	0.499	1.23	0.141	1.73	510	10.9	6.502
3	4.647	0.22	0.443	1.36	0.138	1.75	531	11.8	6.112
4	4.528	0.22	0.429	1.40	0.131	1.82	518	11.9	5.946
5	4.308	0.23	0.446	1.36	0.127	1.88	516	12.0	5.783
D3									
1	5.929	0.19	0.194	2.59	0.117	2.17	420	14.2	6.568
2	5.442	0.20	0.181	2.77	0.116	2.20	453	16.0	6.039
3	5.440	0.20	0.202	2.53	0.118	2.17	455	15.2	6.106
4	6.031	0.19	0.178	2.75	0.133	1.95	473	16.0	6.618
5	6.357	0.18	0.182	2.70	0.124	2.05	420	14.3	6.957
6	6.094	0.19	0.197	2.55	0.134	1.93	468	15.0	6.743
7	5.748	0.19	0.147	3.21	0.118	2.15	446	17.3	6.233
8	5.174	0.20	0.249	2.16	0.130	1.99	510	15.0	5.995
9	4.990	0.21	0.329	1.72	0.125	2.10	484	13.2	6.074
10	6.613	0.18	0.101	4.07	0.134	1.98	454	20.6	6.946
11	7.077	0.17	0.112	3.73	0.162	1.68	512	21.0	7.446
12	6.618	0.18	0.230	2.24	0.158	1.71	504	14.2	7.376
13	5.982	0.19	0.303	1.82	0.126	2.04	426	11.7	6.981
14	5.269	0.20	0.402	1.46	0.130	1.98	464	11.5	6.594
15	5.149	0.20	0.357	1.61	0.127	2.02	473	12.3	6.326
16	4.556	0.22	0.374	1.56	0.108	2.35	440	12.4	5.789
17	4.767	0.21	0.358	1.62	0.122	2.10	483	12.9	5.947
18	5.193	0.20	0.356	1.62	0.126	2.04	466	12.2	6.366
19	5.150	0.20	0.274	2.00	0.120	2.15	467	13.7	6.053
20	4.921	0.21	0.345	1.66	0.129	2.01	501	13.1	6.058
21	5.161	0.20	0.252	2.15	0.120	2.16	472	14.4	5.992
22	6.555	0.18	0.027	8.15	0.131	2.00	464	38.9	6.644
23	6.006	0.19	0.105	4.04	0.121	2.14	449	20.5	6.352
24	4.709	0.21	0.160	3.09	0.104	2.42	468	18.4	5.236
25	5.887	0.19	0.316	1.77	0.144	1.81	489	12.4	6.929
26	6.444	0.18	0.320	1.73	0.156	1.69	489	11.9	7.499
D4									
1	0.195	2.20	0.145	3.91	0.014	8.00	512	47.0	0.672
2	0.204	2.10	0.108	5.16	0.015	7.91	635	61.4	0.560
3	0.217	1.99	0.136	4.15	0.013	8.52	485	47.0	0.665
4	0.201	2.12	0.143	3.94	0.011	8.99	419	42.1	0.672
5	0.462	1.05	0.248	2.36	0.029	5.54	531	32.5	1.278
6	1.448	0.45	0.026	15.7	0.029	6.95	455	78.1	1.534
7	1.495	0.44	0.069	7.22	0.028	7.31	384	39.5	1.722
8	1.067	0.55	0.061	8.26	0.025	7.71	476	53.8	1.268

The error propagation is determined by the mean square of U, Th, and Pb X-ray counting errors (%)

Table 4. U, Th, and Pb compositions of the grain in Figure 19d.

D1	ThO <sub>2</sub>	Th count error %	UO <sub>2</sub>	U count error %	PbO	Pb count error %	Age (Ma)	Age error Ma	ThO <sub>2</sub> *
1	12.306	0.13	0.804	0.82	0.329	0.93	517	6.4	14.965
2	12.704	0.12	0.853	0.79	0.342	0.90	518	6.2	15.526
3	11.959	0.13	0.844	0.79	0.319	0.95	509	6.3	14.751
4	12.519	0.13	0.921	0.74	0.341	0.90	515	6.0	15.565
5	12.903	0.12	0.960	0.72	0.346	0.89	506	5.8	16.078
6	12.831	0.12	0.924	0.74	0.344	0.90	509	6.0	15.887
<b>D2</b>									
1	7.935	0.16	0.404	1.42	0.175	1.57	445	9.4	9.268
2	8.414	0.16	0.294	1.80	0.194	1.43	487	11.2	9.384
3	7.921	0.16	0.383	1.48	0.196	1.43	502	10.4	9.185
4	8.265	0.16	0.420	1.37	0.200	1.40	488	9.6	9.651
5	8.556	0.15	0.200	2.39	0.194	1.44	495	13.8	9.216
<b>D3</b>									
1	8.249	0.16	0.109	3.65	0.176	1.56	481	19.1	8.608
2	8.784	0.15	0.106	3.66	0.177	1.55	456	18.1	9.133
3	8.833	0.15	0.082	4.21	0.177	1.55	458	20.6	9.103
4	9.371	0.15	0.056	5.00	0.194	1.43	478	24.9	9.556
5	9.435	0.15	0.091	3.87	0.195	1.42	472	19.5	9.735
6	8.986	0.15	0.218	2.22	0.190	1.46	461	12.3	9.705
7	8.730	0.15	0.123	3.33	0.183	1.51	472	17.3	9.135
<b>D4</b>									
1	6.349	0.18	0.184	2.66	0.138	1.93	467	15.4	6.956
2	6.348	0.18	0.216	2.36	0.150	1.80	500	14.9	7.060
3	5.647	0.19	0.220	2.36	0.122	2.17	451	14.5	6.372
4	6.130	0.18	0.200	2.52	0.138	1.95	478	15.3	6.789
5	6.435	0.18	0.173	2.79	0.143	1.88	480	16.2	7.005
6	6.556	0.18	0.184	2.65	0.140	1.91	460	15.0	7.163
7	5.550	0.20	0.237	2.23	0.119	2.20	443	13.9	6.331
8	5.675	0.19	0.218	2.38	0.125	2.11	460	14.7	6.394

The error propagation is determined by the mean square of U, Th, and Pb X-ray counting errors (%)

Table 5. U, Th, and Pb compositions of the grain in Figure 19e.

D1	ThO <sub>2</sub>	Th count error %	UO <sub>2</sub>	U count error %	PbO	Pb count error %	Age (Ma)	Age error Ma	ThO <sub>2</sub> *
1	10.763	0.14	0.745	0.87	0.269	1.03	479	6.5	13.220
2	9.825	0.14	0.807	0.83	0.244	1.12	460	6.4	12.486
3	10.425	0.14	0.651	0.97	0.246	1.10	461	6.8	12.572
4	10.938	0.13	0.640	0.98	0.270	1.02	487	6.9	13.048
5	10.653	0.14	0.634	0.99	0.254	1.08	469	6.9	12.744
6	10.625	0.14	0.587	1.05	0.249	1.09	467	7.1	12.561
7	10.913	0.13	0.594	1.04	0.262	1.05	479	7.1	12.872
8	10.868	0.14	0.623	1.00	0.260	1.06	474	6.9	12.922
9	10.567	0.14	0.578	1.06	0.253	1.08	477	7.2	12.473
10	11.149	0.13	0.638	0.98	0.262	1.05	466	6.7	13.253
D2									
1	7.846	0.16	0.497	1.21	0.186	1.40	462	8.6	9.482
2	7.108	0.17	0.491	1.23	0.174	1.49	469	9.1	8.724
3	7.771	0.16	0.43	1.36	0.177	1.46	454	9.1	9.186
4	7.509	0.17	0.441	1.34	0.179	1.45	470	9.3	8.961
5	6.914	0.17	0.223	2.29	0.131	1.87	404	12.0	7.648
6	8.546	0.15	0.232	2.17	0.174	1.46	440	11.5	9.310
7	8.148	0.16	0.225	2.22	0.171	1.48	453	12.1	8.889
8	6.911	0.17	0.211	2.39	0.136	1.81	422	12.7	7.606
D3									
1	8.992	0.15	0.092	3.93	0.179	1.54	454	19.2	9.295
2	8.788	0.15	0.032	6.44	0.178	1.54	471	31.2	8.893
3	9.386	0.15	0.073	4.39	0.183	1.50	448	20.8	9.627
4	9.306	0.15	0.033	6.17	0.179	1.53	448	28.5	9.415
5	9.429	0.15	0.009	8.14	0.181	1.52	451	37.4	9.459
6	9.727	0.14	0.035	5.86	0.195	1.42	467	28.2	9.842
7	10.196	0.14	0.047	5.14	0.207	1.35	471	25.0	10.351
8	9.329	0.15	0.162	2.74	0.195	1.42	466	14.4	9.863
9	9.474	0.15	0.010	7.91	0.189	1.46	468	37.7	9.507
10	9.721	0.14	0.000	9.61	0.193	1.43	468	45.5	9.721
11	10.781	0.14	0.078	4.00	0.220	1.28	469	19.7	11.038
12	9.675	0.14	0.001	8.77	0.190	1.46	462	41.1	9.678
13	10.055	0.14	0.077	4.14	0.209	1.34	477	20.8	10.309
14	9.980	0.14	0.082	4.01	0.198	1.39	455	19.3	10.250
15	9.463	0.15	0.001	9.12	0.181	1.40	450	41.5	9.466
D4									
1	5.683	0.19	0.204	2.45	0.119	2.16	441	14.4	6.354
2	5.829	0.19	0.196	2.57	0.120	2.18	437	14.8	6.473
3	6.219	0.18	0.192	2.58	0.125	2.10	430	14.3	6.850
4	5.865	0.19	0.209	2.44	0.117	2.24	421	14.0	6.552
5	5.898	0.19	0.206	2.47	0.123	2.13	441	14.4	6.575
6	6.032	0.19	0.181	2.72	0.121	2.18	430	15.0	6.627

The error propagation is determined by the mean square of U, Th, and Pb X-ray counting errors (%)

Table 6. U, Th, and Pb compositions of the grain in Figure 19f.

D1	ThO <sub>2</sub>	Th count error %	UO <sub>2</sub>	U count error %	PbO	Pb count error %	Age (Ma)	Age error Ma	ThO <sub>2</sub> *
1	10.16	0.20	0.241	2.88	0.863	2.24	1,779	65.0	11.008
2	11.225	0.19	0.187	3.36	0.937	2.13	1,791	71.3	11.883
3	11.917	0.18	0.206	3.11	1.011	2.18	1,815	69.0	12.642
4	10.484	0.20	0.219	3.05	0.876	1.87	1,768	63.4	11.254
5	9.674	0.20	0.203	3.27	0.814	1.69	1,779	65.6	10.388
6	10.064	0.20	0.208	3.20	0.860	1.46	1,807	63.7	10.796
7	9.867	0.20	0.256	2.75	0.843	1.48	1,776	55.6	10.768
8	8.892	0.21	0.203	3.32	0.756	1.81	1,786	67.6	9.606
D2									
1	5.042	0.29	1.410	0.77	0.788	2.50	1,750	46.1	10.276
2	4.920	0.30	1.374	0.79	0.754	1.53	1,722	30.1	10.021
3	4.572	0.31	0.866	1.12	0.631	1.52	1,838	35.2	7.787
4	4.415	0.31	1.001	1.00	0.672	1.42	1,870	33.0	8.131
5	7.026	0.24	0.304	2.52	0.601	1.35	1,686	48.4	8.155
D3									
1	5.526	0.28	0.784	1.20	0.178	1.55	516	10.2	8.284
2	6.235	0.26	0.821	1.16	0.194	1.34	510	9.1	9.123
3	6.014	0.26	0.766	1.22	0.194	1.39	533	10.0	8.709
4	5.958	0.27	1.044	0.97	0.217	1.03	541	7.8	9.631
5	6.181	0.26	1.102	0.93	0.231	1.08	552	8.0	10.058
6	6.092	0.26	0.807	1.18	0.193	1.09	518	8.4	8.931
7	4.840	0.30	0.555	1.59	0.155	1.05	545	10.5	6.793
8	5.053	0.29	0.849	1.13	0.165	1.06	494	7.8	8.040
9	5.032	0.29	0.871	1.11	0.165	1.49	491	9.2	8.096
10	5.145	0.29	0.809	1.18	0.184	1.46	552	10.5	7.991
11	4.827	0.30	0.653	1.40	0.161	1.45	541	11.0	7.124
12	5.760	0.27	1.196	0.87	0.224	2.11	541	12.4	9.968
D4									
1	6.704	0.25	0.400	2.04	0.165	1.54	484	12.4	8.024
2	7.608	0.23	0.406	2.00	0.175	1.54	461	11.7	8.948
3	7.435	0.23	0.406	2.00	0.179	1.50	480	12.1	8.775
4	6.779	0.25	0.426	1.94	0.154	1.42	444	10.7	8.185
5	6.643	0.25	0.360	2.22	0.150	1.57	451	12.3	7.831
6	11.186	0.19	0.288	2.47	0.256	2.10	496	16.1	12.136
7	11.32	0.19	0.313	2.34	0.264	1.12	503	13.1	12.353
D5									
1	4.491	0.31	0.266	2.91	0.093	2.16	409	14.9	5.427
2	12.132	0.18	0.218	2.96	0.274	1.61	502	16.9	12.899
3	13.203	0.17	0.342	2.13	0.295	1.65	484	13.1	14.406
4	13.656	0.17	0.244	2.66	0.305	1.08	496	14.3	14.514
5	12.88	0.17	0.208	3.00	0.296	1.05	513	16.3	13.612
6	11.481	0.19	0.276	2.54	0.26	1.11	494	13.7	12.452
D6									
1	4.491	0.31	0.266	2.91	0.093	2.16	409	14.9	5.427
2	4.513	0.31	0.263	2.94	0.098	2.18	430	15.8	5.438
3	4.955	0.29	0.355	2.29	0.125	2.40	480	16.0	6.204
4	4.302	0.32	0.274	2.86	0.095	1.46	430	13.9	5.266
5	4.537	0.31	0.253	3.04	0.099	1.43	435	14.7	5.427
6	4.351	0.32	0.261	2.97	0.081	1.46	367	12.2	5.269
7	4.541	0.31	0.200	3.67	0.105	1.52	475	18.9	5.245
8	4.388	0.32	0.261	2.97	0.093	1.10	418	13.3	5.306
9	4.635	0.31	0.271	2.86	0.105	1.02	448	13.7	5.588
10	5.649	0.27	0.299	2.60	0.124	1.40	441	13.1	6.701
11	4.577	0.31	0.282	2.78	0.098	1.35	420	13.0	5.569

The error propagation is determined by the mean square of U, Th, and Pb X-ray counting errors (%)

Table 7. U, Th, and Pb compositions of the grain in Figure 19g.

D1	Th count			U count		Pb count		Age	Age error	ThO <sub>2</sub> *
	ThO <sub>2</sub>	error %	UO <sub>2</sub>	error %	PbO	error %	(Ma)	Ma		
1	2.835	0.29	0.355	1.67	0.306	0.96	1,688	32.9	4.142	
2	2.767	0.29	0.311	1.86	0.295	0.99	1,719	36.6	3.912	
3	3.266	0.27	0.307	1.87	0.357	0.85	1,840	38.1	4.396	
4	2.545	0.31	0.226	2.47	0.233	1.19	1,584	43.7	3.377	
5	2.965	0.28	0.151	3.43	0.264	1.09	1,711	61.8	3.521	
6	3.200	0.27	0.358	1.64	0.319	0.93	1,619	30.8	4.518	
7	3.295	0.27	0.355	1.65	0.299	0.99	1,499	29.1	4.602	
8	3.068	0.28	0.361	1.64	0.331	0.91	1,717	32.6	4.397	
9	3.119	0.27	0.102	4.72	0.266	1.09	1,736	84.2	3.494	
10	2.764	0.26	0.206	1.88	0.260	2.37	1,686	51.2	3.522	
11	3.541	0.25	0.437	1.38	0.356	0.86	1,588	26.1	5.149	
12	3.249	0.19	0.224	3.10	0.291	0.67	1,636	52.0	4.073	
13	5.883	0.20	0.154	3.20	0.490	0.72	1,733	56.9	6.450	
14	5.461	0.26	0.152	1.03	0.447	2.41	1,695	44.6	6.020	
15	4.438	0.22	0.533	1.18	0.472	0.70	1,685	23.4	6.400	
16	4.387	0.26	0.527	0.83	0.469	1.01	1,693	22.6	6.327	
17	1.769	0.39	0.372	1.62	0.268	1.07	1,918	38.0	3.138	
D2										
1	8.885	0.15	0.457	1.28	0.315	0.95	708	11.3	10.416	
2	3.878	0.24	0.773	0.87	0.167	1.63	607	11.3	6.468	
3	3.532	0.25	0.744	0.90	0.154	1.75	601	11.9	6.025	
4	3.802	0.24	0.787	0.86	0.198	1.40	718	11.9	6.439	
5	3.670	0.25	0.846	0.81	0.188	1.46	677	11.4	6.505	
D3										
1	7.286	0.17	0.513	1.18	0.195	1.43	511	9.5	8.982	
2	6.239	0.18	0.457	1.31	0.168	1.63	510	10.7	7.750	
3	5.954	0.19	0.528	1.16	0.170	1.61	519	10.3	7.700	
4	7.290	0.17	0.381	1.49	0.187	1.48	514	10.8	8.550	
5	3.913	0.24	0.465	1.31	0.118	2.17	509	13.0	5.451	
6	4.792	0.21	0.397	1.48	0.122	2.16	471	12.4	6.105	
7	4.690	0.21	0.367	1.58	0.123	2.16	490	13.2	5.903	
8	4.336	0.23	0.595	1.07	0.134	1.99	500	11.4	6.303	
9	4.528	0.22	0.543	1.15	0.141	1.88	524	11.6	6.323	
10	3.500	0.26	0.904	0.77	0.148	1.78	536	10.5	6.489	
11	4.611	0.22	0.456	1.33	0.133	2.02	511	12.4	6.119	
12	3.445	0.26	0.795	0.85	0.146	1.81	564	11.4	6.074	
13	5.676	0.19	0.635	1.01	0.168	1.61	508	9.7	7.776	
14	6.111	0.19	0.521	1.18	0.163	1.68	490	10.1	7.834	
15	5.013	0.21	0.680	0.96	0.156	1.73	505	10.0	7.261	
16	3.756	0.24	0.811	0.84	0.151	1.78	550	10.9	6.438	
17	3.860	0.24	0.670	0.97	0.134	1.99	519	11.6	6.075	
18	4.298	0.23	0.542	1.15	0.118	2.24	457	11.6	6.090	
19	3.747	0.25	0.567	1.11	0.123	2.16	515	12.6	5.622	
20	3.885	0.24	0.629	1.02	0.135	1.99	532	12.0	5.965	
21	4.414	0.22	0.465	1.31	0.125	2.11	494	12.3	5.952	
22	4.154	0.23	0.567	1.12	0.140	1.92	545	12.2	6.029	
23	3.747	0.25	0.816	0.90	0.148	1.75	539	10.7	6.445	
24	4.461	0.22	0.367	1.54	0.116	2.23	481	13.1	5.674	
25	4.701	0.21	0.451	1.33	0.137	1.96	520	12.4	6.192	
26	4.449	0.22	0.484	1.26	0.125	2.13	487	12.1	6.049	
27	3.617	0.25	0.842	0.82	0.133	2.00	489	10.6	6.401	
28	3.778	0.24	0.608	1.06	0.128	2.07	520	12.2	5.788	
29	6.728	0.18	0.348	1.61	0.158	1.70	472	11.1	7.879	
30	3.856	0.24	0.838	0.81	0.149	1.83	528	10.6	6.627	
31	4.088	0.23	0.479	1.28	0.122	2.18	506	12.8	5.672	
32	3.640	0.25	0.812	0.84	0.138	1.92	513	10.8	6.325	
33	4.605	0.22	0.521	1.19	0.133	2.02	495	11.7	6.328	
34	4.255	0.23	0.575	1.10	0.122	2.16	467	11.4	6.156	
35	4.334	0.22	0.482	1.27	0.117	2.23	465	12.0	5.928	
D4										
1	4.022	0.24	0.338	1.70	0.110	2.31	504	14.5	5.139	
2	4.022	0.24	0.432	1.39	0.117	2.19	505	13.2	5.450	
3	3.855	0.24	0.396	1.50	0.114	2.24	519	14.0	5.164	

4	4.142	0.23	0.417	1.43	0.114	2.22	486	12.9	5.520
5	3.981	0.24	0.359	1.62	0.108	2.34	492	14.1	5.168
6	3.626	0.25	0.384	1.54	0.101	2.50	486	14.3	4.895
7	3.641	0.25	0.429	1.41	0.101	2.51	470	13.6	5.059
8	4.445	0.22	0.379	1.55	0.112	2.36	463	13.1	5.698
9	4.523	0.22	0.582	1.09	0.140	1.93	511	11.4	6.447
10	3.834	0.24	0.799	0.85	0.152	1.76	551	10.9	6.475
11	3.550	0.25	0.838	0.82	0.136	1.95	506	10.8	6.320
12	3.617	0.25	0.421	1.43	0.104	2.44	489	13.9	5.009
13	3.808	0.24	0.414	1.45	0.106	2.39	482	13.5	5.176
14	3.527	0.25	0.397	1.50	0.094	2.66	458	14.0	4.839
15	3.597	0.25	0.380	1.56	0.094	2.66	457	14.1	4.853
16	3.904	0.24	0.388	1.52	0.105	2.40	477	13.6	5.187
17	4.063	0.23	0.339	1.70	0.106	2.39	482	14.2	5.184
18	4.551	0.22	0.525	1.18	0.141	1.92	527	11.9	6.286
19	3.408	0.26	0.523	1.19	0.104	2.49	477	13.2	5.137
20	3.353	0.22	0.630	1.17	0.105	0.70	456	6.3	5.435
21	3.726	0.25	0.357	1.64	0.107	2.38	513	14.9	4.906
22	3.479	0.26	0.353	1.67	0.097	2.61	491	15.3	4.646
23	3.957	0.24	0.399	1.49	0.109	2.33	486	13.5	5.276
24	3.435	0.26	0.911	0.76	0.152	1.75	553	10.6	6.446
25	3.458	0.26	0.924	0.76	0.153	1.74	551	10.6	6.512
26	2.942	0.28	0.578	1.10	0.110	2.38	532	14.0	4.853
27	3.082	0.28	0.748	0.89	0.122	2.13	516	12.0	5.554
28	3.114	0.27	0.522	1.20	0.107	2.43	520	14.2	4.839
29	3.390	0.26	0.924	0.75	0.147	1.81	536	10.6	6.444
30	2.850	0.29	0.506	1.23	0.093	2.76	484	14.7	4.523

---

D5

1	5.120	0.20	0.203	2.54	0.104	2.43	424	14.9	5.789
2	5.415	0.20	0.257	2.10	0.117	2.20	440	13.4	6.261
3	5.551	0.20	0.248	2.15	0.114	2.25	422	13.2	6.368
4	4.969	0.21	0.249	2.17	0.118	2.20	480	14.9	5.789
5	5.117	0.20	0.275	2.00	0.114	2.26	446	13.5	6.023
6	5.675	0.19	0.201	2.53	0.130	2.02	483	15.7	6.337
7	6.370	0.18	0.352	1.60	0.153	1.75	478	11.4	7.529
8	6.295	0.18	0.362	1.57	0.155	1.73	487	11.4	7.487
9	4.533	0.22	0.391	1.49	0.128	2.09	517	13.3	5.821
10	4.053	0.23	0.676	0.96	0.125	2.13	469	11.0	6.280
11	4.971	0.21	0.339	1.69	0.108	2.38	419	12.3	6.088
12	5.177	0.20	0.264	2.05	0.116	2.24	452	13.8	6.047
13	5.161	0.20	0.298	1.86	0.107	2.41	411	12.5	6.143
14	4.916	0.21	0.344	1.66	0.117	2.24	456	12.7	6.049
15	4.377	0.22	0.424	1.41	0.122	2.20	497	13.0	5.774
16	4.342	0.23	0.481	1.27	0.130	2.07	515	12.6	5.926
17	5.407	0.20	0.258	2.10	0.116	2.22	437	13.4	6.257
18	5.481	0.20	0.280	1.96	0.115	2.26	424	12.7	6.403
19	5.671	0.19	0.294	1.88	0.123	2.11	437	12.4	6.639

---

The error propagation is determined by the mean square of U, Th, and Pb X-ray counting errors (%)

Table 8. U, Th, and Pb compositions of the grain in Figure 19h.

all	ThO <sub>2</sub>	Th count error %	UO <sub>2</sub>	U count error %	PbO	Pb count error %	Age (Ma)	Age error Ma	ThO <sub>2</sub> *
1	11.752	0.13	0.387	1.40	0.281	1.04	507	8.9	13.028
2	14.253	0.12	0.293	1.68	0.291	1.02	450	8.9	15.219
3	13.243	0.12	0.262	1.84	0.265	1.10	443	9.5	14.107
4	12.767	0.12	0.246	1.93	0.259	1.11	449	10.0	13.578
5	11.234	0.13	0.234	2.03	0.255	1.12	500	11.6	12.005
6	10.518	0.14	0.249	1.98	0.254	1.14	527	12.1	11.339
7	10.821	0.13	0.224	2.11	0.262	1.11	533	12.7	11.559
8	10.974	0.13	0.218	2.10	0.225	1.27	453	11.1	11.693
9	11.833	0.13	0.233	2.04	0.250	1.14	467	10.9	12.601
10	10.285	0.14	0.245	2.02	0.236	1.22	500	11.8	11.093
11	11.727	0.13	0.225	2.09	0.243	1.18	459	11.0	12.469
12	11.513	0.13	0.222	2.12	0.246	1.17	473	11.5	12.245
13	11.686	0.13	0.249	1.94	0.253	1.15	476	10.8	12.507
14	12.953	0.12	0.237	1.98	0.263	1.10	451	10.2	13.734
15	12.604	0.12	0.222	2.07	0.276	1.06	487	11.3	13.336
16	12.810	0.12	0.178	2.38	0.273	1.07	480	12.5	13.397
17	12.828	0.12	0.234	2.00	0.273	1.07	473	10.7	13.599
18	12.840	0.12	0.216	2.11	0.269	1.09	467	11.1	13.552
19	12.758	0.12	0.188	2.31	0.281	1.06	494	12.6	13.378
20	12.492	0.13	0.197	2.26	0.239	1.19	429	11.0	13.141
21	12.812	0.12	0.210	2.15	0.267	1.10	466	11.3	13.504
22	12.465	0.13	0.133	2.87	0.254	1.14	464	14.3	12.903
23	13.072	0.12	0.206	2.17	0.267	1.09	457	11.1	13.751
24	14.138	0.12	0.217	2.06	0.296	1.01	469	10.8	14.853
25	13.985	0.12	0.220	2.04	0.291	1.02	466	10.6	14.710
26	12.588	0.13	0.217	2.11	0.267	1.09	473	11.3	13.303
27	12.765	0.12	0.202	2.21	0.267	1.09	468	11.5	13.431
28	12.700	0.12	0.201	2.22	0.267	1.09	470	11.6	13.363
29	12.917	0.12	0.240	1.97	0.263	1.10	452	10.2	13.708
30	12.642	0.12	0.206	2.19	0.264	1.09	467	11.4	13.321
31	12.658	0.12	0.218	2.10	0.260	1.11	458	10.9	13.377

The error propagation is determined by the mean square of U, Th, and Pb X-ray counting errors (%)